

Correlations in the Cosmic Far-Infrared Background at 250, 350, and 500 μm Reveal
Clustering of Star-Forming Galaxies

by

Marco P. Viero

A thesis submitted in conformity with the requirements
for the degree of Doctor of Philosophy
Graduate Department of Astronomy and Astrophysics
University of Toronto

© Marco P. Viero, 2010

Abstract

Correlations in the Cosmic Far-Infrared Background at 250, 350, and 500 μm Reveal
Clustering of Star-Forming Galaxies

Marco P. Viero

Doctor of Philosophy

Department of Astronomy and Astrophysics

University of Toronto

2010

We demonstrate the application of CMB techniques to measure the clustering of infrared emitting star-forming galaxies. We detect correlations in the cosmic far-infrared background due to the clustering of star-forming galaxies in observations made with the Balloon-borne Large Aperture Submillimeter Telescope, BLAST, at 250, 350, and 500 μm . We perform jackknife and other tests to confirm the reality of the signal. The measured correlations are well fit by a power law over scales of 5–25 arcminutes, with $\Delta I/I = 15.1 \pm 1.7\%$. We adopt a specific model for submillimeter sources in which the contribution to clustering comes from sources in the redshift ranges $1.3 \leq z \leq 2.2$, $1.5 \leq z \leq 2.7$, and $1.7 \leq z \leq 3.2$, at 250, 350 and 500 μm , respectively. With these distributions, our measurement of the power spectrum, $P(k_\theta)$, corresponds to linear bias parameters, $b = 3.8 \pm 0.6, 3.9 \pm 0.6$ and 4.4 ± 0.7 , respectively. We further interpret the results in terms of the halo model, and find that at the smaller scales, the simplest halo model fails to fit our results. One way to improve the fit is to increase the radius at which dark matter halos are artificially truncated in the model, which is equivalent to having some star-forming galaxies at $z \geq 1$ located in the outskirts of groups and clusters. In the context of this model we find a minimum halo mass required to host a galaxy is $\log(M_{\text{min}}/M_\odot) = 11.5_{-0.1}^{+0.4}$, and we derive effective biases $b_{\text{eff}} = 2.2 \pm 0.2, 2.4 \pm 0.2$, and 2.6 ± 0.2 , and effective masses $\log(M_{\text{eff}}/M_\odot) = 12.9 \pm 0.3, 12.8 \pm 0.2$, and 12.7 ± 0.2 , at 250, 350 and 500 μm , corresponding to spatial correlation lengths of $r_0 = 4.9, 5.0$, and $5.2 \pm 0.7 h^{-1}$ Mpc, respectively. Finally, we discuss implications for clustering measurement strategies with *Herschel* and *Planck*.

Acknowledgements

Innumerable thanks to Barth Netterfield and Peter Martin for giving me this chance and believing in me throughout. Likewise to Enzo Pascale, who always made me feel valuable and whose presence lit up a room. Thanks to Mark Devlin, Mark Halpern, and Douglas Scott, for providing encouragement and guidance, and letting me take an idea and run with it. Thanks to Itziar Aretxaga and David Hughes for their warmth, support and understanding. Thanks to Leigh Phoenix for his help and unwavering faith. Thanks to my committee, past and present, including Bob Abraham, Ray Carlberg, Ue-Li Pen, Colin Borys and Brendan Crill, for helping me get on this path to begin with.

To my friends and colleagues, too many to name, but here we go, Ed Chapin, Don Wiebe, Gaelen Marsden, Chris Semisch, Marie Rex, Nick Thomas, Lorenzo Moncelsi, Matt Truch, Guillaume Patanchon, Olivier Doré, Jon Sievers, Natalia Asari, Jean Coupon, Svetlana Starikova, Santiago Gonzalez, Pollo Soler, Sherry Yeh, Natalie Gandilo, Steve Benton, Laura Fissel, Erin Mentuch, Jackie Radigan, Kaitlin Kratter, Arabindo Roy, Daniela Goncalves, Andrew Shannon, Ivana Damjanov, and on and on, thanks, I owe you. A very special thanks to Mattia Negrello for agreeing to be a collaborator on this work, and turning out to be a great friend as well. Thanks to my partners in crime, Mohan Sarovar and Greg Bewley. Thanks to Princess Carolyn, who somehow put up with me. And of course to my family, who were there when I needed them, and gave me more than I could ever possibly give back.

Contents

Abstract	ii
Acknowledgements	iii
List of Figures	v
List of Tables	vi
1 Introduction	1
1.1 Large Scale Structure of the Universe	1
1.1.1 The observed galaxy distribution	2
1.2 Definitions	4
1.3 Cosmic Infrared Background	4
1.3.1 Origin of the CIB	5
1.3.1.1 Galaxies	6
1.3.1.2 Foregrounds	6
1.4 CIB: Observables and Obstacles	7
1.4.1 Mean Level	8
1.4.2 Fluctuations	9
1.4.2.1 Negative K-correction	10
1.4.2.2 Confusion	11
1.4.3 State of Measurements	11
1.4.3.1 Mean Level	11
1.4.3.2 Fluctuations	11
1.5 Chapter Description	12
2 BLAST	13
2.1 Introduction	13
2.1.1 Science Goals	14
2.1.2 Flights and Fields	15
2.2 The Instrument	17
2.2.1 Optics	18
2.2.2 Secondary Support Structure	21
2.2.2.1 Mirror Assembly	21
2.2.2.2 Struts	22
2.2.2.3 Fairings	22
2.2.3 Detectors	23

2.2.4	Gondola	24
2.2.5	Cryostat	26
2.2.6	Attitude Sensors	27
2.2.6.1	Star-Cameras	28
2.2.6.2	Gyroscopes	29
2.3	Data Reconstruction	30
2.3.1	Attitude Determination	31
2.3.1.1	Attitude Matrix and Quaternions	32
2.3.1.2	Kalman Filter	34
2.3.1.3	Non-Linear Kalman Filter applied to BLAST	35
2.3.1.4	Pointing Reconstruction Results	38
2.3.2	Data Reduction	39
2.3.2.1	Timestream Preparation	39
2.3.2.2	Mapmaking	40
2.3.3	BLAST Simulator	42
2.4	Maps	42
2.4.1	GOODS	42
2.4.2	SEP	43
3	The Large Scale Galaxy Distribution	47
3.1	Introduction	47
3.2	Correlations and the Correlation Function: Overview	49
3.2.1	Two-Point Correlation Function	49
3.2.1.1	Angular Correlation Function	50
3.2.1.2	Limber equation	50
3.2.2	Clustering Estimators	51
3.2.2.1	Integral Constraint	52
3.2.2.2	Consequences of a Large Beam	53
3.2.3	Power Spectrum	57
3.2.3.1	Shot Noise	60
3.2.3.2	Power Spectrum in Practice	60
3.3	Halo Model	61
3.3.1	Dark Matter Halos	61
3.3.1.1	Perturbation Theory and Spherical Collapse Model	62
3.3.1.2	Halo Mass Function	63
3.3.1.3	Halo Density Profiles	64
3.3.1.4	Dark Matter Power Spectrum	65
3.3.2	Galaxy Power Spectrum and the Halo Occupation Number	66
3.4	Conclusion	67
4	Measuring Clustering with BLAST	69
4.1	Introduction	69
4.2	Two-Point Correlation Function from Catalogs	70
4.2.1	Preparing Random Catalogs	71
4.2.2	Results	72
4.3	Power Spectrum from Maps	75

4.3.1	Overview	75
4.3.2	Map Preparation	75
4.3.3	Wide-Only	75
4.3.3.1	Transfer Function	76
4.3.3.2	Jackknife tests	78
4.3.4	Deep + Wide	78
4.3.4.1	Polynomial Removal	79
4.3.4.2	Noise-Weighted Deep+Wide Maps	79
4.3.5	Clustered Mock-Maps	79
4.4	Maps	81
4.5	Making the Measurement	90
4.5.1	Wide-Only Power Spectrum	90
4.5.2	Uncertainties	90
4.5.3	Deep+Wide Power Spectrum	90
4.5.3.1	Noise-Weighted Transfer Function	91
4.5.4	Poisson Noise	91
4.5.5	Galactic Foregrounds	92
4.5.6	Clustering Signal	92
4.5.6.1	Wide-Only	92
4.5.6.2	Deep+Wide	94
4.5.7	Power-Law Fit to Normalized Clustering Signal	95
4.5.8	Cross-Band Correlations	97
4.6	Physical Interpretation	99
4.6.1	Source Population Model	99
4.6.2	Linear Bias Model	101
4.6.3	Halo Model	101
4.6.4	Halo Model Fits	103
4.7	Conclusion	106
5	Discussion, Conclusion, and Future Work	108
5.1	Clustering in Context	108
5.2	Comparison with other observations	109
5.3	Clustering Evolution	111
5.4	Implications	113
5.5	Understanding the Clustering Signal	114
5.5.1	Observations	114
5.5.2	Simulations	114
5.5.2.1	The tri-axial nature of dark matter halos	114
5.6	Applications for Future Models	116
5.6.1	Shot Noise Degeneracy	119
5.7	Summary	119
5.8	Future Work	120
	Bibliography	122

List of Figures

1.1	Transmission of the Atmosphere	3
1.2	Dust Mass vs. Luminosity	7
1.3	Negative K-correction	10
2.1	Sampling the Dust SED	15
2.2	BLAST05 Flight Path	16
2.3	BLAST05 Science Targets	17
2.4	BLAST06 Flight Path	18
2.5	BLAST06 Science Targets	19
2.6	BLAST06 Optics	20
2.7	Strehl Ratios	20
2.8	Secondary Support Structure	23
2.9	Finite Element Analysis of Secondary Support Structure	24
2.10	Mechanical Drawing of Fairing	25
2.11	Ray-Trace of Fairings	26
2.12	Spider-Web Bolometer	27
2.13	BLAST Bandpasses	28
2.14	Solidworks Drawing of BLAST	29
2.15	CSBF Launch Vehicle	30
2.16	BLAST Cryostat	31
2.17	Pointing Solution Example	39
2.18	Optbin Map of GOODS-south	43
2.19	SANEPIC Map of GOODS-south	44
2.20	Optbin Map of SEP	45
2.21	SANEPIC Map of SEP	46
3.1	Point Sources Convolved with BLAST Beam	53
3.2	Demonstration of Resolved Sources	54
3.3	Monte Carlo Simulation of Signal-to-Noise of Recovered Sources	56
3.4	Correlation Function of 2.5- σ 250 μ m Catalog	57
3.5	Correlation Function of Random Maps	58
4.1	Comparing Correlation Function Estimators on Random Maps	72
4.2	Correlation Function of 2.5- σ BLAST Catalog	74
4.3	Clustered Mock-Maps	77
4.4	Transfer Function	77
4.5	Jackknife Tests	78
4.6	BGS-Wide Map	81

4.7	BGS-Deep+Wide Flux and Hits Maps	82
4.8	Polynomial Removed BGS-Deep+Wide 250 μm Sub-maps	83
4.9	Polynomial Removed BGS-Deep+Wide 350 μm Sub-maps	84
4.10	Polynomial Removed BGS-Deep+Wide 500 μm Sub-maps	85
4.11	Noise-Weighted BGS-Deep+Wide Maps	86
4.12	250 μm BGS-Wide Flux and Hits Sub-maps	87
4.13	350 μm BGS-Wide Flux and Hits Sub-maps	88
4.14	500 μm BGS-Wide Flux and Hits Sub-maps	89
4.15	BLAST Power Spectra of BGS-Wide	93
4.16	BLAST Power Spectra of BGS-Deep+Wide	94
4.17	IRAS/IRIS HCON maps	95
4.18	Normalized BLAST Power Spectra of BGS-Wide	96
4.19	Cross-Band Power Spectra	98
4.20	Source Population Model Redshift Distribution	100
4.21	Source Population Model Redshift Distribution of Power Spectrum Contributors	100
4.22	Halo-Model Fits to Power Spectra	101
4.23	Best-Fit Halo-Model for $r_{cut} = 3 \times r_{vir}$	102
4.24	Halo Occupation Number and Bias vs. Redshift	104
4.25	Contributions to Clustering Signal from Redshift Slices	104
5.1	Clustering Length of Star-Forming Galaxies	110
5.2	Clustering Length with Evolution	112
5.3	Ellipsoids	115
5.4	Triaxiality vs. Halo Mass	116
5.5	Virial Radius vs. Halo Mass	118
5.6	Shot-Noise/1-Halo Term Degeneracy	120

List of Tables

2.1	Strut Laminate Elements	22
2.2	Quaternion Identities	33
4.1	Normalized Clustering Power Spectra	94
4.2	Best-Fit Values for θ_0 and ϵ	96
4.3	Best-Fit Values for M_{\min} and α	102
4.4	Best-Fit Values for M_1	103

*For my father, who wanted more than anything to see this day and
couldn't.*

Chapter 1

Introduction

1.1 Large Scale Structure of the Universe

Understanding the formation of structure in the Universe remains one of the goals of modern cosmology. Some key questions concern the assembly of structure on large scales, the formation and evolution of galaxies on small scales, and how galaxy formation relates to the underlying structure in general.

The Λ -cold dark matter (Λ CDM) paradigm, also known as the *concordance* or *standard model* of big bang cosmology, is the simplest model which agrees with a large body of observations (e.g., [Spergel et al., 2003](#); [Hinshaw et al., 2009](#); [Komatsu et al., 2009](#)). In the Λ CDM paradigm, over-densities in the primordial dark matter distribution collapse to form dark matter halos ([Mo & White, 1996](#); [Cooray & Sheth, 2002](#)). Galaxies form as baryonic gas cools at the centers of these halos, which continue to grow through mergers in a hierarchical way. These galaxies are regarded as biased tracers of the underlying dark matter, and as such are an indispensable tool in the study of large scale structure.

Additionally, galaxy formation must be closely related to the larger process of structure formation, since the same gravitational processes that brought dark matter together also brought together the gas that became stars and galaxies. However, nonlinear forces such as dissipative friction, heating, feedback, etc., complicates the relationship of galaxies to structure. On the other hand, these complications provide additional information concerning the relationship of galaxy formation to the local environment. Thus, the spatial distribution of galaxies can also teach us about galaxy formation.

1.1.1 The observed galaxy distribution

The galaxy distribution on large and small scales can be quantified through their clustering statistics. Correlations of galaxy positions or brightnesses reveal themselves via n -point statistics, of which there are many, and include counts-in-cells, pair-counts, the two and three-point correlation functions and the auto and bi-power spectra.

The clustering properties of cosmic objects, like the underlying dark matter density distribution it traces, evolves with cosmic time. Therefore, to form a complete picture of the cosmic history of structure and galaxy formation, the galaxy distribution would ideally be measured at all redshifts. In practise, however, obtaining this data has not been easy, since in order to use galaxies as tracers, or to study their formation history, it is first necessary to *see* them, and second to be able to *describe* them. In particular, for redshifts greater than $z \sim 1$, this has proven to be challenging. For example, the redshift interval $1.4 \lesssim z \lesssim 2.5$ is one where no strong spectral lines fall in the range $\sim 4300\text{--}9000 \text{ \AA}$ — the range where most of the spectrographs on large telescopes are optimized. This range has thus been nicknamed the “redshift desert” (e.g., [Steidel et al., 2004](#)). Certain photometric techniques have been developed to break into the redshift desert. In particular, the Lyman-break technique has allowed efficient selection of star-forming galaxies in the redshift range $2 \lesssim z \lesssim 5$ ([Steidel et al., 1996](#)). However, as star formation is often accompanied by dust, it seems likely that the dominant component of star formation is not revealed by optical/UV observations. Instead, UV radiation from young, hot, shortlived stars is absorbed by the dust and reemitted in the infrared and (sub)mm. Fortunately, interstellar dust is optically thin to infrared radiation, and as a result, targeting these galaxies in the IR/submm provides a powerful window onto star-forming galaxies during this epoch. Thus, it follows that submillimeter galaxies are useful as tracers of the large scale matter distribution in this redshift range.

Observing galaxies in the infrared requires a different set of tools. Infrared galaxies emit as modified blackbodies, peaking at $\sim 150 \mu\text{m}$. These low energy, longer wavelength photons require extremely sensitive, cryogenically cooled detectors, and large-diameter primary optics in order to detect and resolve them. Additionally, a wide range of foregrounds and backgrounds make detecting and isolating these galaxies extremely challenging. For example, for typical dusty galaxies at $z = 1$, the wavelengths which roughly bracket the redshifted peak of $\sim 30 \text{ K}$ dust emission are $250 \lesssim \lambda \lesssim 450 \mu\text{m}$. From [Figure 1.1](#) it is shown that the average transparency of the atmosphere over this wavelength range is nearly zero. In other words, except for narrow ‘windows’ at 350, 450, 740 and 850 μm , the atmosphere is nearly opaque to submillimeter light.

As a result, two strategies exist to observe in the FIR/(sub)mm. The first is to put the observatory on the highest, driest sights available, and to target the narrow windows through

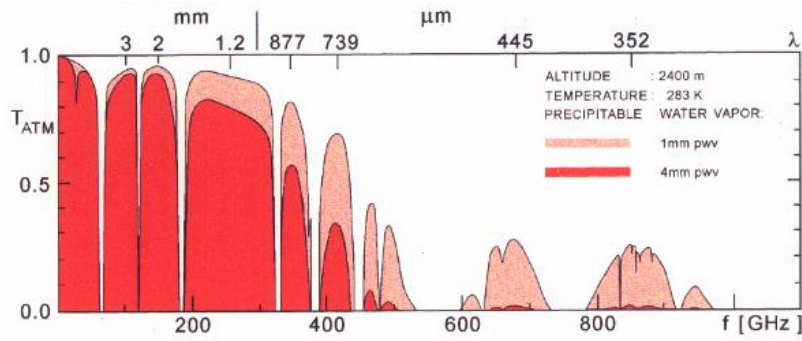


FIGURE 1.1: Transpission of the atmosphere in dependence of the precipitable water vapor. 1 corresponds to a completely transparent atmosphere, while 0 is completely opaque. Precipitable water vapor (pwv) refers to the depth of the ocean if every molecule of water vapor above you could be condensed. 4 mm is a typical level found on a very dry day at sea level, whereas 1 mm is a very dry day on the summit of Mauna Kea. Note that even under the best conditions, the atmosphere is relatively opaque in the submillimeter. Image from the Arizona Radio Observatory

the atmosphere (e.g., SCUBA at 450 and 850 μm , SHARC at 350 μm , AzTEC at 1.1 mm, MAMBO at 1.2 mm). The second is to put the observatory above the atmosphere, either by launching it into space or by a tethering it to a long duration balloon. Placing the observatory above the atmosphere has the advantage of opening up wave-bands unavailable from the ground, but since the physical size of the primary mirror that can reasonably be put into space or on a balloon-born payload is limited to a few meters in diameter, the resolving capabilities of these telescopes is limited. The resolving power depends on the aperture and wavelength as $\Omega = 1.22\lambda/D$, where Ω is the diffraction limit in radians, so that at, say, 250 μm , a 2 meter primary can resolve ~ 31 arcseconds. To put that into context, a complete 24 micron catalog down to 30 μJy (e.g., [Magnelli et al., 2009](#)) resolves ~ 13 sources per square arcminute, and the typical distance between sources in a random field with that source density is ~ 15 arcseconds. In other words, the 250 μm beam of a 2 meter primary is twice the average distance between galaxies.

Therefore, due to the limited mapping speeds of submillimeter telescopes from the ground, and the large beams of balloon born and space telescopes, it has not yet been possible to simultaneously fully resolve these distant infrared emitting galaxies, and make large-area surveys. Subsequently, the state of observations of the clustering of submillimeter galaxies to date is very poor. For example, all the SCUBA fields combined make up $\sim 0.25 \text{ deg}^2$, and the best measurement of the clustering of galaxies in these fields comes from a re-analysis of this data by [Scott et al. \(2006\)](#). Although they claim to have found tentative evidence for strong clustering, their errors were too large to adequately constrain the correlation length.

So, while it may seem that no significant progress can be made without major advances in the mapping speed of ground-based submillimeter observatories, or the ability to put

extremely large primary dishes into space (or on balloons), not all hope is lost. Even if the radiation reprocessed by dusty galaxies is not easily resolved into individual galaxies, it is still observable. This energy reveals itself as a cosmic infrared background (CIB), spanning the wavelength range $2 \lesssim \lambda(\mu\text{m}) \lesssim 1000$ (Puget et al., 1996; Schlegel et al., 1998; Fixsen et al., 1998; Hauser et al., 1998). And provided that all of the background originates from discrete sources (i.e., galaxies), then statistics describing the spatial distribution of the galaxies which make up the CIB can be determined from analysis of the fluctuations in the unresolved background.

This thesis is concerned with that measurement, and details each of the steps taken to observe, measure and interpret that measurement with data collected by the Balloon-borne Large Aperture Submillimeter Telescope (BLAST: Pascale et al., 2008), in December 2006. BLAST is a stratospheric balloon-borne 1.8 meter diameter telescope with bolometric detectors operating at 250, 350 and 500 μm . By observing above 99% of the atmosphere, it was able survey large areas with incredible speed, enabling it to make large area maps ($\sim 9 \text{ deg}^2$), with enough depth to measure correlations in the CIB, allowing us to make the first measurement of clustering of submillimeter galaxies at these wavelengths.

1.2 Definitions

The specific (or *spectral*) intensity of the CIB at a given frequency is denoted as I_ν , and has units $\text{Wm}^{-2}\text{Hz}^{-1}\text{sr}^{-1}$. If the source is discrete, then the total power received by a detector of unit projected area is the flux density, $S_\nu = \int I_\nu d\Omega$. Flux densities of astronomical sources are typically measured in narrow bands, thus photometric results are reported in terms of νI_ν . The flux density units used in IR astronomy is the Jansky, $1 \text{ Jy} = 10^{-26} \text{Wm}^{-2}\text{Hz}^{-1}$. The flux density of the CIB is typically reported in MJy/sr or $\text{nWm}^{-2}\text{sr}^{-1}$, which are related by

$$1 \frac{\text{nW}}{\text{m}^2\text{sr}} = \frac{3000 \text{ MJy}}{\lambda(\mu\text{m}) \text{ sr}}. \quad (1.1)$$

When required, we adopt the concordance model, a flat ΛCDM cosmology with $\Omega_{\text{M}} = 0.274$, $\Omega_{\Lambda} = 0.726$, $H_0 = 70.5 \text{ km s}^{-1} \text{ Mpc}^{-1}$, and $\sigma_8 = 0.81$ (Hinshaw et al., 2009).

1.3 Cosmic Infrared Background

With the discovery of the cosmic microwave background (CMB; Penzias & Wilson, 1965), the idea of a hot evolving Universe began to gain acceptance, and led to the idea that the cosmic infrared background (CIB) could be useful for cosmology. Peebles (in unpublished lectures)

considered this background while noting the lack of knowledge of the sky brightness in the wavelength range 1–1000 μm . The extreme infrared luminosities observed in some local galaxies led [Low & Tucker \(1968\)](#) to predict an infrared background peaking at wavelengths beyond 50 μm with a total energy 1–10% that of the then recently discovered CMB.

The first tentative detection of the CIB was made with the FIRAS instrument on the *COBE* satellite ([Puget et al., 1996](#)), and later confirmed with DIRBE at 140 and 240 μm ([Fixsen et al., 1998](#); [Hauser et al., 1998](#)) and at 60 and 100 μm ([Finkbeiner et al., 2000](#)). The intensity of the CIB was found to exceed the sum of all of the optical light from galaxies in the Hubble Deep Field by ~ 2.5 , and all of the *IRAS* light by ~ 5 –10, pointing to a larger contribution from high redshift dusty galaxies than was previously supposed.

The background was first partially resolved into point sources at 850 μm from observations with the SCUBA camera ([Holland et al., 1999](#)) on the James Clerk Maxwell Telescope (JCMT). From these observations (e.g., [Smail et al., 1997](#); [Blain, 1997](#); [Hughes et al., 1998](#); [Barger et al., 1999](#); [Eales et al., 1999](#)) it was found that the brightest sources in the sub-millimeter had very weak or no optical counterparts, suggesting all but of order 1% of the activity is hidden ([Hughes et al., 1998](#)). These observations pointed to an epoch of star formation where dusty starburst galaxies — such as the rare local luminous and ultra-luminous infrared galaxies (LIRGS and ULIRGS) previously observed with *IRAS* ([Soifer et al., 1987](#)) — were much more abundant.

Indeed, it is now well established that the star formation rate density steadily increases from $z \sim 0$ –1, and appears to remain relatively constant thereafter to redshifts of ~ 3 –5 ([Dickinson et al., 2003](#); [Hopkins, 2004](#)). This range from $1 \lesssim z \lesssim 3$ is what we will refer to as the “peak epoch” of star formation. There is also mounting evidence that star formation in the peak epoch increasingly took place within LIRGS and ULIRGS, so much so that by $z \sim 1$ they made up 51% the IR luminosity density, rising to 93% by $z \sim 2$ ([Le Floc’h et al., 2005](#); [Rodighiero et al., 2009](#)). Considering that the the bulk of present day stars are found in local elliptical galaxies ([Fukugita & Peebles, 2004](#)), and that these galaxies have typically undergone little or no star formation since a redshift of $z \sim 1$ ([Oke, 1971](#); [Stanford et al., 1998](#)), then the peak epoch is also when the majority of present day stars were formed.

1.3.1 Origin of the CIB

The CIB is the projection of radiation integrated over the entire age of the Universe, roughly spanning the wavelength range 3–1000 μm . The near-infrared (NIR) background arises from the stellar component of galaxies at very early times. The mid-infrared (MIR) and far-infrared (FIR) background originate from reprocessed radiation emitted by dusty galaxies,

heated by stars and active galactic nuclei (AGN). We will now overview the contributors to the CIB, from galaxies to foregrounds, as well as summarize the measurements of the CIB leading up to BLAST.

1.3.1.1 Galaxies

The primary extragalactic contributor to the CIB are dusty starburst galaxies, which absorb UV radiation emitted by young, hot stars and reradiate it in infrared. Their emission spectrum in the wavelength range $\sim 50 - 1000 \mu\text{m}$ can be described as a modified blackbody in thermal equilibrium

$$f_\nu \propto \epsilon_\nu B_\nu, \quad (1.2)$$

with the emissivity, $\epsilon_\nu \propto \nu^\beta$ where ($\beta = 1-2$) depending on the physical properties of the dust ($\beta \sim 2$ for typical $\sim 0.1 \mu\text{m}$ diameter silicates (Li & Draine, 2001), and B_ν is the Planck function,

$$B_\nu = \frac{2\pi h\nu^3}{c^2} \frac{1}{e^{\frac{h\nu}{kT}} - 1}, \quad (1.3)$$

where h is Planck's constant, k is Boltzmann's constant and c is the speed of light. For dust in typical LIRGs, the average temperature is $\sim 30 \text{ K}$ (Dye et al., 2009), and is detectable in the FIR and submillimeter, peaking at $\sim 150 \mu\text{m}$.

For $h\nu \ll kT$, thermal dust emission simplifies to a modified Rayleigh-Jeans law:

$$I_\nu^{\text{RJ}}(T) = \epsilon_\nu \frac{2\nu^2}{c^2} kT. \quad (1.4)$$

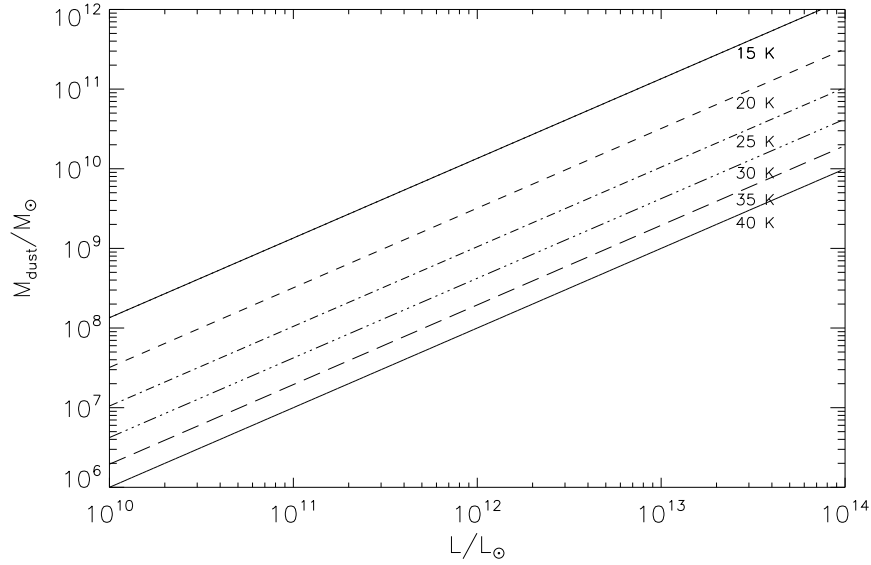
For $h\nu \gg kT$, thermal dust emission simplifies to a modified Wein law:

$$I_\nu^{\text{W}}(T) = \epsilon_\nu \frac{2h\nu^3}{c^2} \exp\left(\frac{-h\nu}{kT}\right). \quad (1.5)$$

Not much dust is needed to light up a galaxy in the infrared. Soifer et al. (1987) showed, using the Draine & Lee (1984) dust model, that the amount of dust needed to produce a given FIR luminosity is

$$L_{\text{FIR}} = 10^4 \frac{M_{\text{dust}}}{M_\odot} \left(\frac{T_{\text{dust}}}{40 \text{ K}}\right)^5 L_\odot, \quad (1.6)$$

which is illustrated in Figure 1.2. Since the stellar mass of a typical LIRG ($L \sim 10^{11-12} L_\odot$) is of order $\sim 10^{10-11} M_\odot$ (Daddi et al., 2005), dust fractions of order $\lesssim 1\%$ of the stellar mass are enough to make a galaxy very bright in the FIR.



s

FIGURE 1.2: Dust mass vs. luminosity according to the simple model of [Soifer et al. \(1987\)](#) using the dust model of [Draine & Lee \(1984\)](#). Even in the most extreme case dust mass is only 1/100 of the stellar mass.

1.3.1.2 Foregrounds

The dominant foreground varies with the wavelength range in question. In the NIR/MIR, the atmosphere is the largest contribution to the sky background at 295 MJy/sr in the K band ($2.2 \mu\text{m}$). Longward of $2.5 \mu\text{m}$, the spectrum is best described as a blackbody at $\sim 250 \text{ K}$ (i.e., atmospheric temperature). At wavelengths $\lesssim 200 \mu\text{m}$, zodiacal light is a contaminant as well.

In the MIR/FIR ($\sim 50\text{--}200 \mu\text{m}$), galactic cirrus is the dominant signal in much of the sky. There are “windows” through which the cirrus is as low as $\sim 1\text{--}2 \text{ MJy sr}^{-1}$, but for very large maps or full sky surveys, cirrus is a serious contaminant for all but point source studies.

In the FIR/submillimeter ($\sim 200\text{--}850 \mu\text{m}$), due to pressure-broadened water lines at sea level the atmosphere is opaque except for very narrow windows at 350, 450, 850 μm . Approaching the millimeter ($\gtrsim 500 \mu\text{m}$), the CMB begins to dominate the signal. Fortunately the CMB behaves as a perfect blackbody at 2.726 K ([Fixsen, 2009](#)), and is uniform across the sky, meaning that it can be subtracted down to levels $\ll 1 \text{ nWm}^{-2}\text{sr}^{-1}$.

1.4 CIB: Observables and Obstacles

Measurements of the unresolved, extragalactic CIB can be roughly divided into those concerned with measuring the mean level — which constrains the total energy emitted by the

CIB contributors — and those concerned with measuring fluctuations — which informs both the number counts and spatial distribution of dusty galaxies.

1.4.1 Mean Level

The total CIB intensity is a measure of the bolometric energy output of the Universe, and is a projection of radiation from all redshifts. As such, it contains information on the entire history of star formation. Teasing out that history requires properly accounting for and separating the individual components. After considering foreground emission such as Galactic dust, stars and zodiacal emission, the background is described by integrating the number density of sources at each redshift. Naturally, as the Universe ages and small things become big things, these evolve, and this evolution must also be accounted for.

The flux density at a given wavelength from individual galaxies with an absolute bolometric luminosity L and redshift z is

$$F = \frac{L}{4\pi d_L^2 (1+z)} f_\lambda, \quad (1.7)$$

where f_λ is the spectral energy distribution of the galaxy population, and the extra $(1+z)$ in the denominator accounts for the fact that the flux in band λ come from a redshifted galaxy. $f_\lambda d\lambda$ is the fraction of total light emitted in the wavelength interval $[\lambda; \lambda + \Delta\lambda]$, and the contribution to the total CIB flux from galaxies in the interval $[z; z + dz]$ is

$$\frac{dF}{dz} = \frac{R_H}{4\pi} \frac{1}{(1+z)^2} \frac{d(H_0 t)}{dz} \sum_i \mathcal{L}_i(z) \lambda f_{\lambda,i}, \quad (1.8)$$

which sums over all galaxy populations, i , contributing to the background at the rest-frame wavelength.

Additionally, $R_H = cH_0^{-1}$, and \mathcal{L} is the luminosity density, and is given by

$$\mathcal{L}_\nu(z) = \sum_i \int \Phi_{z,i}(L_\nu) L_\nu dL_\nu, \quad (1.9)$$

where $\Phi_{z,i}$ is the luminosity function (or number density) of galaxy population i at redshift z , in the dL_ν interval, at frequency ν .

The dependence of the luminosity density on redshift, $\mathcal{L}_\nu(z)$, can be described by the evolution of three parameters: i) luminosity evolution, \mathcal{E}_ν ; ii) density evolution, \mathcal{N}_ν ; and iii) the SED, which is described in terms of k-correction \mathcal{K}_ν , such that

$$\mathcal{L}_\nu(z) = 10^{-0.4[\mathcal{K}_\nu(z) + \mathcal{E}_\nu(z) + \mathcal{N}_\nu(z)]} \mathcal{L}_\nu(0), \quad (1.10)$$

where $\mathcal{L}_\nu(0)$ is the luminosity density in the local Universe. Finally, the total CIB flux emitted by *evolving* galaxy populations is

$$F_{total} = \sum_i \frac{\mathcal{L}_{\nu,i}(0)}{4\pi} \frac{R_H}{(1+z)^2} \int \frac{1}{dz} \frac{d(H_0 t)}{dz} 10^{-0.4(\mathcal{K}_{\nu,i} + \mathcal{E}_{\nu,i} + \mathcal{N}_{\nu,i})} dz, \quad (1.11)$$

where dt/dz is given by the Friedman equation for a flat Universe, with $R \equiv (1+z)^{-1}$, and

$$\dot{R}^2 = H_0^2 \left(\frac{\Omega_m}{R} + \frac{1 - \Omega_m}{R^{1+3\omega}} \right). \quad (1.12)$$

1.4.2 Fluctuations

Unlike measuring the mean level of the CIB, which requires properly accounting for contributions from bright foreground contributors (e.g., Galactic stars, interplanetary and interstellar dust (e.g., [Arendt et al., 1998](#); [Kelsall et al., 1998](#))), one can much more easily measure the fluctuations in the CIB because of its distinct spectral signal. Since the CIB originates from clustered luminous galaxies, the fluctuations in the sky brightness will reflect that behaviour through its angular power spectrum (or correlation function) which distinguishes it from local sources of background emission.

If fluctuations in sky brightness are described as $\delta F(\theta) = F(\theta) - \langle F \rangle$, where $\langle F \rangle$ is the mean and θ is the two dimensional coordinate on the sky, then the Fourier transform is $\delta F(\theta) = (2\pi)^{-2} \int \delta F_k \exp(-i\mathbf{k} \cdot \theta) d^2\mathbf{k}$. The first moment of the fluctuation field is the two-dimensional (or projected) correlation function, $w(\theta) = \langle \delta F(\mathbf{x} + \theta) \delta F(\mathbf{x}) \rangle$, and the two-dimensional power spectrum is $P(k) \equiv \langle |\delta F_k|^2 \rangle$, where the average is performed over all phases. Thus, the correlation function and the power spectrum are a Fourier transform pair related by

$$\begin{aligned} P(k) &= 2\pi \int_0^\infty w(\theta) J_0(k\theta) \theta d\theta, \\ w(\theta) &= \frac{1}{2\pi} \int_0^\infty P(k) J_0(k\theta) k dk, \end{aligned} \quad (1.13)$$

where J_n is the n -th order cylindrical Bessel function. Other considerations must be taken into account, such as the window function of the beam, or the finite sampling of the sky. These will be addressed in detail in Chapters 3 and 4.

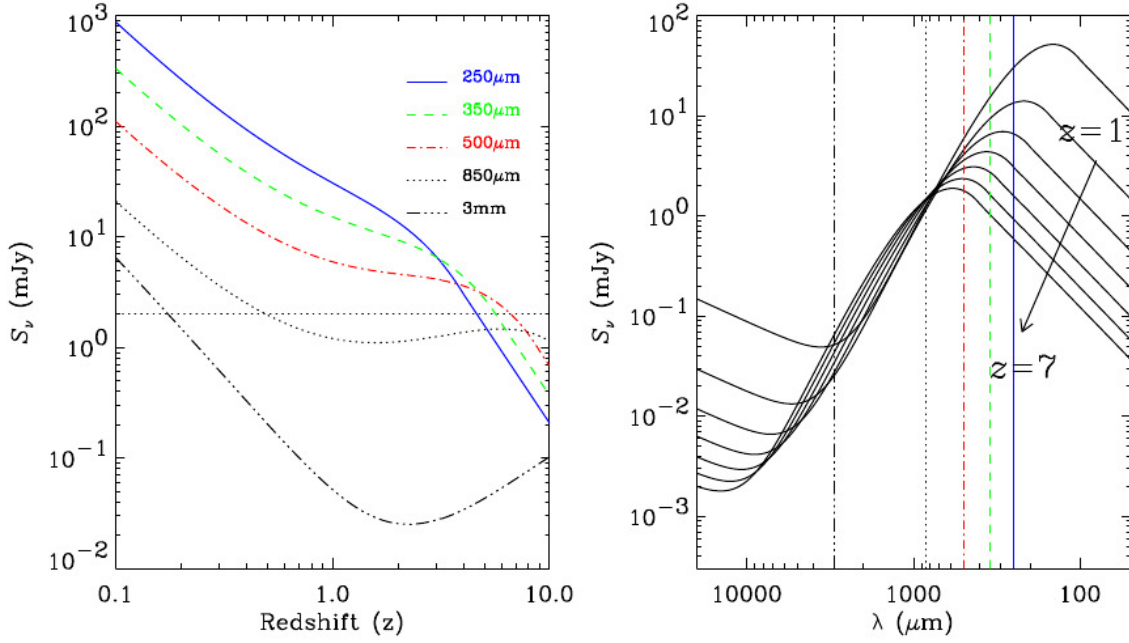


FIGURE 1.3: Negative K-correction for wavebands 250 μm to 3 mm. Increasing redshifts benefit from increasing negative K-correction, to the point where the apparent luminosity of sources at 850 μm and above remains constant or even increases beyond redshift of 1.

1.4.2.1 Negative K-correction

For a greybody with $L_\nu \propto \nu^\beta B_\nu(T)$, the measured flux density, S_ν for an object at z is

$$S_\nu d\nu \propto \frac{L_{\nu'} d\nu'}{4\pi D_L^2}, \quad (1.14)$$

where $\nu' = (1+z)\nu$, i.e., the emitted frequency at the source redshift, and D_L is the luminosity distance at redshift z . This is easily recast in terms of specific luminosity at the rest frame frequency ν

$$S_\nu d\nu \propto \left[(1+z) \frac{L_{\nu'}}{L_\nu} \right] \frac{L_\nu d\nu}{4\pi D_L^2}, \quad (1.15)$$

where the term in square brackets is the K-correction.

By falling onto the Rayleigh-Jeans side of the grey-body spectrum, submillimeter observations benefit from the fact that as the redshift of the source increases, the waveband samples a more luminous part of the redshifted SED — in other words there is a *negative* K-correction (Humason et al., 1956; Peebles, 1980, e.g.,). This is illustrated in Figure 1.3 for a grey-body at 40 K and $\beta = 1.5$. This results in sources luminosities which do not reduce as quickly as would be expected for an inverse square law. In the most extreme cases, (i.e., at wavelengths greater than 750 μm but shorter than radio), the apparent luminosity actually *increases* beyond a redshift of 1.

BLAST was designed to take advantage of this negative K-correction by bracketing the peak of the thermal SED of sources ~ 30 K and in the redshift range $z \sim 1-3$.

1.4.2.2 Confusion

Source confusion arises when multiple sources occupy the beam of a telescope. The convention is that a field is considered confused when there is one source per thirty beams (Scheuer & Ryle, 1957; Condon, 1974), although it has been argued that a more appropriate (and conservative) estimate is one source in fifty beams (Hogg, 2001). A confusion limited map is one where confusion noise dominates over instrument noise, at which point further integration is counterproductive.

The consequences of source confusion are profound. We detail several problems directly related to confusion in § 4.2.2 and § 3.2.2.2.

1.4.3 State of Measurements

1.4.3.1 Mean Level

The CIB is observationally difficult to distinguish from generally brighter foregrounds. A number of groups have worked to measure the mean level from ground-based and satellite observatories. The first tentative detection of the CIB was made with the FIRAS instrument on the *COBE* satellite (Puget et al., 1996), and later confirmed with DIRBE at 140 and 240 μm (Hauser et al., 1998) and at 60 and 100 μm (Finkbeiner et al., 2000). Still, the best measurements to-date remain uncertain by $\sim 30\%$. This is because they are dominated by systematic uncertainties related to the modelling and removal for foreground emission of zodiacal light, Galactic stars, and the interstellar medium.

1.4.3.2 Fluctuations

Anisotropies (or correlations) in the background fluctuations have a distinct spectral signal that makes isolating it from (some) foregrounds trivial. In some cases, such as in regions of significant Galactic cirrus, foreground contamination is still significant.

The first attempts to measure anisotropies in the CIB with FIRAS (on scales greater than 7°) at 400 μm (Burigana & Popa, 1998); with DIRBE at 25 μm (Kashlinsky & Odenwald, 2000); with SCUBA at 850 μm (Peacock et al., 2000); and with the ISOPHOT instrument

at $170\ \mu\text{m}$ on the *ISO* satellite (Lagache et al., 2000), each provided upper limits on CIB fluctuations.

The first successful measurements of correlations from galaxies at high redshift were measured nearly simultaneously by Grossan & Smoot (2007) and Lagache et al. (2007) using $24\ \mu\text{m}$ data from the *Spitzer* space observatory. They both detected a signal in excess of that expected from galactic cirrus and Poisson noise, although the cirrus contribution dominated the signal on scales where the clustering signal is strongest.

1.5 Chapter Description

This thesis is organized as follows. Chapter 2 describes the BLAST instrument in detail, including instrumentation, flights and targeted extragalactic fields. Chapter 3 outlines the theory large scale structure and how it is measured and modelled using the statistics of galaxy clustering. It details the advantages and limitations of different techniques to measure correlations of galaxies. In Chapter 4 we make the measurement, discussing each step in the mapmaking, power spectrum calculation, and simulations to determine errors. We use the data to constrain a halo model and with it measure the bias. In Chapter 5 we interpret the result and put it in the wider context of our understanding of galaxy and structure formation.

Chapter 2

BLAST

2.1 Introduction

Apart from the CMB, the sum of all radiation in the Universe can be lumped into two broad peaks — the optical and infrared (IR) backgrounds — in roughly equal parts. The cosmic infrared background (CIB) is made up of emission from interstellar dust, warmed in large part by the absorption of UV radiation emitted primarily from young, hot, short-lived O and B stars (Bond et al., 1986), and to a lesser degree by AGN. Since interstellar dust is optically thin to IR/submm wavelengths, the CIB is a good tracer of star formation during an epoch when star formation is at its peak. Despite this, the challenges inherent in observing in the IR/submm has resulted in observations of the IR background to fall behind its optical counterpart, such that the areal coverage of even the largest surveys is relatively small. For example, at submillimeter wavelengths — where thermal emission from high-redshift galaxies peaks — the largest survey pre-dating BLAST has been SHADES (Coppin et al., 2006); a quarter-square degree survey observed at $850\ \mu\text{m}$ by the SCUBA instrument (Holland et al., 1999) on the JCMT.

The dominant obstacle restricting submillimeter observations from the ground is that the atmosphere is largely opaque to submillimeter radiation, with only narrow “windows” through which ground based telescopes have any hope of observing. Therefore, in order to efficiently observe at submillimeter wavelengths, it is critical that the observatory is located above most of the atmosphere; whether on top of high mountains (i.e., $> 14,000$ feet), in space, or as is described here, from a balloon.

BLAST, the Balloon-borne Large Aperture Submillimeter Telescope (Pascale et al., 2008) is a stratospheric balloon-borne 2 meter telescope with bolometric detectors operating at 250, 350 and $500\ \mu\text{m}$. It is the first experiment to bracket the redshifted peak of resolved

galaxies, filling a gap between *Spitzer* on the blue side, and SCUBA, AzTEC and Laboca on the red side (see Figure 2.1). By observing above 99% of the atmosphere, it is able to survey large areas with speeds much higher than ground based instruments (e.g., 10 times faster than SCUBA 2; Holland et al., 2003), enabling it to significantly extend the wavelength range, sensitivity, and area of existing ground-based extragalactic and Galactic surveys. The under-illuminated primary results in nearly diffraction limited optics with full-width at half-maxima (FWHM) of 36" 42", and 60" in each band, respectively. The detectors are adapted from those used on the SPIRE instrument (Griffin et al., 2003) aboard *Herschel*.

BLAST was collectively designed and built by a large number of institutions. The principal investigators were the University of Toronto in Canada, and the University of Pennsylvania in the United States. The final design of the instrument, and the highly successful Antarctic science flight, were the culmination of lessons learned during previous, less successful iterations. The Fort Sumner test flight (2004) and Kiruna science flight (2005) are described in detail in Truch (2007); Marsden (2007); and Wiebe (2008). In this chapter we describe the instrument and Antarctic science flight (2006). We will discuss science goals (§ 2.1.1), and science flights and fields (§ 2.1.2). The instrument, including optics (§ 2.2.1), detectors (§ 2.2.3), gondola (§ 2.2.4), cryostat (§ 2.2.5) and attitude sensors (§ 2.2.6), are described in § 2.2. The data reconstruction, including attitude determination (§ 2.3.1), Kalman filter (§ 2.3.1.2) and how it applies to BLAST (§ 2.3.1.3) are discussed in § 2.3. For more details about the instrument see Pascale et al. (2008) and for flight performance and calibration see Truch et al. (2008, 2009).

2.1.1 Science Goals

BLAST's science case can be divided roughly into galactic and extragalactic science cases. Its extragalactic science cases were:

- to conduct blank-field, wide-area extragalactic surveys at or near the confusion limit in order to identify $\sim 10^4$ sources;
- to calculate statistically significant estimates of the number counts;
- to constrain the redshift distribution, star formation history, and evolution of luminous infrared galaxies;
- to study the spatial clustering of this population;
- to measure the confusion limit at the BLAST wavelengths.

Its galactic science cases were:

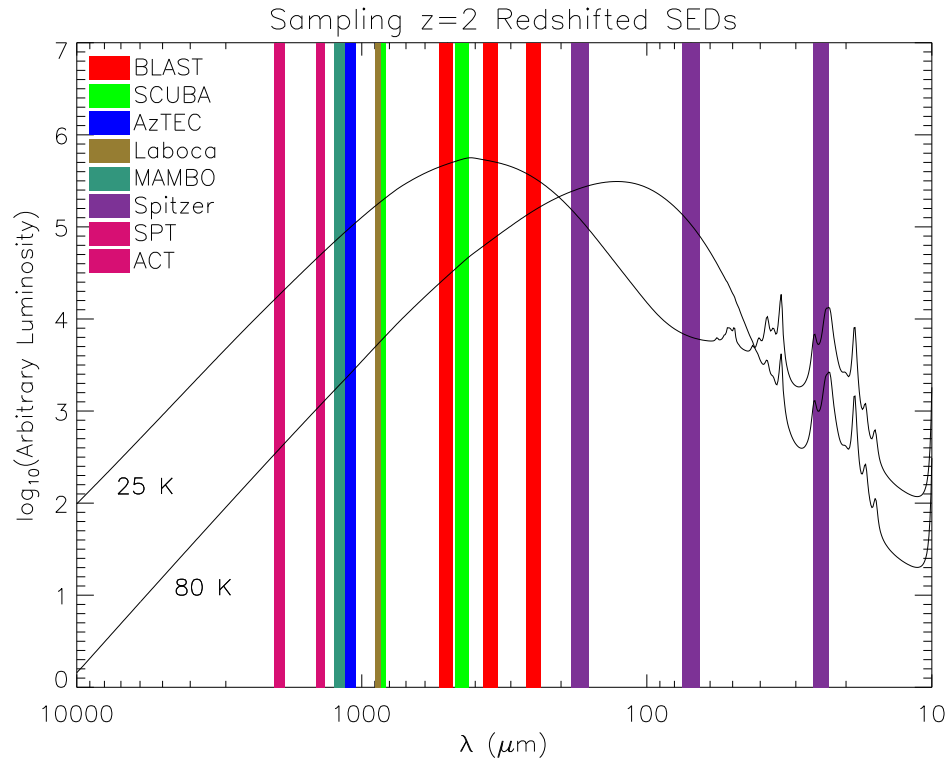


FIGURE 2.1: Redshifted ($z = 2$) template SEDs of emission from dust at 25 and 80 K (Draine & Lee, 1984), overlaid with bands illustrating the sampling from different observatories. Other observatories include: *Spitzer* (24, 70, & 160 μm – Heim et al., 1998); SCUBA (450, 850 μm – Holland et al., 1999); Laboca (870 μm – Siringo et al., 2009), AzTEC (1.1 mm – Wilson et al., 2008), MAMBO (1.2 mm – Bertoldi et al., 2000), SPT (1.4, 2 mm – Ruhl et al., 2004); and ACT (1.4, 2 mm – Fowler, 2004). BLAST fills a gap between the mid-infrared and millimeter bands, and is the only experiment to bracket the peak of redshifted dust emission of *resolved* typical ($T = 20\text{--}40$ K, $\beta = 1\text{--}2$) dusty galaxies.

- to understand the physical properties and mass function of cold pre-stellar cores and their efficiency of star formation;
- estimate column densities, masses and luminosities of regions surrounding pre-stellar cores in order to disentangle the degeneracy between β and T ;
- to study the nature and structure of the interstellar medium by making high resolution maps of diffuse Galactic emission.

2.1.2 Flights and Fields

BLAST had a test flight in September 2003, followed by two science flights. The first science flight was from Kiruna, Sweden, in June 2005 (hereafter BLAST05), and lasted 5 days (see Figure 2.2). Due to irregularities in the optics as a result of a still unknown problem, it was limited to surveys of Galactic targets (Figure 2.3). The most notable fields observed are

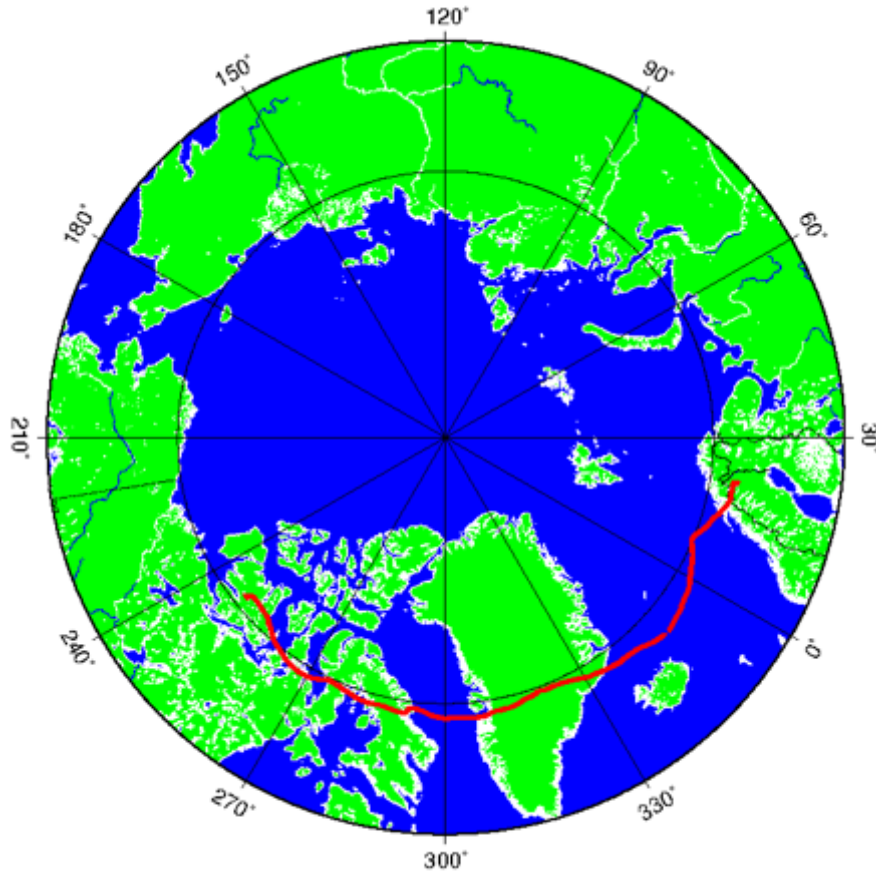


FIGURE 2.2: BLAST05 science flight path. Five day flight path shown in red, originating from ESRANGE base in Kiruna, Sweden, and terminating in Victoria Island, Canada. Figure courtesy of NASA.

Cygnus-X, three intermediate/high velocity clouds, and the supernova remnant, Cas-A. For a more detailed description of the BLAST05 flight and fields see [Truch \(2007\)](#); [Marsden \(2007\)](#); and [Wiebe \(2008\)](#).

The second flight was from McMurdo Station, Antarctica, in December 2006, lasting 11 days (see Figure 2.4). The majority of time was spent observing three major targets: two were extragalactic blank-fields of approximately 9 deg^2 each, and one was an approximately 50 deg^2 Galactic field centered on the Vela molecular ridge. In addition, several targeted fields of galaxy clusters or other interesting objects were observed. For a full description of all fields observed see [Wiebe \(2008\)](#). Figure 2.5 shows the relative depth of the fields observed, scaling from blue (shallow) to green (deep).

Of the two extragalactic blank-fields, this study is concerned with the field centered on the Great Observatories Origins Deep Survey South (GOODS-South). This 8.7 deg^2 patch, centered on $3^{\text{h}}32^{\text{m}}35^{\text{s}}, -28^{\circ}15'$, (hereafter BGS-Wide), was observed with mean $1-\sigma$ sensitivities of $36, 31, \text{ and } 20 \text{ mJy beam}^{-1}$ at $250, 350, \text{ and } 500 \mu\text{m}$. Additionally, a deep,

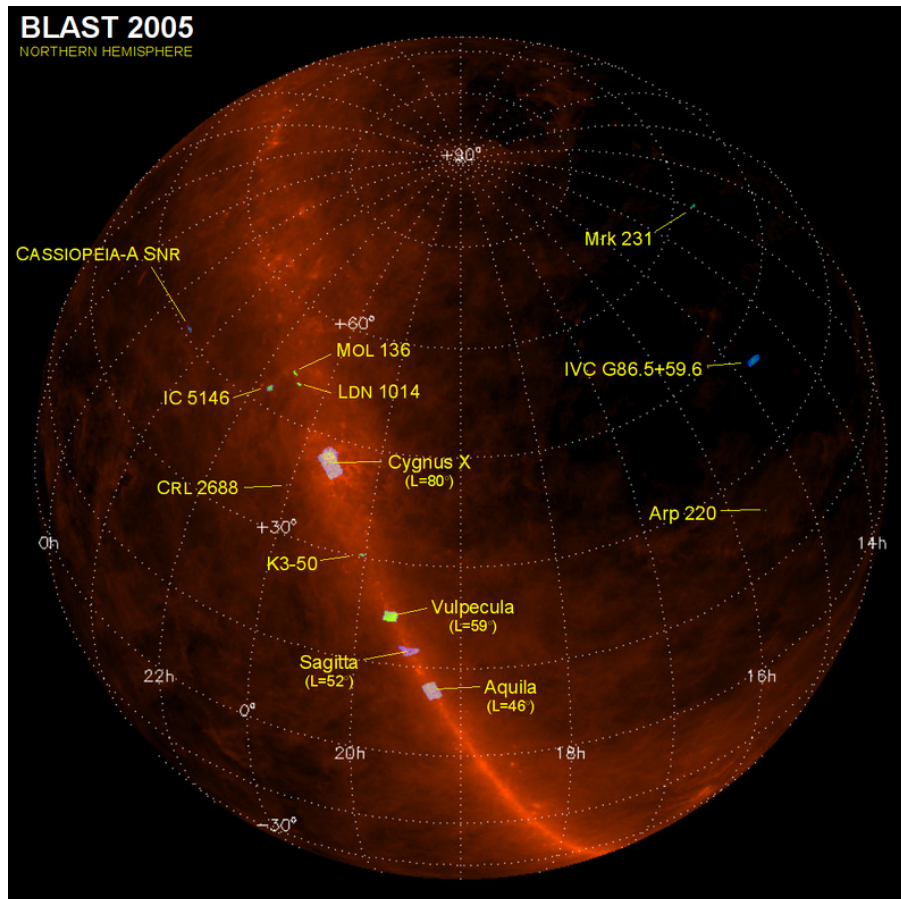


FIGURE 2.3: BLAST05 science targets overlaid on IRAS plus DIRBE $100\ \mu\text{m}$ dust maps of [Schlegel et al. \(1998\)](#). The colour of the area indicates the amount of time dedicated to the scan (from blue to green is increasingly deep). BLAST05 focused primarily of galactic targets, due to under-performing optics. Image courtesy of Ed Chapin.

nested field of $0.8\ \text{deg}^2$, centered on $3^{\text{h}}32^{\text{m}}30^{\text{s}}$, $-27^{\circ}48'$ (hereafter BGS-Deep) was observed with mean $1\text{-}\sigma$ sensitivities of 11, 9 and $6\ \text{mJy beam}^{-1}$, respectively¹.

2.2 The Instrument

Here we briefly describe the configuration of BLAST which was flown from Antarctica in 2006, and which will be referred to hereafter as BLAST06. For a detailed treatment of BLAST06 as a whole see [Marsden \(2007\)](#); [Pascale \(2007\)](#) and [Wiebe \(2008\)](#). The systems for which the author was responsible receive the most in-depth coverage.

¹BLAST maps and catalogs are publicly available at <http://www.blastexperiment.info>

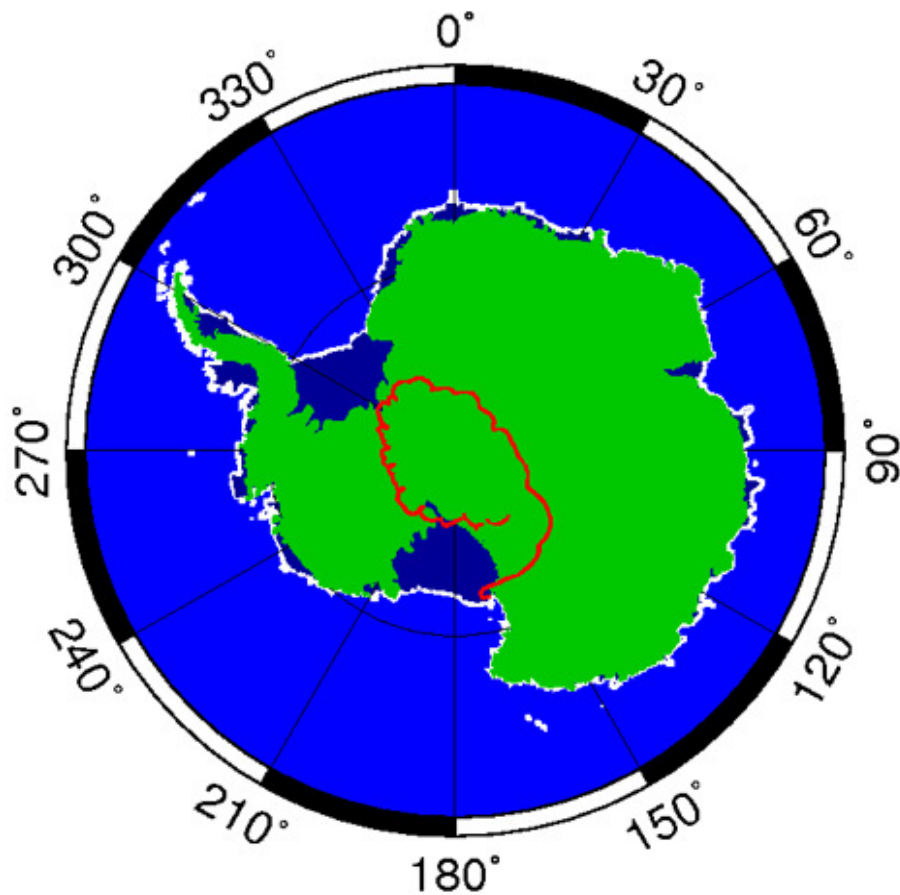


FIGURE 2.4: BLAST06 science flight path. Eleven day flight path shown in red, originating from McMurdo Station, Antarctica. Figure courtesy of NASA.

2.2.1 Optics

The optical design of BLAST06 is illustrated in Figure 2.6. The primary (M1) is a 1.8 m aluminum F/5 Cassegrain, which focuses incoming radiation through a window which opens to a re-imaging optical system located inside a cryostat whose temperature is ~ 2 K.

The correct alignment of M1/M2 is critical. Simulations (using Zemax software) show that the distance between the primary and secondary must be kept to within half of a wavelength, beyond which the focus is dramatically compromised (see Figure 2.7). This corresponds to about one eighth of a millimetre over 2 meters. The beam is kept in focus by a novel system which the author was responsible for designing (Figure 2.8). In flight, the temperature of BLAST is slowly but constantly changing. The focus of the aluminum primary mirror therefore changes as the radius of curvature varies. If each of the optical elements and support structure were made from the same material, and the temperature changed *uniformly* throughout, then the changes in the location of the focus would be compensated by the changes in lengths of the support structure. As the BLAST test flight

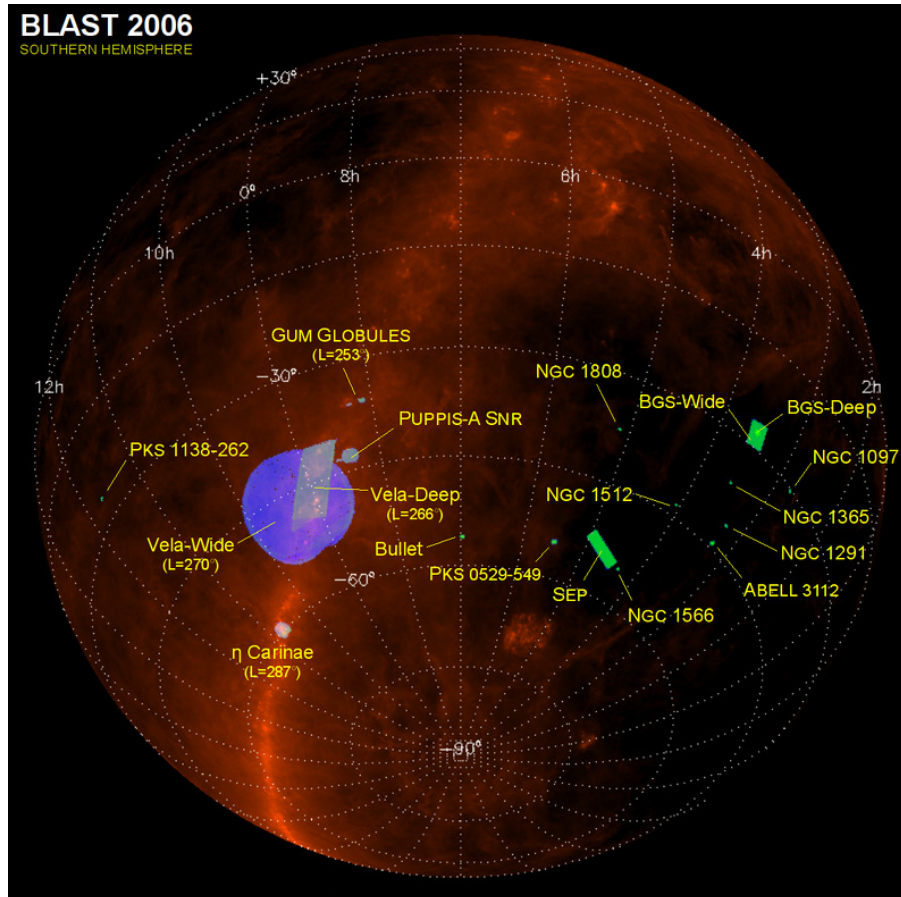


FIGURE 2.5: BLAST06 science targets overlaid on IRAS plus DIRBE $100\ \mu\text{m}$ dust maps of Schlegel et al. (1998). The colour of the area indicates the amount of time dedicated to the scan (from blue to green is increasingly deep). The major galactic field is a $50\ \text{deg}^2$ (21 hours) region of the Vela molecular ridge. The two major extragalactic fields are $\sim 9\ \text{deg}^2$ regions centred on GOODS-south (90 hours) and the so-called south ecliptic pole (SEP; 70 hours), which is actually a relatively dust-free region near to the south ecliptic pole. Figure courtesy of Ed Chapin.

showed, this idealized system does not work. The author’s solution was to keep the distance between the primary and secondary fixed with struts whose length remained unchanged with changes in temperature (see § 2.2.2.2), and to reposition the secondary based on changes in temperature using three motorized actuators. The correct position is found empirically and recorded to a lookup-table.

The re-imaging optical system is located inside a light-tight, cold ($T \sim 1.5\ \text{K}$) box, and comprises of two off-axis mirrors (M3 and M5) that feed smooth-walled conical feedhorns at the focal plane (not shown). Between these mirrors is a “Lyot stop” (M4), whose function is to control the illumination of the primary. It ensures that unwanted stray radiation is terminated at the 2 K stop. To make observations in three bands simultaneously, two dichroic beam splitters (not shown) are located in the optical path, which combined with appropriate filters/feedhorns, feed each detector with radiation, whose bandwidths are \sim

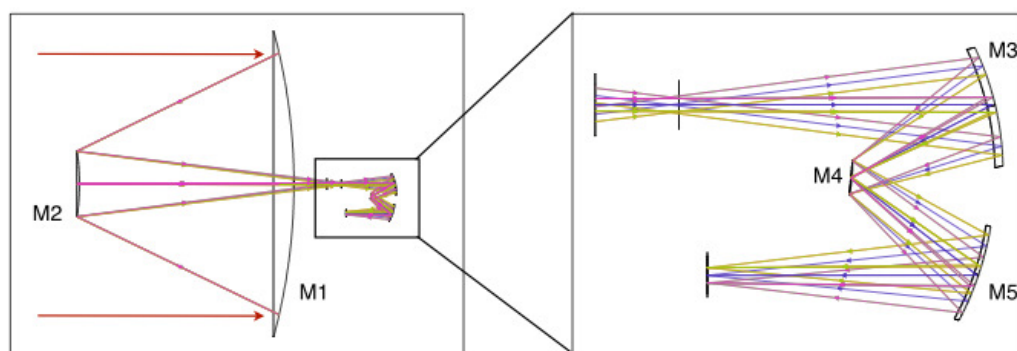


FIGURE 2.6: Ray-trace schematic of BLAST warm and cold optics. Left: Rays originating from infinity are imaged by the primary and secondary through the cryostat window to the cold optics. Right: Zoom-in of cold optics. Rays are re-imaged by M3 and M5. Stray radiation is attenuated at M4, the “Lyot” stop, i.e., this is where the primary is “under-illuminated”. Figure from Pascale (2007).

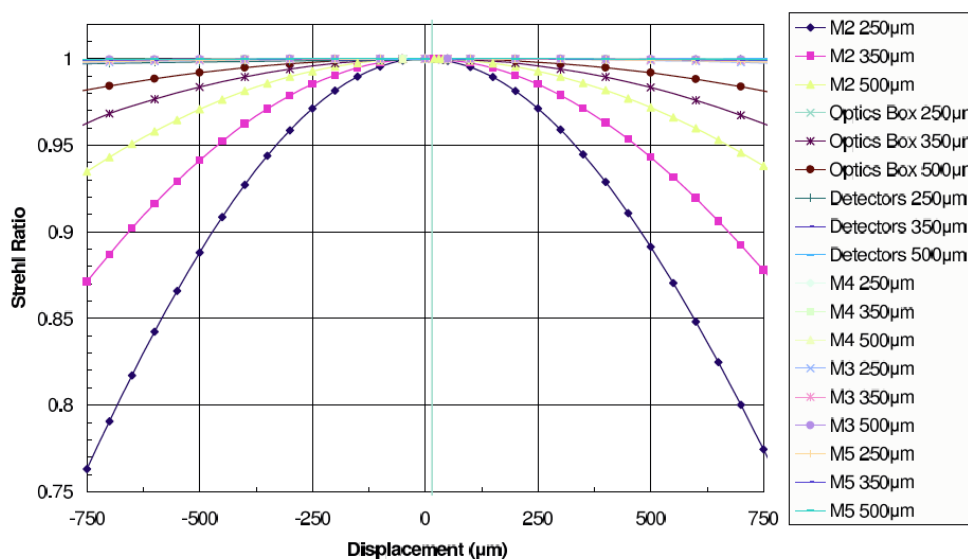


FIGURE 2.7: Strehl ratio of optical elements as a function of displacement from nominal position. Note the rapid degradation of the image as the secondary (M2) moves from its optimal position. It is for this reason that the correct position of the secondary is of utmost importance, necessitating the implementation of a tuneable secondary support structure.

30% wide, at their respective wavelengths. The band-passes, which were measured with a Fourier transform spectrometer, are illustrated in Figure 2.13. The under-illuminated primary results in nearly diffraction limited optics with full-width at half-maxima (FWHM) of 36” 42”, and 60” in each band, respectively.

2.2.2 Secondary Support Structure

The objectives of the secondary support structure are to: 1) deflect less than 0.15 mm with changes in elevation; 2) remain at a fixed length (less than $1.41 \times 10^{-6} \text{ K}^{-1}$) with changes in temperature; and 3) allow for axial displacement of the secondary mirror. The first two objectives are achieved by designing the struts from carbon fiber. The last is achieved with a novel design involving aluminum rings connected with leaf-springs, and positioned with motorized actuators (Figure 2.8). For more details on the actuator system see [Semisch \(2009\)](#). Here we describe the mirror assembly, carbon fiber struts, and sheet aluminum fairings in detail.

2.2.2.1 Mirror Assembly

The mirror assembly (Figure 2.8) was designed with Solidworks, and made from 6061 aluminum. The assembly is made from a number of unique parts, designed by the author, including

- Inserts: which are glued to the struts with epoxy. On one end, they are designed to mount to the primary mirror. On the other end, they provide a surface for the airplanes to mount;
- Airplanes: which join the mounting ring to the struts (and look like airplanes, thus the name);
- Mounting ring: which provides structural support, and is the mounting point for the linear actuators and leaf-springs;
- Movable secondary mount: which supports the secondary mirror, and is attached to the mounting ring with leaf-springs.

Thus, the position of the secondary is controlled with the linear actuators. The leaf springs provide force on the secondary mount towards the mounting ring, and the linear actuators push the secondary mount away from the mounting ring. The system is designed with enough room to allow 1.5 cm of travel peak-to-peak. This is more than enough play to focus the telescope at all possible temperatures of the primary and secondary mirrors. It is not enough play, however, to focus the near field. To do that, extra plates are designed to fit between the strut inserts and airplanes which increase the distance between the primary and secondary. These plates are installed for ground tests only. To ensure all of the parts are mounted very precisely, dowels are press fitted into the inserts and alignment holes are machined into the airplanes.

2.2.2.2 Struts

It is well established that well-designed carbon fiber parts are stronger and lighter than parts made from steel, aluminum or titanium. Carbon fiber has the additional peculiar quality that with changes in temperature, the axial direction will expand while the radial direction contracts, or vice versa. Thus, one can orient the fibers in such a way as to negate any change in length with change in temperature. This was the philosophy behind the design of the carbon struts. They were manufactured by Innovative Composite Engineering (ICE)¹. The struts are 1650 mm long (determined by the size of the tool in-house; any longer would increase the cost significantly), with a rectangular cross section whose inner dimensions are 35.6×73.7 mm, and corner radii of 3.2 mm. Each strut cost \$860, with a \$950 non-recurrent engineering charge.

Laminate order and orientation are summarized in Table 2.1. The final CTE is 0.007×10^{-6}

No.	Angle	Thickness (mm)	Material
2	0	0.229	7781
3	0	0.208	CARBNEWT30139
6	0	0.152	Toray M40J
1	45	0.208	CARBNEWT30139
1	-45	0.208	CARBNEWT30139
1	45	0.208	CARBNEWT30139
1	-45	0.208	CARBNEWT30139
6	0	0.152	Toray M40J
3	0	0.208	CARBNEWT30139
2	0	0.229	3k Plaine Weave Carbon

TABLE 2.1: Table lists the elements of the laminate, beginning with the top ply. The number in the first column tells how many times the given ply element repeats. Note the laminate is asymmetric. The total laminate thickness is 4.826 mm, for 26 total plies.

K^{-1} , which is about 100 times better than needed. The maximum deflection from 25 to 60° elevation is 0.117 mm (see Figure 2.9 for finite element analysis).

2.2.2.3 Fairings

The black carbon struts, if unshielded, are visible to the detectors, and thus are a source of ~ 270 K loading. To avoid this, sheet-aluminum fairings were designed (Figure 2.10) to redirect those rays to the sky (Figure 2.11), whose background loading of ~ 3 K is

¹ <http://innovativecomposite.com>
 Innovative Composite Engineering
 139 East Columbia River Way
 Bingen, WA 98605

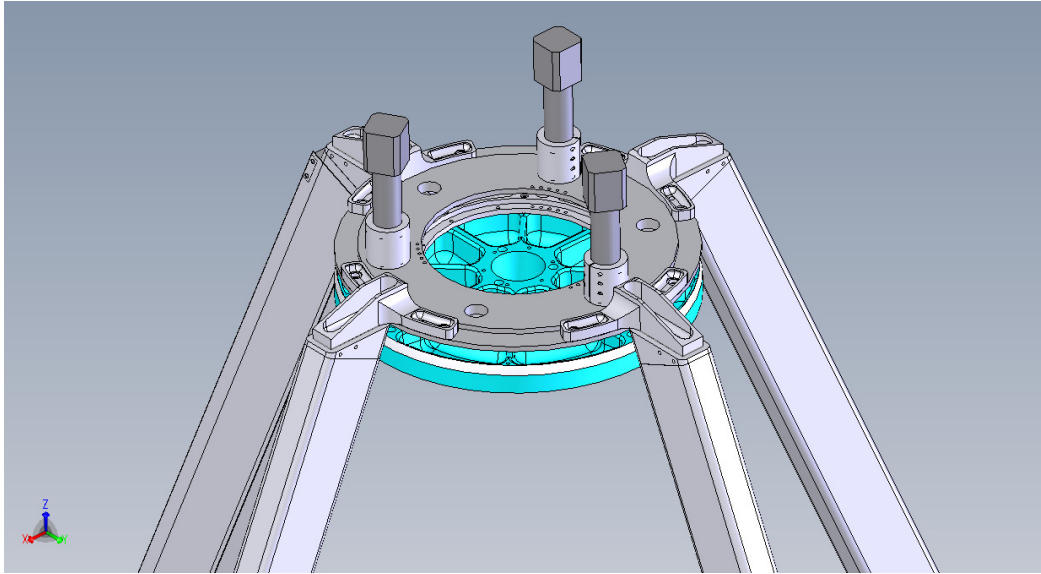


FIGURE 2.8: Solidworks assembly of final manufactured secondary support structure components, including actuators (schematic). Secondary mirror is shown in blue. Struts are carbon fiber, while the rest of the components are 6061 aluminium. Leaf springs connecting the two rings are not shown.

substantially less. Because they are mounted to the struts, and thus have a large moment arm, they needed to be extremely lightweight, and angled so that all the rays were directed to the sky, and none fell onto other parts of the telescope. They were made from bent sheet aluminum, 1/64 inches thick, in two parts ~ 825 mm in length. They were (carefully) mounted to the struts with aluminum tape.

2.2.3 Detectors

The detectors are adapted from those used on the SPIRE instrument (Griffin et al., 2003) aboard *Herschel*. The detector arrays comprise of 149, 88 and 43 silicon-nitride (spider-web) bolometers (see Figure 2.12), at 250, 350 and 500 μm , respectively. They are spaced at a distance of $2F\lambda$ to maximize optical efficiency, which results in fewer overall detectors for increasing wavelengths.

Each bolometer consists of a silicon nitride mesh absorber (the spider-web), which is an efficient absorber over a wide range of wavelengths, but whose cross-section for high-energy cosmic rays is quite small. A neutron-transmission doped (NTD) germanium thermistor sits in the middle of the spider web; by measuring its resistance, $R_b(T) = R_0 e^{\Delta/T}$, (where $R_0 = 55\Omega$ and $\Delta = 50K$ characterize the bolometers), we are able to determine the temperature of the mesh. Each bolometer has a unique thermal and electrical response, τ_T and τ_e , which must be measured using cosmic ray hits. The detectors are biased with an AC voltage,

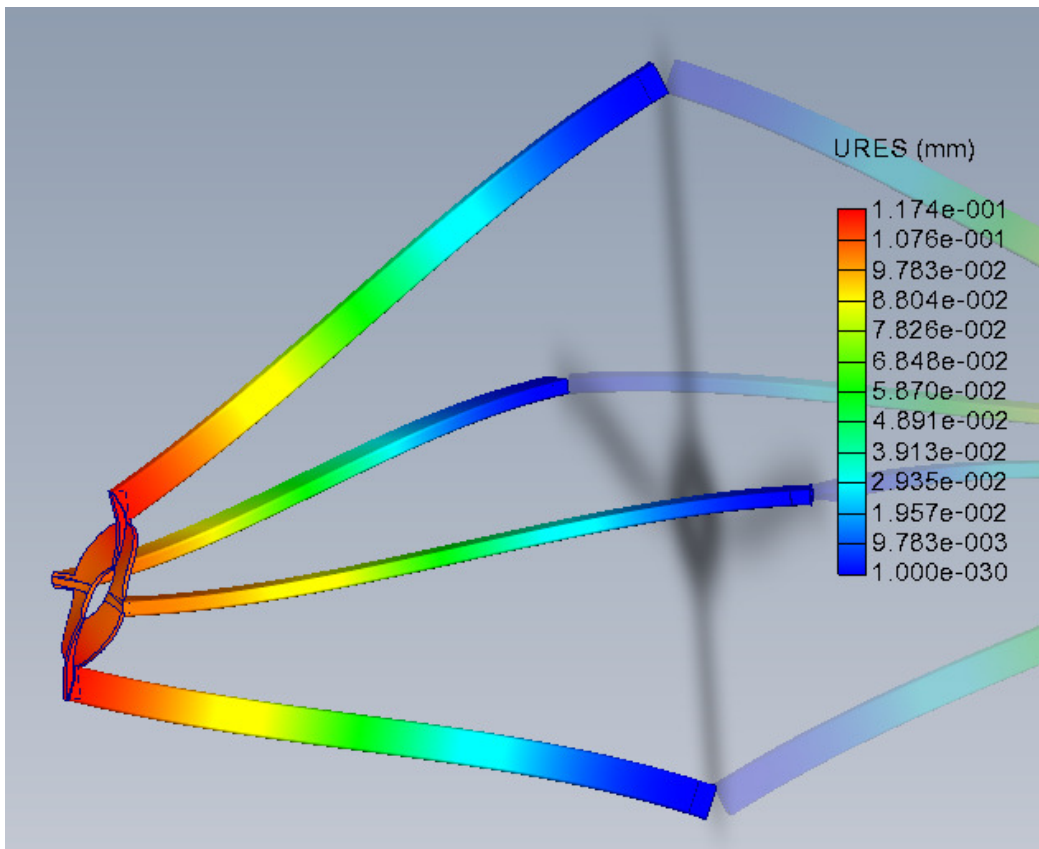


FIGURE 2.9: Finite element analysis performed with Solidworks proprietary software. This is an exaggerated example of the displacements which the part undergoes (i.e., deformation scale ~ 1670). This is a simplified version of the system, including the struts, ends and mounting ring. Displacement is colour coded and shown in the color-bar. The maximum displacement is 0.117 mm at the secondary support ring.

$V(t) = V_0 \sin(2\pi\nu t)$, with $\nu = 200.32$ Hz, in order to reduce the effects of $1/f$ noise. The signal is then amplified by a differential JFET, and then passed onto the receiver, where they are further amplified and filtered.

2.2.4 Gondola

The gondola refers to the structure which supports all parts of telescope, and is the attachment point to the balloon flight train. It must be designed to withstand violent forces (~ 10 g) at launch and descent, and enormous temperature variations ($\sim 100^\circ$ C), while being light enough (< 2000 kg) to fly from a balloon. The major components are illustrated in Figure 2.14. The maximum height and width are determined by the dimensions of the working high-bays in the field, as well limitations set by the launch vehicle (Figure 2.15²). The gondola frame consists of three main components: i) the outer frame, which is suspended

²Documentation can be found at <http://www.csbf.nasa.gov/docs.html>

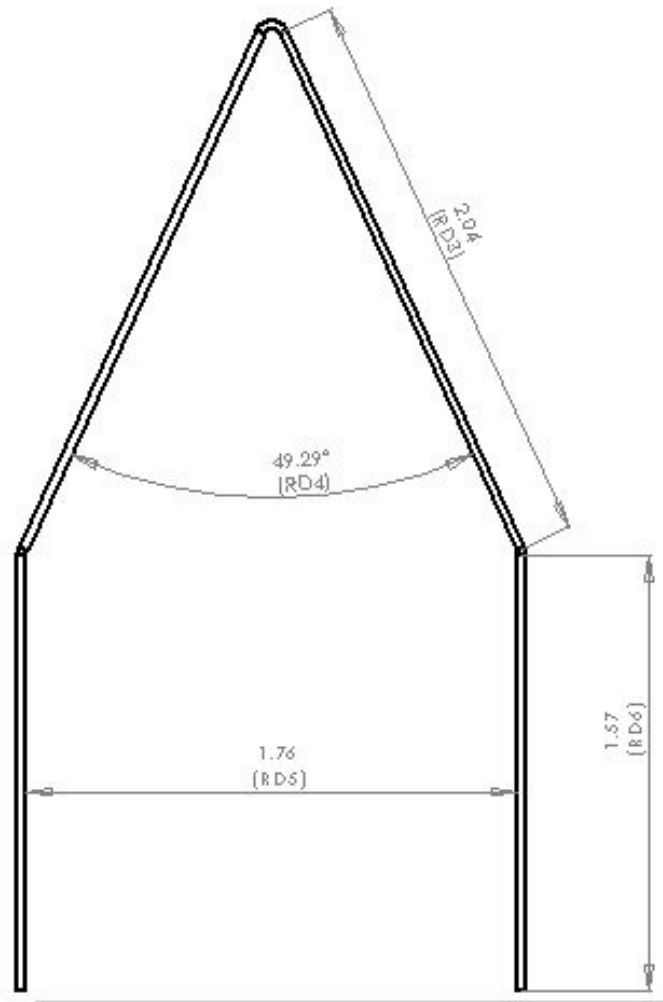


FIGURE 2.10: Mechanical drawing of bent sheet-aluminum fairing cross-section. Dimensions in inches. They are ~ 32.5 inches (825 mm) long.

from the balloon by four steel cables and a pivot motor. It is also responsible for scanning in azimuth, which it does through accelerations of the motorized reaction wheel; ii) the inner frame, which attaches to the outer frame by a motor and bearing which allows it to scan in elevation from $25 - 60^\circ$. It houses the cryostat and all of the optical elements; and iii) the sun-shields, which attach to the outer frame and keep the telescope shaded from unwanted radiation. They consist of an aluminum frame covered by aluminized mylar, which also supports the solar panels, which charge the batteries during flight.

The outer frame houses much of the warm electronics, which can be divided into three broad categories: i) the attitude control system (ACS), which runs the motors and pointing sensors; and ii) the flight computers, which control the telescope and write all data to two redundant hard drives. The computers are housed in a cylindrical pressure vessel which maintains an environment at 1 atm at float. The three systems communicate over serial RS485 through a custom made BLASTbus, which transmits 32-bit requests and responses. Its bandwidth is

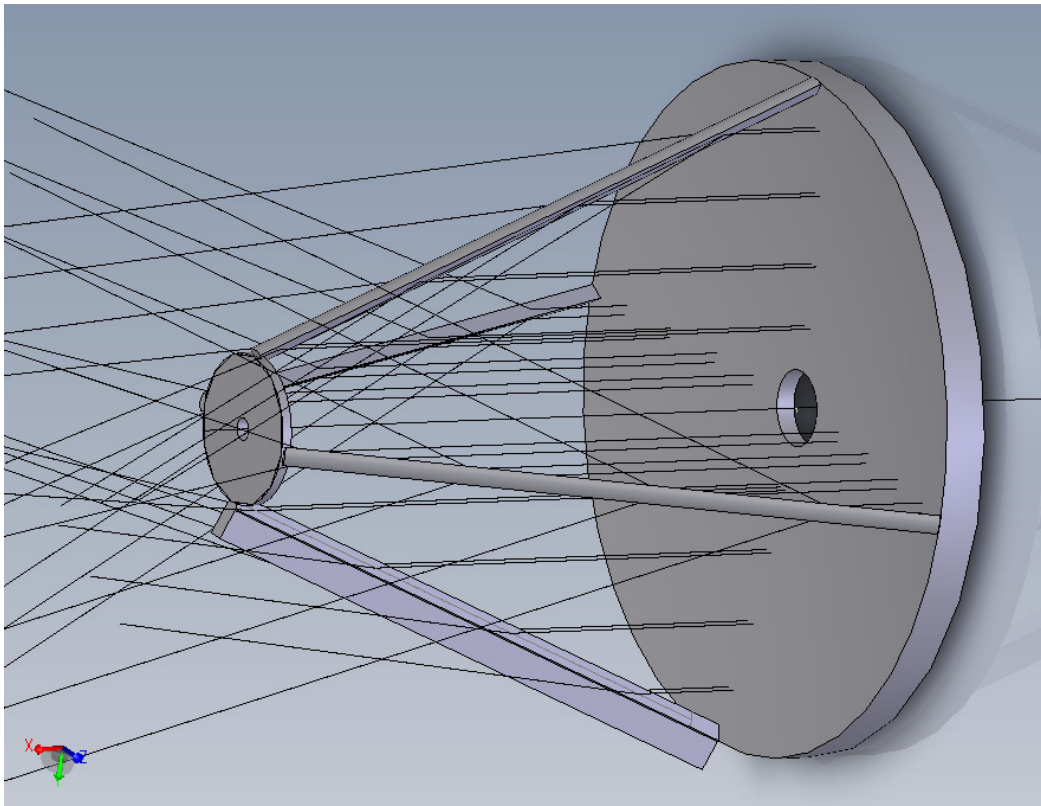


FIGURE 2.11: Solidworks schematic showing rays which would have originated from the carbon struts instead redirected to the sky as a result of the aluminum fairings. Therefore the detectors, rather than seeing the relatively warm struts, sees the cold sky, significantly reducing loading.

1 Mbits^{-1} . The outer frame also holds the reaction wheel, a 59 inch diameter, 2 inch thick, motor-controlled disk used to point the gondola in azimuth; as well as the batteries and charge-controller, which provide power to the gondola. The inner frame houses the preamp and the data acquisition system (DAS), which is responsible for housekeeping signals.

The warm electronics are kept cool by either radiating to the sky, or when necessary with an active cooling system, which channels cooling Dynalene fluid through plates thermally attached to the housing of the various units. This liquid is cycled back to a radiating plate thermally attached to the inner frame, which radiates to the shields inside.

2.2.5 Cryostat

The re-imaging optical system and detectors are held inside a long-duration cryostat (Figure 2.16). The cryostat is responsible for holding the detectors, cold-optics and JFETS/cold plate at their required operating temperatures of $\sim 300 \text{ mK}$, $\sim 1.5 \text{ K}$, and $\sim 130 \text{ K}$, respectively. This is achieved by cooling in stages.

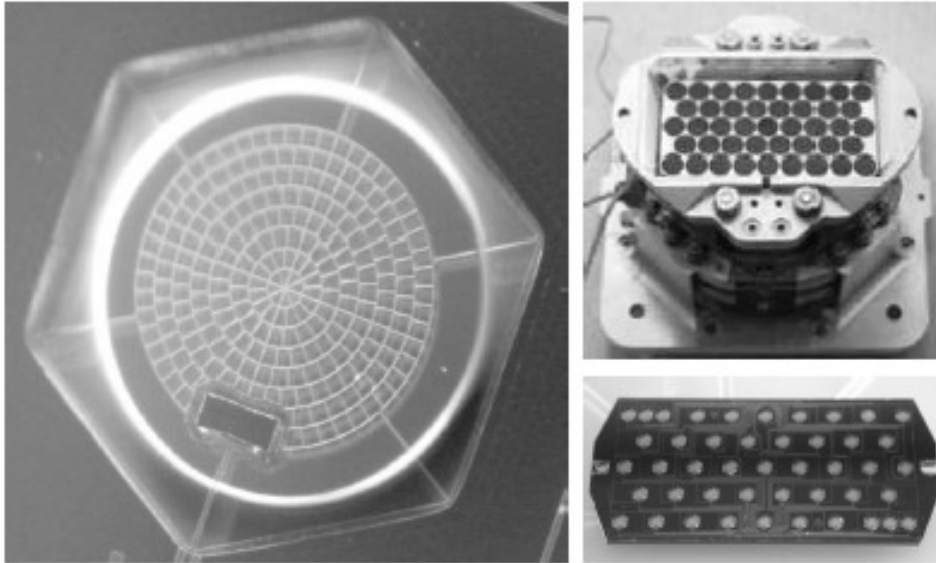


FIGURE 2.12: Left: Close up of a spider-web bolometer detector. Bottom-Right: Array of spider-web bolometers. Top-Right: Complete detector assembly highlighting conical feedhorns. Figure courtesy of JPL.

The first two stages are the liquid nitrogen (LN) and liquid helium (LHe) stages, which provide cooling to 77 and 4.2 K, respectively. Next is the pumped ^4He stage, which is pumped by being open to the atmosphere at float, providing cooling down to 1.5 K. The final stage is the ^3He refrigerator, which cools the detectors down to ~ 300 mK. This final stage pumps on liquid ^3He with cooled charcoal, which absorbs gaseous ^3He . Once all the ^3He is absorbed, it must be released again, which is done by simply raising the temperature of the charcoal to ~ 10 K, at which point the ^3He is released, condenses and is collected for the next cycle. A complete cycle takes approximately two days, and therefore the fridge would be cycled several times during a long-duration flight.

2.2.6 Attitude Sensors

The optimal, diffraction-limited, BLAST beam is 30 arcsec at $250 \mu\text{m}$, which therefore requires pointing reconstruction to better than $5''$, or a fifth of the beam. In order to achieve this ambitious goal, considering the platform is suspended from a balloon and observing during the day-time, pointing reconstruction relies on a combination of coarse and fine attitude sensors. The two primary pointing sensors are: i) two “star-cameras”, which provide absolute pointing with respect to the sky, mounted side-by-side on the top of the inner frame, and ii) a set of fiber-optic gyros that provide velocity information, which must be integrated to reconstruct position. Other coarse sensors are: i) a sun-sensor, ii) magnetometer, and iii) a GPS. Here we focus on the two primary sensors.

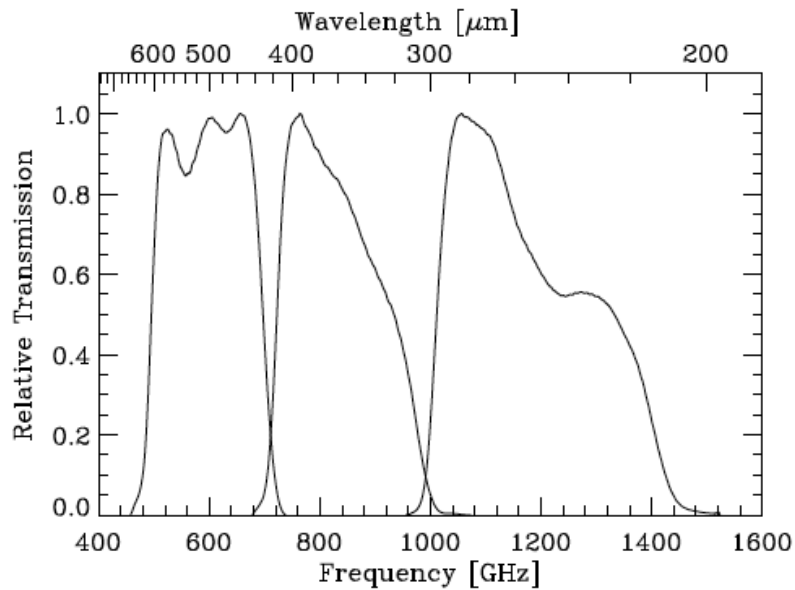


FIGURE 2.13: BLAST bandpasses measured with a Fourier transform spectrometer. Bandpasses here are averaged from many detectors, and have been corrected for the spectrum of the source. Note that each band is $\sim 30\%$ wide by design. Figure from Marsden (2007).

2.2.6.1 Star-Cameras

The so-called “star-cameras” are two day-time, CCD-based imagers, and are the primary absolute-pointing sensors for BLAST, providing pointing solutions to better than $2''$ (depending on the scan speed and integration time). They have come to be referred to as the ISC (inner star-camera) and the OSC (outer star-camera). Each camera is self-contained pressurized unit consisting of a detector, lens, computer and motorized aperture. A 4 foot baffle is attached to the front to reduce scattered light entering the aperture. The ISC (OSC) uses a 1312×1024 (1360×1036) CCD with 6.8 (6.45) μm pixels, and a 200 mm $f/2$ Nikon lens with a $2^\circ \times 2.5^\circ$ field of view. A red filter is used to increase the contrast between the stars and sky.

Since BLAST operates during continuous daylight, the star-cameras must integrate for a relatively long time (300 ms) in order to see stars fainter than $9 m_v$, and in order to form a solution, the algorithm requires three stars in each frame. However, because the telescope is continuously scanning, integrations that are that long would result in images of streaks rather than stars. Therefore, as the telescope scans back and forth, 300 ms exposures are timed to occur at turnarounds, when the angular velocity is low. Shorter exposures (~ 60 ms), usually detecting one or two stars, are taken during scans. These may not form robust solutions, but are useful for reconstruction with the Kalman filter (see § 2.3.1.3). For an in-depth description of the star-camera hardware and pointing solution algorithms see Pascale (2007).

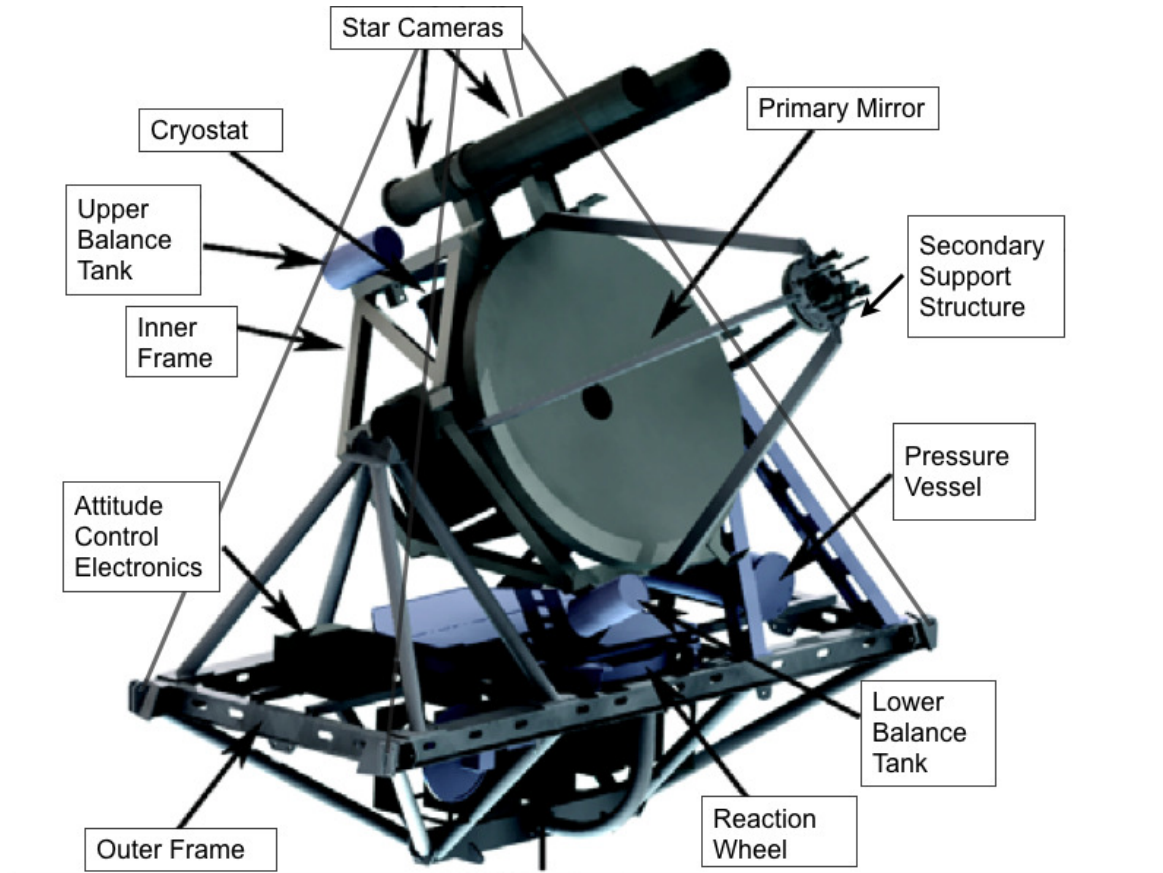


FIGURE 2.14: Solidworks schematic of the BLAST gondola and mounted components which make up the instrument.

2.2.6.2 Gyroscopes

For redundancy, BLAST uses two sets of three gyroscopes. Each set has three orthogonal, single-axis optical gyroscopes. One set consists of ECORE 2000 analogue output gyroscopes and the other of DSP 3000 digital output gyroscopes. They have noise levels of $N = 5$ and $4'' \text{ s}^{-1/2}$, respectively. Both sets are mounted orthogonally inside a magnetically shielded box, which is mounted to the inner frame.

Gyroscopes measure the rotation rate about one axis. In order to convert the measurement from rotation to position, the gyroscopes must be integrated

$$\Omega = \int_{t_1}^{t_2} \omega \, dt = \sum_{i=t_1}^{t_2} \omega_i \, \Delta t = \omega \Delta t + C, \quad (2.1)$$

where Δt is the discrete time-step of 10 ms. Since the integration results in a *relative* position measurement, then $C = \Omega_{i-1}$, the position of the telescope prior at each time-step $t - 1$, is required to form a solution, which is why the gyroscopes are considered *relative-pointing*

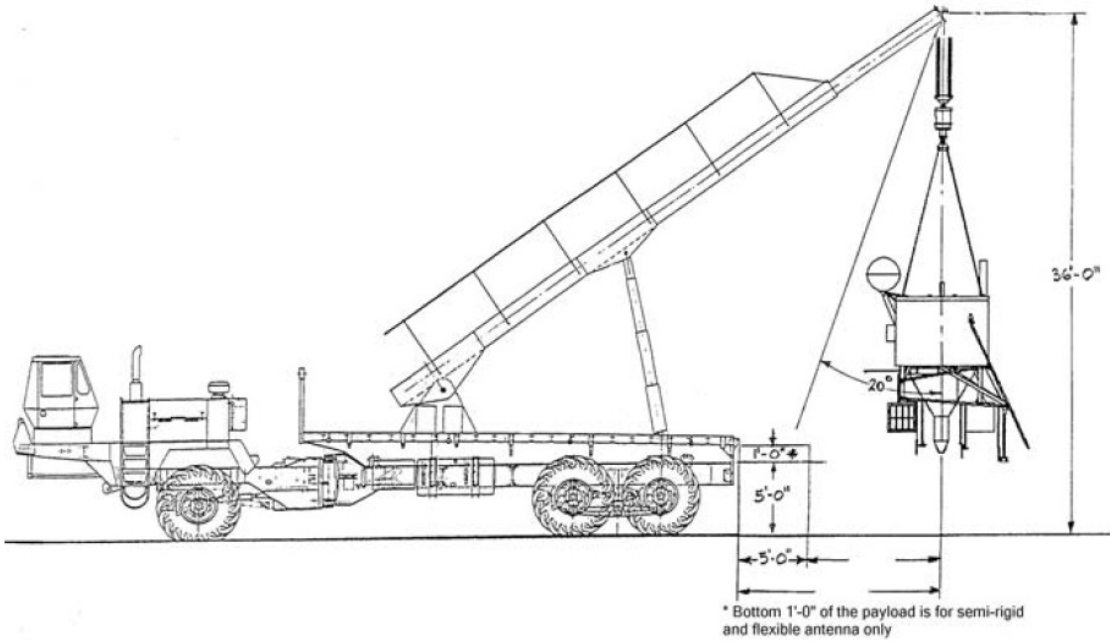


FIGURE 2.15: CSBF launch vehicle schematic. Gondola design must comply with limitations of the flight vehicle shown here. Figure from NASA CSBF gondola design recommendations manual.

sensors. If this were the whole story, then the gyroscopes would simply be calibrated once and the pointing solution problem would be solved. However, the gyroscopes suffer from $1/f$ noise, such that

$$\Omega = \int_{t_1}^{t_2} (\omega + N) dt = \sum_{i=t_1}^{t_2} (\omega_i + N) \Delta t = \omega \Delta t + N_i + \Omega_{i-1}. \quad (2.2)$$

The integrated noise results in large scale drifts equivalent to a random walk, and becomes dominant on timescales longer than 2 seconds. Therefore, the gyroscopes must be re-calibrated less than every 1.5 – 2 seconds, and preferably even more often, with pointing solutions provided by the star-cameras. This algorithm is presented in § 2.3.1.2; for a detailed description see [Pascale \(2007\)](#).

2.3 Data Reconstruction

To turn raw data into astronomical maps is multi-step process. The data itself must be cleaned of unwanted artifacts, and then calibrated. Additionally, where the telescope was pointed at any one time must be determined from secondary information, in order to relate raw data to the point in the sky that it represents. Here we briefly describe the treatment of raw data, the pointing solution algorithm, and the instruments used to acquire pointing

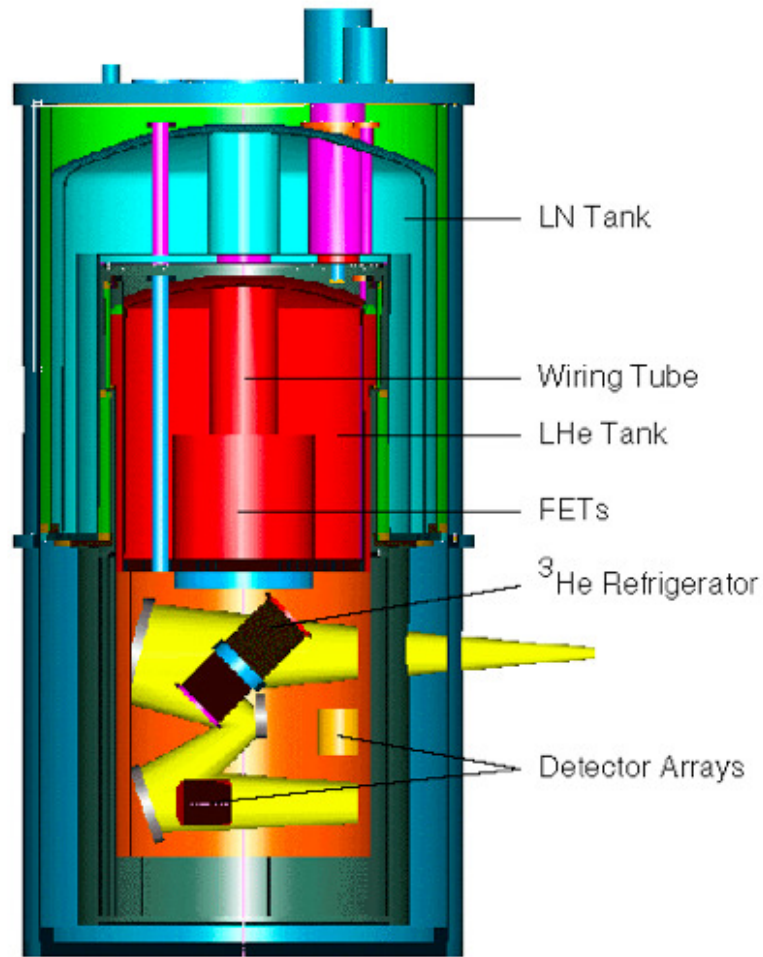


FIGURE 2.16: Solidworks cross-section of the BLAST cryostat highlighting major components, including the cryogenic tanks, electronics tube, and cold optics. Yellow path illustrates the beam as it enters the cryostat through a cryo-window, and is re-imaged by the cold optics.

data. For a more in depth treatment see [Marsden \(2007\)](#). We summarize the various map-makers and their applications and provide references to comprehensive descriptions of each one.

2.3.1 Attitude Determination

Determining the pointing of the telescope at any one time requires the use of multiple sensors in unison. The two primary sensors, the star-cameras and gyroscopes, provide enough information that together, through the use of the Kalman filter, an optimal solution can be found. Other, coarser sensors, which were flown for redundancy, were subsequently not used to form the pointing solution.

2.3.1.1 Attitude Matrix and Quaternions

The attitude of the payload describes the orientation of a rigid body in three-dimensions. It requires three Euler angles to measure its rotation relative to the stars. It is represented through an attitude matrix, \mathcal{A} , such that bore-sight positions \vec{b} and \vec{b}' are related via

$$\vec{b}' = \mathcal{A}\vec{b}, \quad (2.3)$$

and \mathcal{A} can be decomposed into three orthogonal components, which in telescope coordinates are best represented as

$$\mathcal{A} = \mathcal{A}_{\text{yaw}}(\alpha) \mathcal{A}_{\text{pitch}}(\gamma) \mathcal{A}_{\text{roll}}(\rho), \quad (2.4)$$

and

$$\mathcal{A}_{\text{yaw}}(\alpha) = \begin{pmatrix} \cos(\alpha) & -\sin(\alpha) & 0 \\ \sin(\alpha) & \cos(\alpha) & 0 \\ 0 & 0 & 1 \end{pmatrix} \quad (2.5)$$

$$\mathcal{A}_{\text{pitch}}(\gamma) = \begin{pmatrix} 1 & 0 & 0 \\ 0 & \cos(\gamma) & -\sin(\gamma) \\ 0 & \sin(\gamma) & \cos(\gamma) \end{pmatrix} \quad (2.6)$$

$$\mathcal{A}_{\text{roll}}(\rho) = \begin{pmatrix} \cos(\rho) & 0 & \sin(\rho) \\ 0 & 1 & 0 \\ -\sin(\rho) & 0 & \cos(\rho) \end{pmatrix} \quad (2.7)$$

Throughout this section we will use the mathematical notation of quaternions, which provide an alternative to the more cumbersome rotation matrices. Just as rotations in the complex plane can be represented by a multiplication of a complex number, e.g., $e^{i\phi}$, rotations in three-dimensional space can be represented with quaternions. Briefly, a quaternion is a four-element extension of a complex number,

$$q = (a, b, c, d) = (a, \vec{v}) = a \cdot 1 + b \cdot i + c \cdot j + d \cdot k, \quad (2.8)$$

where $1, i, j,$ and k are the orthogonal basis quaternions. As is written on the Brougham (Broom) Bridge in Dublin, where Sir William Rowan Hamilton, “in a flash of genius”, discovered the fundamental formula for quaternion multiplication

$$i^2 = j^2 = k^2 = ijk = -1. \quad (2.9)$$

Unit	$I = (1, \vec{0})$
Norm	$\ (s, \vec{v})\ = a^2 + \vec{v} \cdot \vec{v}$
Conjugate	$(a, \vec{v})^* = (a, -\vec{v})$
Inverse	$q^{-1} = q^*/\ q\ $
Addition	$(a1, \vec{v}1) + (a2, \vec{v}1) = (a1 + a2, \vec{v}1 + \vec{v}2)$
Subtraction	$(a1, \vec{v}1) - (a2, \vec{v}1) = (a1 + a2, \vec{v}1 - \vec{v}2)$
Multiplication	$(a1, \vec{v}1)(a2, \vec{v}1) = (a1a2 - \vec{v}1 \cdot \vec{v}2, a1\vec{v}1 + a2\vec{v}2 + \vec{v}1 \times \vec{v}2)$
Division	$q1/q2 = q1q2^{-1}$

TABLE 2.2: Quaternion Identities

Addition of two quaternions is performed element by element, while multiplication is distributive,

$$qr = (a, \vec{v})(b, \vec{w}) = (ab - \vec{v} \cdot \vec{w}, a\vec{w} + b\vec{v} + \vec{v} \times \vec{w}), \quad (2.10)$$

where \times is the cross product. The inverse of a quaternion, q^{-1} , is

$$q^{-1} = q^*/|q|^2 = (a, -\vec{v})/|q|^2, \quad (2.11)$$

so that $q \cdot q^{-1} = 1$, and $q^* = (a, -\vec{v})$ is the conjugation operator, which is equal to the inverse for a normalized quaternion.

Thus, a rotation of vector \vec{v} by angle α about the axis \hat{n} in quaternion notation is calculated as

$$(0, \vec{v}') = Q(0, \vec{v})Q^*, \quad (2.12)$$

where

$$Q = q_{\hat{n}}(\alpha) = \left(\cos\left(\frac{\alpha}{2}\right), \hat{n} \sin\left(\frac{\alpha}{2}\right) \right), \quad (2.13)$$

where $q_{\hat{n}}(\alpha)$ is a unit quaternion. Finally, the quaternion analogs to the rotation matrices are

$$\mathcal{A}_{\text{yaw}}(\alpha) \Rightarrow q_{\text{yaw}}(\alpha) = \begin{pmatrix} \cos(\alpha) \\ \hat{z} \sin(\alpha) \end{pmatrix} \quad (2.14)$$

$$\mathcal{A}_{\text{pitch}}(\gamma) \Rightarrow q_{\text{pitch}}(\phi) = \begin{pmatrix} \cos(\gamma) \\ \hat{x} \sin(\gamma) \end{pmatrix} \quad (2.15)$$

$$\mathcal{A}_{\text{roll}}(\rho) \Rightarrow q_{\text{roll}}(\rho) = \begin{pmatrix} \cos(\rho) \\ \hat{y} \sin(\rho) \end{pmatrix} \quad (2.16)$$

Operations of quaternions are summarized in Table 2.2. For a more in-depth description of quaternions see [Pascale \(2007\)](#).

2.3.1.2 Kalman Filter

The Kalman filter (Kamen & Su, 1999) is an iterative predictor-corrector which finds the least-squares estimate to the state quaternion, whose inputs are time-ordered position and noise matrices. Applied to BLAST, the Kalman filter receives star-camera solutions and gyroscope positions, and outputs bore-site pointings.

The attitude of the telescope, which we refer to here as the “state”, $x(n)$, is related to the signal, $s(n)$, through a “measurement matrix”, C , such that

$$s(n) = Cx(n), \quad (2.17)$$

where n is the discrete time index. The state moves forward in time as

$$x(n+1) = \Phi x(n) + \Gamma w(n), \quad (2.18)$$

where Φ is the time-update matrix, $w(n)$ is the “process noise”, and Γ is the noise propagation matrix. The process noise is caused by external perturbations to the gondola, such as winds or motor-induced pendulations. Alternatively, $v(n)$ describes noise in the measurement, such that

$$z(n) = s(n) + v(n). \quad (2.19)$$

Thus, if $\hat{x}(n)$ is the estimate of the state, then the error in the estimate is

$$\tilde{x}(n) = x(n) - \hat{x}(n), \quad (2.20)$$

which can be rewritten as the error covariance matrix, $P(n)$

$$P(n) = E[\tilde{x}(n) \tilde{x}^T(n)]. \quad (2.21)$$

The Kalman filter is a predictor-corrector algorithm, which means estimate of the state happens in two steps: the prediction (*a priori*) estimate, or the *time* update; and the correction (*a posteriori*) estimate, or *measurement* update. The prediction is done through the time-update matrix, Φ , and the correction through the actual measurement z .

Given *a priori* solutions \hat{x}^- and $P^-(n)$ at time n , then the *a posteriori* values are calculated from $z(n)$ as

$$K(n) = P^-(n)C^T[CP^-(n)C^T + R]^{-1}, \quad (2.22)$$

$$\hat{x}(n) = \hat{x}^-(n) + K(n)[z(n) - C\hat{x}^-(n)], \quad (2.23)$$

$$P(n) = P^-(n) - K(n)CP^-(n), \quad (2.24)$$

where $K(n)$ is known as the “Kalman gain”, and R is the measurement noise covariance matrix. The state is then updated to the next time step, $n + 1$, by

$$\hat{x}^-(n+1) = \Phi \hat{x}(n) \quad (2.25)$$

$$P^-(n+1) = \Phi P(n) \Phi^T + \Gamma Q \Gamma^T, \quad (2.26)$$

where Q is the process noise covariance matrix.

In the case of a non-linear time-update matrix, represented by ϕ , Equation 2.18 is rewritten as

$$x(n+1) = \phi(x(n)) + \Gamma w(n), \quad (2.27)$$

and ϕ can be Taylor expanded about $\hat{x}(n)$ such that

$$\phi(x(n)) = \phi(\hat{x}(n)) + J_\phi(\hat{x}(n))[x(n) - \hat{x}(n)] + \dots, \quad (2.28)$$

where $J_\phi(x)$ is the Jacobian of ϕ evaluated at x

$$(J_\phi(x))_{ij} = \frac{\partial \phi_i}{\partial x_j}. \quad (2.29)$$

Finally, the time-update is modified such that

$$\hat{x}^-(n+1) = \phi(\hat{x}(n)) \quad (2.30)$$

$$P^-(n+1) = J_\phi(\hat{x}(n))P(n)J_\phi^T(\hat{x}(n)) + \Gamma Q \Gamma^T, \quad (2.31)$$

2.3.1.3 Non-Linear Kalman Filter applied to BLAST

The BLAST pointing solution combines input from one star-camera (ISC) and the digital gyroscopes. They are chosen because of their superior performance and noise properties. The final pointing solution strikes the optimal balance between star-camera solutions, whose position uncertainties are roughly constant, but whose rate of solutions is low, and the gyroscopes, which provide continuous solutions, but whose error grows with time. In words, the algorithm favours the solution whose error is the smaller of the two. When that happens to be the star-camera, the gyroscopes are re-calibrated so that their drift is reset to zero.

The state of the telescope, x , is describe by 3 gyroscope biases, b_i , and 4 components of the quaternion, q_i , which describes the orientation of the telescope at i . Thus

$$x(n) = \begin{pmatrix} \vec{b}(n) \\ q(n) \end{pmatrix}, \quad (2.32)$$

is a 7 component vector. Defined explicitly,

$$b(n+1) = b(n) + w_{process}(n), \quad (2.33)$$

$$q(n+1) = \begin{pmatrix} 1 \\ \frac{1}{2}\omega(n)\Delta T \end{pmatrix} q(n) + \begin{pmatrix} 0 \\ \frac{1}{2}b(n)\Delta T \end{pmatrix} q(n) + \begin{pmatrix} 0 \\ \frac{1}{2}w_\omega(n)\Delta T \end{pmatrix} q(n), \quad (2.34)$$

where $\omega(n)$ is the gyroscope angular rate measurement, and $w_\omega(n)$ is the noise on that measurement. Since the biases cannot be measured, they are left as free parameters in the fit.

The state quaternion can be described by the orientations in yaw, pitch and roll,

$$q = q_{yaw} \ q_{pitch} \ q_{roll}, \quad (2.35)$$

and is updated through each time-step

$$q(n+1) = \delta q(n) \ q(n), \quad (2.36)$$

where

$$\delta q(n) = \left(\cos\left(\frac{|\vec{w}\Delta t}{2}\right), \frac{\vec{w}}{|\vec{w}|} \sin\left(\frac{|\vec{w}\Delta t}{2}\right) \right) \approx \left(1, \frac{\vec{w}\Delta t}{2} \right), \quad (2.37)$$

whose form follows Equation 2.13, and the right hand term follows from a first-order Taylor expansion, whose higher order terms are negligible since Δt is small.

\vec{w} must account for the varying biases \vec{b} , as well as the signal from the gyroscope, which we call $\vec{\Omega}$, such that

$$\vec{w} = \vec{\Omega} + \vec{b}, \quad (2.38)$$

and $\vec{b}(n+1) = \vec{b}(n)$, given no other information about b . Finally, the time update matrix is

$$\phi(\hat{x}(n)) = \begin{pmatrix} \vec{b}(n) \\ \left(1, \frac{\Delta t}{2} \left(\vec{\Omega}(n) + \vec{b}(n) \right) q(n) \right) \end{pmatrix},$$

and the Jacobians (Equation 2.29) are calculated numerically at each time-step, which for small changes can be approximated as

$$\frac{\partial \phi_i}{\partial x_j} \approx \left(\frac{\phi(x + h e^j) - \phi(x)}{h} \right), \quad (2.39)$$

where e^j is the unit vector along the direction j . In order to propagate the noise, \vec{w} , which consists of bias noise, \vec{n} , and angular velocity noise \vec{N} , such that

$$\vec{w} = \begin{pmatrix} \vec{n}(n) \\ \vec{N}(n) \end{pmatrix}, \quad (2.40)$$

we construct the noise propagation matrix

$$\Gamma = \frac{\Delta}{2} \left(\begin{array}{ccc|ccc} 1 & 0 & 0 & 0 & 0 & 0 \\ 0 & 1 & 0 & 0 & 0 & 0 \\ 0 & 0 & 1 & 0 & 0 & 0 \\ \hline 0 & 0 & 0 & -q_1 & -q_2 & -q_3 \\ 0 & 0 & 0 & q_0 & q_3 & -q_2 \\ 0 & 0 & 0 & -q_3 & q_0 & q_1 \\ 0 & 0 & 0 & q_2 & -q_1 & q_0 \end{array} \right), \quad (2.41)$$

and the noise covariance matrices Q and R , which describe \vec{w} and \vec{v} , respectively, are

$$Q = \left(\begin{array}{ccc|ccc} \sigma_{b_1}^2 & 0 & 0 & 0 & 0 & 0 \\ 0 & \sigma_{b_2}^2 & 0 & 0 & 0 & 0 \\ 0 & 0 & \sigma_{b_3}^2 & 0 & 0 & 0 \\ \hline 0 & 0 & 0 & \sigma_{\omega_1}^2 & 0 & 0 \\ 0 & 0 & 0 & 0 & \sigma_{\omega_2}^2 & 0 \\ 0 & 0 & 0 & 0 & 0 & \sigma_{\omega_3}^2 \end{array} \right), \quad (2.42)$$

and

$$R = \begin{pmatrix} \sigma_1^2 & 0 & 0 & 0 \\ 0 & \sigma_2^2 & 0 & 0 \\ 0 & 0 & \sigma_3^2 & 0 \\ 0 & 0 & 0 & \sigma_4^2 \end{pmatrix}, \quad (2.43)$$

and are estimated from the expected noise properties of the gyroscopes and star cameras, respectively.

The gyroscopes provide solutions at 100 Hz, but the star-camera solutions are much less frequent. In the cases when the star-camera solutions are not available, the measurement update steps (Equations 2.22–2.24) are skipped and the values \hat{x}^- and P^- are simply copied onto \hat{x} and P .

However, when star-camera solutions are available, in order to reject spurious solutions, its credibility is judged by whether it falls into the range defined by an error envelope. The error envelope is determined by the time since the last accepted star-camera solution, and is

based on the expected gyroscope error. Since the gyroscope error increases as \sqrt{t} , the scale of the error envelope is set to the nominal value of $\sigma_{gyro} = 4'' \text{ s}^{-1/2}$, and grows exponentially with time. The error envelope, $\epsilon(t)$, is thus defined as

$$\epsilon(t) = \sigma_{gyro} = \sqrt{t} \cdot f(t), \quad (2.44)$$

where t is the elapsed time since the last accepted star-camera solution, and $f(t)$ is the exponential envelope

$$f(t) = \begin{cases} 1 & t \leq t_0, \\ e^{\frac{t-t_0}{\tau_{err}}} & t > t_0. \end{cases} \quad (2.45)$$

The parameters in the exponent are chosen empirically to be $t_0 = 5 \text{ s}$ and $\tau_{err} = 3 \text{ s}$. Each star-camera solution is compared to error envelope, and is rejected if it falls outside of 5ϵ .

The filter can be run forward or backward in time, which produce independent solutions. Both solutions are found and the two are smoothed together

$$q_{smoothed} = \frac{\epsilon_{backward}^2 q_{forward} + \epsilon_{forward}^2 q_{backward}}{\epsilon_{forward}^2}, \quad (2.46)$$

$$\epsilon_{smoothed} = \sqrt{\frac{\epsilon_{forward}^2 \epsilon_{backward}^2}{\epsilon_{forward}^2 + \epsilon_{backward}^2}}. \quad (2.47)$$

The solutions are translated into yaw, pitch and roll and written to disk. Figure 2.17 illustrates the forward, backward and smoothed solutions in pitch.

2.3.1.4 Pointing Reconstruction Results

The offset between the star cameras and the submillimeter telescope was measured by repeated observations of pointing calibrators throughout the flight. We found that the relative pointing between the star cameras and submillimeter telescope varied as a function of telescope elevation. We apply an elevation-dependent correction to pitch and yaw with approximate peak-to-peak amplitudes of $260''$ and $36''$, respectively, over the full $25 - 60^\circ$ elevation range of the telescope.

Pointing accuracy was verified with a stacking analysis performed on one of the extragalactic maps. Using a very deep 1.4 GHz VLA map of the Extended Chandra Deep Field South (E-CDFS) (Miller et al., 2008), patches of the BLAST maps centered on the radio coordinates were summed pixel by pixel. The peak in the stacked map is located within $2''$ from the nominal position of the catalog.

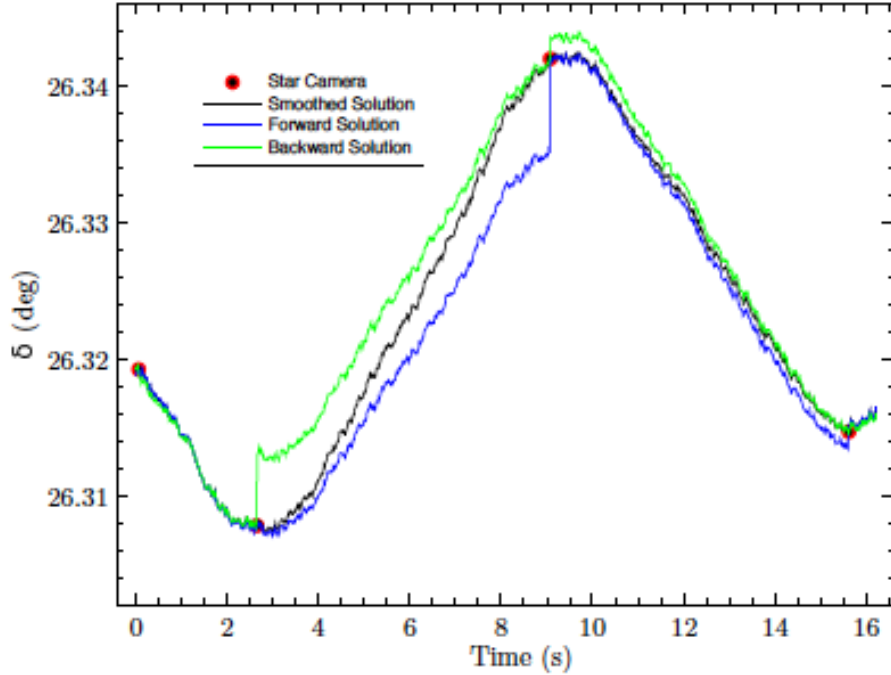


FIGURE 2.17: Forward (blue), backward (green) and smoothed (black) pointing solution. Star camera solutions are shown as red/black points. Figure from Marsden (2007).

Finally, assuming random Gaussian pointing errors, we superimposed a synthetic scaled PSF on the stacked maps and convolved it with a Gaussian profile, to reproduce broadening due to pointing jitter. We compute the minimum χ^2 of the convolved PSF to estimate the pointing error, finding an upper limit of $5''$.

2.3.2 Data Reduction

In order to turn raw data into maps, the data must be treated in a number of ways, and then combined with the pointing solution described above through the use of a mapmaker. A comprehensive description of the data reduction pipeline can be found in Truch (2007), and of the different mapmakers can be found in Pascale (2007) and Patanchon et al. (2008).

2.3.2.1 Timestream Preparation

Before raw bolometer data can be assembled into maps it must be treated in a number of ways. First, spikes in the time-streams due to cosmic rays and other glitches must be identified and flagged. Cosmic rays cause the bolometer to spike in temperature, and falls off again exponentially with time, with a time constant of $\tau \sim 2$ ms.

Next, the data must be deconvolved, in Fourier space, to account for the low-pass filter which was applied during observations. This filter has a cut-off frequency of ~ 35 Hz, and is designed to keep out high-frequency noise aliasing.

The data are then calibrated using measurements of the calibration lamp taken throughout the flight. The lamp is pulsed for 150 ms every 15 minutes. These regions are flagged and filled with an appropriate level of white noise. The responsivity of each bolometer is compared to a reference bolometer by measuring their response to an astronomical point source. The final absolute calibration is calculated by fitting the data to the spectral energy density of a well known point source (in this case the galaxy Arp 220).

2.3.2.2 Mapmaking

Cleaned time-ordered data (TOD) can be assembled into maps in a variety of ways, some more sophisticated than others. The simplest mapmaker, which directly assigns data to pixels according to the pointing solution, and returns the mean of these entries. Said in the language of linear algebra,

$$Pm = d, \quad (2.48)$$

where d is the time-ordered data vector with length n_d , m is the map vector, which contains the values of each pixel in the map (and has size n_m , i.e., number of pixels in the map), and P is the $n_d \times n_m$ pointing matrix, which assigns d to m according to the pointing solution. In the case of BLAST, which has many detectors per array, $n_d = n_t n_b$, where n_t is the number of time samples, and n_b is the number of bolometer detectors. If all of the data in a time sample is assigned to a single pixel, then the rows of P will consist of one 1 and the rest 0, resulting in

$$m = (P^T P)^{-1} P^T d, \quad (2.49)$$

where \cdot^T is the matrix transpose, and \cdot^{-1} is the matrix inverse. Said simply, each element of $P^T d$ is the sum of the data placed into that map pixel by the pointing matrix, and $P^T P$ contains the number of “hits” in each pixel. In other words, each element on the right side of Equation 2.49 is the average of the data points projected into each pixel.

If errors associated with the data are known or can be approximated, then the mapmaking algorithm can be extended to take them into consideration such that

$$m = (P^T P)^{-1} P^T N^{-1} d, \quad (2.50)$$

where N is the $n_d \times n_d$ noise correlation matrix,

$$N = \begin{pmatrix} \sigma_1^2 & \sigma_{12}^2 & \cdots & \sigma_{1n}^2 \\ \sigma_{12}^2 & \sigma_2^2 & \cdots & \sigma_{2n}^2 \\ \vdots & \vdots & \ddots & \vdots \\ \sigma_{1n}^2 & \sigma_{2n}^2 & \cdots & \sigma_n^2 \end{pmatrix}, \quad (2.51)$$

σ_i is the noise variance of each measurement d_i , and σ_{ij} is the noise covariance of the measurements d_i and d_j . Thus, for each pixel

$$m_j = \frac{\sum_k d_k w_k}{\sum_k w_k}, \quad (2.52)$$

which is equivalent to the weighted least-squares solution where the sum is over data binned in pixel j and weighted by $w_k \equiv \sigma^{-2}$.

In the simplest case, data is uncorrelated so that $\sigma_{ij}^2 = 0$ for $i \neq j$, and N is diagonal. As a result, $P^T N^{-1} P$ is also diagonal, and is easily calculated. This is referred to as a “naive” mapmaker and is the basis for Optbin (Pascale et al., 2008), the naive mapmaker used for many of BLAST’s scientific analyses. However, in order for this to work the input data must be relatively “flat”, in other words, any large scale drift must be removed (via high-pass or other filters) in order to avoid striping. In the case of BLAST maps, the data is first “whitened”, which means the mean of each TOD is removed, and then filtered with a high-pass 8th order Butterworth filter with cut-off frequency $f_0 = 0.05$ Hz. To prevent ringing, the first and last 2000 samples of TOD are apodized and are not used in the map.

Such aggressive filtering inevitably removes large-scale signal as well. To avoid high-pass filtering, and thus retain those spatial scales, the noise correlation matrix can be extended to include correlated noise between data points, including correlations in time (due to $1/f$ drift) and correlations between bolometers (from sky noise, cross-talk, telescope loading, etc.). This will appear as non-zero off-diagonal elements, i.e., $\sigma_{ij}^2 \neq 0$. Unfortunately, such a solution quickly becomes computationally limited for large maps, since it requires matrix inversion of rather large matrices ($\propto n^3$ for $n \times n$ maps). Therefore, in order to make the algorithm more computationally feasible, simplifying assumptions or approximations must be made. For a full account of the algorithm used for BLAST optimal mapmaker, SANEPIC, see Patanchon et al. (2008). In short, SANEPIC is successfully able to retain scales of order 60’, with a transfer function within 3% of unity.

2.3.3 BLAST Simulator

In order to perform Monte Carlo simulations of BLAST maps, we require a way to simulate what a realization of the sky would look like if it were observed by BLAST. Therefore, a simulator was developed to receive an input map and pointing solution, and return a simulated BLAST map. The following steps are performed by the simulator:

The input map must first be convolved with the BLAST beam. Asymmetries in the beam are accounted for by rotating the beam by the rotation angles provided by the pointing solution. The convolved map is then scanned with the pointing solution, to generate a signal-only timestream.

Noise is added to the timestream by randomly sampling the noise power spectrum (PSD), corrected for correlated signal, of each detector. Correlated signal is also generated and added to the noise timestream, after being multiplied by the appropriate amplitude coefficient.

The signal and noise timestreams are written separately, and can be added to generate signal plus noise timestreams. Thus, output maps of signal only, noise only, or signal plus noise are output by the simulator. Extensive use of the simulator was made in analyzing the noise properties of the BLAST power spectrum, as is described in Chapter 4.

2.4 Maps

BLAST06 circumnavigated the south pole, and therefore only southern fields were available to observe. The extragalactic fields observed by BLAST were chosen to overlap with fields that had, or would eventually have, rich or unique ancillary data. GOODS-south is one of the most heavily observed fields in the sky, with publicly available maps and catalogues in the xray, optical, NIR and radio. The SEP is one of two targeted deep fields of the *AKARI* satellite, a MIR and otherwise all-sky observatory. BLAST maps were made with both Optbin and SANEPIC, and the maps used for analyses was chosen depending on the task at hand. For example, analyses concerned with resolved sources used Optbin maps, since the large scales, which are filtered out, are not needed. Flight performance and calibration can be found in [Truch et al. \(2009\)](#).

2.4.1 GOODS

BLAST observed a wide 8.7 deg^2 patch, centered on the GOODS-South field ($3^{\text{h}}32^{\text{m}}35^{\text{s}}, -28^{\circ}15'$; hereafter BGS-Wide), with mean $1\text{-}\sigma$ sensitivities of 36, 31, and 20 mJy beam $^{-1}$ at 250, 350,

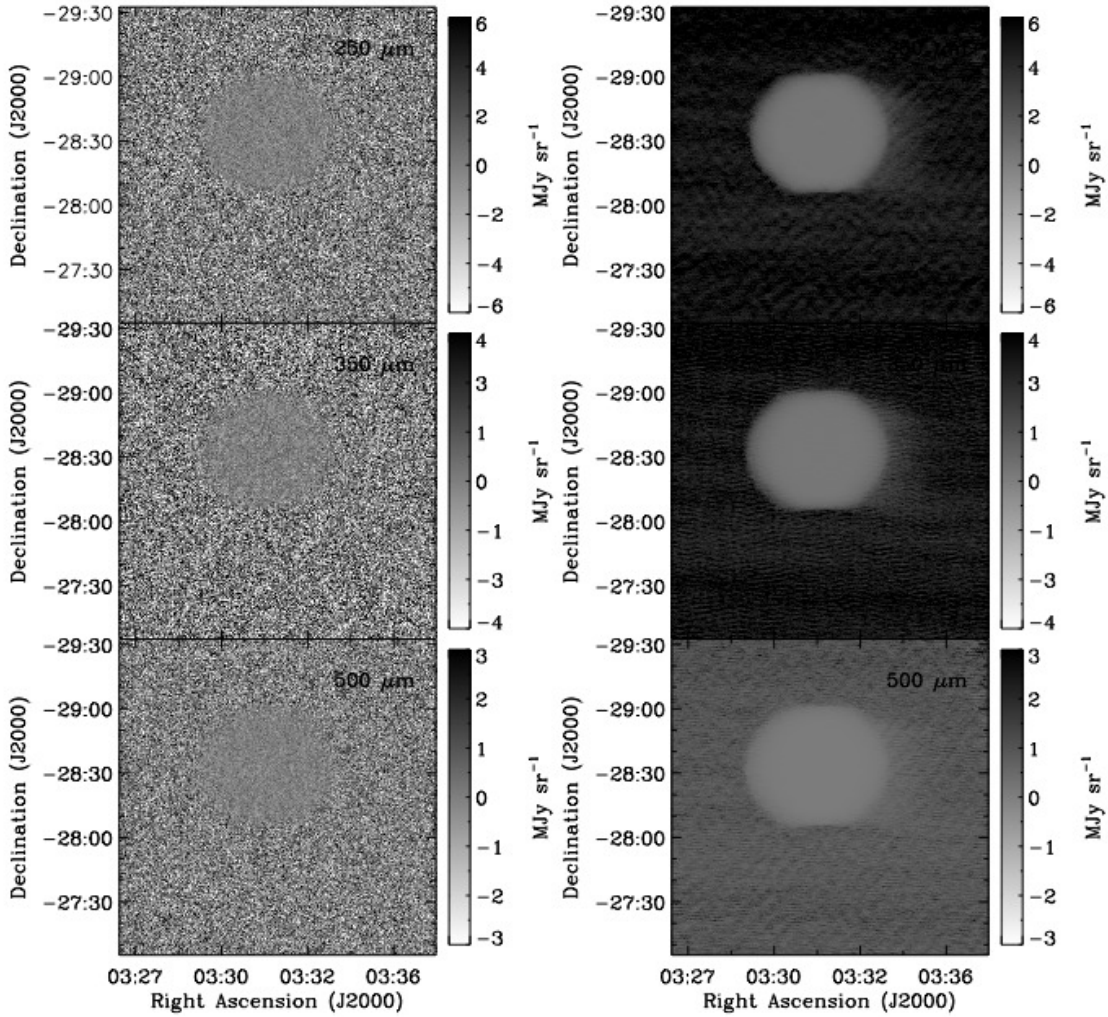


FIGURE 2.18: GOODS-south maps made with Optbin. Left: Flux. Right: Variance

and $500\ \mu\text{m}$, as well as a deep, nested field of $0.8\ \text{deg}^2$, centered on $(3^{\text{h}}32^{\text{m}}30^{\text{s}}, -27^{\circ}48')$; hereafter BGS-Deep) with mean $1\text{-}\sigma$ sensitivities of 11, 9 and $6\ \text{mJy beam}^{-1}$, respectively¹. Approximately 500 sources with signal-to-noise greater than 5 are resolved, with ~ 253 of them in BGS-Deep, and ~ 261 of them in BGS-Wide. More detail concerning maps and sources in BGS-Deep and Wide can be found in [Devlin et al. \(2009\)](#), [Iverson et al. \(2009\)](#), and [Dunlop et al. \(2009\)](#).

2.4.2 SEP

Near the south ecliptic pole (SEP) there is a nearly rectangular “window” through the galactic cirrus which was targeted by the *AKARI* satellite ([Matsuhara et al., 2006](#)). *BLAST* observed an overlapping region, whose corners are given by: $[(4^{\text{h}}57^{\text{m}}00^{\text{s}}, -51^{\circ}34'), (5^{\text{h}}03^{\text{m}}22^{\text{s}}, -52^{\circ}50')]$,

¹BLAST maps and catalogs are publicly available at <http://www.blastexperiment.info>

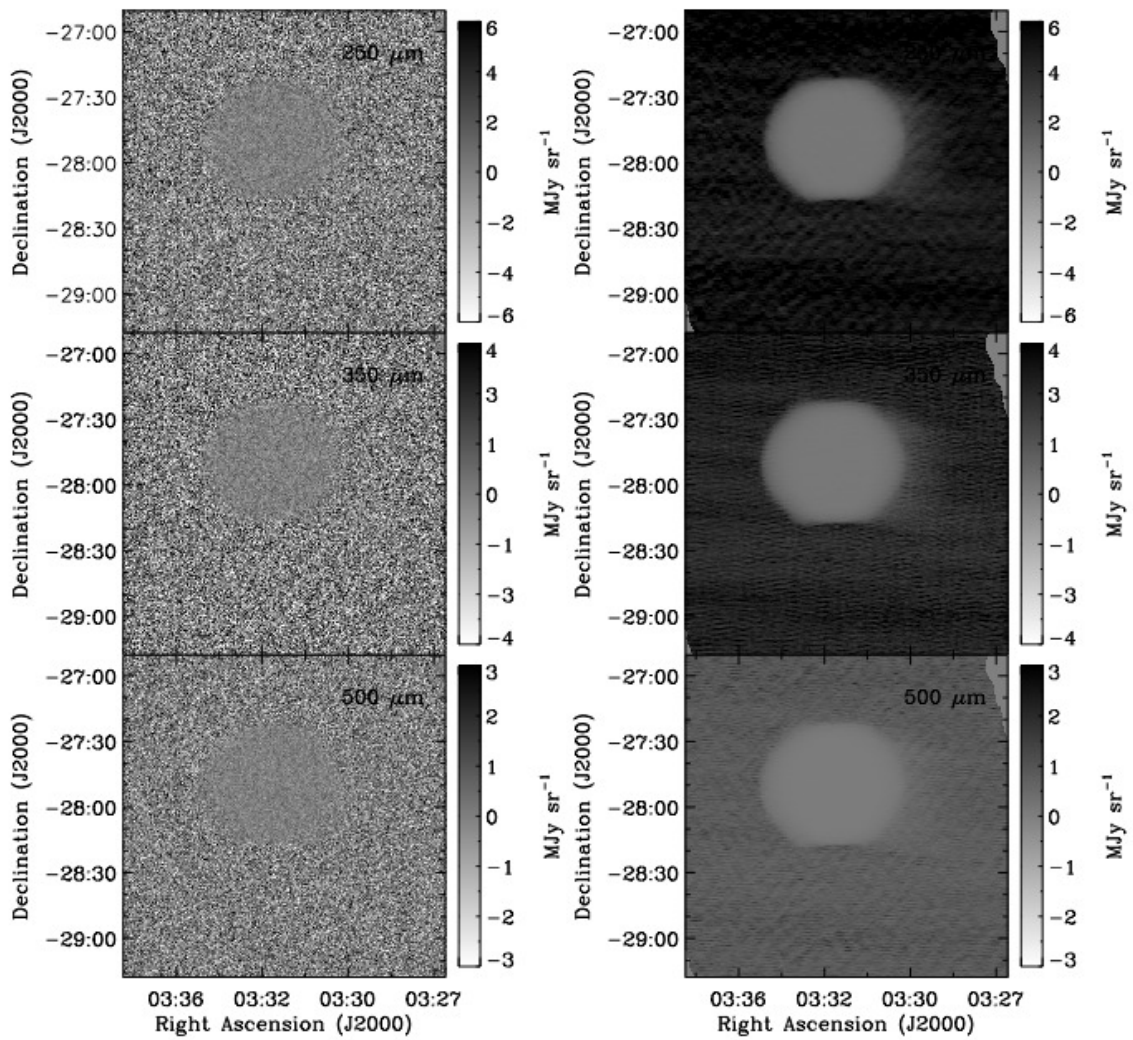


FIGURE 2.19: GOODS-south maps made with SANEPIC. Left: Flux. Right: Variance

$(4^{\text{h}}24^{\text{m}}24^{\text{s}}, -54^{\circ}14')$, $(4^{\text{h}}29^{\text{m}}20^{\text{s}}, -55^{\circ}40')$]. The mean $1\text{-}\sigma$ sensitivities of 36, 27, and 19 mJy beam^{-1} at 250, 350, and 500 μm .

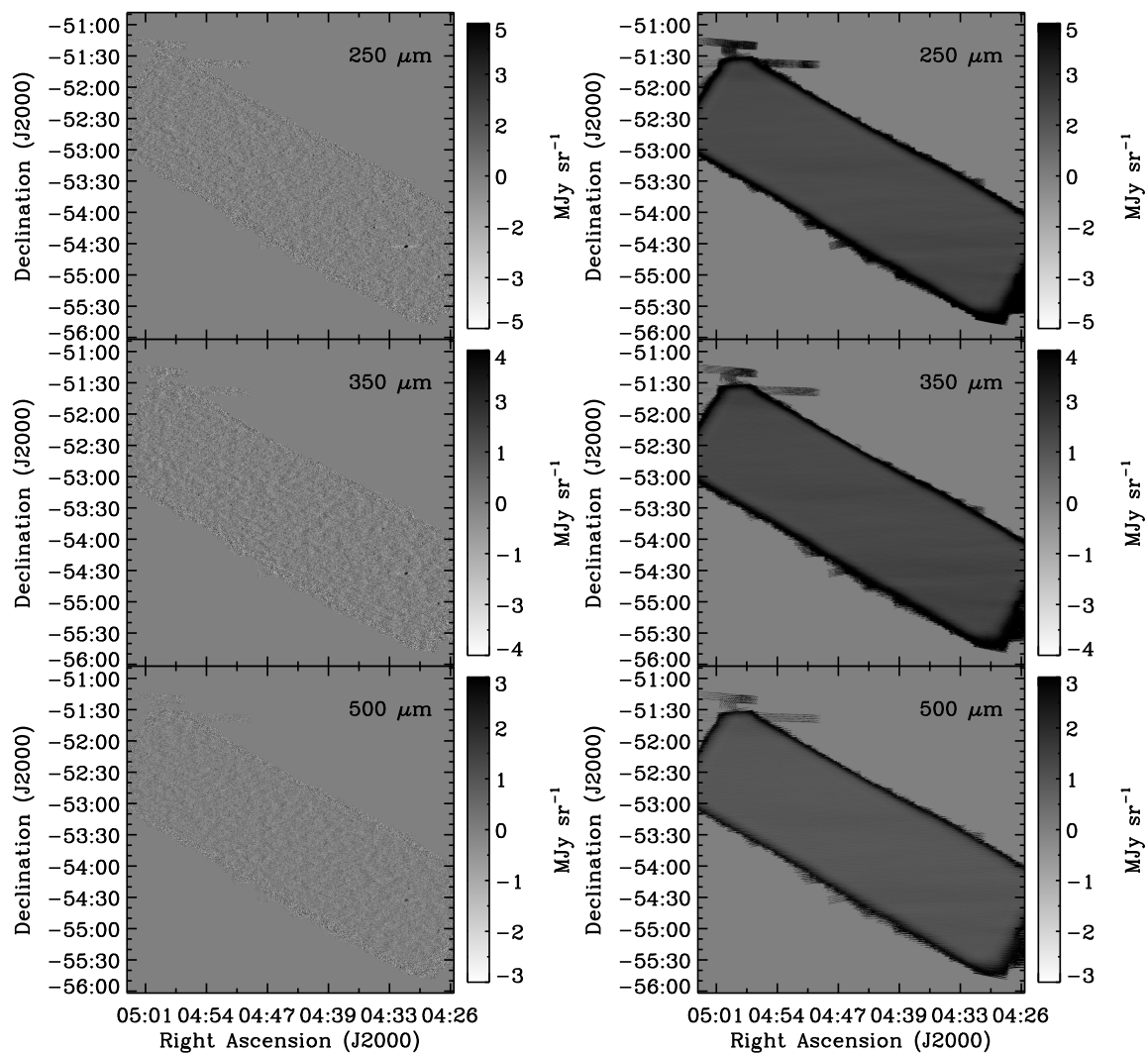


FIGURE 2.20: SEP maps made with Optbin. Left: Flux. Right: Variance

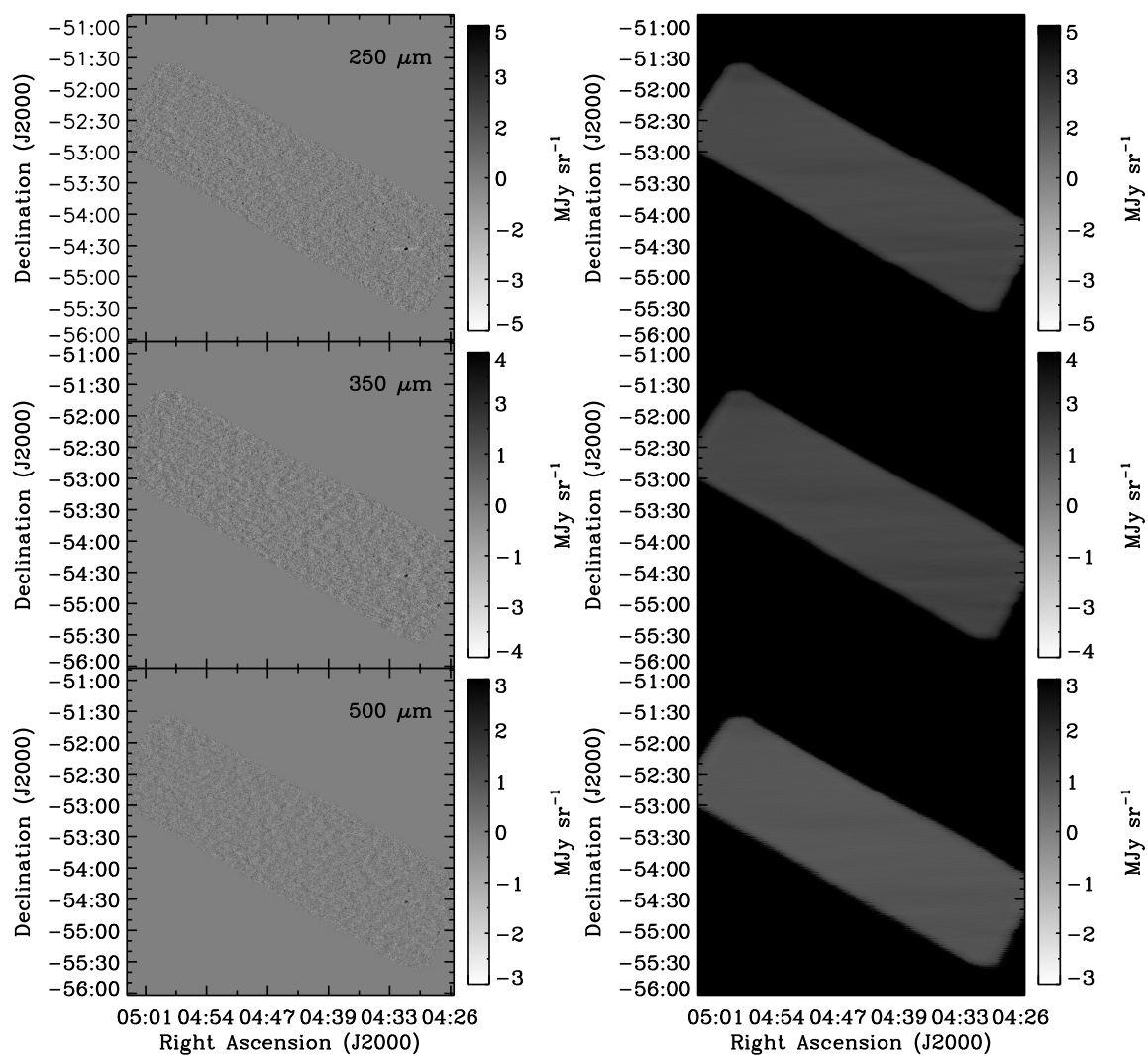


FIGURE 2.21: SEP maps made with SANEPIC. Left: Flux. Right: Variance

Chapter 3

The Large Scale Galaxy Distribution

3.1 Introduction

The initial motivation for studying the spatial distribution of galaxies was to understand the structure of the Universe on large scales (e.g., [Neyman, Scott, & Shane, 1953](#); [Totsuji & Kihara, 1969](#); [Peebles & Hauser, 1974](#)). As it became clear that the galaxies, rather than representing all of the matter in the Universe, were merely test particles tracing a much more massive distribution of dark matter, the focus shifted to understanding in what way the distribution of galaxies related to the distribution of dark matter (e.g., [Dekel & Silk, 1986](#); [Cole & Kaiser, 1989](#)).

Along the way it became clear that this relationship in fact told us quite a lot about the *galaxies* themselves (e.g., [Kolatt et al., 1999](#)); their shapes, dynamics, how the stars they are composed of form, and how that star formation is shut off. In other words, the spatial distribution of galaxies contains information about their local environments, which plays a critical role in a galaxies' life. This of course seems obvious. Galaxy formation *must* be related to the abundance and distribution of gas and dust which feeds them, as well as the number of nearby galaxies with which they can interact; both of which are strong functions of the matter density distribution. Improving our understanding of this relationship, and using this information to inform and constrain galaxy formation models, is of fundamental importance to modern cosmology.

Much of observational cosmology relies on the idea that the distribution of luminous matter is related to the underlying distribution of dark matter in a simple way. The simplest model — that the galaxy distribution is a Poisson sampling of the underlying dark matter

distribution — was quickly ruled out by observations of different clustering strengths for different galaxy types. What followed was another simple model; that the galaxy and dark matter mass fluctuations are related by a constant of proportionality, b , which has come to be known as the “bias parameter”: $\delta_{\text{gal}} = b\delta_{\text{mass}}$.

As data from observations improved, it became clear that a model with a higher level of sophistication was necessary. This came in the form of the “halo model” (Peacock & Smith, 2000). The halo model relies on the idea that over-dense regions of dark matter can be approximated as dark matter halos (Kaiser, 1984; Bardeen et al., 1986). In other words, gravitational instabilities in the primordial dark matter distribution lead to over-densities in the the dark matter distribution which collapsed and virialized to form dark matter “halos”. The distribution and clustering properties of halos can in principle be determined from simulations relatively easily, given a cosmological model (Mo & White, 1996; Kauffmann et al., 1997; Jing & Suto, 1998; Baugh et al., 1999; Hinshaw et al., 2009). Since galaxies form in halos (e.g., White & Rees, 1978), the halo model then simply assigns galaxies to halos as a function of their mass and profile in such a way as to best reproduce the measured power spectra.

Of course, all of these models assume that the properties of the observables, i.e., the luminous galaxies, behave in a predictable and reliable way, namely, that they trace the the dark matter in a consistently biased way. On large scales it appears that this is a fairly good description. For example, Adelberger et al. (1998) show that the volume density and clustering strength of Lyman-break galaxies (LBGs; Steidel et al., 1996) are similar to those predicted for dark matter halos with mass $M \geq 10^{11}M_{\odot}$. It also appears that smaller and fainter LBGs cluster less strongly than brighter more massive ones (Giavalisco & Dickinson, 2001), suggesting that the star-formation rate is regulated by the mass of the galaxy, which is related to the mass of the host dark matter halo. More generally, however, star and galaxy formation is still relatively poorly understood, and appear to be strong functions of the local environment (e.g., Elbaz et al., 2007). This is clear from the observation that different types of galaxies cluster in different ways, meaning they favour different environments (e.g., Giavalisco & Dickinson, 2001). Thus, the clustering properties on small scales of different types of galaxies are key to understanding where and how those galaxies form and evolve through cosmic time.

Galaxy clustering can be measured in a number of ways, the most common being the two-point correlation function (or just *correlation function*) of resolved sources. Alternatively, the power spectrum — which is the Fourier transform of the correlation function — is a more appropriate choice for certain situations. We will discuss the correlation function in § 3.2.1, including estimators for measuring it in § 3.2.2; as well as the power spectrum in

§ 3.2.3. In § 3.3 we detail the halo model, including the theory of dark matter halos in § 3.3.1, and its application to the halo model in § 3.3.2.

3.2 Correlations and the Correlation Function: Overview

Although the measurement of galaxy clustering can become quite complicated, the heart of the argument can be expressed very simply: clustered galaxies are galaxies which are not randomly located. In other words, their locations are not Poisson distributed. Correlations of galaxy *locations* can be expressed in a number of ways, the most common being the two-point correlation function, $w(\theta)$, which measures the number of pairs at a given distance in excess of what would be expected of a Poisson distribution, i.e., how the distribution departs from random. Equivalently, the clustering of galaxies can be expressed as the component of the power spectrum, $\tilde{P}(k_\theta)$, in excess of Poisson. This is because the correlation function and the power spectrum of galaxy correlations are related; as we will see in § 3.2.3, they form a Fourier transform pair.

The rest of this section is devoted to putting this simple idea — that a clustered distribution is *not random* — into robust mathematical terms.

3.2.1 Two-Point Correlation Function

The two-point correlation function, $\xi(r)$, has proven to be the most widely used measure of clustering due to its simplicity. Defined as the probability *in excess* of a random (Poisson) point process of finding two sources in the two volume shells, δV_1 and δV_2 , separated by $r_{1,2}$, i.e.,

$$\delta P = \bar{n}^2 \delta V_1 \delta V_2 [1 + \xi(r_{1,2})], \quad (3.1)$$

where $\bar{n} \equiv \langle N \rangle / V$ is the mean density of sources. Alternatively, if it is known that there is a galaxy in shell δV_1 , then the conditional probability of finding a galaxy in shell δV_2 is

$$\delta P(2|1) = \bar{n}^2 \delta V_2 [1 + \xi(r_{1,2})]. \quad (3.2)$$

Therefore, for any random source in the sample, the probability of finding another source at a distance r is

$$\delta P = \bar{n}^2 \delta V [1 + \xi(r)]. \quad (3.3)$$

In practice, the correlation function is typically found to be well described by a power-law, $\xi(r) = (r/r_0)^{-\gamma}$ over a wide range of separations ($0.05 \lesssim r \lesssim 10 h^{-1}$ Mpc), where $\gamma \approx 1.8$ is the canonical slope (e.g., [Zehavi et al., 2002](#)).

3.2.1.1 Angular Correlation Function

Of course, the galaxies we observe are a two-dimensional projection onto a sphere of the true three-dimensional distribution. In the absence of redshift information, we are limited to measuring the angular correlation function, $w(\theta)$, defined as

$$\delta P = \bar{n}^2 \delta\Omega [1 + w(\theta)], \quad (3.4)$$

which, much like the spatial correlation function, happens to be well described by a power-law, such that $w(\theta) = (\theta/\theta_0)^{-\epsilon}$, and $\epsilon = 1 - \gamma \approx 0.8$ (e.g., [Giavalisco et al., 1998](#))

3.2.1.2 Limber equation

In practice, it is unusual to have a very large catalogue of sources with precise redshifts; instead, the redshift distribution of the population, $N(z)$, is typically all we know. With this information an estimate of the spatial correlation function can be found from the angular correlation function through the use of the relativistic Limber equation ([Limber, 1953](#)):

$$w(\theta) = \frac{H_0 H_\gamma \theta^{1-\gamma} \int_0^\infty N^2(z) r_0^\gamma(z) x(z)^{1-\gamma} E(z) F(z) dz}{c \left[\int_0^\infty N(z) dz \right]^2}, \quad (3.5)$$

where $x(z)$ is the comoving radial distance

$$x(z) = \frac{c}{H_0} \int_0^z \frac{dz}{E(z)}, \quad (3.6)$$

and

$$H_\gamma = \Gamma[1/2] \frac{\Gamma[(\gamma-1)/2]}{\Gamma[\gamma/2]}. \quad (3.7)$$

$E(z)$ describes the evolution of the Hubble parameter

$$\frac{\dot{a}}{a} = H_0 E(z) = H_0 \sqrt{\Omega_M(1+z)^3 + \Omega_k(1+z)^2 + \Omega_\Lambda}, \quad (3.8)$$

where $\Omega_M + \Omega_k + \Omega_\Lambda = 1$ ([Peebles, 1993](#)). $F(z)$ describes the evolution of clustering with redshift, $\xi(r, z) = \xi(r, 0)F(z)$, which is usually modelled as $F(z) = (1+z)^{-(3-\gamma+\eta)}$, where $\eta = \gamma - 3$ for constant clustering in comoving coordinates, $\eta = 0$ for “stable” clustering, and $\eta = \gamma - 1$ for “linear growth” (e.g., [Moscardini et al., 1998](#); [Overzier et al., 2003](#))

Armed with the redshift distribution, and assuming that r_0^γ is roughly constant across the redshift range, the angular correlation function, $w(\theta) = (\theta/\theta_0)^{1-\gamma}$, can then be de-projected

such that

$$r_0^\gamma(z_{\text{eff}}) = A_w \left[\frac{H_0 H_\gamma \int_{z_1}^{z_2} N(z)^2 x(z)^{1-\gamma} E(z) dz}{c [\int_{z_1}^{z_2} N(z) dz]^2} \right]^{-1} \quad (3.9)$$

where $A_w = (1/\theta_0)^{1-\gamma}$, and

$$z_{\text{eff}} = \frac{\int_{z_1}^{z_2} z N(z)^2 x(z)^{1-\gamma} E(z) dz}{\int_{z_1}^{z_2} N(z)^2 x(z)^{1-\gamma} E(z) dz} \quad (3.10)$$

3.2.2 Clustering Estimators

Measuring clustering from catalogs requires comparing the statistics of the catalog to those of a random catalog in an unbiased way. The simplest and most widespread method is to construct a histogram of distances between each possible pair of sources (pair-counts) in the catalog, DD, and compare it to a histogram of pair-counts made from mock catalogs of randomly located sources, RR. The simplest estimator one can construct is

$$w = \frac{N_r DD}{N_d RR} - 1, \quad (3.11)$$

(which also goes by the name *natural* estimator; [Davis & Peebles, 1983](#); [Kerscher et al., 2000](#)), where the N_i are the number of sources in the real and mock catalogs. This simple estimator has been shown to be biased at small angular scales: two estimators developed (simultaneously) to overcome this bias are the [Landy & Szalay \(1993\)](#) (hereafter LS)

$$w = \frac{N_r^2 DD - 2N_r N_d DR + N_d^2 RR}{N_d^2 RR} - 1, \quad (3.12)$$

and the [Hamilton \(1993\)](#)

$$w = \frac{DD \times RR}{DR \times DR} - 1, \quad (3.13)$$

where DR is a histogram of the distances between each possible pair of sources drawn from the real and mock catalogues. The LS estimator has been shown to be the least biased of the estimators ([Kerscher et al., 2000](#)), but as we will see, there are limitations to using it when confronted with confused maps and large beams.

Typically, many mock catalogs are constructed, and a Monte-Carlo is performed to estimate RR and DR. One must take special care in constructing a mock catalog with a selection function identical to the real data, i.e., the source counts redshift distribution, shape, masks, etc. of the mock maps should be identical to that of the real map. In particular, for low signal-to-noise maps, and especially those with large beams, mock catalogs should be drawn from mock maps whose noise properties mimic those of the real maps, because deeper, lower-noise regions will resolve more sources, and thus appear to be more strongly clustered.

Furthermore, if the counts and the beam are not identical, then confusion noise will not be accurately reproduced. This would result in a catalog which does not reproduce the selection bias (although arguably, clustering further biases confused maps). Clearly, rigorous simulations must be performed in estimating the true clustering signal in such maps. Such simulations are discussed in § 3.2.2.2.

3.2.2.1 Integral Constraint

After normalization, these estimators are a matter of simply comparing the DD, RR (and where appropriate DR) histograms. In other words, the presence of clustering at a given angular scale, θ , means there are more “hits” in the θ bin of the DD histogram than in the same bin of the RR histogram. However, since the total number of sources, and thus the total number of pairs (or hits) is the same, an excess of hits at one scale must necessarily mean there is a dearth of hits at other scales; i.e. there is an integral constraint such that

$$\int \int w_{\text{obs}}(\theta_{1,2}) d\Omega_1 d\Omega_2 \approx 0. \quad (3.14)$$

This is unphysical, and forces the observed correlation function, $w_{\text{obs}}(\theta)$, to fall below the intrinsic value, $w(\theta)$ (Groth & Peebles, 1977). The size of the bias increases with increasing clustering strength and decreases with field size. The correction is approximately constant and equal to the fractional variance of source counts,

$$IC \approx \sigma^2 = \frac{1}{\langle N_{\text{gal}} \rangle} + \sigma_w^2, \quad (3.15)$$

where the first term on the right is due to Poisson variance, and the second term accounts for the additional variance due to clustering

$$\sigma_w^2 = \frac{1}{\Omega^2} \int \int w(\theta_{1,2}) d\Omega_1 d\Omega_2, \quad (3.16)$$

(Peebles, 1980). We can estimate σ_w directly from mock catalogues

$$IC = \frac{\sum_i RR(\theta_i)(\theta_i/\theta_0)^{-\epsilon}}{\sum_i RR(\theta_i)}, \quad (3.17)$$

(Infante, 1994; Roche & Eales, 1999; Waddington et al., 2007). The amplitude A_w of the angular correlation function is related to the observations through

$$w_{\text{obs}}(\theta) = A_w \theta^{-\epsilon} - IC, \quad (3.18)$$

and found by iterating Equations 3.14, 3.15, and 3.16.

3.2.2.2 Consequences of a Large Beam

Particularly steep source counts will result in many more faint sources than bright ones, and more than would be expected from typical Euclidean behaviour. As a result, once the angular resolution of the telescope is significantly larger than the angular resolution of typical individual sources (or the average distance between sources), problems arise. Multiple galaxies occupying a beam they will inevitably blend together, sometimes resulting in the brightest source having its flux density “boosted”, but just as often combining in such a way as to appear as one “resolved” source.

Figure 3.1 illustrates this point: the left panel is a simulation of sources placed randomly in a map with $10''$ pixels. The counts obey those found by Patanchon et al. (2009). The right panel is the same map after being convolved with the BLAST $250\ \mu\text{m}$ beam. The green box, drawn for illustrative purposes, encloses ~ 2.2 square-arcminutes. Notice that on the left there are clearly many (~ 30) sources in the box, whereas on the right there are between 1 and 3, depending on the criteria used to define a “source”. Below the green box a small cluster of brighter sources appears as a monster of a source on the right, which would easily be confused as a very bright galaxy. Only in one place in the convolved map (top right) does a bright resolved source seem to correspond to one bright source on the left.

To emphasize this point further, we show another, similarly made map ($\sim 2\ \text{deg}^2$, 11560 sources), before and after convolution with the BLAST $250\ \mu\text{m}$ beam in Figure 3.2. Here, the 50 brightest sources on the left are circled in green, and the 50 brightest resolved sources after convolution on the right are circled in red. The two coincide $\sim 35/50 = 70\%$ of the time. Remember, these are the brightest 50 of 11560 sources in the map, which conventional wisdom would claim are not subject to boosting from confusion. Note also that the circles are very rarely perfectly concentric. On average they are 1.38 pixels, or $13.8''$ apart.

Measuring the correlation function begins with a source catalog. The catalog may be provided, or may be drawn from the map as part of the analysis; the latter has the added advantage of being more realistically simulated. Those used to make the measurement will typically be chosen to be above some flux or signal-to-noise cut, again, because conventional wisdom says that above some cut your sources are reliable. From the above simulation it should come as no surprise that this can pose problems. A more realistic simulation, including confusion and detector noise, to quantify the mean amount that sources are boosted in the BLAST catalogues is performed by Monceli et al. (in prep. 2010), and is shown in Figure 3.3. The y-axis is the signal-to-noise (S/N) of the input source, and the x-axis is the S/N of the same source after convolution of the map and source extraction. The diagonal dashed line is where the signal-to-noise of recovered sources would be equivalent to the input source. Solid points are for BGS-deep, and dotted points are for BGS-wide.

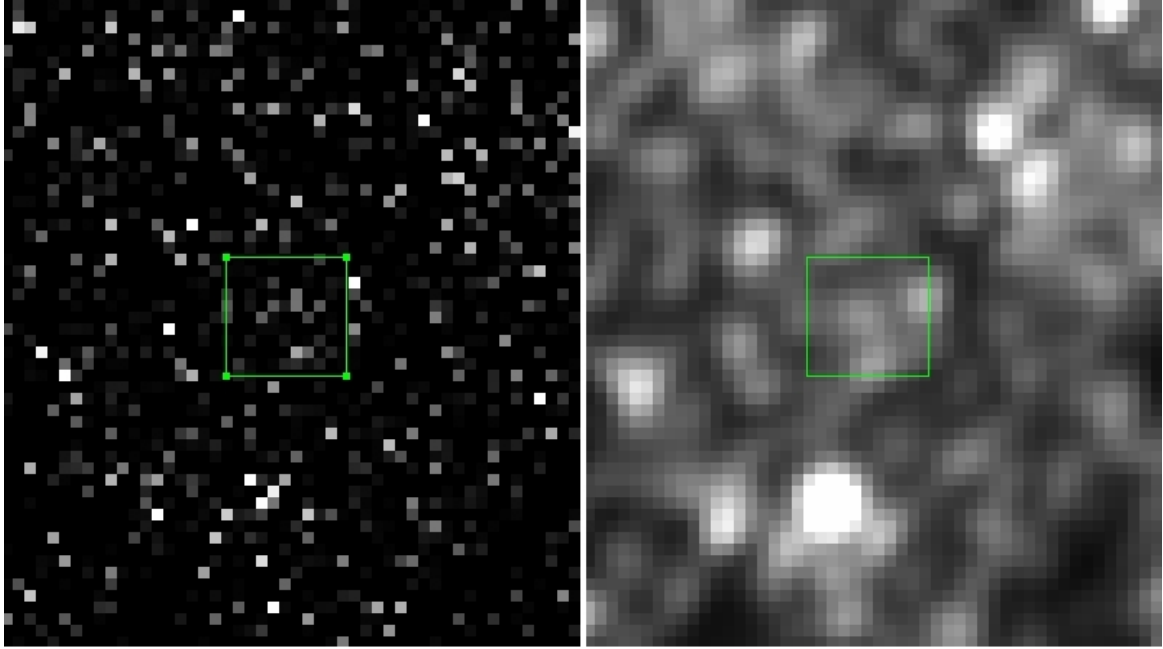


FIGURE 3.1: Effects of convolution by BLAST $250\ \mu\text{m}$ beam on a map of point sources. In the left panel, sources are randomly placed in a map with $10''$ pixels. The counts obey those found by Patanchon et al. (2009). The right panel is the same map after being convolved with the BLAST $250\ \mu\text{m}$ beam. The green box, drawn for illustrative purposes, encloses one square arcminute. Notice that on the left there are clearly many (~ 30) sources in the box, whereas on the right there are between 1 and 3, depending on the criteria used to define a “source”.

Recall, conventional wisdom says that for high S/N sources, or in unconfused maps, boosting is irrelevant, and typically sources with S/N greater than ~ 5 are considered “safe” (e.g., Coppin et al., 2006). This simulation clearly disputes that claim. As expected, larger beams in highly confused regions ($500\ \mu\text{m}$) perform worst of all, with $S/N \sim 6$ recovered sources having on average an input S/N of about 2, and as low as 0. But even at $250\ \mu\text{m}$, whose beam is equivalent to that of SPIRE’s $500\ \mu\text{m}$ beam, an average $S/N \sim 6$ recovered source has an average input of $S/N \sim 3.5$, (nearly half!), and can be as low as 2.

Finally, and perhaps most problematic, is the effect that the beam can have on the measured correlation function. Because a large beam will blend sources closer than $\sin\theta = 1.220\lambda/D$ together, there will be a radius on the map, $r = \arcsin(1.220\lambda/D)$ radians, within which no sources are found. This “zone of avoidance” will appear as an anticorrelation in the correlation function, i.e., there will be *fewer* sources at distances $0 < z < r$ than would be expected from a random distribution. This, it turns out, has the unpleasant effect of making it more likely to find sources at a distance slightly greater than r , which then appears as a very large correlation over a small range centered on r . At $250\ \mu\text{m}$, $r \sim 35''$. This behaviour is indeed observed in data as well as in simulations, as is shown in Figure 3.4. Here correlation functions are estimated using the LS estimator from catalogs of sources extracted from the

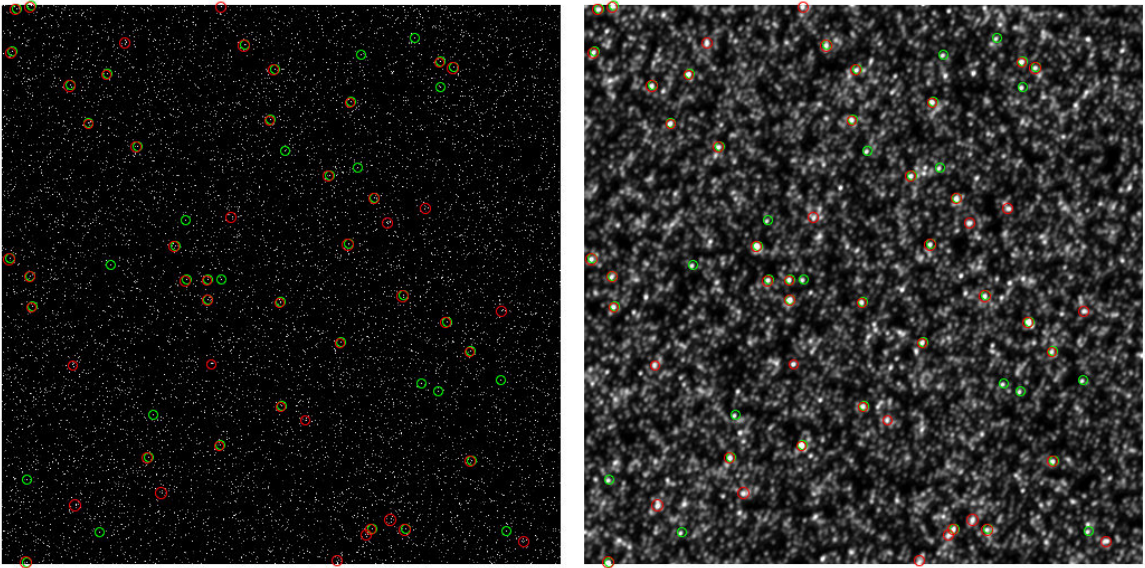


FIGURE 3.2: Demonstration of resolved sources. In the left panel, 11560 sources are randomly placed in a $\sim 2 \text{ deg}^2$ map with $10''$ pixels. The counts obey those found by Patanchon et al. (2009). The right panel is the same map after being convolved with the BLAST $250 \mu\text{m}$ beam. The 50 brightest sources on the left are circled in green, and the 50 brightest resolved sources after convolution on the right are circled in red. The two coincide $\sim 35/50 = 70\%$ of the time. Remember, these are the brightest 50 of 11560 sources in the map, which conventional wisdom would claim are not subject to boosting from confusion. Note also that the circles are very rarely perfectly concentric. On average they are 1.38 pixels, or $13.8''$ apart

BLAST map (DD of ~ 800 sources with $S/N > 2.5$. For source extraction algorithm see Marsden, 2007; Wiebe, 2008), as well as 99 noise-added, beam-convolved random maps (RR of ~ 800 sources each). For reference, they are both compared to the catalog UU. UU is defined as follows: just as RR is the histogram of pair-counts of random sources extracted from random maps *after* convolution, UU is the histogram of pair-counts of the sources in the map *before* convolution. For both clustered and random maps, clear anti-correlations are measured at angular scales smaller than ~ 0.01 degrees = 36 arcseconds, and a clear excess is measured on scales $\sim 0.15 \pm 0.05$ deg, or around 50 arcsec, well beyond the scale of the 36 arcsec FWHM $250 \mu\text{m}$ beam, followed by yet another slight decrement. In other words, though the beam is only 36 arcsec FWHM, the effects of the beam are felt out to ~ 0.09 deg = 325 arcseconds!

Figure 3.5 shows the correlation function of beam-convolved random maps compared to other beam-convolved random maps. In this case the simple estimator is used, because DR, which the LS estimator, uses, would allow sources to occupy the zone of avoidance. In this case, the correlation function is consistent with zero, as required. Clearly, rigorous Monte Carlo simulations to determine the level of bias introduced is necessary when using the

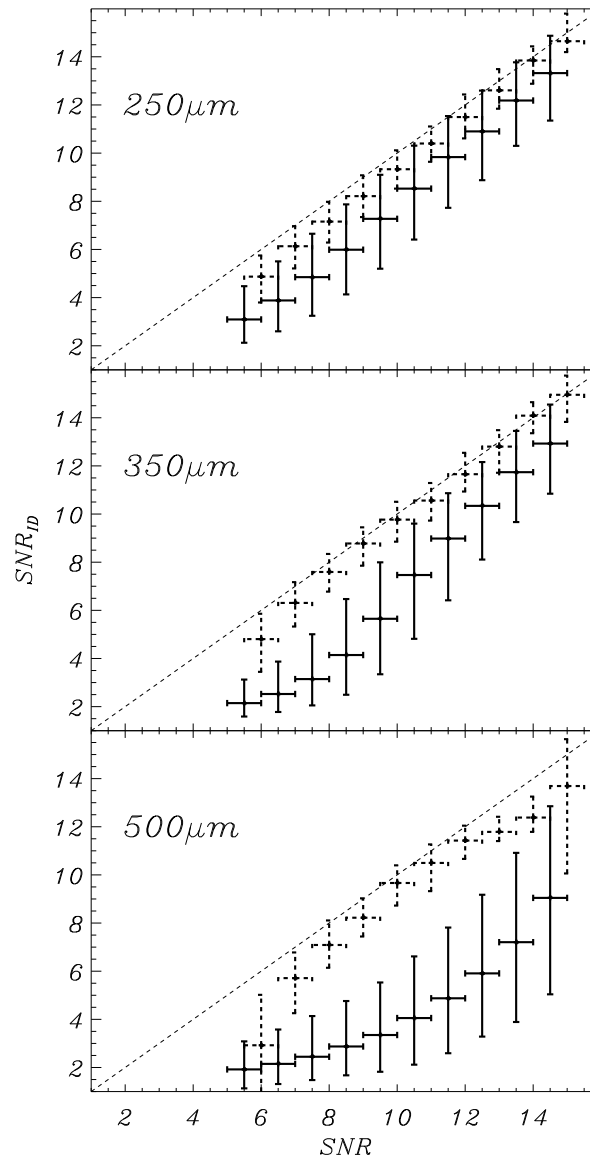


FIGURE 3.3: Monte Carlo simulation of effects of confusion and noise on signal-to-noise (S/N) of resolved sources. The y-axis is the S/N of the input source, and the x-axis is the S/N of the same source after convolution of the map and source extraction. The diagonal dashed line is where recovered sources would be equivalent to the input source. Solid points are for BGS-deep, and dotted points are for BGS-wide. Even sources with S/N greater than 5, which may mistakenly be considered “robust”, are subject to boosting.

Figure from Monceli et al. (in prep. 2010)

simple estimator with actual data, , however, this appears to be the appropriate estimator to use.

Much time was devoted to measuring the correlation function of BLAST galaxies, without success. The attempts to make this measurement are described in § 4.2. This failure led to

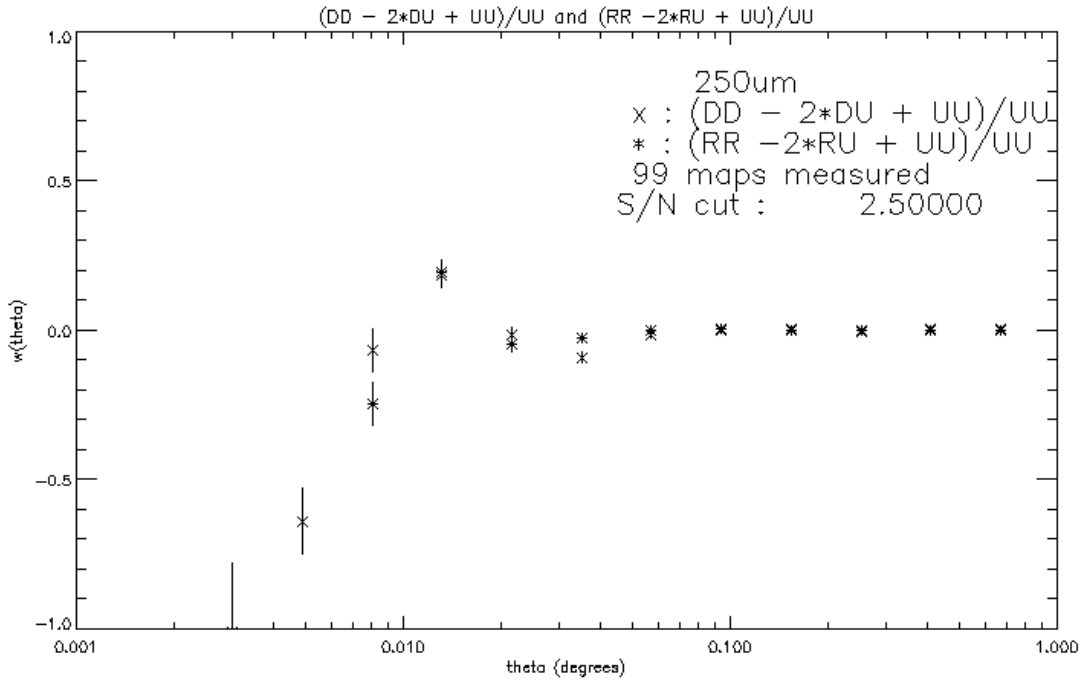


FIGURE 3.4: Correlation function of $2.5\text{-}\sigma$ $250\ \mu\text{m}$ ~ 800 BLAST sources (DD) in BGS-south, as well as 99 noise-added, beam-convolved random mock-maps (RR). These were measured with the [Landy & Szalay \(1993\)](#) estimator, which requires the pair-counts of randomly located, unconvolved sources, UU. Below the scale of the $35''$ beam there is an anticorrelation (i.e., less than Poisson probability of finding a source), whereas, just beyond the scale of the beam there is an excess probability of finding sources. This behaviour is a consequence of the large beam and must be corrected to properly measure the correlation function.

a rethinking of how to measure galaxy clustering in BLAST maps, and was the inspiration for switching to a CMB style power spectrum analyses, described in the next section.

3.2.3 Power Spectrum

Following the notation of [Peacock \(1999\)](#), the density perturbation field $\delta(\mathbf{x})$, can be represented as

$$\delta(\mathbf{x}) \equiv \frac{\rho(\mathbf{x}) - \langle \rho \rangle}{\langle \rho \rangle}, \quad (3.19)$$

where $\langle \rho \rangle$ is the average density over the scale of interest. Now recall that any function can be expanded into its orthogonal Fourier components. Assuming the density field is periodic within some box of length L , then the sum over the wave modes is

$$F(\mathbf{x}) = \sum F_{\mathbf{k}} e^{-i\mathbf{k}\cdot\mathbf{x}}, \quad (3.20)$$

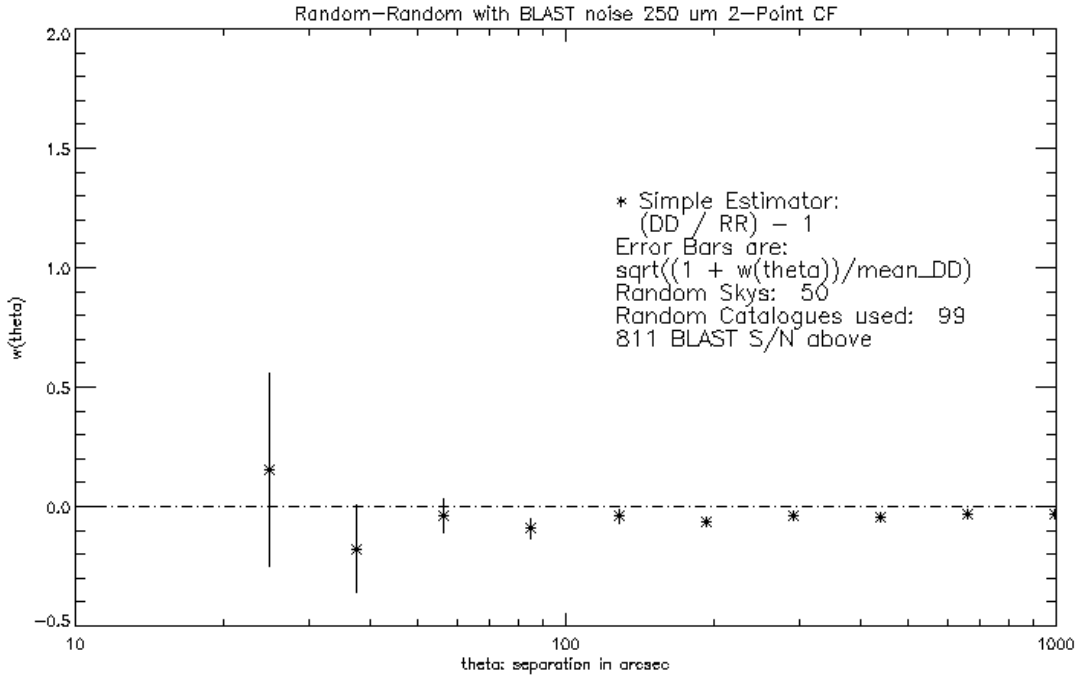


FIGURE 3.5: Average correlation function of 50 noise-added, $250\ \mu\text{m}$ beam-convolved, random mock-maps, each with ~ 800 resolved sources in them. Correlation function estimated by comparing DD and RR with the simple estimator, and thus compensates for the zone of avoidance. As a result, the correlation function is consistent with zero on all scales, as it should be.

which requires periodic boundary conditions

$$k_{x,y,z} = n \frac{2\pi}{L}, n = 1, 2, \dots \quad (3.21)$$

For an infinitely large box, this becomes the familiar Fourier transform

$$\begin{aligned} F(x) &= \left(\frac{L}{2\pi}\right) \int F_k(k) e^{-i\mathbf{k}\cdot\mathbf{x}} d^n k \\ F_k(k) &= \left(\frac{1}{L}\right) \int F(x) e^{i\mathbf{k}\cdot\mathbf{x}} d^n x. \end{aligned} \quad (3.22)$$

This can be applied to the correlation function, $\xi(\mathbf{r})$, which is written here as a

$$\xi(\mathbf{r}) \equiv \langle \delta(\mathbf{x}) \delta(\mathbf{x} + \mathbf{r}) \rangle, \quad (3.23)$$

where the angle brackets imply an average over the normalization volume V . If we express $\delta(\mathbf{x})$ as a sum

$$\delta(\mathbf{x}) = \sum_{\mathbf{k}} \delta_{\mathbf{k}} e^{-\mathbf{k}\cdot\mathbf{x}}, \quad (3.24)$$

and apply that to Equation 3.23, we can Fourier transform it to get

$$\xi = \left\langle \sum_{\mathbf{k}} \sum_{\mathbf{k}'} \delta_{\mathbf{k}} \delta_{\mathbf{k}'}^* e^{-i(\mathbf{k}-\mathbf{k}') \cdot \mathbf{x}} e^{-i\mathbf{k} \cdot \mathbf{r}} \right\rangle, \quad (3.25)$$

which we can do because δ is real. Expressed as an integral

$$\xi(\mathbf{r}) = \frac{V}{(2\pi)^3} \int |\delta_{\mathbf{k}}|^2 e^{-i\mathbf{k} \cdot \mathbf{r}} d^3k, \quad (3.26)$$

where alternatively,

$$P(k) \equiv \langle |\delta_{\mathbf{k}}|^2 \rangle. \quad (3.27)$$

In other words, the correlation function is the Fourier transform of the power spectrum.

Since the Universe has no preferred direction, the power spectrum is isotropic, i.e., $\langle |\delta_{\mathbf{k}}|^2(\mathbf{k}) \rangle = |\delta_k|^2(k)$, and Equation 3.26 can be expressed as

$$\xi(r) = \frac{V}{(2\pi)^3} \int P(k) \frac{\sin kr}{kr} 4\pi k^2 dk, \quad (3.28)$$

or in two-dimensions as

$$w(r) = \frac{A}{(2\pi)^2} \int P(k) J_0(kr) 2\pi k dk. \quad (3.29)$$

In keeping with the notation of Peacock (1999), the power spectrum can be written in dimensionless form, as the variance per $\ln k$, i.e.,

$$\Delta^2(k) = \frac{d\langle \delta^2 \rangle}{d \ln k} \propto k^3 P(k), \quad (3.30)$$

so that Equation 3.28 in dimensionless form is

$$\Delta^2(k) \equiv \frac{V}{(2\pi)^3} 4\pi k^3 P(k) = \frac{V}{(2\pi)^3} \int \xi(r) \frac{\sin kr}{kr} r^2 dr, \quad (3.31)$$

or in two-dimensions

$$\Delta_{\theta}^2(k) \equiv \frac{A}{(2\pi)^2} 2\pi k^2 P(k) = \frac{A}{(2\pi)^2} \int w(r) J_0(kr) 2\pi k^2 dr. \quad (3.32)$$

Two and three dimensional power spectra can be related with the Limber equation as before

$$\Delta_{\theta}^2(k) = \frac{\pi}{k} \int \Delta^2(k) \left(\frac{k}{y} \right) y^5 \phi^2(y) dy, \quad (3.33)$$

where y is the comoving distance, and $\phi(y)$ is the selection function normalized so that $\int y^2 \phi(y) dy = 1$. Note that this form of the Limber equation happens to be much simpler than the $w - \xi$ analog.

3.2.3.1 Shot Noise

Poisson (or shot) noise will be present in a field with a finite number of galaxies. Formally, shot noise is

$$P_{\text{shot}} = \int_0^\infty S^2 \frac{dN}{dS} dS. \quad (3.34)$$

If the source counts are known, it can be calculated analytically or determined from Monte Carlo simulations. If counts are not known, it can be measured from the power spectrum, appearing as a horizontal signal (or power-law with slope 2 in Δ^2).

For Euclidean counts, $dN/dS \propto S^{-5/2}$, and the shot noise diverges at high flux densities. In this case, it is practical to remove the brightest sources from the map to reduce shot noise. For much steeper counts, the faint sources dominate and the removal of sources has much less impact. In the submillimeter, counts tend to be much steeper than Euclidean, except for the very brightest sources, which tend to approach Euclidean, therefore cutting sources or not is dependent on survey depth.

3.2.3.2 Power Spectrum in Practice

When measuring correlations of galaxies in a map, one must choose between measuring correlations between positions or brightnesses. The obvious advantage to measuring correlations of brightnesses is that all of the information contained in the map is used, which is of particular importance in confused maps with large beams. The distinction between positions and brightnesses will hereafter be made with through the use of a tilde when addressing positions, e.g., $P(\tilde{k})$ and $\tilde{\Delta}^2$ represent the power spectrum of galaxy locations, and its dimensionless counterpart.

For small surveys, the angular correlation function is related to the angular power spectrum through

$$\begin{aligned} \tilde{\Delta}_{k_\theta}^2 &= (2\pi k_\theta)^2 \int_0^\infty w(\theta) J_0(2\pi k_\theta \theta) \theta d\theta, \\ w(\theta) &= \int_0^\infty \tilde{\Delta}_{k_\theta}^2 J_0(2\pi k_\theta \theta) dk_\theta / k_\theta, \end{aligned} \quad (3.35)$$

where J_0 is the zeroth order cylindrical Bessel function, and k_θ is the angular wavenumber, which is also known as σ in the literature, and is expressed in inverse angular scale as $k_\theta = 1/\lambda$. It is related to the multipole index, ℓ , by $\ell = 2\pi k_\theta$.

Just as the correlation function is approximated by a power law, $w(\theta) = (\theta/\theta_0)^{-\epsilon}$, with $\epsilon \approx 0.8$ (see § 3.2.1.1), the power spectrum can be approximated with a power law

$$\tilde{\Delta}_{k_\theta}^2 = (2\pi k_\theta \theta_0)^\epsilon 2^{1-\epsilon} \frac{\Gamma(1 - \epsilon/2)}{\Gamma(\epsilon/2)}, \quad (3.36)$$

which equals $3.35(k_\theta \theta_0)^{0.8}$ for $\epsilon \approx 0.8$.

3.3 Halo Model

The halo model of large scale structure has proven to be a powerful tool for describing the clustering properties of cosmic objects (for a review, see [Cooray & Sheth, 2002](#)). It relies on the idea that gravitational instabilities in the primordial density distribution — imprinted in the power spectrum of the cosmic microwave background (CMB) — led to over-densities in the the dark matter distribution collapsing into virialized dark matter halos. These would then serve as the places where luminous galaxies would form, and the distribution of galaxies is described by the halo model. The main ingredient of the halo model is the parameterization of the *halo occupation distribution* (HOD, [Peacock & Smith, 2000](#)), which describes how galaxies populate dark matter halos as a function of halo mass.

Since dark matter in principle is governed strictly by gravitational interactions, halo properties can be determined numerically given the appropriate cosmological parameters. When required, we adopt the concordance model, a flat Λ CDM cosmology with $\Omega_M = 0.274$, $\Omega_\Lambda = 0.726$, $H_0 = 70.5 \text{ km s}^{-1} \text{ Mpc}^{-1}$, and $\sigma_8 = 0.81$ ([Hinshaw et al., 2009](#)). Here we follow the notation of [Cooray & Sheth \(2002\)](#), which is also an excellent source for a more in-depth treatment of the material presented in this section.

3.3.1 Dark Matter Halos

The large scale structure in the present day Universe is thought to originate from gravitational evolution of tiny, initially Gaussian, fluctuations in an otherwise completely uniform space. In places where the overdensity was such that gravitational forces were able to overcome the expansion of the universe, virialized collections of dark matter, which we call halos, of various shapes and sizes formed. Here we briefly describe the formation and properties

of dark matter halos, which are the building blocks of the halo model, and indeed much of our modern understanding of galaxy formation.

3.3.1.1 Perturbation Theory and Spherical Collapse Model

The local density perturbations in the universe are expressed as fluctuations relative to the mean background density, $\bar{\rho}$:

$$1 + \delta(\mathbf{r}) = \frac{\rho(\mathbf{r})}{\bar{\rho}}. \quad (3.37)$$

The evolution of these local density perturbations over large scales obey the continuity equation

$$\frac{\partial \delta}{\partial t} + \frac{1}{a} \nabla \cdot (1 + \delta) \mathbf{u} = 0, \quad (3.38)$$

and the Euler equation,

$$\frac{\partial \delta}{\partial t} + H \mathbf{u} + \frac{1}{a} [(\mathbf{u} \cdot \nabla) \mathbf{u} + \nabla \phi] = 0, \quad (3.39)$$

where \mathbf{u} is the peculiar velocity, which relates to the Hubble flow by $\mathbf{u} = \mathbf{v} - H\mathbf{x}$, and the fluctuations in the potential, ϕ , are described by the Poisson equation

$$\nabla^2 \phi = 4\pi G \bar{\rho} a^2 \delta, \quad (3.40)$$

where G is the gravitational constant, and a is the scale factor. The linear regime is that which $\delta \ll 1$. In the linear regime, the continuity and Euler equations can be combined to give

$$\frac{\partial^2 \delta}{\partial t^2} + 2H \frac{\partial \delta}{\partial t} - 4G\bar{\rho}\delta = 0. \quad (3.41)$$

The two solutions correspond to modes which grow and decay with time. We focus on the growing mode, which takes the form

$$\delta(k, r) = G(r)\delta(k, 0), \quad (3.42)$$

where

$$\begin{aligned} G(r) &\propto \frac{H(r)}{H_0} \int_{z(r)}^{\infty} dz' (1+z') \left[\frac{H_0}{H_{z'}} \right]^3 \\ &\approx \frac{5}{2} \frac{\Omega_m(z)/(1+z)}{\Omega_m(z)^{4/7} - \Omega_\Lambda(z) + (1 - \Omega_m(z)/2)(1 - \Omega_\Lambda(z)/70)}. \end{aligned} \quad (3.43)$$

The approximation is good to a few percent (Carroll et al., 1992). Simply put, the linear theory density field can be scaled in redshift with the growth solution.

In the non-linear regime, gravitational forces cause dark matter overdensities to collapse into halos. The simplest such model is that of *spherical collapse* of an initially tophat density

perturbation (Gunn & Gott, 1972), which can be summarized as follows. Starting with a region of initial comoving size R_0 , and supposing the initial fluctuations were Gaussian, with an r.m.s. value over the scale R_0 small enough that $\delta \ll 1$, then the mass within R_0 is $M_0 = (4/3\pi R_0^3)\bar{\rho}(1 + \delta_i) \approx (4/3\pi R_0^3)\bar{\rho}$. At some later time, when the comoving size of the region is R , the density within the region is $(R_0/R)^3 \equiv (1 + \delta)$.

In an Einstein de-Sitter Universe, the growth of this region can be described by

$$\frac{R(z)}{R_0} = \frac{(1+z)}{(5/3)|\delta_0|} \frac{1 - \cos\theta}{2}, \quad (3.44)$$

$$\frac{1}{1+z} = \left(\frac{3}{4}\right)^{2/3} \frac{(\theta - \sin\theta)^{2/3}}{(5/3)|\delta_0|}, \quad (3.45)$$

where θ initially equals 0. As the Universe expands, the size of this region, R , will initially grow as well, but gravitational forces will slowly pull it back together. The moment when dark matter switches from expanding to collapsing is known as the turnaround, and occurs when $\theta = \pi$, and $(R_0/R(z))^3 = (3/4\pi)^2$, so that the average density within the region is ~ 5.55 times higher than the background. The region will have completely collapsed at $\theta = 2\pi$. Formally, R at collapse is 0, but of course in reality it virializes to a non-zero value. Assuming that the object virializes at half the value of the turnaround radius, and that in the meantime the background has itself been expanding at a rate of $(1 + z_{\text{turnaround}})/(1 + z_{\text{collapse}}) = 2^{2/3}$, then the average density within the virialized halo is 8 times its density at turnaround, and the background is 4 times less dense than it was at turnaround. In all, at the moment it becomes virialized the density of the object is $(3/4\pi)^2 \times 8 \times 4 = 18\pi^2$ times the density of the background.

The initial minimum over-density required for a region to later collapse (at some later redshift z) into a halo is given by

$$\frac{\delta_{\text{crit}}(z)}{1+z} = \frac{3}{5} \frac{3\pi^{2/3}}{2}, \quad (3.46)$$

which again diverges at the limit, but can be approximated such that the initial over-density is around 178 times denser than the background.

3.3.1.2 Halo Mass Function

The mass function, $n(m, z)$, is the number density of halos of a given mass, which naturally evolves with redshift z . It depends on number density of regions in the initial density field which were dense enough to collapse. The most well known is that of Press & Schechter

(1974)

$$\frac{m^2 n(m, z)}{\bar{\rho}} \frac{dm}{m} = \nu f(\nu) \frac{d\nu}{\nu}, \quad (3.47)$$

where $\bar{\rho}$ is the comoving density of the background, and $\nu f(\nu) = \sqrt{\nu/2\pi} e^{-\nu/2}$, $\nu \equiv \delta_{crit}^2/\sigma^2(m)$. A better fit to the data from numerical simulations is given by [Sheth & Tormen \(1999\)](#)

$$\nu f(\nu) = A(p)(1 + (q\nu)^{-p}) \left(\frac{q\nu}{2\pi}\right)^{1/2} e^{-q\nu/2}, \quad (3.48)$$

where $p \approx 0.3$, $A(p) = [1 + 2^{-p}\Gamma(1/2 - p)/\sqrt{\pi}]^{-1} \approx 0.3222$, and $q \approx 0.75$. For small $\nu \ll 1$, the mass function scales as $\nu f(\nu) \propto \nu^{0.5-p}$. The value $\nu = 1$ defines a characteristic mass scale, which is $\sim 2 \times 10^{13} M_{\odot}$ at $z = 0$. We use the [Sheth et al. \(2001\)](#) mass function in our halo model (§ 4.6.3).

3.3.1.3 Halo Density Profiles

Some functions that describe the dark matter halo density profiles include:

$$\rho(r|m) = \frac{\rho_s}{(r/r_s)^{\alpha}(1 + r/r_s)^{\beta}}, \quad (3.49)$$

and

$$\rho(r|m) = \frac{\rho_s}{(r/r_s)^{\alpha}[1 + (r/r_s)^{\beta}]}, \quad (3.50)$$

and in particular, setting $(\alpha, \beta) = (1, 2)$ in the top equation gives the famous (NFW [Navarro et al., 1997](#)) density profile. The mass within the virial radius, r_{vir} , of an NFW halo is

$$m = 4\pi\rho_s r_s^3 \left(\ln(1+c) - \frac{c}{1+c} \right), \quad (3.51)$$

where $c \equiv r_{vir}/r_s$ is the concentration parameter. The concentration of halos, even of the same mass, can vary, and are well-fit by a log-normal distribution ([Bullock et al., 2001](#)). For the NFW profile,

$$\bar{c}(m, z) = \frac{9}{1+z} \left[\frac{m}{m_*(z)} \right]^{-0.13}, \quad (3.52)$$

where $\bar{c}(m, z)$ is the mean concentration of the log-normal distribution, which depends on halo mass, and $m_*(z)$ is the characteristic mass scale.

One of the remarkable properties of the NFW halo profile is that it appears to be independent of scale. Further studies confirm this behaviour ([Moore et al., 1998](#); [Jing, 2000](#); [Jing & Suto, 2000](#)). Of course, the spherical collapse model is a simplified version of reality. N-body simulations (e.g., [Barnes & Efstathiou, 1987](#); [Dubinski, 1994](#); [Jing & Suto, 2000](#)), as well

as observations (e.g., [Law et al., 2009](#)), point towards non-spherical behaviour for collapsed dark matter halos.

In order to implement the halo model, the Fourier transform of the dark matter distribution within a halo of mass m , $u_{\text{DM}}(\mathbf{k}|m)$, is needed

$$u_{\text{DM}}(\mathbf{k}|m) = \frac{\int d^3\mathbf{x}\rho(\mathbf{x}|m)e^{-i\mathbf{k}\cdot\mathbf{x}}}{\int d^3\mathbf{x}\rho(\mathbf{x}|m)}. \quad (3.53)$$

Typically, it is assumed that the halo profile is truncated at r_{vir} , even though the NFW profile extends formally to infinity. This is done because the profiles fall as r^{-3} at large radii, and the mass within them diverges logarithmically. Therefore, by truncating at the virial radius, the mass within the profile equals the mass described by the halo mass function. For spherically symmetric NFW profiles truncated at the virial radius,

$$\begin{aligned} u_{\text{DM}}(k|m) &= \frac{4\pi\rho_s r_s^3}{m} \left(\sin(kr_s) [\text{Si}([1+c]kr_s) - \text{Si}(kr_s)] - \frac{\sin(ckr_s)}{(1+c)kr_s} \right. \\ &\quad \left. + \cos(kr_s) [\text{Ci}([1+c]kr_s) - \text{Ci}(kr_s)] \right), \end{aligned} \quad (3.54)$$

where

$$\text{Ci}(x) = - \int_x^\infty \frac{\cos t}{t} dt, \quad (3.55)$$

and

$$\text{Si}(x) = \int_x^\infty \frac{\sin t}{t} dt, \quad (3.56)$$

([Cooray & Sheth, 2002](#)). Note, this analytic solution turns out to be very handy for calculating the best-fit halo model in an efficient manner. Should a more complicated halo profile be desired, numeric solutions for each profile would need to be calculated, which would significantly increase the time to calculate the best-fit halo model.

3.3.1.4 Dark Matter Power Spectrum

If we assume that all of the dark matter in the Universe has collapsed into halos of varying sizes, then the statistics of the mass density can be estimated by treating the distribution

as the sum of two components: the linear, 2-halo term, and non-linear 1-halo term,

$$\begin{aligned}
 P_{\text{DM}}(k) &= P_{\text{DM}}^{\text{1h}} + P_{\text{DM}}^{\text{2h}}, \text{ where} \\
 P_{\text{DM}}^{\text{1h}}(k) &= \int dm \, n(m) \left(\frac{m}{\bar{\rho}}\right)^2 |u_{\text{DM}}(k|m)|^2 \\
 P_{\text{DM}}^{\text{2h}}(k) &= \int dm_1 \, n(m_1) \left(\frac{m_1}{\bar{\rho}}\right) |u_{\text{DM}}(k|m_1)| \\
 &\quad \int dm_2 \, n(m_2) \left(\frac{m_2}{\bar{\rho}}\right) |u_{\text{DM}}(k|m_2)| P_{hh}(k|m_1, m_2), \tag{3.57}
 \end{aligned}$$

and $P_{hh}(k|m_1, m_2)$ is the power spectrum of halos of mass m_1 and m_2 , approximated by

$$P_{hh}(k|m_1, m_2) \approx \prod_{i=1}^2 b_i(m_i) P_{\text{DM}}^{\text{lin}}(k) \tag{3.58}$$

3.3.2 Galaxy Power Spectrum and the Halo Occupation Number

Similarly, the power spectrum of galaxies is written as the sum of two components: the 1-halo term, P_{1h} , which describes pairs of objects within the same dark matter halo, and the 2-halo term, P_{2h} , which accounts for pairs of objects in different halos, resulting in $P(k, z) = P_{\text{1h}}(k, z) + P_{\text{2h}}(k, z)$. The number of pairs of galaxies within an individual halo is related to the variance of the halo occupation distribution, $\sigma^2(M, z) = \langle N_{\text{gal}}(N_{\text{gal}} - 1) \rangle$, while the number of pairs of galaxies in separate halos is simply the square of the mean halo occupation number, $N(M, z) = \langle N_{\text{gal}} \rangle$ (HON, hereafter). We model the HON using a central-satellite formalism (see e.g. [Zheng et al., 2005](#)): this assumes that the first galaxy to be hosted by a halo lies at its center, while any remaining galaxies are classified as *satellites* and are distributed in proportion to the halo mass profile. Different HODs for central and satellite galaxies are then applied. For central galaxies, the mean HON, N_{cen} , is described by a step function such that halos above a minimum mass threshold M_{min} contain a single central galaxy and halos below this threshold contain no galaxies. For satellite galaxies, a power-law in mass describes their mean HON (e.g., [Zehavi et al., 2005](#))

$$N_{\text{sat}}(M) = \left(\frac{M}{M_1}\right)^\alpha, \tag{3.59}$$

where M_1 is the mass-scale at which a halo hosts exactly one satellite galaxy (in addition to the central galaxy). Both semi-analytic models (e.g., [Berlind et al., 2000](#)) and hydrodynamical simulations (e.g., [Berlind et al., 2003](#)) show that the distribution of galaxies within a halo is close to Poisson in the high-occupancy regime, i.e., when $N_{\text{sat}} \gg 1$, and (strongly) sub-Poissonian in the low-occupancy regime. In order to agree with these results, satellite galaxies are assumed to be Poisson distributed at fixed halo mass. The distinction between

central and satellite galaxies then automatically accounts for the sub-Poissonian behaviour of the HOD in the low-occupancy regime (Zheng et al., 2005).

The 1- and 2-halo power spectra are

$$\begin{aligned}
 P_{1h}(k, z) &= \int_{\mathcal{M}} n_{\text{halo}}(M, z) [2N_{\text{cen}}(M)N_{\text{sat}}(M)u_{\text{DM}}(k, z|M) + \\
 &\quad N_{\text{sat}}^2(M)u_{\text{DM}}^2(k, z|M)] dM / n_{\text{gal}}^2(z), \\
 P_{2h}(k, z) &= P_{\text{DM}}^{\text{lin}}(k, z) \times \\
 &\quad \left[\int_{\mathcal{M}} n_{\text{halo}}(M, z) N_{\text{gal}}(M, z) \times \right. \\
 &\quad \left. b(M, z) u_{\text{DM}}(k, z|M) dM \right]^2 / n_{\text{gal}}^2(z).
 \end{aligned} \tag{3.60}$$

The meaning of the symbols here is as follows: P_{DM} is the linear power spectrum of dark matter, derived using the recipes of Eisenstein & Hu (1998) for the matter transfer function; n_{halo} is the halo-mass function (see Sheth et al., 2001); b is the linear bias parameter; u_{DM} is the normalized dark matter halo density profile in Fourier space; and n_{gal} is the mean number of observed galaxies per unit comoving volume at redshift z ,

$$n_{\text{gal}}(z) = \int_{\mathcal{M}} n_{\text{halo}}(M, z) \left[1 + \left(\frac{M}{M_1} \right)^\alpha \right] dM. \tag{3.61}$$

The expression for the 1-halo term implicitly assumes that the distribution of galaxies traces that of the dark matter, for which we have adopted the profile of Navarro, Frenk, & White (1997, NFW), with the same concentration parameter as Bullock et al. (2001). Since the NFW profile formally extends to infinity, it is necessary to artificially truncate the distribution at some radius, typically chosen to be the virial radius, $r_{\text{cut}} \approx r_{\text{vir}}$. On large scales, where clustering is predominantly linear, $u_{\text{DM}} \sim 1$, so that the 2-halo power spectrum simplifies to $P_{2h} = b_{\text{eff}}^2(z) P_{\text{DM}}(k, z)$, where $b_{\text{eff}}(z)$ is the effective large-scale bias,

$$b_{\text{eff}}(z) = \int_{\mathcal{M}} n_{\text{halo}}(M, z) N_{\text{gal}}(M) b(M, z) dM / n_{\text{gal}}(z). \tag{3.62}$$

3.4 Conclusion

Measurements of the clustering of galaxies has multiple applications, from cosmological on large scales, to informing galaxy formation models on small scales. Actually measuring galaxy clustering can become quickly complicated, as biases due to selection effects or systematics must be accurately accounted for. These problems becomes particularly difficult to deal with in heavily confused maps, and require significant effort to measure and interpret properly. To date, this problem has not yet found an adequate solution, but the advent of very large maps from *Herschel*, with tens to hundreds

of resolved sources, will require some serious thought very soon. Here we identified some of the challenges that must be overcome.

Choosing the most appropriate technique to measure clustering is the first challenge. Although the correlation function is typically used, here we argued that the power spectrum, which is the Fourier transform of the correlation function, is in fact the better choice. Measurements of the clustering of star-forming galaxies in confused maps with large beams is the subject of the next chapter.

Additionally, the halo model provides a way to interpret clustering measurements, and provides constraints for galaxy formation models on large and small scales. We will use the formalism laid out here to try and interpret the measurement of the power spectrum physically at the end of the next chapter.

Chapter 4

Measuring Clustering with BLAST

4.1 Introduction

BLAST was the first submillimeter telescope to map areas large enough to do statistically significant astronomical analysis. Prior to BLAST, the areal coverage of even the most ambitious submillimeter surveys had been relatively small (e.g., SHADES mapped approximately a quarter square degree at $850\ \mu\text{m}$; Coppin et al., 2006) due primarily to limited mapping speeds. In addition, as a result of steeply falling counts and modest resolutions of single-dish submillimeter telescopes, source confusion made it difficult to resolve any sources other than those with very high signal-to-noise. These sources span a relatively wide redshift range, roughly $1 \leq z \leq 4$, peaking at $z \sim 2.4$ (Chapman et al., 2005), which has the effect of washing out the angular clustering signal, further complicating measurements. Therefore, direct measurements of the clustering properties of resolved submillimeter galaxies to-date had been elusive.

This difficulty was confirmed by Scott et al. (2006), who re-analyzed all the SCUBA fields and found tentative evidence of strong angular clustering, but with errors too large to adequately constrain the spatial correlation length. Furthermore, relatively large beams have made it difficult to efficiently identify direct counterparts (Barger et al., 1999; Ivison et al., 2000) in order to obtain spectroscopic or photometric redshifts. Blain et al. (2004) attempted to measure the spatial clustering properties combining 73 sources with spectroscopic information, but again were only able to tentatively measure the clustering length. Other SCUBA galaxy clustering measurements, some tentatively detecting clustering, have been made by Webb et al. (2003) and Blake et al. (2006); meanwhile Almaini et al. (2003) claim to have found evidence for strong angular clustering between X-ray and submillimeter populations, although Borys et al. (2004) were unable to confirm the result using another, seemingly less biased, estimator. Using a nearest-neighbor analysis, Greve et al. (2004) find that most significant MAMBO (1.2 mm) sources come in pairs, separated by ~ 23 arcsec. Put together, these limitations have made it extremely difficult to measure the clustering signal robustly.

To study the clustering properties of submillimeter galaxies it is more powerful to consider the statistics of the *unresolved* CIB, which contains the full intensity, rather than working from a limited

catalog. In other words, instead of measuring a correlation among numbers of galaxies, use the background fluctuations of the total intensity to measure correlations among brightnesses of galaxies. [Devlin et al. \(2009\)](#) and [Marsden et al. \(2009\)](#) have demonstrated that the CIB is composed of emission by discrete sources. Since submillimeter galaxies are optically thin, this signal will be proportional to the total star formation rates of those sources. Correlations in the CIB will have a contribution in excess of white noise – which arises from Poisson sampling of a background made up of a finite number of sources – in the presence of clustering, with an amplitude that should be detectable with current surveys ([Scott & White, 1999](#); [Haiman & Knox, 2000](#); [Knox et al., 2001](#); [Magliocchetti et al., 2001](#); [Perrotta et al., 2003](#); [Amblard & Cooray, 2007](#); [Negrello et al., 2007](#)). Initial attempts to detect correlations by [Peacock et al. \(2000\)](#), for the Hubble Deep Field observed by SCUBA at $850\ \mu\text{m}$, and by [Lagache & Puget \(2000\)](#) for a $0.25\ \text{deg}^2$ *ISO* field at $170\ \mu\text{m}$, were only able to measure a signal consistent with the Poisson contribution. More recently, [Grossan & Smoot \(2007\)](#) and [Lagache et al. \(2007\)](#) reported the weak detection of a clustering component in $160\ \mu\text{m}$ data from $\sim 9\ \text{deg}^2$ *Spitzer* fields.

In this section we report the detection of correlations in the submillimeter part of the CIB due to the clustering of star-forming galaxies, in a $6\ \text{deg}^2$ field centered on the Great Observatories Origins Deep Survey South field (GOODS-South; [Giavalisco et al., 2004](#)). These data were collected by the Balloon-borne Large Aperture Submillimeter Telescope (BLAST; [Devlin et al., 2009](#)), which is designed to bracket the peak of redshifted thermal emission from dust by observing at 250, 350, and $500\ \mu\text{m}$. Operating above most of the atmosphere, BLAST is able to make observations in bands which are difficult or impossible to observe from the ground. A detailed description of the instrument and calibration can be found in [Pascale et al. \(2008\)](#) and [Truch et al. \(2009\)](#).

4.2 Two-Point Correlation Function from Catalogs

The clustering of resolved sources is typically first explored with the two-point correlation function, described in § 3.2.1, because of its relative simplicity, as well as the intuitive nature of the results. Therefore, with BLAST maps in hand, we sought to measure the correlation function of the resolved sources in them. Along the way we learned many lessons about measuring the correlation function of “sources” in confused maps, most of which are explained in § 3.2.2.2. Ultimately, it became obvious that attempting to measure the clustering of ~ 800 (barely) resolved sources of the 400,000 or so in the 9 square-degree BLAST maps was a mistake; the power spectrum of pixel brightnesses was clearly the way to go. Here we describe the methods used in our attempt to measure the correlation function, highlighting challenges and pitfalls.

To briefly summarize § 3.2.1, given a source at \mathbf{x}_0 , the two-point function describes the probability *in excess of Poisson* of finding another source at a distance $|\mathbf{x} - \mathbf{x}_0|$, i.e.,

$$\delta P = \bar{n}^2 \delta(V)(1 + \xi(r)), \quad (4.1)$$

where \bar{n} is the average number density of sources, and $\delta(V)$ is the comoving volume element. The corresponding angular correlation function, which is what we measure, is

$$\delta P = \bar{n}^2 \delta(V)(1 + w(r)). \quad (4.2)$$

Approximating $w(\theta)$ as a power-law

$$w(\theta) = \left(\frac{\theta}{\theta_0} \right)^{-\epsilon} \quad (4.3)$$

with $\epsilon \approx 0.8$ (e.g., [Giavalisco et al., 1998](#)).

Estimators of the angular two-point function from catalogues include the simple one

$$w = \frac{N_r}{N_d} \frac{DD}{RR} - 1, \quad (4.4)$$

the [Hamilton \(1993\)](#),

$$w = \frac{DD \times RR}{DR \times DR} - 1, \quad (4.5)$$

which has been shown to be less biased on small scales, and the [Landy & Szalay \(1993\)](#),

$$w = \frac{N_r^2 DD - 2N_r N_d DR + N_d^2 RR}{N_d^2 RR} - 1, \quad (4.6)$$

which has been shown to be both less biased and best takes edge effects into account. This last estimator is most commonly used, although there are limitations to it as well, as we will show.

Poisson errors on the binned values of $w(\theta)$ are estimated as

$$\delta w(\theta) = \sqrt{(1 + w(\theta))/DD(\theta)}, \quad (4.7)$$

however, the bins are highly correlated, and the cross-correlation matrix must be calculated to accurately describe the errors, which in turn is necessary to properly fit the data.

Another technique to estimate errors is the bootstrap technique ([Press, 2002](#)). In this method, correlation functions are calculated from randomly selected subsets of the data, and the fluctuations from those measurements determine the errors in the measurement. Unsurprisingly, this requires many sources to pull from, but is a more realistic estimate of errors than simply Poisson.

4.2.1 Preparing Random Catalogs

As discussed in § 3.2.2.2, beams much larger than the average distance between galaxies can significantly bias estimates of the correlation function. To adequately compensate for this bias, one approach is to compile random catalogs from maps whose properties are as similar as possible to real maps, with the important difference that that sources are Poisson distributed. Sources are then extracted from these random maps with the same code used to extract BLAST sources. Thus, “random” sources will suffer the same systematics that “real” sources do, and comparing these two should potentially return an unbiased estimate of the clustering measurement.

Mock uncorrelated BLAST maps were made in the following way: Sources whose fluxes and number densities were drawn from the [Patanchon et al. \(2009\)](#) counts were Poisson distributed in a map with 10" pixels. These were convolved with the appropriate simulated beam. Finally, noise-maps are made whose uniformity follows those of the BLAST *hits* maps, such that $n \propto 1/\sqrt{\text{hits}}$, and scaled so that the histogram of the noise-map equals the negative side of the BLAST map histogram. These noise-maps are added to the convolved source-maps.

Sources are extracted from these mock-maps using the same algorithm used to extract sources from the BLAST maps (see § 5.5 of [Marsden, 2007](#)), including assigning a signal-to-noise to the measurement.

4.2.2 Results

In order to estimate the clustering of BLAST sources, we used the simple estimator (Equation 4.4). The justification for this is shown in Figure 4.1, where the correlation functions of random maps — with RR calculated as described in the previous section — is found using each of the estimators and compared. Random maps by definition should have $w(\theta) = 0$ on all scales. There are clearly non-zero correlations found with the [Landy & Szalay \(1993\)](#) estimator, which are due to the DR pair-counts, which allow sources to occupy the “zone of avoidance” (see § 3.2.2.2). Thus it would appear that the simple estimator is the correct one to use.

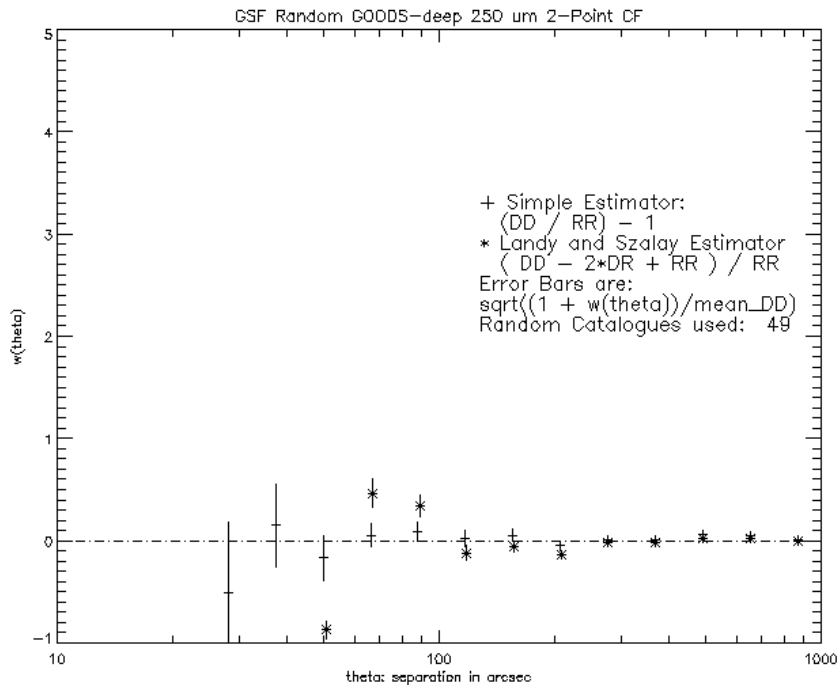


FIGURE 4.1: Correlation functions of random catalogs RR, compiled as described in § 4.2.1, and estimated with both the simple and [Landy & Szalay \(1993\)](#) estimators. Truly random catalogs by definition have a correlation function of zero on all scales. We see here that the simple estimator adequately measures zero, whereas the [Landy & Szalay \(1993\)](#) is biased.

A detailed discussion describing this bias can be found in § 3.2.2.2.

It should be noted that it is often claimed that the simple estimator is biased, and should not be used. However, according to Kerscher et al. (2000), the simple (or *natural* estimator in his nomenclature) performs equally well on scales less than $\sim 30 h^{-1} \text{ Mpc} \approx 30'$ at $z \sim 1$, much larger than the measured effects of the beam. The problem here is not the estimator, but the lack of large numbers of sources on scales where the clustering signal is large enough to detect. This is because in the case of FIR/submillimeter maps, negative K-correction (discussed in § 1.4.2.1) results in observations which are sensitive to a wide range of redshifts, thus the clustering of galaxies occupying different redshift slices are superposed onto one another, strongly diluting the angular correlation function. If the angular correlation function has a $w_0 \sim 3''$, then for arguments sake, lets ask what the signal would be at $300''$. Recalling Equation 4.3, $w(300'') \approx 0.025$. In order to distinguish such a weak signal from zero robustly would require ~ 6500 pairs in the DD($300''$) bin, or at least ~ 3000 sources in one square degree degree. Instead, in BGS-deep we have approximately 250 sources in one square degree, which means we would expect a Poisson error $dw(300'') \sim 0.15$, i.e., consistent with zero. On smaller angular scales, say $60''$, where the signal is stronger, $w(60'') \approx 0.09 \pm 0.34$. This is simply due to the dearth of source-pairs in the smallest angular scale bins.

This is consistent with what we find. For a $2.5\text{-}\sigma$ catalog with 412, 348 and 228 sources extracted from 250, 350 and $500 \mu\text{m}$ respectively, Figure 4.2 shows the measured correlation function compared to 95 random catalogs using the simple estimator. While by-eye it may seem that there is some evidence of an excess on small scales, but attempts to fit this with any power-law finds a signal consistent with zero.

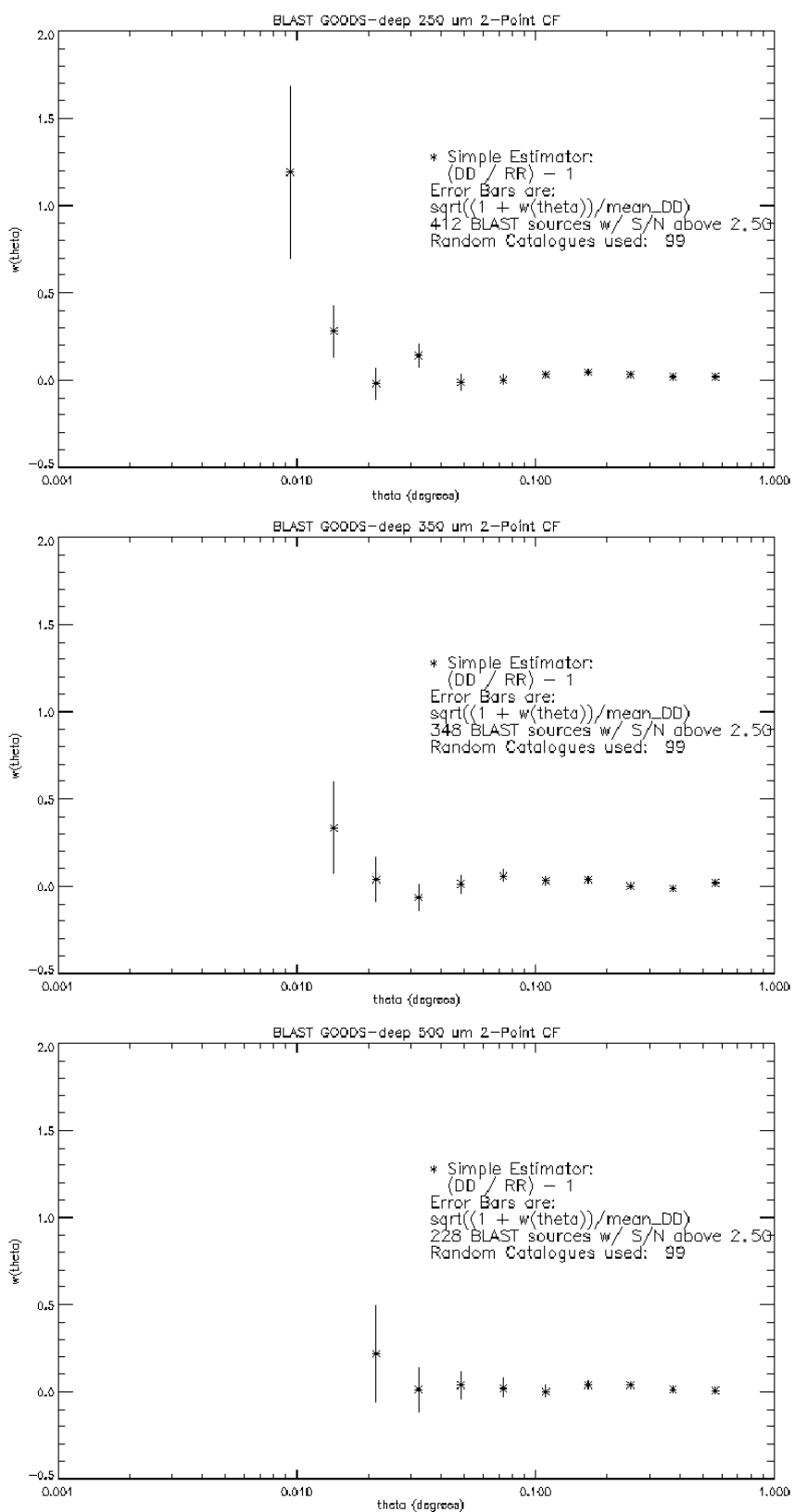


FIGURE 4.2: Correlation functions of BLAST sources with flux-cut of $2.5\text{-}\sigma$, found using the simple estimator. From top to bottom are 250, 350 and 500 μm . Though by-eye it seems that there are correlations on small scales, the resulting χ^2_{min} of the best-fit power-law is consistent with zero.

4.3 Power Spectrum from Maps

4.3.1 Overview

The map intensity, S_{map} , can be written as

$$S_{\text{map}} = (T \otimes [S_{\text{sky}} \otimes B + N]) W, \quad (4.8)$$

where we use \otimes to represent a convolution, S_{sky} is the true sky surface brightness, T is the transfer function of the map-maker, B is the measured instrumental beam, N is the instrumental noise, and W is the ‘aperture function’, which is zero beyond the region of interest. The autocorrelation of a map will contain a contribution from detector noise. To suppress this instrumental noise, cross-power spectra are taken among a set of four maps which are made by dividing the time-stream into four roughly equal parts and then making four separate maps (hereafter referred to as sub-maps). The timestreams, which are made up of numerous chunks, are divided into every fourth chunk (e.g., 1, 5, 9, ..., and 2, 6, 10, ..., etc.), so that the sub-maps have as similar coverage as possible. The number of sub-maps chosen maximizes the number that can be made while maintaining uniformity in hits, retaining some cross-linking, and avoiding holes in the maps.

In the cross-spectrum, noise which is uncorrelated between sub-maps averages to zero. Consequently, the spectrum does not depend on modelling the potentially complicated or non-stationary noise.

4.3.2 Map Preparation

BLAST observed a wide 8.7 deg² patch, centered on the GOODS-South field (3^h32^m35^s, −28°15′; hereafter BGS-Wide), with mean 1- σ sensitivities of 36, 31, and 20 mJy beam^{−1} at 250, 350, and 500 μm , as well as a deep, nested field of 0.8 deg², centered on (3^h32^m30^s, −27°48′; hereafter BGS-Deep) with mean 1- σ sensitivities of 11, 9 and 6 mJy beam^{−1}, respectively¹. A 6 deg² region, centered on BGS-Wide, is selected from the map (Figure 4.6), because of its uniformity in observed depth.

We do an analysis on two sets of maps, which target different angular scales: (i) on large scales, those whose data are from the wide region of the map, and are made with OPTBIN (hereafter OPT; Pascale et al., 2009); and (ii) on small scales, those which include all the deep and wide data, and are made with SANEPIC (hereafter SANE; Patanchon et al., 2008). For what follows, the treatments of each of the maps will be described separately, in sections labeled Wide-Only and Deep+Wide.

4.3.3 Wide-Only

We first analyze the wide-only maps — which were also the subject of the Viero et al. (2009) paper — where the scan rates are 0.1 deg s^{−1}, and the r.m.s. of the maps are 2.4, 1.9, 1.0 MJy sr^{−1}, at 250,

¹BLAST maps and catalogs are publicly available at <http://www.blastexperiment.info>

350, and 500 μm (applicable to calculating uncertainties of *point-source* flux densities). The data for the nested deep region, whose scan rate is only 0.05 deg s^{-1} , are not included.

In order to calculate the uncertainties of the power spectrum of the maps, a Monte-Carlo analysis must be performed on a large number of simulated maps, which must be made. To make these simulated maps in a reasonable time-scale, a naive mapmaker, as is described in § 2.3.2.2, is required. Since the BLAST bolometers are prone to drifts on timescales greater than ~ 10 seconds, in order to bin them into naive maps, the timestreams must be filtered. To retain as much large angular scale signal as possible, a fast scan rate is preferred because larger scales will survive the high-pass filtering, designed to remove noise below the 0.1 Hz $1/f$ knee. Thus, large-scale noise is removed by high-pass filtering the time-streams at 0.2 Hz. Correlated noise – a drift of multiple detectors in unison – is not removed because it would inevitably suppress large scale signal as well. Instead, a cross-correlation of a subset of the maps. The maps are made with OPTBIN, a fast, naive, mapmaker whose transfer function is calculated using a Monte-Carlo simulation (see § 4.3.3.1) is used to remove large-scale correlated noise (described below). The r.m.s. of the resulting sub-maps is 4.6, 3.6, and 2.0 MJy sr^{-1} , at 250, 350, and 500 μm . The sub-maps are shown in Figures 4.12–4.14

4.3.3.1 Transfer Function

BLAST maps made with filtered timestreams are not exact representations of the sky (Equation 4.8). Simulations are required to determine how the sky map observed by BLAST relates to the real sky; this ratio in Fourier space is what we call the transfer function, T . In order to statistically determine the transfer function, many simulated maps must be made. These simulated maps are made with the BLAST simulator (§ 2.3.3), receiving mock-clustered maps as inputs. The mock-clustered maps are described in § 4.3.5.

Each convolved, clustered signal-only mock map is ‘observed’ with the simulator four times, once with each of the four pointing solutions corresponding to the given sub-map. An example of convolved, clustered signal-only maps before and after simulation is shown in Figure 4.3. Approximately 4×1000 maps are made this way, and the average of their cross power spectra (using the same pipeline as that used for the measurement) are compared to the power spectrum of the input maps. This ratio is the transfer function, and is shown in Figure 4.4

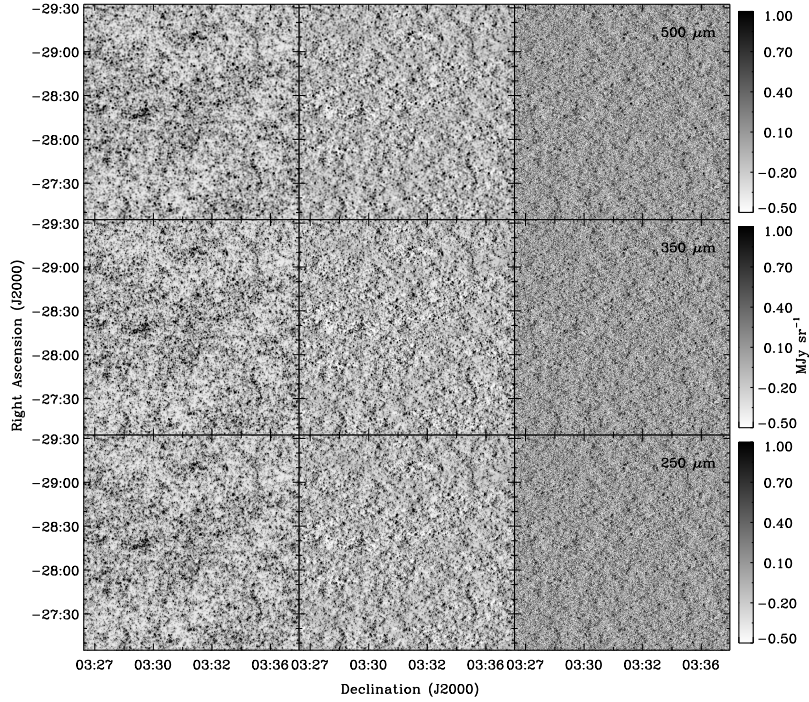


FIGURE 4.3: Clustered mock-maps described in § 4.3.5 which are used to calculate both the transfer function (§ 4.3.3.1) and the uncertainties in the power spectrum measurement (§ 4.5.2). Left Column: Clustered, convolved maps without noise; Center Column: Output simsky maps, whose input is the left column; Right Column; Hits-weighted noise maps added to Simsky maps

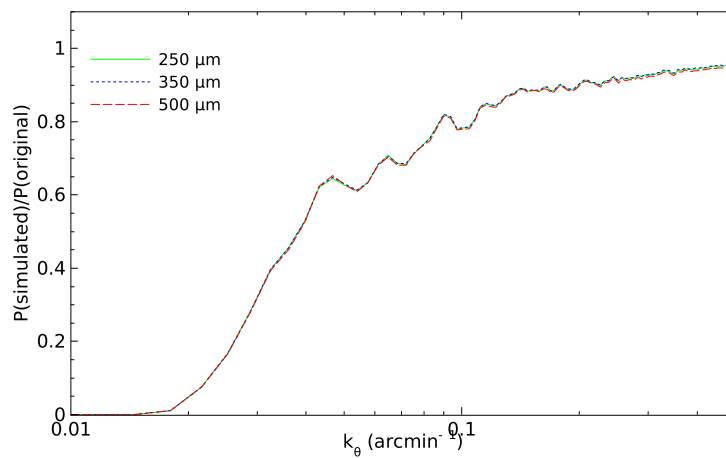


FIGURE 4.4: Transfer functions calculated with a Monte-Carlo simulation involving 500 mock-maps observed with the BLAST simulator. The lines are identical beyond the scale of the beams, which implies that the map-maker is linear, as we would expect. Figure from [Viero et al. \(2009\)](#).

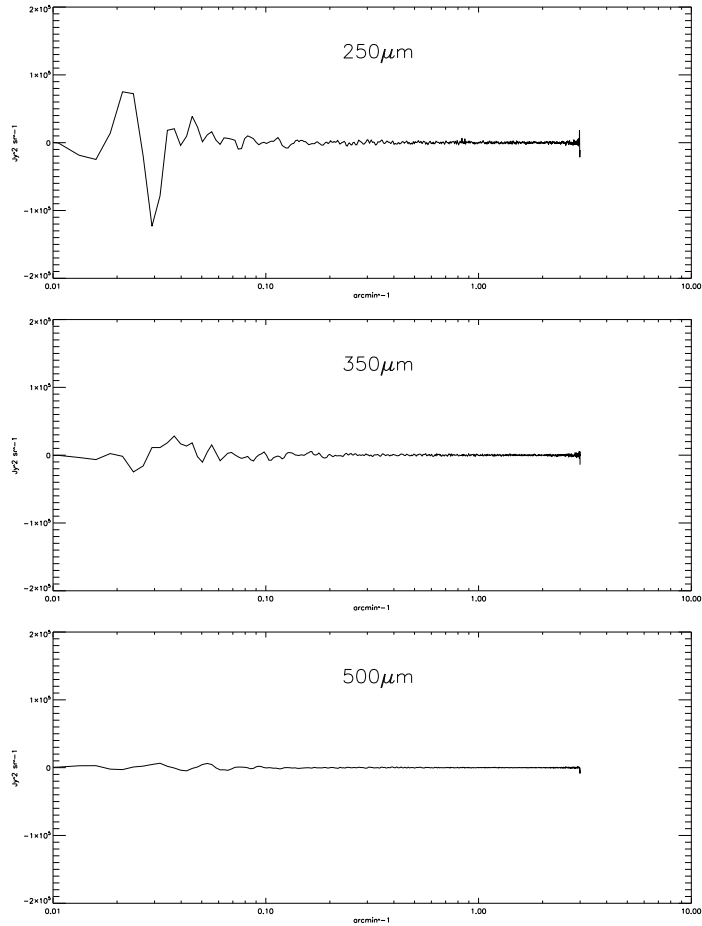


FIGURE 4.5: Jackknife tests in all three bands. Signal consistent with zero at all scales, but noise is much larger at the largest angular scales. Since we only consider scales $k_\theta < 0.4$, we are unaffected by the large noise regions.

4.3.3.2 Jackknife tests

We performed jackknife tests in which a correlation is calculated between two distinct difference maps. Specifically, we take the cross-correlation of: (sub-map 1 – sub-map 2) and (sub-map 3 – sub-map 4). If the cross-correlation measures only signal, then taking a difference between sub-maps should cancel sky signal and result in a cross-correlation power spectrum consistent with zero. As is shown in Figure 4.5, our results are consistent with zero, in the range of interest, in all three bands.

4.3.4 Deep + Wide

Of the ~ 90 hours dedicated to observing GOODS-south, about 50% of it was spent on each BGS-wide and deep. As mentioned before, BGS-wide is a 8.7 deg^2 patch, centered on the GOODS-South field ($3^{\text{h}}32^{\text{m}}35^{\text{s}}$, $-28^\circ 15'$ and has mean $1-\sigma$ sensitivities of 36, 31, and 20 mJy beam^{-1} at 250, 350, and $500 \mu\text{m}$, whereas BGS-deep is a nested field of 0.8 deg^2 , centered on $3^{\text{h}}32^{\text{m}}30^{\text{s}}$, $-27^\circ 48'$ with mean $1-\sigma$ sensitivities of 11, 9 and 6 mJy beam^{-1} , respectively. We will exploit the low noise properties of the deep region by weighting the map by the noise, as described in § 4.5.3.

Unlike BGS-wide, the deep region was observed with a scanning speed of 0.05Hz, and as a result, the same filter that was applied to the wide TODs would attenuate signal on scales half the size of those in BGS-wide. Rather than filter this aggressively, we attempted a different approach. For this analysis, the sub-maps were prepared using SANEPIC (Patanchon et al., 2008), an optimal mapmaker which does not require filtering of the TODs. As with wide-only, the same 6 deg² region is selected from the map because of its uniformity in observed depth, and are shown in Figure 4.7. What is immediately obvious is that the maps have giant waves in them. This is because the cross-scan direction is poorly constrained; a consequence of observing from near the south-pole, where rising and setting fields only differ by at most 15°. We can account for this “wave” in two steps: 1) by fitting and removing a fourth order polynomial; and 2) by filtering in the Fourier domain and correcting for the filter with another transfer function. These steps are described in detail below.

4.3.4.1 Polynomial Removal

A disadvantage to filtering in the Fourier domain is that discrete Fourier transforms requires periodic boundaries. For a map with arbitrary waves in it, that is clearly unrealistic. Instead, by fitting a polynomial to the wave and removing it in map-space, the ends are able to freely follow the shape of the wave. Provided the polynomial does not have too many free parameters, the scales affected will be much larger than those we want to probe. Since the SANEPIC transfer function is unity on scales less than about a degree, we are not interested in scales larger than that, and can safely remove a 4th order polynomial. The original sub-maps, fitted polynomials, and polynomial subtracted maps are shown in Figures 4.8, 4.9, and 4.10. The r.m.s. of the resulting sub-maps are 1.8, 1.2, and 0.6 MJy sr⁻¹, at 250, 350, and 500 μm. The sub-maps are shown in Figures 4.8, 4.9, and 4.10.

4.3.4.2 Noise-Weighted Deep+Wide Maps

To exploit the excellent noise properties of the deep region, after removing a polynomial from the deep+wide sub-maps, we weight them by their respective sub-noise-maps. Examples of weighted sub-maps are shown in Figure 4.11.

4.3.5 Clustered Mock-Maps

A number of simulations discussed this Chapter require mock-maps. Sometimes these mocks have sources which are uncorrelated, and other times correlated sources are more appropriate. In the latter case, different levels of sophistication may lead to more realistic mocks, but at the heavy price of complexity. Ideally, a mock clustered map would have filaments, voids, groups, clusters and occasionally superclusters. Bright sources would cluster more strongly than faint ones, and halos at different redshifts would be appropriately biased. In practice, this would require semi-analytical modelling with all of the appropriate constraints already in place, or nearly so. Clearly, for situations where less realistic simulations are adequate, this is overkill.

Here we adopt the algorithm of [Almaini et al. \(2005\)](#), see their appendix for algorithm). Briefly, they assume that galaxies live in spherical dark matter halos whose density profile is $\rho^{-\epsilon}$, and place these halos down at random in a map. The resulting population will have an angular correlation function with slope $\epsilon = 2\gamma - 2$, and therefore, to reproduce the desired slope of $\epsilon = 0.8$, the halo density profile takes the form

$$\rho \propto r^{-1.4}. \quad (4.9)$$

This map of halos then acts as a density, or probability map, upon which sources are randomly placed. The more halos that are randomly placed, the more diluted the correlation function. We tune this algorithm to produce maps with $\theta_0 \sim 3''$. We chose this number both because it is the upper limit found by [Peacock et al. \(2000\)](#), and because realizations with stronger clustering clearly do not *look* anything like BLAST maps. Finally, the maps are convolved with the BLAST beams to make three sets. Examples of clustered mock-maps are shown in the leftmost panels of [Figure 4.3](#)

4.4 Maps

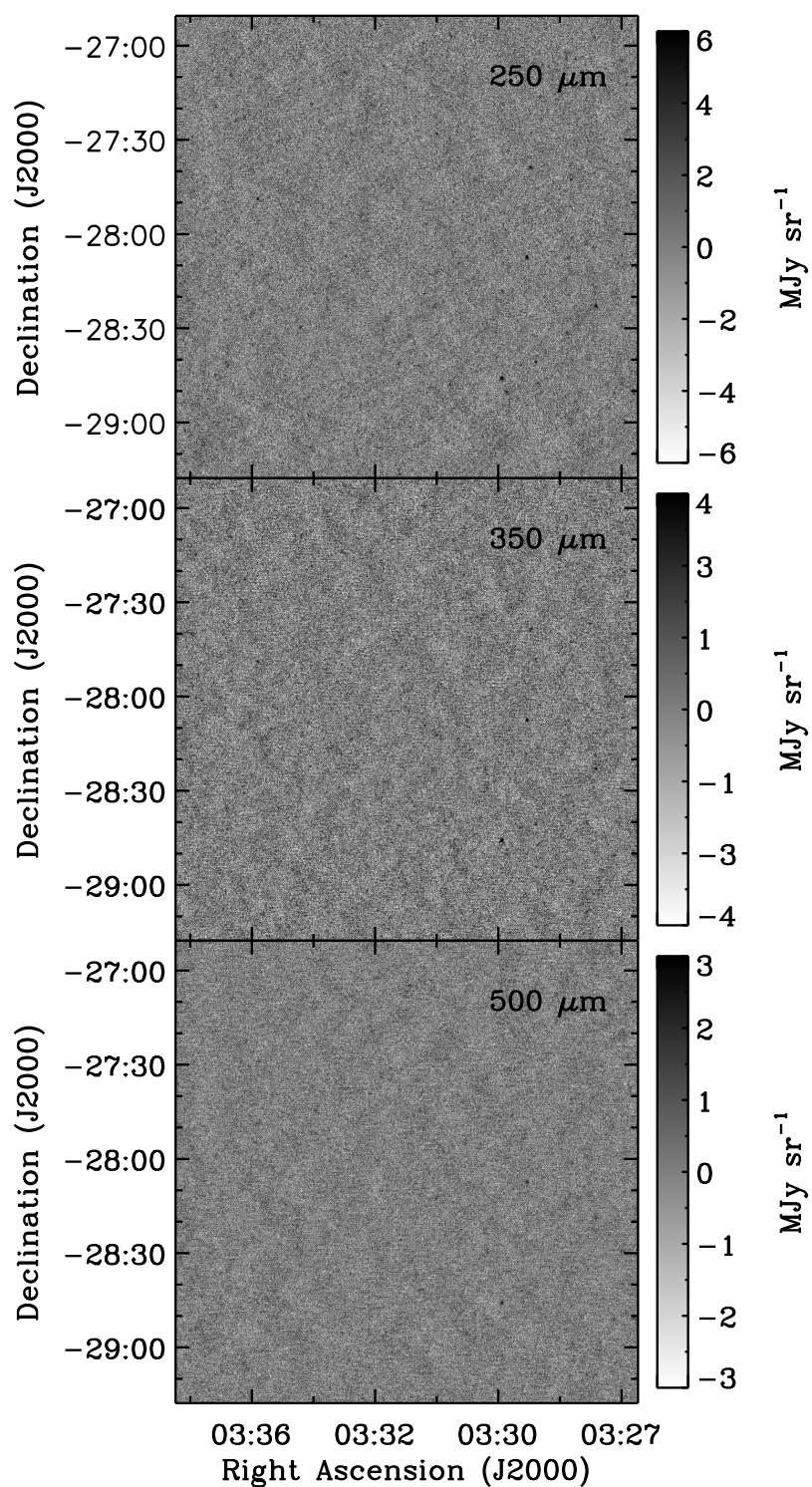


FIGURE 4.6: Wide-only maps of 6 deg^2 region, centered on BGS-Wide, selected from the map because of their uniformity in observed depth. These are shown for illustrative purposes only, and are not the maps used in the analyses (see § 4.3.3 for preparation of sub-maps.)

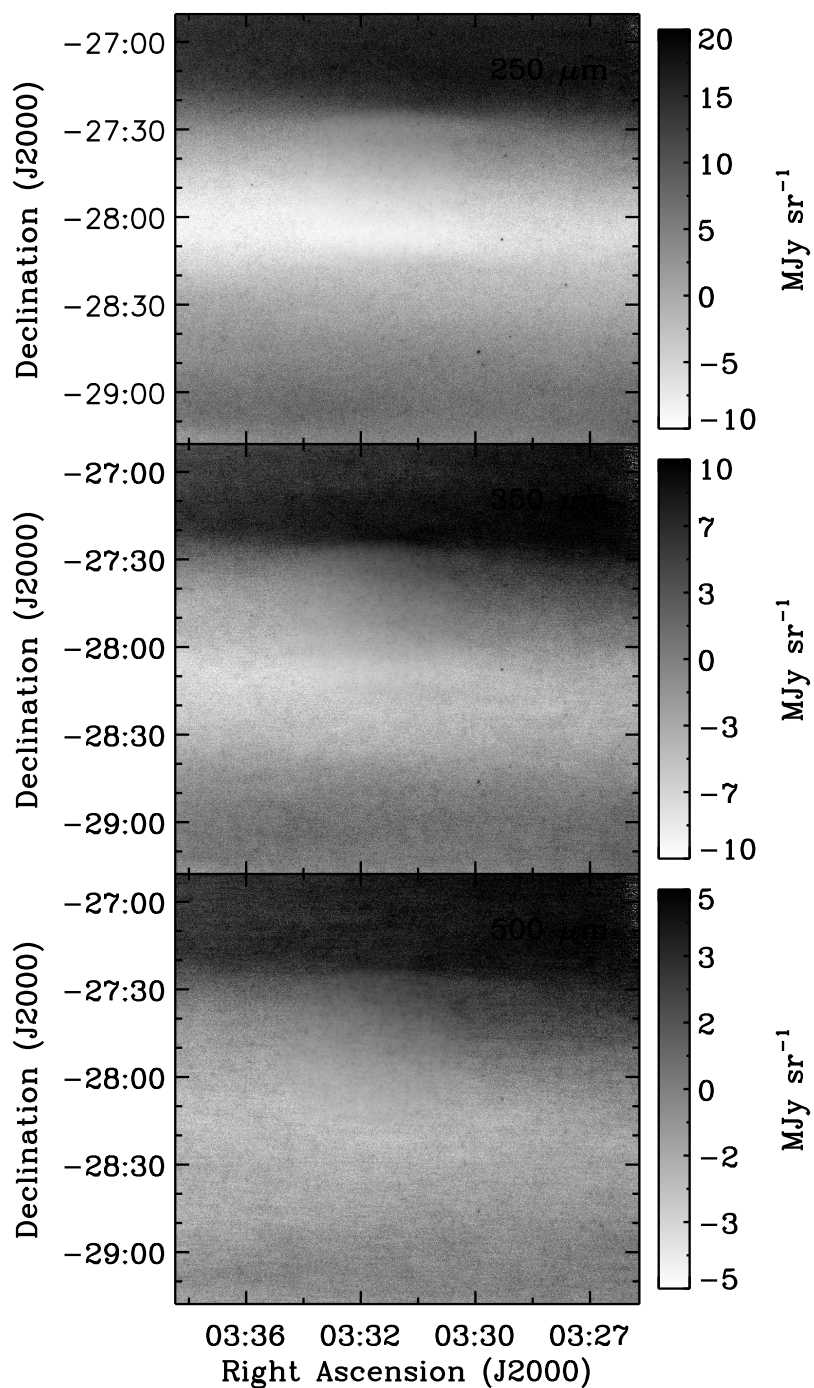


FIGURE 4.7: Deep+Wide maps of 6 deg² region made with SANEPIC, centered on BGS-Wide, selected from the map because of their uniformity in observed depth. These are shown for illustrative purposes only, and are not the maps used in the analyses (see § 4.3.3 for preparation of sub-maps.)

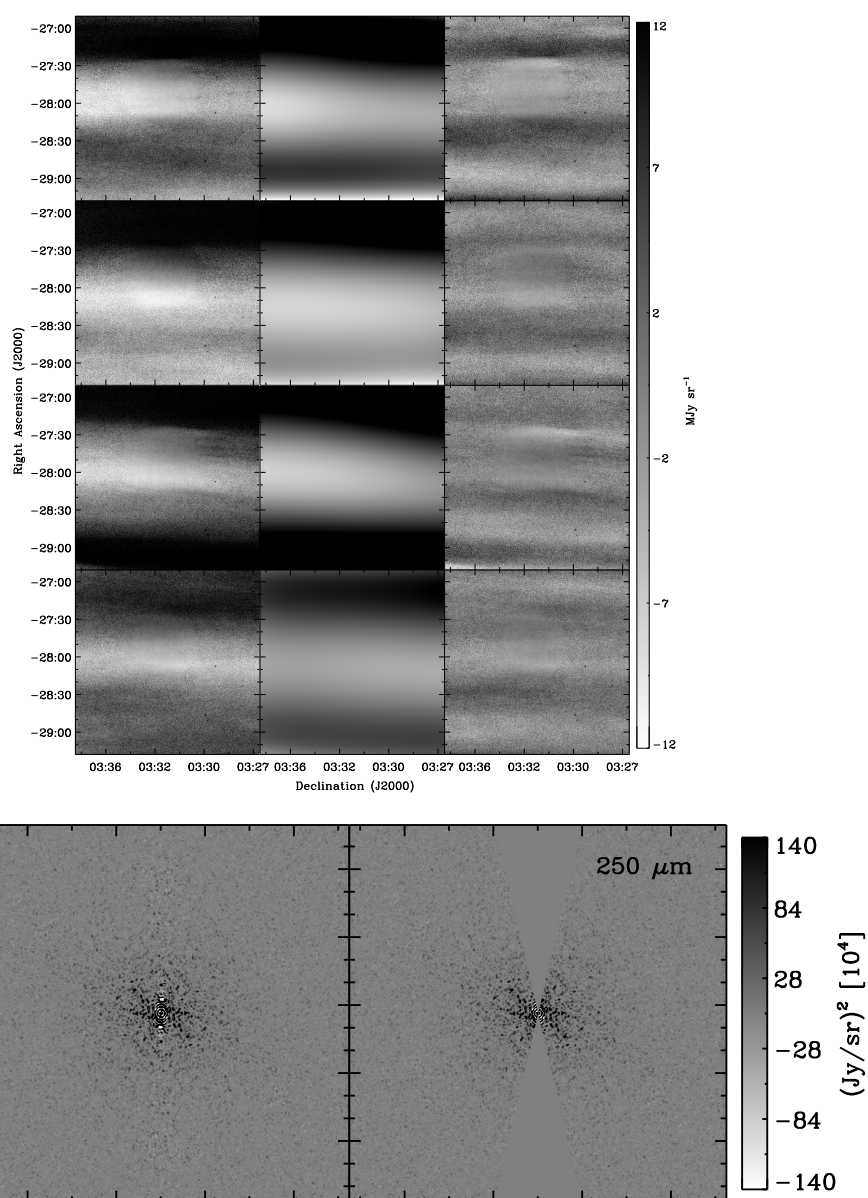


FIGURE 4.8: Top-Left: Deep+Wide $250\ \mu\text{m}$ sub-maps of $6\ \text{deg}^2$ region made with SANEPIC. Center: Best-fit 4^{th} -order polynomial fit to the sub-map. Right: Polynomial-removed sub-map. Bottom-Left: 2D-FFT of cross-power spectrum of polynomial-removed noise-weighted sub-maps. Notice there is still significant power in the cross-scan direction, evident as a vertical strip. Right: Cross-scan power removed in with a wedge-mask, angle 26 degrees.

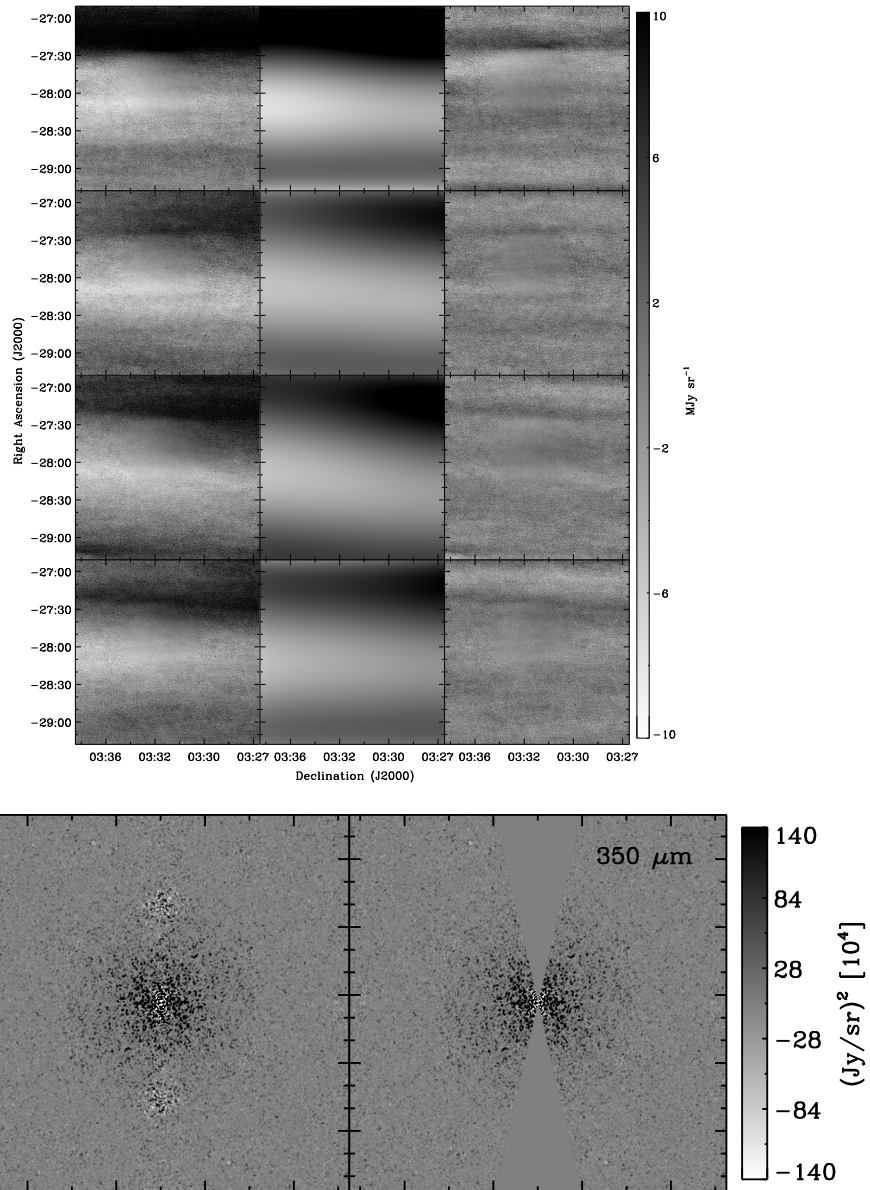


FIGURE 4.9: Top-Left: Deep+Wide $350\ \mu\text{m}$ sub-maps of $6\ \text{deg}^2$ region made with SANEPIC. Center: Best-fit 4^{th} -order polynomial fit to the sub-map. Right: Polynomial-removed sub-map. Bottom-Left: 2D-FFT of cross-power spectrum of polynomial-removed noise-weighted sub-maps. Notice there is still significant power in the cross-scan direction, evident as a vertical strip. Right: Cross-scan power removed in with a wedge-mask, angle 26 degrees.

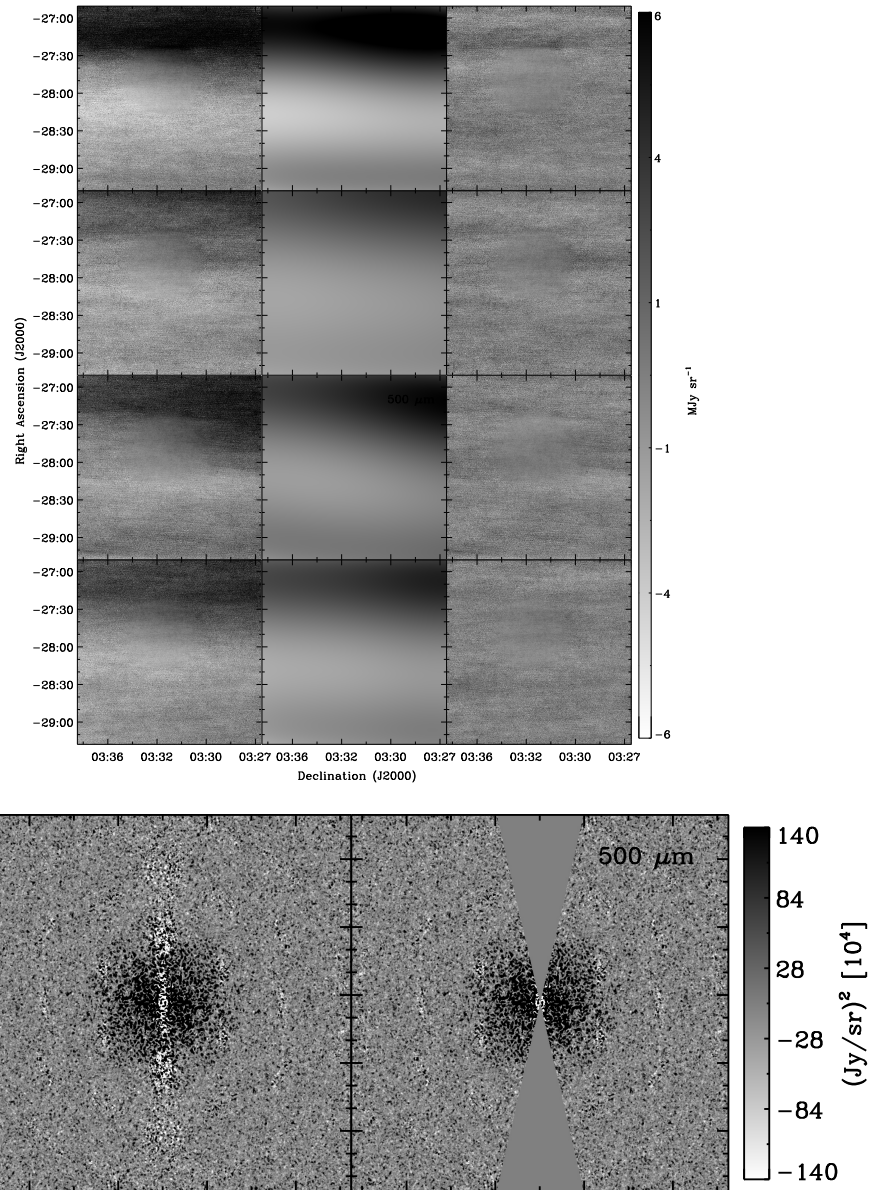


FIGURE 4.10: Top-Left: Deep+Wide $500\ \mu\text{m}$ sub-maps of $6\ \text{deg}^2$ region made with SANEPIC. Center: Best-fit 4^{th} -order polynomial fit to the sub-map. Right: Polynomial-removed sub-map. Bottom-Left: 2D-FFT of cross-power spectrum of polynomial-removed noise-weighted sub-maps. Notice there is still significant power in the cross-scan direction, evident as a vertical strip. Right: Cross-scan power removed in with a wedge-mask, angle 26 degrees.

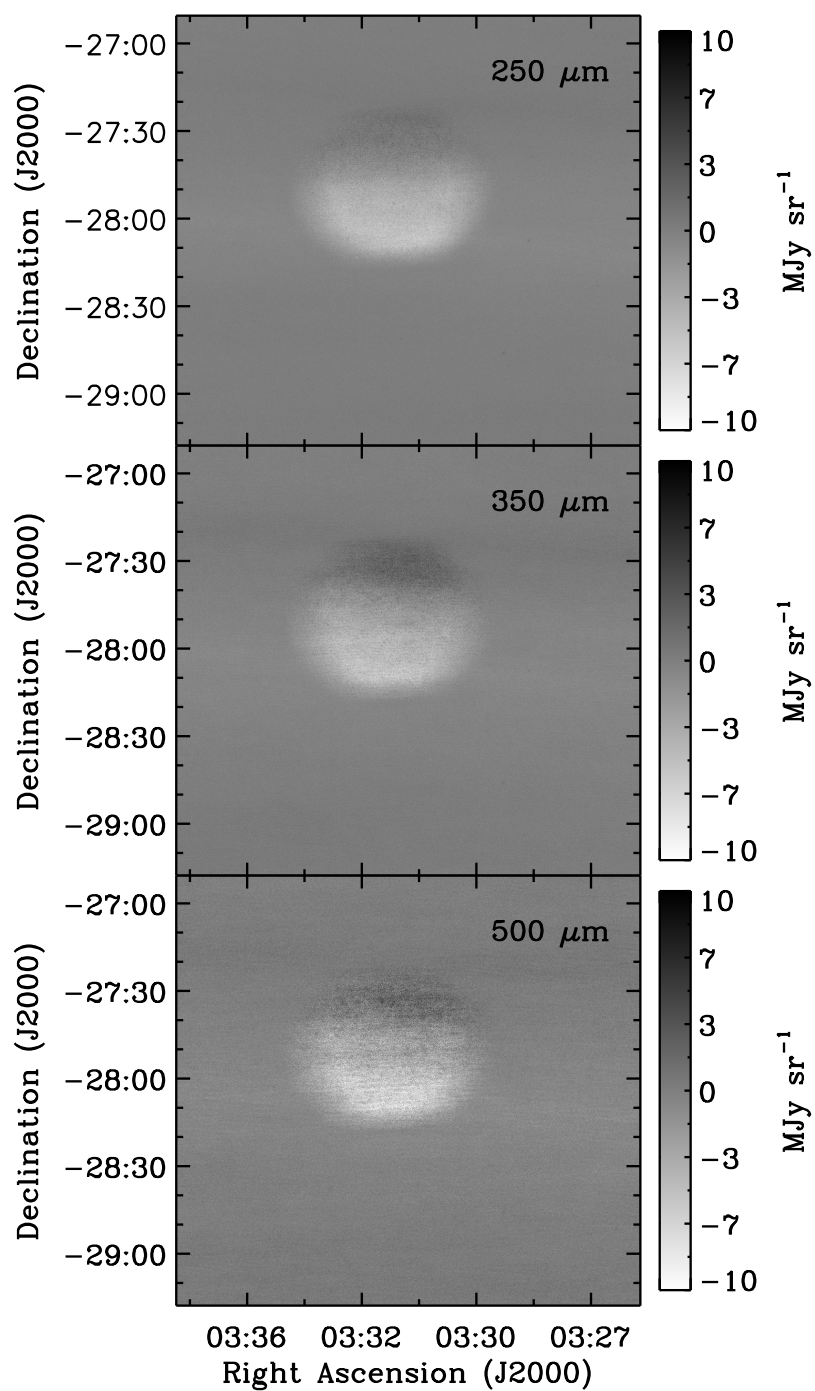


FIGURE 4.11: Deep+Wide noise-weighted maps of 6 deg^2 region made with SANEPIC. These are shown for illustrative purposes only, and are not the sub-maps used in the analyses.

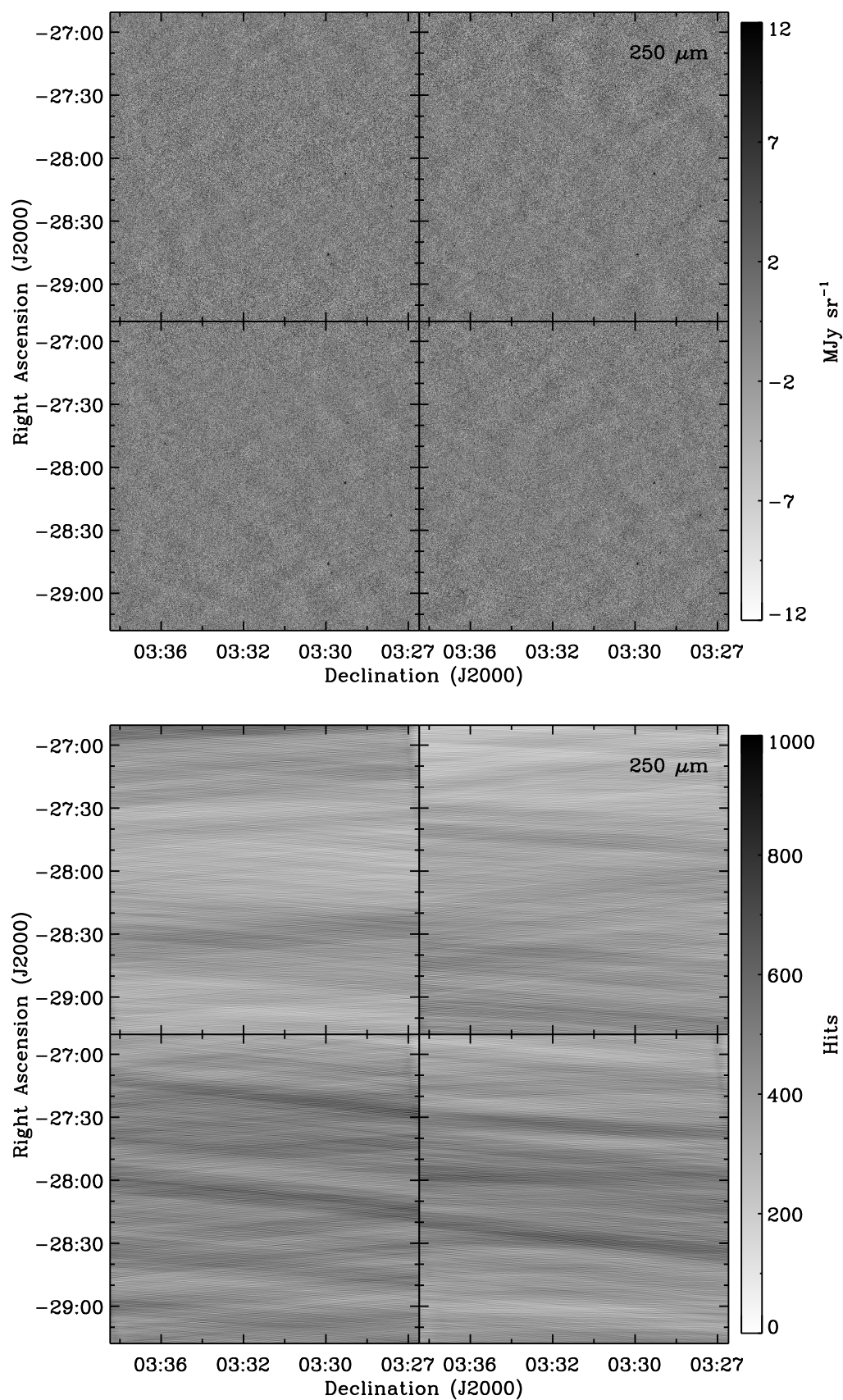


FIGURE 4.12: Wide-only sub-maps of 6 deg² region, centered on BGS-Wide, selected from the map because of their uniformity in observed depth. Top: 250 μm sub-maps. Bottom: 250 μm sub-hits maps

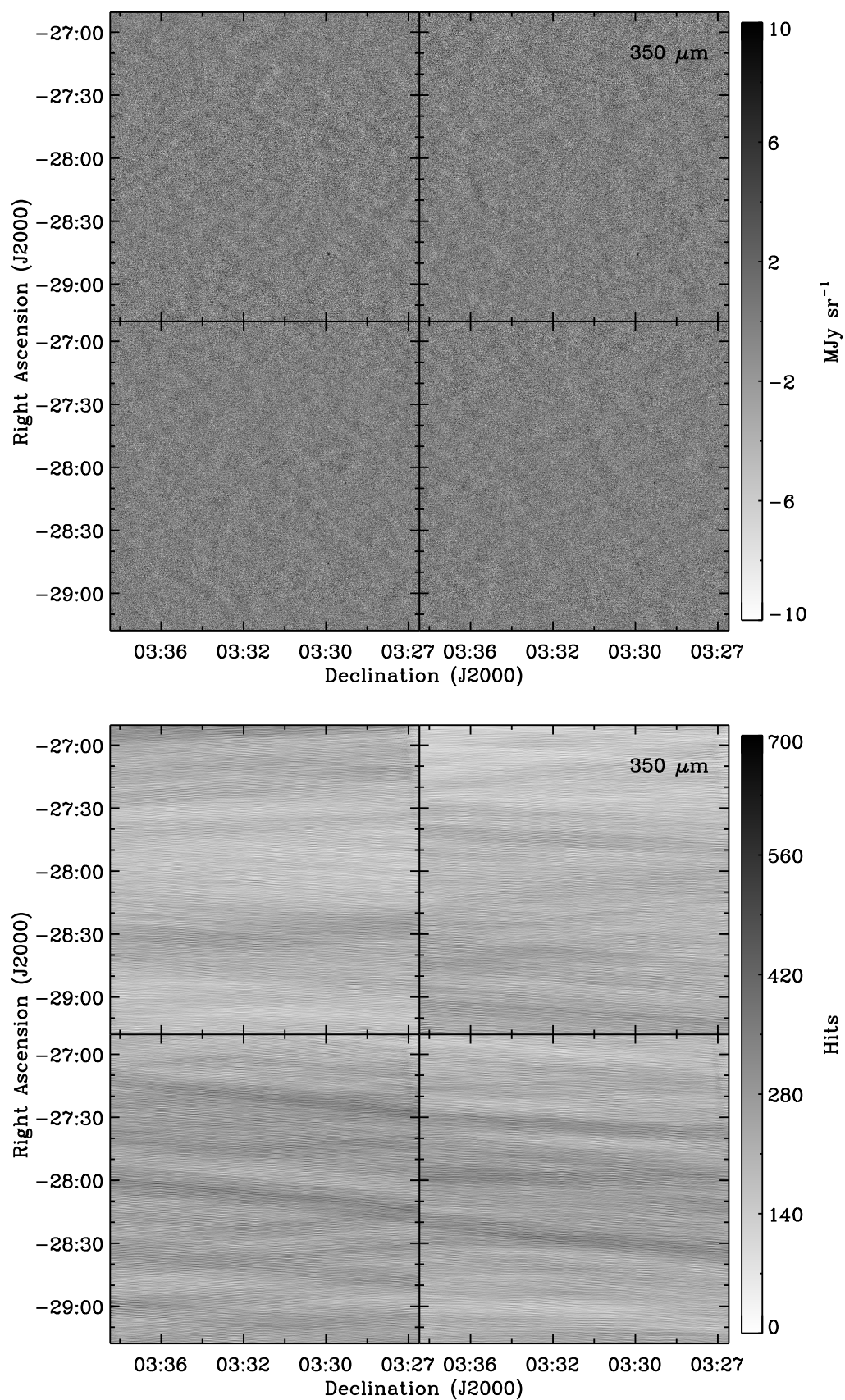


FIGURE 4.13: Wide-only sub-maps of 6 deg² region, centered on BGS-Wide, selected from the map because of their uniformity in observed depth. Top: 350 μm sub-maps. Bottom: 350 μm sub-hits maps

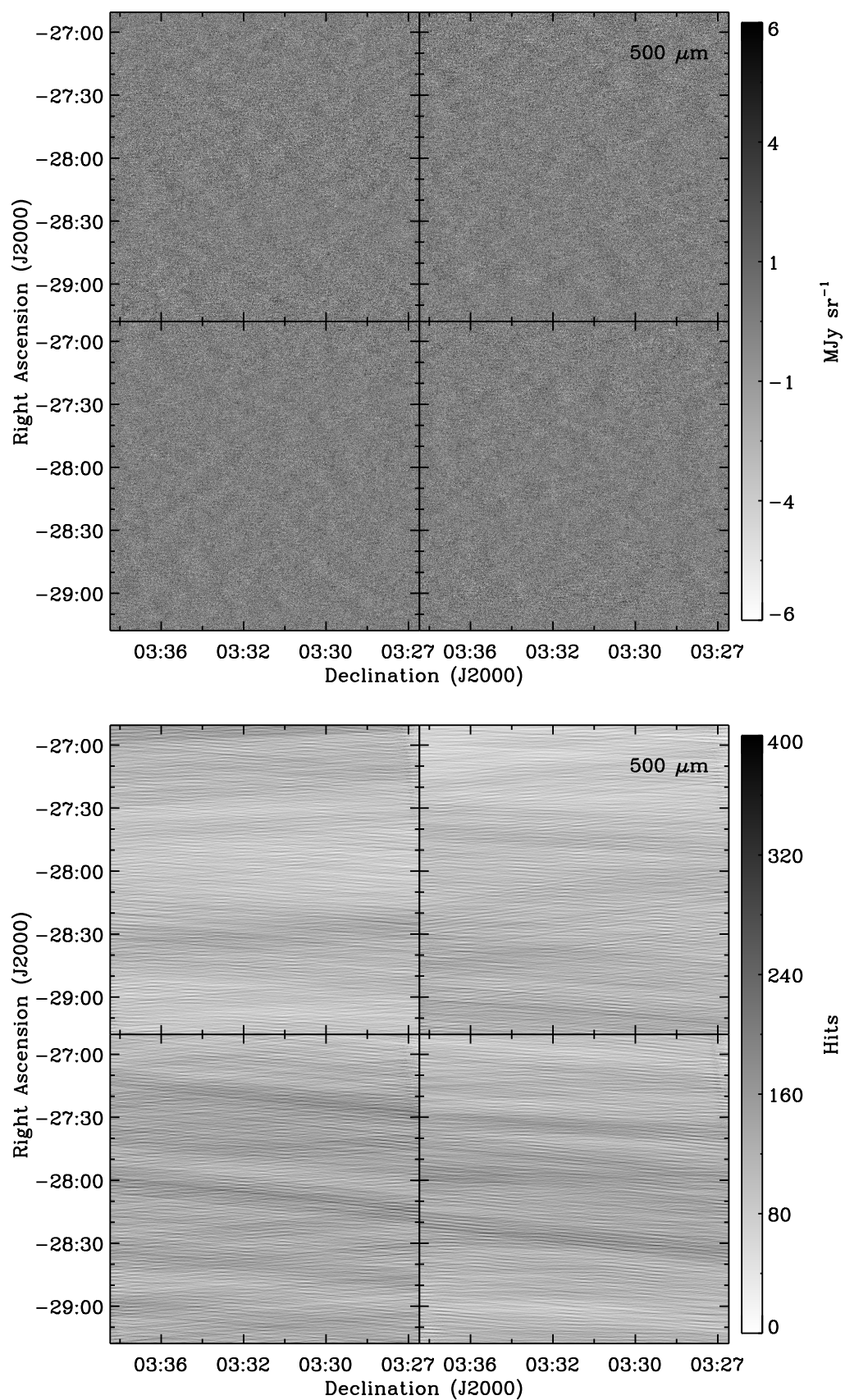


FIGURE 4.14: Wide-only sub-maps of 6 deg² region, centered on BGS-Wide, selected from the map because of their uniformity in observed depth. Top: 500 μm sub-maps. Bottom: 500 μm sub-hits maps

4.5 Making the Measurement

We are interested primarily with the signal from clustered galaxies, however, in addition to the clustering signal, the total power spectrum has contributions from instrumental noise, Poisson (shot) noise from individual background galaxies, and cirrus emission:

$$P_{tot}(k_\theta) = P_{clus}(k_\theta) + P_{shot}(k_\theta) + P_{cirrus}(k_\theta) + N(k_\theta), \quad (4.10)$$

In addition to calculating the power spectrum, we will address each contribution individually.

4.5.1 Wide-Only Power Spectrum

We prepare the maps before calculating the power spectrum by removing their means, apodizing them with a Welch window (Press, 2002, chapter 13.4), and zero-padding them with a width on each side equal to half the map. The window function of this procedure is calculated by comparing the power spectra made with this code, of a 1000 mock maps whose correlations are known beforehand, to the original power spectrum. We find that the window function is negligible on these scales.

The cross-correlation two-dimensional power spectrum (2D-FFT) of each pair of maps is calculated. Finally, the azimuthal average of the amplitudes (which in two-dimensional k -space appears to be isotropic), is taken to find the one-dimensional power spectrum, $P(k)$. The resulting spectra are averaged and divided by the power spectrum of the beam and by the transfer function described in § 4.3.3.1. At angular scales which are large compared to the high-pass filter (< 0.04 arcmin $^{-1}$) and approaching the cut-off of the beam (> 0.9 arcmin $^{-1}$), the transfer function is unreliable. Therefore, we are interested in the scales bracketed by these limits.

4.5.2 Uncertainties

To estimate uncertainties in our angular power spectra, we adopt a Boomerang-style Monte Carlo approach (e.g., Netterfield et al., 2002). 1000 clustered signal-plus-noise simulated maps (see § 4.3.5) are analyzed with the same pipeline as the astronomical data. The simulations include clustering in case the amplitude or shape of the transfer function depends on the input, but we found that not to be the case. Uncertainties are simply derived from the standard deviation of the mock power spectra and scaled to match the BLAST signal's amplitude.

4.5.3 Deep+Wide Power Spectrum

As was done for wide-only maps, deep+wide maps have their means removed, are apodized with Welch windows and finally padded with zeros to twice their size.

The cross-correlation two-dimensional power spectrum (2D-FFT) of each pair of maps is calculated. Due to the leftover waviness of the SANEPIC maps, additional filtering must be performed on the

2D-FFT. As can be seen in Figures 4.8–4.10, the waves are nearly constant in the horizontal direction, which is evident in the 2DFFT (i.e., bottom-left panels of Figures 4.8–4.10), as vertical stripe in power. These are filtered out by simply masking with wedges of 26° (i.e., bottom-right panels of same Figures). Lost power is accounted for in the calculation of the noise-weighted transfer function, described in § 4.5.3.1.

Finally, the azimuthal average of the amplitudes (which in two-dimensional k -space appears to be isotropic), is taken to find the one-dimensional power spectrum, $P(k)$. The resulting spectra are averaged and divided by the power spectrum of the beam and the noise-weighted transfer function, which we describe in § 4.5.3.1

4.5.3.1 Noise-Weighted Transfer Function

Weighting the central $\sim 0.8 \text{ deg}^2$ of the map will significantly bias the power spectrum. This can be easily corrected with a transfer function in the following way: Correlations are introduced to a random map by multiplying its 2D-FFT by a power-law, k^{-2} , and taking the inverse FFT of the product. This map is then convolved with the BLAST beam, and noise-maps (which vary just like real maps) are added to make sets of mock sub-maps. Finally, the cross-correlation 2D-FFT of the mock sub-maps is taken, and this is then filtered by masking with wedges of 26° . The mean of the ratio of the cross-spectrum of these sub-maps to the initial slope of -2 is the transfer function, and the variance of the ratio determines the uncertainties of the measurement.

4.5.4 Poisson Noise

Poisson (or shot) noise arises from the finite number of galaxies per unit area. It can be calculated analytically from the source counts as

$$P_{\text{shot}} = \int_0^\infty S^2 \frac{dN}{dS} dS. \quad (4.11)$$

Alternatively, Poisson noise levels can be estimated from Monte-Carlo simulations using mock-maps which are populated with uncorrelated sources whose fluxes are drawn from the measured BLAST counts (Patanchon et al., 2009). This has the added advantage that realistic (neglecting clustering) uncertainties can be calculated as well. Since the counts are so steep, care must be taken to reproduce the bright end of the counts faithfully, so that extremely rare bright sources do not unrealistically appear in the realizations. We find that the two methods of estimating the level of shot noise agree within the $1\text{-}\sigma$ uncertainties.

Due to the steep nature of the source counts, the Poisson noise is dominated by the contributions of the fainter population. Furthermore, Marsden et al. (2009) find only 15% of the total sky intensity is associated with a $3\text{-}\sigma$ catalog. We find that removal of only the brightest sources results in an approximately 5% reduction in Poisson noise at $250 \mu\text{m}$, and that more aggressive cuts lead to removal of correlations beyond just Poisson noise. We find behaviour consistent with this in our simulations. Therefore, we subtract only 5 sources above 500 mJy at $250 \mu\text{m}$, 2 sources above 400 mJy at $350 \mu\text{m}$,

and no sources at $500\ \mu\text{m}$. To subtract sources, first we make a source list by performing a noise-weighted convolution of the maps with the effective BLAST point-spread function (PSF) and identify local maxima in the smoothed map. We then subtract a scaled effective PSF with amplitude taken from the source list. We perform the same operation on our mock-maps, from which we calculate Poisson levels of $11.4 \pm 1.0 \times 10^3$, $6.3 \pm 0.5 \times 10^3$, and $2.7 \pm 0.2 \times 10^3 \text{Jy}^2 \text{sr}^{-1}$ at 250, 350, and $500\ \mu\text{m}$. These are shown as dashed lines in Figure 4.15.

4.5.5 Galactic Foregrounds

Gautier et al. (1992) show that the power spectrum of Galactic cirrus, on scales of 5– 500 arcmin, can be approximated by a power law,

$$P_{\text{cirrus}}(k_\theta) = P_0 \left(\frac{k_\theta}{k_0} \right)^{-\alpha}, \quad (4.12)$$

where k_θ is the angular wavenumber in inverse arcminutes, and P_0 is the power spectrum value at $k_0 = 0.01 \text{ arcmin}^{-1}$. We measure the cirrus component at $100\ \mu\text{m}$ from the cross-correlation of the three co-added IRIS (HCON³, see Figure 4.17) maps (reprocessed *IRAS*: Miville-Deschênes & Lagache, 2005) for a $\sim 15 \text{ deg}^2$ region surrounding the BGS-Wide field. The amplitude of the observed power spectrum has a contribution from cirrus emission which is highly variable on the sky. The GOODS region was specifically chosen because it is a low cirrus region, with a mean intensity of $1.39 \pm 0.18 \text{ MJy sr}^{-1}$. At scales $0.008 < k_\theta < 0.03 \text{ arcmin}^{-1}$, which is larger than the scales probed by BLAST, we find that the cirrus is well approximated by a power law, $P_0 = (0.47 \pm 0.18) \times 10^6 \text{ Jy}^2 \text{sr}^{-1}$ and $\alpha = 2.91 \pm 0.11$, values which are similar to those found in low cirrus emission regions measured by Lagache et al. (2007) and Miville-Deschênes et al. (2007). We assume the power spectrum continues to smaller angular scales, and scale it to the BLAST bands using the average dust emission color $(I_{\text{BLAST}}/I_{100})^2$, which is found by assuming cirrus emission behaves as a modified blackbody, $\nu^\beta B(\nu)$, where $B(\nu)$ is the Planck function, and β is the emissivity index (Draine & Lee, 1984). The scaled power spectrum and errors are calculated with a Monte-Carlo simulation, varying temperature ($17.5 \pm 1.5 \text{ K}$) and β (1.9 ± 0.2) (Boulanger et al., 1996). The resulting power law approximations and uncertainties are illustrated as dotted lines in Figure 4.15, which show that we are negligibly affected by Galactic cirrus on all recovered angular scales.

4.5.6 Clustering Signal

4.5.6.1 Wide-Only

Figure 4.15 shows an unambiguous signal in excess of Poisson noise on scales of $0.04 - 0.2 \text{ arcmin}^{-1}$ which cannot be explained by Galactic cirrus, and which we interpret as correlations from clustered star-forming galaxies. The vertical dashed line indicates the angle at which the distribution of $24\ \mu\text{m}$

³HCON refers to each survey. For more information and maps see <http://www.cita.utoronto.ca/mamd/IRIS/IrisOverview.html>

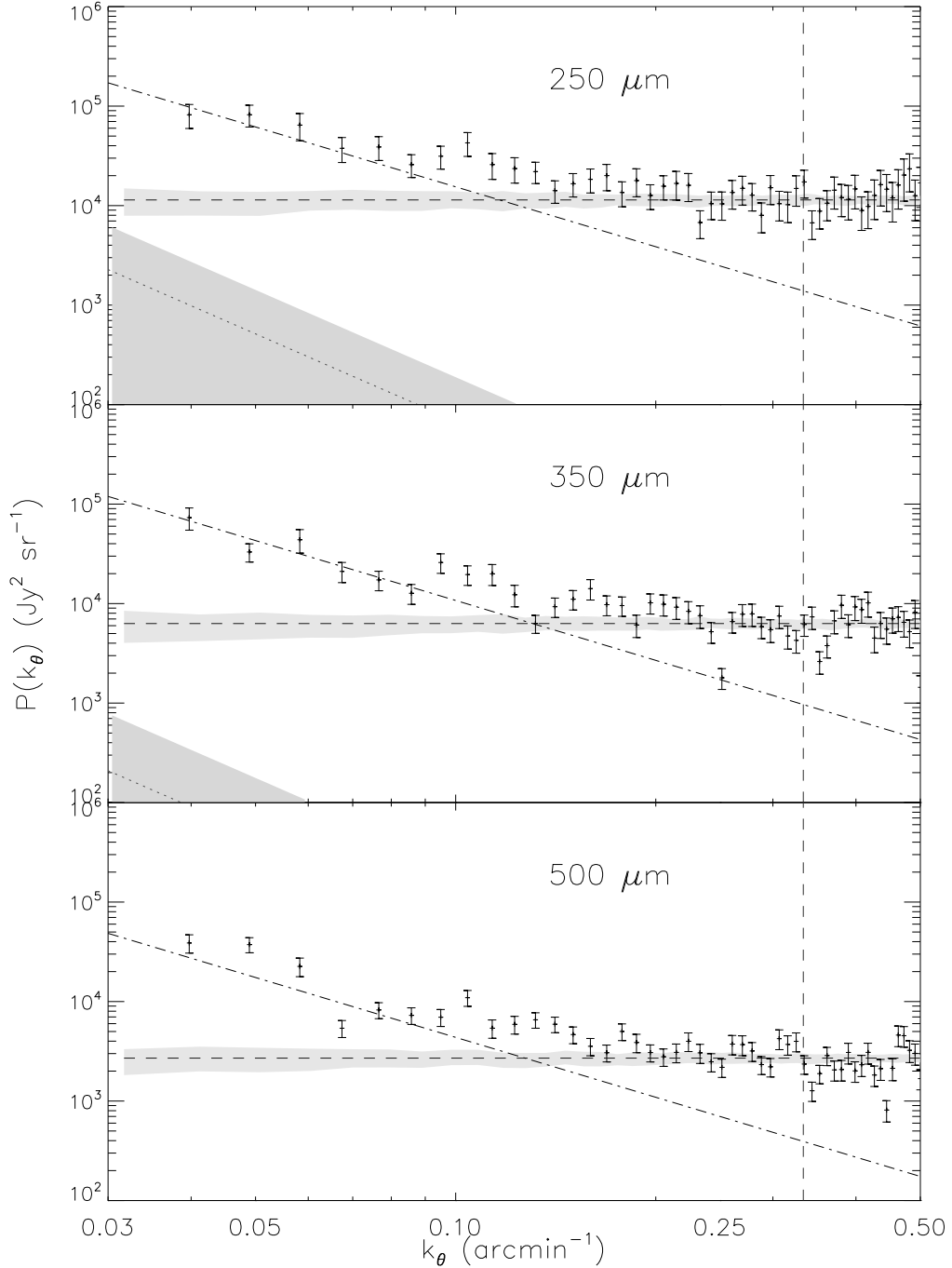


FIGURE 4.15: Power spectra of 6 deg² regions selected from the BGS-Wide maps at 250, 350, and 500 μm are shown with 1- σ uncertainties. Color-corrected fits to galactic cirrus measured from IRIS 100 μm maps are shown as dotted lines with shaded region representing 1- σ uncertainties, sloping down from the left side (500 μm cirrus is too low to make it onto the region plotted). Poisson noise contributions are found with Monte-Carlo simulations, and are shown as horizontal dashed lines with similar error regions. Scale invariant, k^{-2} , power spectra are shown as dot-dashed lines. Vertical dashed line at $k_\theta = 0.33 \text{ arcmin}^{-1}$ represents the scale at which the variance in the FIDEL catalog — which Marsden et al. (2009) show resolves most of the CIB — is no longer Poisson noise dominated. For angular scales greater than 0.33 arcmin^{-1} , signal in excess of Poisson noise is attributed to the clustering of star-forming galaxies. Figure from Viero et al. (2009).

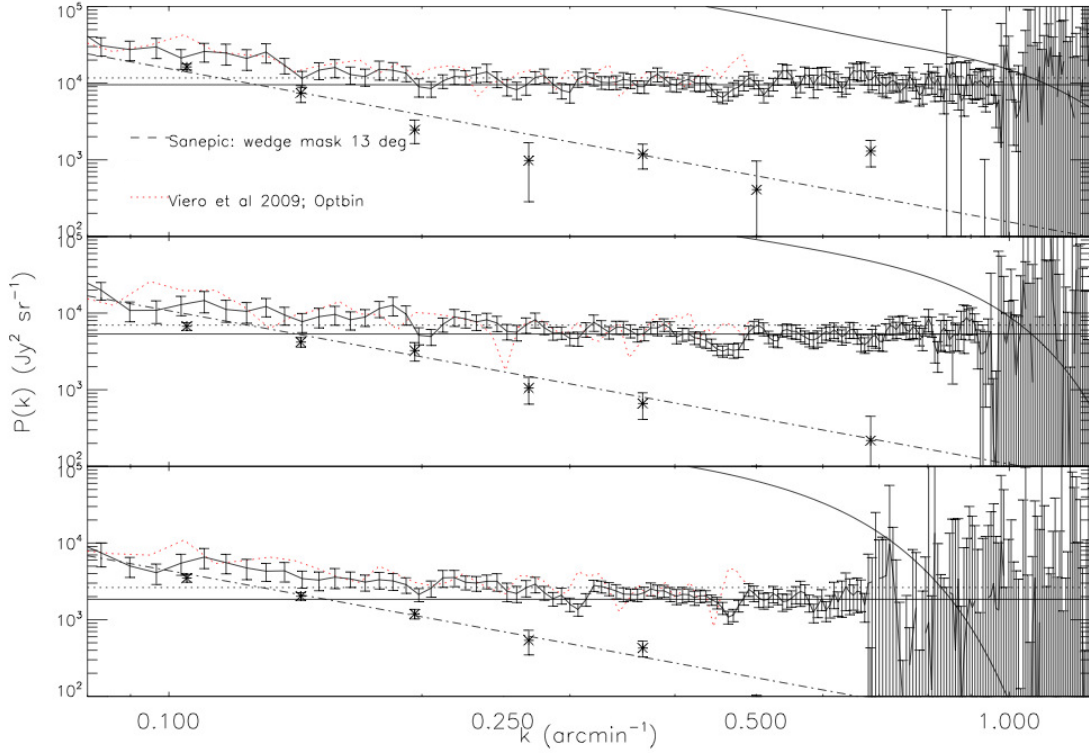


FIGURE 4.16: Power spectra of 6 deg² regions selected from the BGS-deep+wide maps at 250, 350, and 500 μm are shown with 1- σ uncertainties (black dashed lines). Poisson noise are shown as horizontal black solid lines. They are fit to the data, as opposed to modelled from counts, because the noise properties are much better on small angular scales, allowing for a robust fit. The clustering signal is found by subtracting the Poisson noise from the data, and are logarithmically binned. For reference, shown are the wide-only i) power spectra are shown as red dotted lines; ii) and the best-fit power-law with slope -2 as a black dot-dashed line. Scaled power spectra of the BLAST beams are shown as solid black curves which fall from the top center to bottom right. Note how error bars explode as beam turns over, confirming the methods used to calculate uncertainties. Remarkably, the clustered data points appear to have a power law down to scales of $k_\theta \approx 0.5$, or 2'.

selected FIDEL galaxies (Magnelli et al., 2009) begin to show variance in excess of Poisson. Indeed, the similarity to Figure 3 of Marsden et al. (2009) is striking.

k_θ (arcmin ⁻¹)	BLAST 250 (steradian ⁻¹)	BLAST 350 (steradian ⁻¹)	BLAST 500 (steradian ⁻¹)
0.044	$(1.39 \pm 0.52) \times 10^{-7}$	$(1.33 \pm 0.47) \times 10^{-7}$	$(2.47 \pm 1.17) \times 10^{-7}$
0.070	$(5.94 \pm 2.02) \times 10^{-8}$	$(4.98 \pm 1.83) \times 10^{-8}$	$(5.71 \pm 2.06) \times 10^{-8}$
0.113	$(2.99 \pm 0.95) \times 10^{-8}$	$(2.62 \pm 0.90) \times 10^{-8}$	$(2.98 \pm 1.00) \times 10^{-8}$
0.183	$(9.81 \pm 7.51) \times 10^{-9}$	$(9.94 \pm 6.92) \times 10^{-9}$	$(6.91 \pm 4.62) \times 10^{-9}$

TABLE 4.1: CIB normalized clustering power spectra, $P(k_\theta)/I_\nu^2$. The errors do not include uncertainties in the CIB. CIB values are listed in § 4.6.4

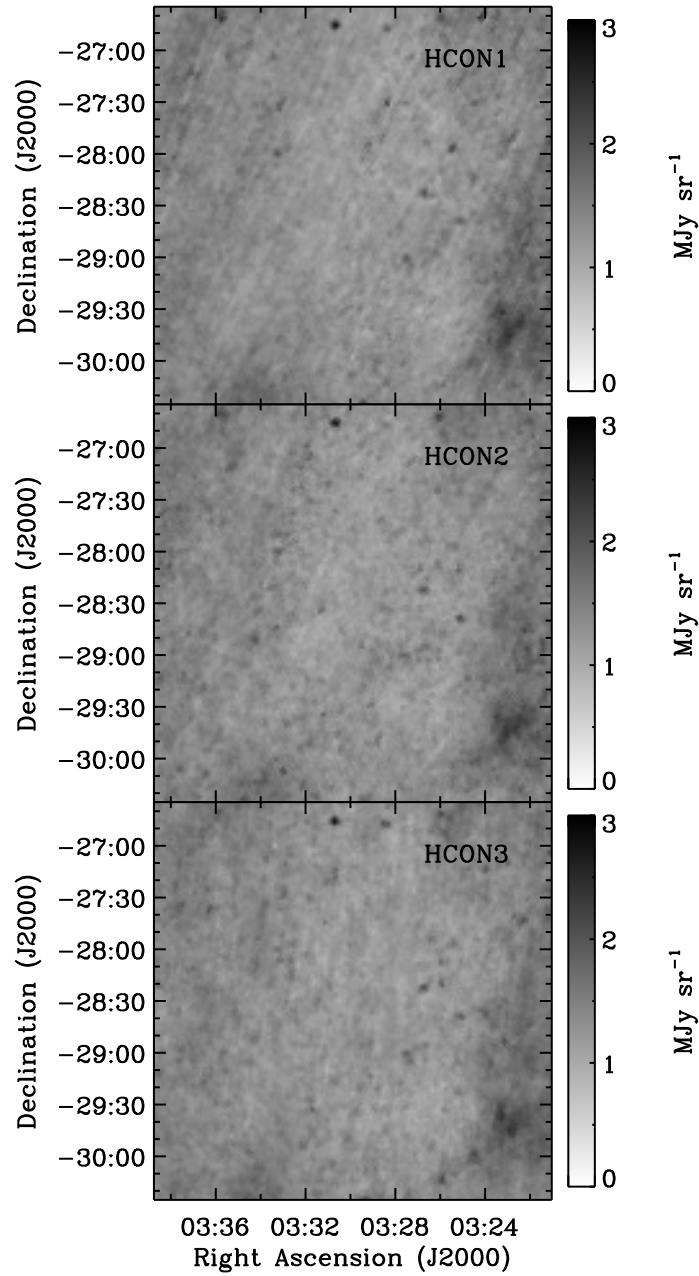


FIGURE 4.17: IRAS/IRIS $100\ \mu\text{m}$ HCON maps of a $\sim 15\ \text{deg}^2$ region surrounding the BGS-Wide field. The GOODS region was specifically chosen because it is a low cirrus region, with a mean intensity of $1.39 \pm 0.18\ \text{MJy sr}^{-1}$.

4.5.6.2 Deep+Wide

Similarly, Figure 4.16 shows the results of the deep+wide power spectra, before and after correcting for cirrus and shot noise. The best-fit power-law agrees with that found for wide-only, and extends to (slightly) smaller angular scales. Although this does not provide much new information, its value is to confirm that the signal measured is real.

BAND	θ_0 (arcsec)	ϵ
250 μm	0.017 ± 0.020	0.27 ± 0.19
350 μm	0.008 ± 0.006	0.26 ± 0.19
500 μm	0.0	0.0

TABLE 4.2: Best-fit values obtained for θ_0 and ϵ .

4.5.7 Power-Law Fit to Normalized Clustering Signal

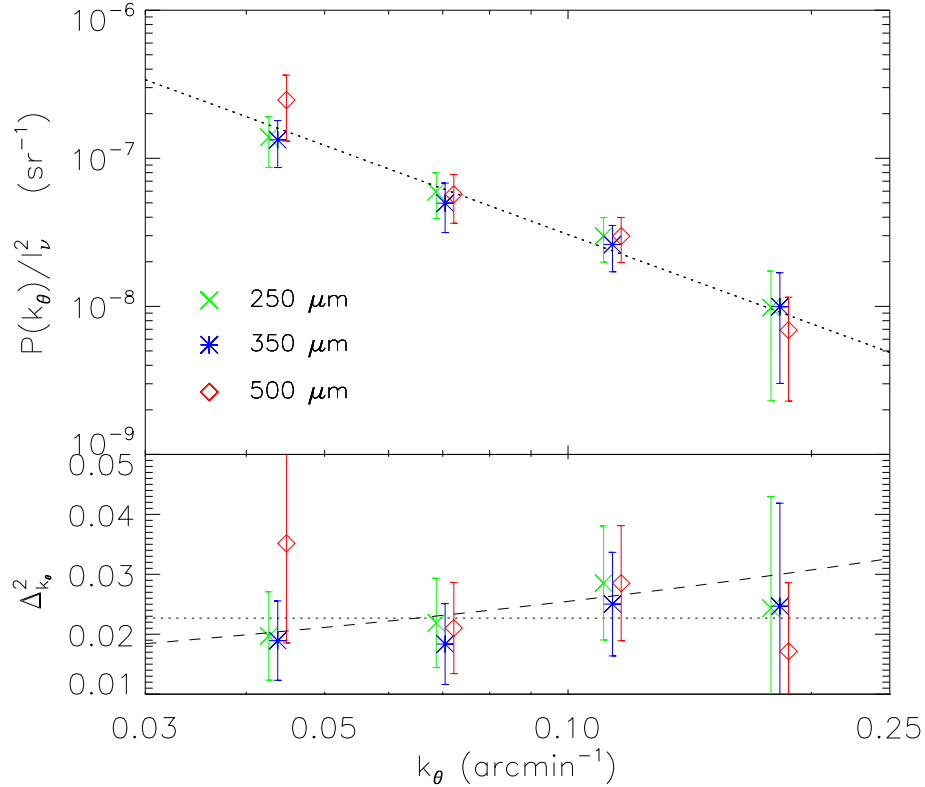


FIGURE 4.18: Top: Power Spectra of the clustering component, after removal of cirrus and Poisson noise, and normalized by $(I_\nu^{\text{CIB}})^2$. The best-fit power spectrum, proportional to k^{-2} , is shown as a dotted line. Bottom: $\Delta_{k_\theta}^2$ shown along with best-fit power spectra (horizontal dotted line); as well as best-fit parameters (dashed line) for 250 μm data. The 250 and 500 μm points are offset horizontally for clarity, by factors of -0.025 and $+0.025$, respectively. Clearly, the power spectrum signal of clustered star-forming galaxies is well fit by a power law power spectrum proportional to k^{-2} . Figure from [Viero et al. \(2009\)](#).

The CIB has an amplitude I_ν^{CIB} measured to be 0.71 ± 0.17 , 0.59 ± 0.14 , and 0.38 ± 0.10 MJy sr^{-1} at 250, 350, and 500 μm , respectively ([Marsden et al., 2009](#)). Figure 4.18 shows the clustering component of the power spectrum normalized by I_ν^{CIB} in the three BLAST bands, where the 250 μm and 500 μm data have been displaced slightly for visual clarity. The contributions of cirrus and Poisson noise have been subtracted, and the data re-binned in logarithmic intervals. These results are also listed in Table 4.1. We use the BLAST estimates for the CIB because they are the most precise estimate available of the CIB in these wavelength bands. Doing so has the additional benefit in this case that calibration uncertainties completely vanish in the ratio. The fit to a single power

law, and also the agreement in amplitude across the BLAST bands, once the power spectra are normalized to the sky intensity, are excellent.

The relative variance of the CIB, $\Delta_{k_\theta}^2$, formed by dividing $P(k_\theta)$ by $2\pi k_\theta^2$, is shown in the bottom panel of Figure 4.18, where the 250 μm and 500 μm data have been displaced slightly for visual clarity. (Amplitudes have been additionally converted from arcmin^{-2} to steradian^{-1} in the figure and in the discussion below.) The best fits of Equation 3.36 are shown in Table 4.2. The data are consistent (to within $1-\sigma$) with $\Delta_k^2 = \text{Constant}$, with the same amplitude in all three bands, even taking into account that the error bars shown contain a large component of uncertainty which is common mode between channels, and thus overestimate the anticipated scatter. The best-fit amplitude for a power law with slope of -2 is shown as a dotted line in the bottom panel, corresponding to $\Delta_{k_\theta} = \delta I/I = 15.1 \pm 1.7\%$. This is directly analogous to the square root of the ‘band-power’ measured in Cosmic Microwave Background (CMB) anisotropy experiments, where typically $\delta T/T \sim 10^{-5}$. From this point of view the CIB is much clumpier than the CMB, as one would expect since the galaxies are observed after a much longer period of linear growth. The dotted line in the upper panel of Figure 4.18 is $2\pi k_\theta^2 \Delta_{k_\theta}^2$, corresponding exactly to the fit in the lower panel.

The best-fit values of the parameters ϵ and θ_0 are shown in Table 4.2. The large uncertainty quoted for θ_0 is due partly to the awkwardness of this parameterization near to zero slope. The bottom panel of Figure 4.18 shows the best-fit for 250 μm data as a dashed line. Such a small θ_0 , despite significant power in excess of Poisson noise, requires that the sources which make up the CIB are distributed over a wide range of redshifts, and has implications for future clustering measurement strategies (e.g., with *Herschel* or *Planck*).

4.5.8 Cross-Band Correlations

We have calculated the correlations between different bands (e.g., 250 \times 350) using the same pipeline and set of sub-maps. The cross-spectra are normalized by the square root of the auto-spectra of the two bands, so that the final curve would be unity at all scales for identical maps, and zero at all scales for two completely different maps. Figure 4.19 shows that the cross-correlations are 0.95 ± 0.06 , 1.06 ± 0.09 , and 0.92 ± 0.04 , for 250 \times 350, 350 \times 500, and 250 \times 500, respectively, over the range of angular scales $0.04 < k_\theta < 0.5 \text{ arcmin}^{-1}$. Neighboring bands are more correlated with each other than are the 250 and 500 μm bands. While we find the same spectrum in all three bands, the phases are different, as one would expect if the three BLAST bands have different selection functions and sample the galaxies in the CIB at different redshifts. While the cross-band correlation provides a powerful tool for testing the redshift distributions and spectral energy densities of source population models, a more detailed analysis is required before making any strong conclusions, and is beyond the scope of this thesis.

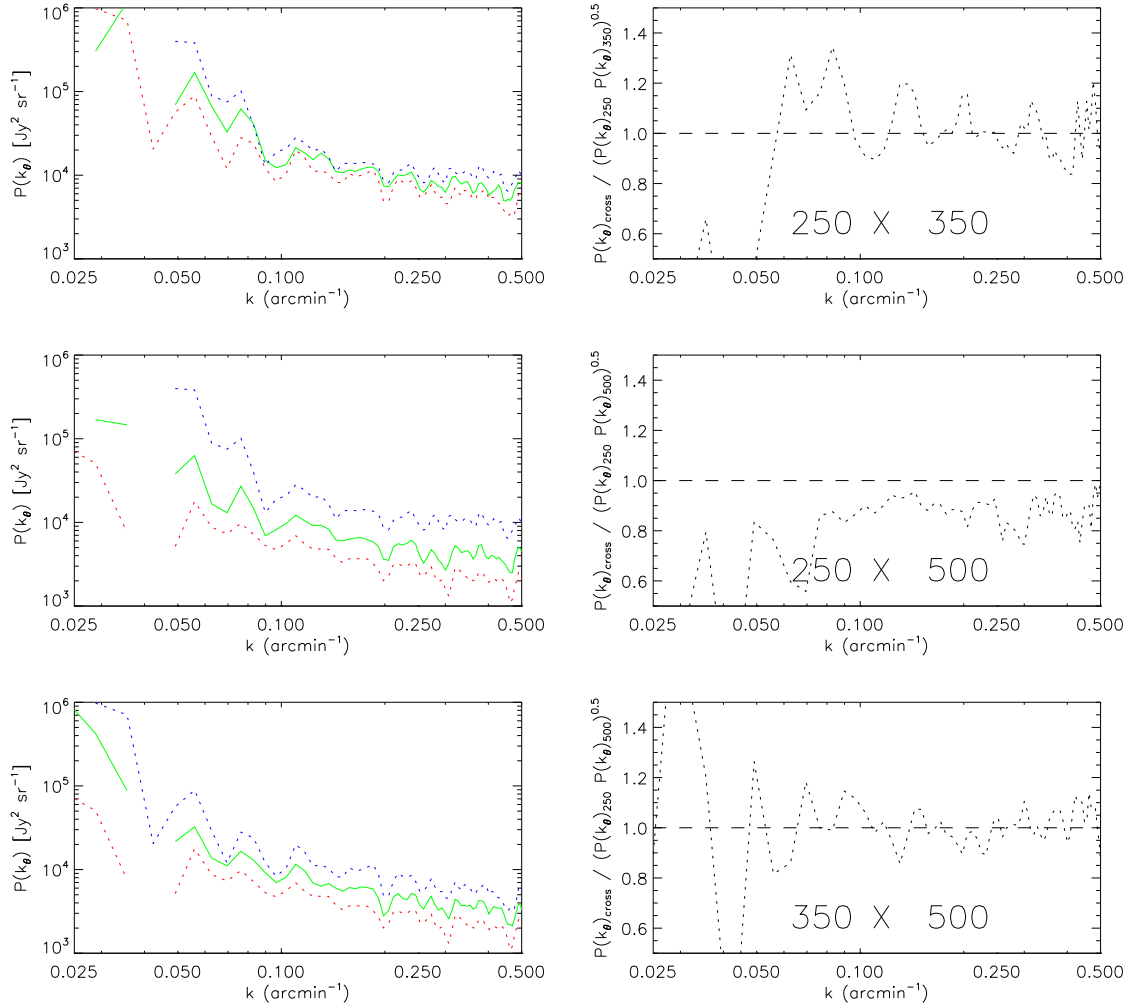


FIGURE 4.19: Original and normalized Cross-Band Correlations of 6 deg² regions selected from the BGS-wide-only maps. Left: Dotted blue and red curves represent the auto-cross-spectra of the first (A) and second bands (B) in each panel, respectively. From top to bottom A=250, 250 and 350, and B=350, 500 and 500. The solid green curve is the cross-band-spectra, i.e., $A \times B$, which falls between the two in each case, signifying a high level of correlation between bands. Right: Same green curve as in right panel, but normalized by $\sqrt{P_A(k_\theta) P_B(k_\theta)}$. Thus, a value of zero would signify no correlations, and a value of unity would signify perfectly correlated (i.e., exactly the same map). The data is very noisy, but it appears there is a high level of correlation between neighbouring maps ($\sim 100\%$), with slightly less in common between the 250 and 500 μ mmaps ($\sim 90\%$).

4.6 Physical Interpretation

To interpret our detection of correlations requires comparison to an underlying model whose parameters the data constrain. Such a model could contain details of the complete source population, including number counts, i.e. intensity distributions, and redshift distributions, as well as a framework for describing the linear and non-linear clustering regimes. This latter part might involve, for example, a halo occupation distribution which accounts for the galaxy distribution in a given dark matter halo as a function of luminosity (i.e., the so-called conditional luminosity function; Cooray, 2006). For a background of primarily unresolved sources, the conditional luminosity function model is an improvement on the simple halo occupation distribution; however, its increase in complexity comes with an increase of free parameters.

Given the very good fit to a constant $\Delta_{k\theta}^2$, we first explore the physical meaning of the BLAST power spectra in the context of a purely linear model. We assume that the galaxies which comprise the CIB have a power spectrum which is scaled from the power spectrum of dark matter at every redshift, $P(k) = b^2 P_{\text{DM}}(k)$. Because P_{DM} is redshift dependent, estimating b^2 requires knowledge of the redshift distribution of the galaxies which comprise the BLAST signals. To find this distribution we adopt the model of Lagache et al. (2004), described in Section 4.6.1. It is worth noting that since we are really measuring an emission-weighted bias at rest-frame far-IR wavelengths, there will be some degeneracy between the value of b and changes in the redshift distribution or far-IR spectral shapes assumed for the sources.

We extend the fit into the non-linear regime to study whether the BLAST data can constrain parameters of the halo occupation distribution. We can check whether our correlations are consistent with the model (e.g., by judging whether the same bias fits all three BLAST wavebands, and that the cross-band correlations of simulations made with the model agree with the data), but we will not explore how the model might be improved. It is important to understand that if the distribution of source redshifts or counts were different, then we would infer a different bias level. However, since the model we've adopted agrees with a large body of multi-wavelength observations, we are confident that these prescriptions are a reasonable first attempt.

4.6.1 Source Population Model

Knowledge of the full redshift distribution of BLAST sources would allow us to estimate the redshift distribution of the measured clustering signal, i.e., the redshift range probed by the power spectrum of correlations due to clustering described by the $P \times dS/dz$ distribution. Devlin et al. (2009), and in more detail Patanchon et al. (2009), find the number counts of the BLAST sources, and Pascale et al. (2009) divides the redshift distribution roughly into four redshift bins. Precisely understanding the redshift distribution of those sources is a work in progress (e.g., Chapin et al., in prep.). In the meantime we adopt the model of Lagache et al. (2004) – a model which approximates the counts and redshift distributions of the populations expected to make up the CIB – to describe the underlying source population⁴. Specifically, it is a phenomenological model which extrapolates the local 60 μm

⁴Documentation and IDL files can be found at <http://www.ias.u-psud.fr/irgalaxies/model.php>

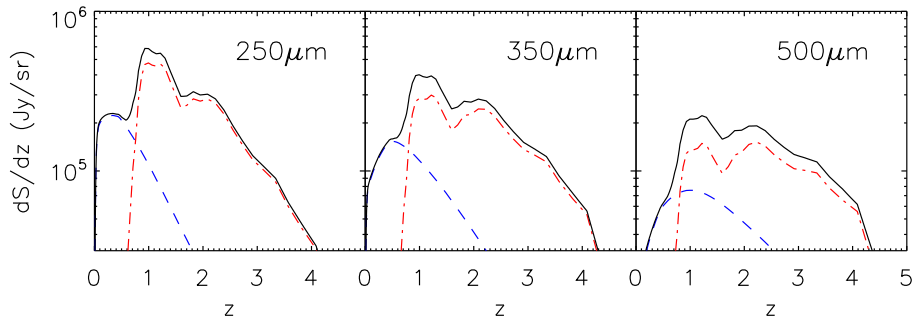


FIGURE 4.20: Redshift distribution of the cumulative flux contributed by the background sources at the BLAST bands, according to the [Lagache et al. \(2004\)](#) model. The dashed (blue) and dot-dashed (red) curves are for ‘regular’ and ‘star-forming’ *IRAS* galaxies respectively, while the solid line is the total. Figure from [Viero et al. \(2009\)](#).

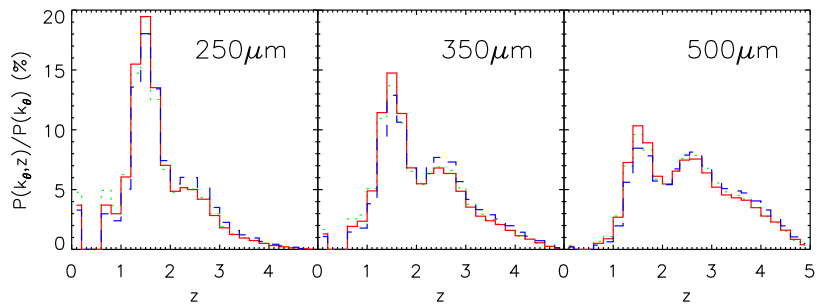


FIGURE 4.21: Contribution to the angular power spectrum from different redshift slices, inferred from Figure 4.20, at specific angular scales probed by the data. The different curves correspond to the following scales: dotted (green) – $k_\theta = 0.04 \text{ arcmin}^{-1}$; solid (red) – $k_\theta = 0.1 \text{ arcmin}^{-1}$; dashed (blue) – $k_\theta = 0.18 \text{ arcmin}^{-1}$. Whereas the redshift distribution of sources (Figure 4.20) has a significant contribution from $z < 1$, the contribution from those sources to the angular power spectrum is negligible. Figure from [Viero et al. \(2009\)](#).

luminosity function of *IRAS* sources (divided into ‘regular’ and ‘star-forming’ components) to longer wavelengths, assuming a set of spectral energy distribution templates. The extrapolation to higher redshift is parameterized as a mixture of luminosity and density evolution, and is constrained to be consistent with most of the available data on source counts, redshift distributions and the far-infrared background intensity. It becomes less reliable with greater extrapolation to longer wavelengths, and therefore should be considered an approximation; however, it does reproduce the BLAST ([Patanchon et al., 2009](#)) counts at a level which is sufficient for our purposes. Furthermore, since the clustering signal is dominated by the faint source population, it is critical that the model is consistent with the level of the background at the BLAST wavelengths, and that the cross-band correlations of simulated maps agree with those measured, which we find to be the case.

Most of the clustering signal is coming from relatively high redshifts. The medians of the redshift distributions in Figure 4.21 are $z = 1.61, 1.88$ and 2.42 , at $250, 350$ and $500 \mu\text{m}$, respectively, and

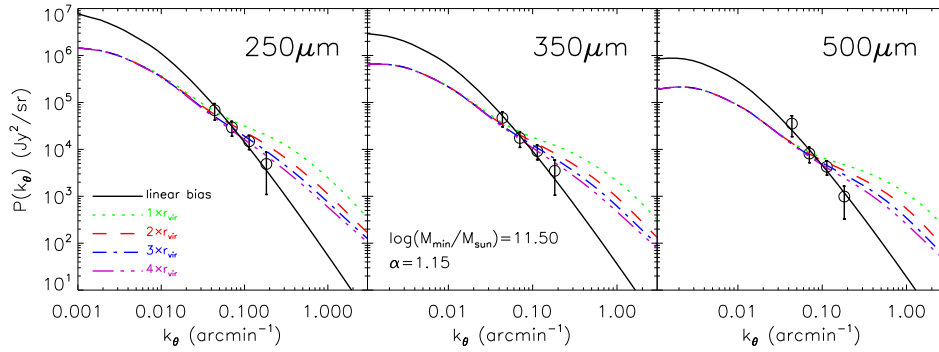


FIGURE 4.22: Power spectrum of background correlations (circles with error bars) overlaid with the best-fit linear bias (solid line), as well as predictions obtained for halo models different values of r_{cut} . See Table 4.3 for the fit parameters. Although the power spectra shown here have different amplitudes in the three channels, $P(k_\theta)/I_\nu$ is the same in all three bands, as shown in Figure 4.18. The data are fit best by a model which includes a linear term only. Figure from Viero et al. (2009).

the upper and lower quartiles of the distributions are $z = (1.3, 2.2)$, $(1.5, 2.7)$, $(1.7, 3.2)$, respectively. At the representative scale of 0.1 arcmin^{-1} (red solid line in Figure 4.21), 95% of the background originates from sources $1.1 < z$, $1.2 < z$, and $1.4 < z$ in the three bands.

4.6.2 Linear Bias Model

We first carry out a simple fit to a scaled version of the linear theory power spectrum of the dark matter P_{DM} . As can be seen in Figure 4.22, a simple biasing prescription provides a good fit to the BLAST data. The required bias levels are $b = 3.8 \pm 0.6$, 3.9 ± 0.6 , and 4.4 ± 0.7 at 250, 350 and 500 μm , respectively, with a reduced $\chi_{\text{min}}^2 \sim 0.4$ (with 10 degrees of freedom) in all three bands.

More detailed modelling could be attempted. In principle the cross-band measurements and wavelength dependence of the measured correlation amplitudes could be used to estimate the variation of bias with redshift, as discussed by Knox et al. (2001). However, we leave this to a future study.

4.6.3 Halo Model

As illustrated in Figure 4.22, a simple biasing prescription provides a good fit to our data. The main drawback of this simple fit is that it may not realistically account for the 1-halo, nonlinear clustering component. Our data are expected to bracket the physical scales corresponding to the transition from linear to non-linear clustering regimes, and though these two contributions appear to have combined to look very much like a scaled linear bias, to conclude that there is no contribution from a 1-halo term may be unphysical. Therefore, in this section we use a particular implementation of the ‘halo model’, which assigns galaxies to halos as a function of mass, and consequently probes into the territory of non-linear fluctuations, to explore how the 1-halo term could contribute power

on small scales. This also allows us to discuss our results in the context of other measurements of galaxy clustering.

$r_{\text{cut}}/r_{\text{vir}}$	χ_{min}^2	$\log(M_{\text{min}}/M_{\odot})$	α
1	16.3	$11.50^{+0.40}_{-0.05}$	$0.95^{+0.05}_{-0.95}$
2	13.6	$11.50^{+0.40}_{-0.05}$	$1.00^{+0.10}_{-1.00}$
3	11.5	$11.50^{+0.40}_{-0.05}$	$1.10^{+0.05}_{-1.10}$
4	9.7	$11.50^{+0.40}_{-0.05}$	$1.15^{+0.05}_{-0.75}$

TABLE 4.3: Best-fit values obtained for M_{min} and α for different choices of the radius r_{cut} . The minimum- χ^2 (with 10 degrees of freedom) are also shown.

Our model has two free parameters, M_{min} and α , which we vary through $0 \leq \alpha \leq 2$ and $10 \leq \log(M_{\text{min}}/M_{\odot}) \leq 16$, with steps of 0.05 in both $\log M$ and α . The best-fit values of the parameters are determined through a χ^2 minimization technique by fitting the observed power spectrum at each of the three BLAST bands simultaneously.

Throughout we assume that both M_{min} and α remain constant in time, although in principle they are functions of redshift. Whether these parameters evolve with redshift would be difficult to constrain from our data alone; nevertheless, our assumption is consistent with what is observed for other classes of high-redshift sources (e.g., quasars, see [Porciani et al., 2004](#)). For each $M_{\text{min}}-\alpha$ pair, the mass-scale M_1 is fixed by requiring that at every redshift, z , the number density of the background sources derived from the halo model formalism matches that predicted by the adopted source-population model, i.e.,

$$\int_0^{\infty} \frac{dN}{dS dz}(S, z) dS = n_{\text{gal}}(z) dV_c(z). \quad (4.13)$$

4.6.4 Halo Model Fits

Under the assumption that the dark matter halos are described by an NFW profile truncated at the virial radius, i.e., where $r_{\text{cut}} = r_{\text{vir}}$, and that galaxies within the halo trace the underlying dark matter distribution, the best fit to the observed angular power spectrum gives $\log(M_{\text{min}}/M_{\odot}) = 11.5^{+0.4}_{-0.1}$ and $\alpha \leq 1.0$, with $\chi_{\text{min}}^2 = 16.3$ with 10 degrees of freedom; i.e., the model is marginally consistent at the $2\text{-}\sigma$ level.

While this model is not formally ruled out by the data, as shown by a dotted line in [Figure 4.22](#), it poorly reproduces the shape of the observed power spectrum, which exhibits a steeper slope. If we were to weight this model to fit the large scale power spectrum (e.g., $k \lesssim 0.08 \text{ arcmin}^{-1}$), then it would over-predict the power on small scales. Arguing that perhaps the model describes the small scale, 1-halo term correctly, but is under-predicting the large-scales, is not a good description because: (i) the 2-halo term is less sensitive to the underlying assumptions than the 1-halo term (for a discussion see [Tinker et al., 2009](#)); and (ii) the observed small-scale power spectrum is still too steep to be accounted for by the shallower 1-halo term. Another possibility is that the redshift distribution of the background cumulative flux predicted by the adopted source count model is incorrect. In order

z	M_1/M_\odot
0.010000	8.852426e+13
0.050000	2.287658e+12
0.100000	2.004142e+12
0.200000	1.640854e+12
0.400000	1.212545e+12
0.600000	9.810376e+11
0.800000	6.540657e+11
1.000000	4.712985e+11
1.200000	4.179639e+11
1.400000	3.961268e+11
1.600000	3.580811e+11
1.800000	2.721604e+11
2.000000	2.159460e+11
2.200000	1.669856e+11
2.400000	1.381190e+11
2.600000	1.150687e+11
2.800000	9.602077e+10
3.000000	7.802615e+10
3.200000	6.137227e+10
3.400000	4.966518e+10
3.600000	4.146160e+10
3.800000	3.346902e+10
4.000000	3.091198e+10
4.200000	2.945345e+10
4.400000	2.791823e+10
4.600000	2.463084e+10
4.800000	2.078349e+10
5.000000	1.714020e+10

TABLE 4.4: Best-fit values obtained for M_1 given $M_{\min} = 2.238721 \times 10^{11} M_\odot$ and $\alpha = 0.95$. M_1 becomes smaller than M_{\min} at $z \gtrsim 2$, meaning that at higher redshifts, in order to match the abundance of sources predicted by the source population model, halos begin to be populated with two, three or more sources right away.

to reproduce the observed shape of the angular power spectrum, the bulk of the background would have to originate from sources at $z < 1$, which is ruled out by [Devlin et al. \(2009\)](#), [Marsden et al. \(2009\)](#), and [Pascale et al. \(2009\)](#). However, a full investigation of the leeway in changing the redshift distribution (and degeneracies with other changes to the model) are beyond the scope of the present study.

In light of this, we explore the possibility that the discrepancy between the predicted power spectrum and the observed one is related to the modelling of the 1-halo term. There are two obvious ways to modify the shape and normalization of the 1-halo power spectrum. One is to allow the dark matter halos, although still following an NFW profile, to be truncated at a scale $r_{\text{cut}} > r_{\text{vir}}$. Thus, satellite galaxies are distributed over a larger volume. This idea is not new; [Magliocchetti & Porciani \(2003\)](#) find that in order to adequately fit the 1- and 2- halo term to the 2dF Galaxy Redshift Survey data-set it is necessary that the satellite galaxies are allowed to reside out to 2 times the virial

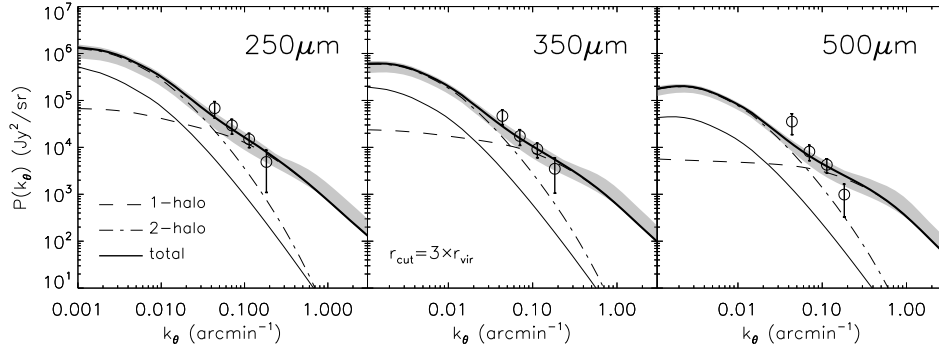


FIGURE 4.23: Power spectrum of background correlations from clustering of extra-galactic sources measured in the BLAST maps (circles with error bars) overlaid with the best-fit halo model (thick solid line), under the assumption that dark matter halos are NFW spheres truncated to $3 \times$ the virial radius, and the galaxies within the halo follow the underlying dark matter distribution. The shaded region shows the 99% confidence region in the M_{\min} – α parameter space. The dashed and the dot-dashed curves show the 1- and 2-halo contributions to the power spectrum, respectively. For comparison, the power spectrum obtained under the assumption that galaxies are unbiased tracers of the underlying dark matter distribution, i.e., $P_{3D}(k, z) = P_{DM}(k, z)$, is plotted as a lighter solid line. According to the model, the BLAST data occupy a range of angular scales which should be sensitive to both the linear and non-linear clustering terms. Figure from [Viero et al. \(2009\)](#).

radius. Furthermore, from semi-analytic models [Diaferio et al. \(1999\)](#) show that blue (and hence star-forming) galaxies tend to reside in the outskirts of their host halos, while red galaxies are found closer to the halo center.

The second possibility is that the distribution of galaxies within the halos does not follow that of the underlying dark matter. For example, a power-law distribution $\rho(r) \propto r^{-\gamma}$ with $\gamma < 2$ would make the 1-halo angular power spectrum steeper than that predicted by an NFW profile. Similar arguments have been made by [Watson et al. \(2009\)](#), who found that by allowing the inner slope of the density profile to vary, they fit the small-scale clustering of luminous red galaxies quite well.

Here we only explore the first possibility, examining $r_{\text{cut}} = 1, 2, 3,$ and $4 \times r_{\text{vir}}$. The results are shown in Figure 4.22, and summarized in Table 4.3. The best-fit model angular power spectrum for the case $r_{\text{cut}} = 3 \times r_{\text{vir}}$ is shown in Figure 4.23, while the corresponding HON and large-scale effective bias are shown in Figure 4.24. Note that while the value of the reduced χ_{min}^2 approaches unity for increasing values of r_{cut} , the best-fit values of M_{\min} are negligibly affected by the changes, while α only marginally increases with increasing r_{cut} . The effective mass of the halo, M_{eff} , is the weighted mean over the halo-mass distribution:

$$M_{\text{eff}}(z) = \int_{\mathcal{M}} n_{\text{halo}}(M, z) N(M, z) M dM / n_{\text{gal}}(z). \quad (4.14)$$

The results for the large-scale effective bias b , and mass $\log(M/M_{\odot})$, at the respective medians of the redshift distributions of the sources contributing to the background in each band (see Figure 4.21) are $2.2 \pm 0.2, 2.4 \pm 0.2,$ and 2.6 ± 0.2 , and $12.9 \pm 0.3, 12.8 \pm 0.2,$ and 12.7 ± 0.2 , at 250, 350 and

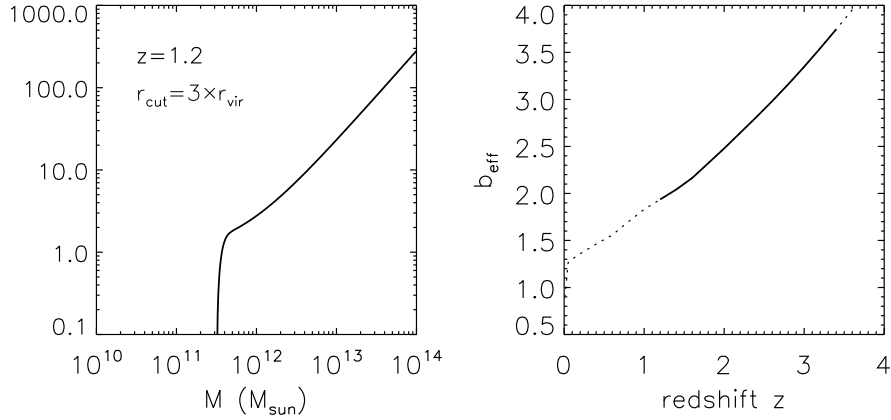


FIGURE 4.24: *Left-hand panel:* Halo Occupation Number (HON) as a function of the mass of the halo at a representative redshift $z \sim 1.2$, assuming the best-fit values $M_{\min} = 10^{11.5} M_{\odot}$ and $\alpha = 0.95$. *Right-hand panel:* Redshift dependence of the large-scale effective bias, resulting from the best fit to the observed power spectrum of correlations due to clustering. The redshift interval over which 68% of the signal originates, $0.7 \lesssim z \lesssim 2.5$, is shown as a thick solid curve. Figure from Viero et al. (2009).

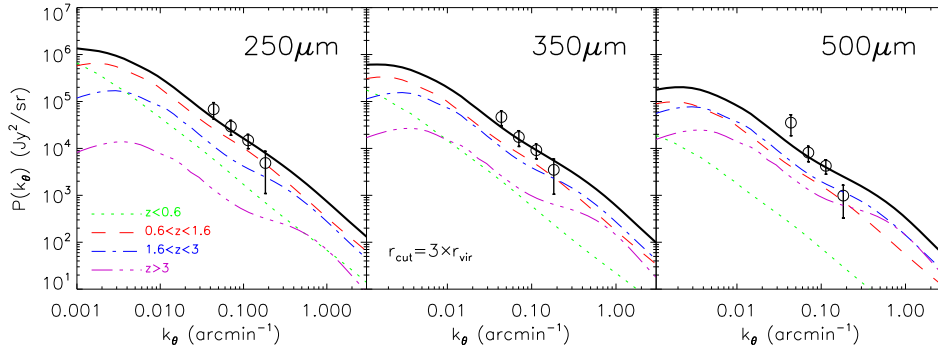


FIGURE 4.25: Contributions to the total clustering power spectrum from sources in increasing redshifts slices. BLAST measurements and the best fit to the halo model (with $r_{\text{cut}} = 3 \times r_{\text{vir}}$) are shown as circles with error bars and a solid line, respectively. Overlaid are the contributions from: dotted line (green), $0 < z < 0.7$; dashed line (red), $0.7 < z < 1.5$; dot-dashed line (blue), $1.5 < z < 3.0$; and triple-dot-dashed line (magenta), $z > 3$. It is clear that at $250 \mu\text{m}$, the bulk of the signal comes from galaxies in the redshift range $0.7\text{--}1.5$, and that the contribution from galaxies in the redshift range $1.5\text{--}3.0$ increases with increasing wavelength. Figure from Viero et al. (2009).

$500 \mu\text{m}$, respectively. They are minimally affected by the change in r_{cut} , changing by less than 8% for the bias, and 3% for the mass, over the full range of r_{cut} explored.

Figure 4.25 shows the contribution to the total clustering power spectrum from sources in different redshift slices, within the assumed source population model. As expected, the power is dominated by the contribution from sources in the range $0.7 < z < 1.5$, with an increasing contribution from sources at $z = 1.5\text{--}3.0$ for increasing wavelengths, as is expected from Figure 4.21. This is consistent with the findings of Devlin et al. (2009); Marsden et al. (2009); and Pascale et al. (2009), who through

stacking show that of the sources making up the CIB, the fraction at $z > 1.2$ increases from 40% at $250 \mu\text{m}$, to 50% and 60% at 350, and $500 \mu\text{m}$.

Finally, we can use the model to interpret the clustering in terms of a 3D spatial correlation length, r_0 . To do that, we Fourier transform the best-fit power spectrum to find the spatial correlation function, $\xi(r)$, from which r_0 is then simply the linear comoving scale at which the correlation function equals 1 at each redshift. This is a model-dependent approach to estimating r_0 , and as such should be considered an approximation. The more typical approach, which involves finding the angular correlation length, the redshift distribution, and de-projecting the signal by inverting the Limber equation, would result in very large uncertainties. The model-dependent r_0 is only mildly sensitive to the choice of r_{cut} , varying by 10% over the full range. The model-dependent values for r_0 are illustrated in Figure 5.1 as a solid line with a shaded area representing $3\text{-}\sigma$ uncertainties. The three BLAST points are plotted at the flux-weighted median redshifts of the unique redshift distributions probed by the three bands (i.e., the distributions shown in Figure 4.20), and should not be interpreted as the locations of all the sources contributing power in those bands. At these effective redshifts, (i.e., $z = 1.60, 1.86$ and 2.15), we find $r_0 = 4.9, 5.0$, and $5.2 \pm 0.6 h^{-1} \text{ Mpc}$ at 250, 350 and $500 \mu\text{m}$, respectively.

4.7 Conclusion

We report the detection of correlations in excess of Poisson noise in the CIB, over scales of approximately 5–25 arcmin, with BLAST at 250, 350, and $500 \mu\text{m}$, at a level with respect to the CIB of $\Delta I/I = 15.1 \pm 1.7\%$.

The CIB is made almost entirely out of individual sources distributed over a wide range of redshifts. We find that within the context of a reasonable model for the source population, the signal originates from galaxies in the redshift ranges $1.3 \leq z \leq 2.2$, $1.5 \leq z \leq 2.7$, and $1.7 \leq z \leq 3.2$, with median redshifts $z = 1.61, 1.88$ and 2.42 , at 250, 350 and $500 \mu\text{m}$, respectively. Fitting to the linear theory power spectrum, we find that the BLAST galaxies responsible for the CIB fluctuations have a bias parameter, $b = 3.8 \pm 0.6, 3.9 \pm 0.6$ and 4.4 ± 0.7 .

We further interpret our results in terms of the halo model. We find that the simplest prescription does not fit very well. One way to improve the fit is to increase the radius at which we artificially truncate dark matter halos to well outside the virial radius. This may imply that the star-forming galaxies that we are seeing at $z \sim 1$ are preferentially found in the outskirts of groups and clusters. This is consistent with related phenomena that have been observed at other wavelengths (Magliocchetti et al., 2004; Marcillac et al., 2007), as well as in simulations (Diaferio et al., 1999).

For a HOD with ‘satellite’ galaxies occupying halos out as far as $r_{\text{cut}} = 3r_{\text{vir}}$, we find parameters $\log(M_{\text{min}}/M_{\odot}) = 11.5_{-0.1}^{+0.4}$, and $\alpha = 1.1_{-0.1}^{+0.8}$, resulting in effective biases $b_{\text{eff}} = 2.2 \pm 0.2, 2.4 \pm 0.2$, and 2.6 ± 0.2 , and effective masses $\log(M_{\text{eff}}/M_{\odot}) = 12.9 \pm 0.3, 12.8 \pm 0.2$, and 12.7 ± 0.2 at 250, 350 and $500 \mu\text{m}$, corresponding to spatial correlation lengths of $r_0 = 4.9, 5.0$, and $5.2 \pm 0.7 h^{-1} \text{ Mpc}$, respectively.

In the context of the model, we see that star formation is highly biased at $z \gtrsim 1$, unlike in the local Universe, where analogous galaxy populations, such as *IRAS* galaxies, are found to be mildly anti-biased (e.g., $M_{\text{eff}} \lesssim 10^{11} M_{\odot}$ and $b = 0.86$, [Saunders et al., 1992](#)).

We find relatively small values for θ_0 , further confirming that the sources which make up the CIB are distributed over a wide range of redshifts, which has implications for planning future submillimeter clustering measurements. For example, as [Knox et al. \(2001\)](#) have argued, to match the precision of the bias measurement made from correlations in the background by using discrete sources will be very challenging. To achieve $\sim 5\%$ accuracy would effectively require thousands of sources with exact redshifts, over tens of square degrees. When redshifts are only approximately known, this increases to hundreds of thousands of sources over hundreds of square degrees, which is only possible with instruments whose beams are smaller than 5 arcsec. Thus, while measuring the clustering from resolved sources has numerous advantages – for example studying the clustering properties of a subset of galaxies – accurately measuring the large scale bias is best achieved through correlation analysis of the background fluctuations. This will be a focus of future studies with BLAST, as well as with the *Herschel* and *Planck* satellites, and the ground based AzTEC and SCUBA-2 cameras.

Chapter 5

Discussion, Conclusion, and Future Work

5.1 Clustering in Context

The large-scale structure of the Universe has long fascinated cosmologists and astronomers alike. Until dark matter detectors are invented, measuring the large-scale distribution of matter in the Universe will depend on indirect methods, such as: the redirection of light by deep potential wells (i.e., very massive dark matter halos) in the form of strong and weak lensing (e.g., [Bartelmann & Schneider, 2001](#); [Refregier, 2003](#); [Munshi et al., 2008](#)); or by hot gas in halo centers giving CMB photons a kick, a process known as the Sunyaev-Zel'dovich effect ([Sunyaev & Zeldovich, 1972](#)); or by the use of galaxies as tracers of the dark matter distribution. The latter has a rich history (e.g., [Groth & Peebles, 1977](#); [Blumenthal et al., 1984](#); [Davis et al., 1985](#); [Peacock et al., 2001](#); [Abazajian et al., 2005](#)), and has been the primary focus of this thesis as well.

In addition, the spatial distribution of galaxies appears to reveal several properties of the galaxies themselves. For example, most famously “red and dead” galaxies cluster more strongly than blue galaxies (e.g., [Guzzo et al., 1997](#)), a consequence of their advanced age; meaning that halos which were large enough to seed galaxies at such early times were themselves clustered over-densities in the dark matter distribution. Furthermore, it appears evident that the the sights of star formation have evolved from highly biased regions at redshifts > 1 , as shown in § 4.6, to anti-biased in the local Universe (e.g., [Saunders et al., 1992](#)). Finally, as shown in § 4.6.4, the locations of star formation within halos appears to be still uncertain, as we show that the centers of massive halos may not favour star formation. Clearly, the spatial distribution of galaxies has much to add to the understanding of galaxy formation and evolution.

Historically, measuring the spatial distribution of galaxies in the submillimeter has not been easy (e.g., [Scott et al., 2006](#)). Due to negative K-correction, (sub)mm bands are sensitive to sources over a wide range of redshifts, which results in diluting the clustering signal and overwhelming the sky

with faint sources ($\sim 15 \text{ arcmin}^{-2}$). Meanwhile, relatively large beams ($\sim 15''$ for SCUBA, $36''$ for BLAST) blend all of these faint sources together, and boosts the flux of the occasional bright source. The end result is that it is very difficult to say which “source” is a source, and which galaxy it corresponds to (e.g., § 3.2.2.2). For these reasons, and also due to a lack of data, the submillimeter community has been largely unable to measure the clustering of galaxies.

Here we have measured the clustering properties of star-forming galaxies at submillimeter wavelengths. We accomplished this by measuring correlations, in excess of Poisson, of the CIB power spectrum, rather than the correlation function of galaxies in a catalog. We determined how star-forming galaxies, in the peak epoch of star and galaxy formation, trace the dark matter distribution, and along the way found some tantalizing hints about the nature of the galaxies themselves. On large scales, we measured the bias, and found estimates for the effective mass of host dark matter halos, M_{eff} , and the minimum mass of halos which will host a galaxy, M_{min} . On small scales, we found that we were unable to adequately fit a halo model to the seemingly power-law behaviour of the data. This suggested that the galaxies that BLAST is sensitive to, primarily star-bursting LIRGS and ULIRGS at $z \sim 1 - 3$, may not trace the dark matter in a simple way.

We will now explore how these results fit into the larger picture. First, we’ll compare the clustering strength of BLAST galaxies to other star-forming populations. Next, we will ask, according to N-body simulations, how do the typical halos which host the BLAST galaxies evolve forward and backwards in time. We will use that to explore possible evolutionary links to galaxy populations earlier and later in cosmic history. Finally, we will explore possible explanations for the measured clustering behaviour of BLAST galaxies on small scales, and propose future measurements with *Herschel*, *Planck*, and SCUBA 2.

5.2 Comparison with other observations

Comparisons must be made with care because the models used to derive the parameters in question vary. Consequently, although these parameters may go by the same name (e.g., ‘bias’), they may not refer to the same thing exactly. Additionally, for a subset of sources, whether distinguished by galaxy type, mass, luminosity, or flux density, these parameters may be different. In physically motivated halo models, these parameters will typically be a function of halo-mass and redshift, but are usually quoted in literature as a single value. In particular, the bias parameter is commonly reported as either: b_{eff} , the effective bias parameter, which is the weighted mean over the halo-mass distribution and the redshift distribution of the cumulative flux; or b , the redshift-independent bias parameter, which only considers the 2-halo term, and may be expressed as the square root of the ratio of the galaxy and dark matter power spectra, $P(k) = b^2 P_{DM}(k)$. Furthermore, b may be expressed as the ratio of the emissivity and dark matter density fluctuations, $\delta j/\bar{j} = b \delta\rho/\bar{\rho}$; or the square root of the ratio of the galaxy and dark matter correlation functions, $\xi(r) = b^2 \xi_{DM}(r)$. In particular, some variations of the bias parameter commonly reported in literature include: i) $b(M, z)$, the linear bias parameter, which is a function of halo-mass and redshift; ii) b_{eff} , the effective bias parameter, which is the weighted mean over the halo-mass distribution of galaxies, and is a function of redshift, but is typically quoted b_{eff} after weighting over dS/dz ; and iii) b , the redshift independent bias, which

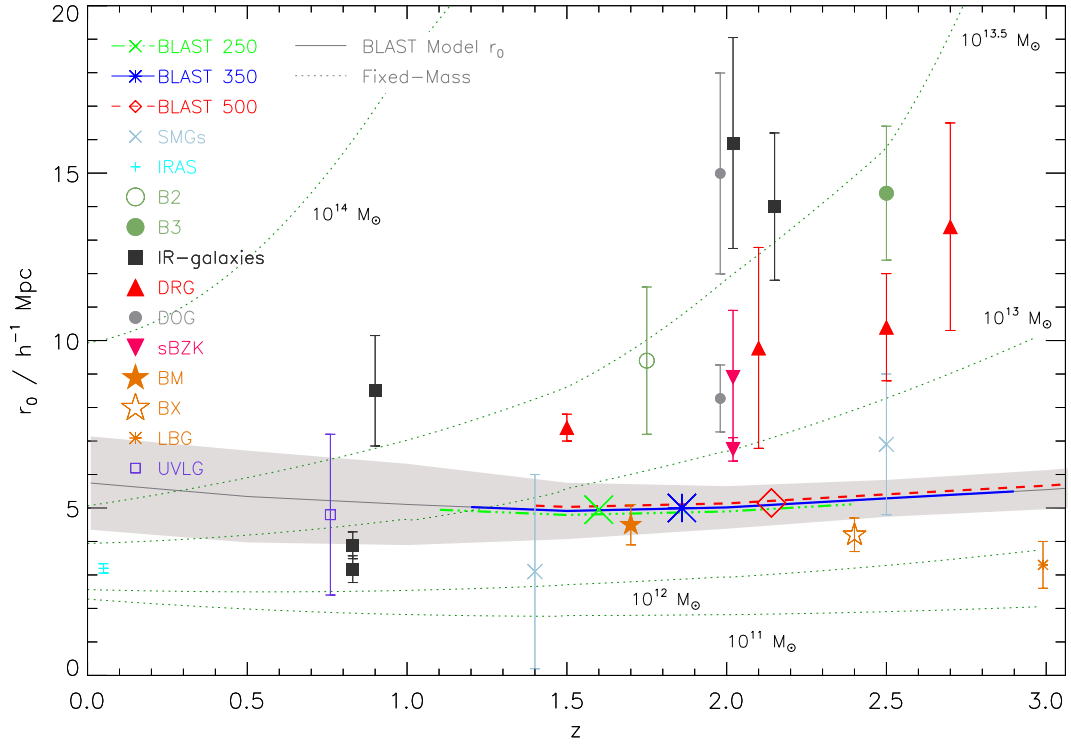


FIGURE 5.1: Comoving correlation length vs. redshift for star-forming galaxies selected with a variety of techniques. Other data taken from: IRAS – Saunders et al. (1992); SMG – Webb et al. (2003); Blain et al. (2004); B2 and B3 – Farrah et al. (2006); IR – Magliocchetti et al. (2007, 2008); Gilli et al. (2007); DRG – Grazian et al. (2006); Quadri et al. (2008); DOG – Brodwin et al. (2008); BzK – Blanc et al. (2008); Hartley et al. (2008); BM and BX – Adelberger et al. (2005); LBG – Giavalisco et al. (1998); Adelberger et al. (2005); and UVLG – Basu-Zych et al. (2009). The dotted fixed mass lines show the predicted clustering lengths of halos of a given mass at a given redshift, found with the *Millennium Simulation* (Springel et al., 2005). The model-dependent BLAST values for r_0 are shown as a solid line with a shaded area representing $3\text{-}\sigma$ uncertainties. The three BLAST points are plotted at the median redshifts of the distributions from which the signal originates (i.e., the distributions shown in Figure 4.21). The ranges from which 90% of the power originates are illustrated as corresponding colored lines. In the context of the model, the clustering strength of BLAST galaxies is compatible with the Webb et al. (2003) and Blain et al. (2004) estimates for clustering of submillimeter galaxies, but less strong than the that of other resolved populations of galaxies. Figure from Viero et al. (2009).

also only considers the 2-halo term. Furthermore, the bias of a subset of sources, whether by galaxy type, mass, luminosity, or flux density, may be different from the bias of the whole. Lastly, on small scales (described by the 1-halo term), the bias parameter is scale dependent.

Nevertheless it is interesting to put our measurements into the context of the large body of literature on the clustering of galaxies selected in different ways, in order to understand how they might be related. In Figure 5.1 we compare the correlation lengths vs. redshift of star-forming populations selected using a wide variety of techniques. It should be noted that in some cases these techniques select overlapping populations (see Reddy et al., 2005, for a nice discussion on the overlap between color

selected samples). This list is by no means exhaustive, and is meant only to be an illustration. The reported values of r_0 were converted assuming a fixed slope $\gamma = 1.8$, such that $r_{0,1.8} = (r_{0,\gamma})^{-\gamma/1.8}$. The BLAST best-fit model estimates are shown as a line and shaded $3\text{-}\sigma$ confidence region. The three BLAST points are located at the median locations of their respective redshift distributions (Figure 4.21). In addition, the simulated clustering lengths of dark matter halos of given mass and redshift are measured from the *Millennium Simulation*⁵ (Springel et al., 2005), by fitting a single power-law with slope of -1.8 to the correlation function, and are shown as dotted lines.

It is immediately clear that the galaxies which make up the background are not as strongly clustered as the more luminous sets of resolved sources (with the exception of those identified by their Lyman break, i.e., LBG, as well as optically selected BM/BX). Furthermore, the strength of the clustering increases with increasing luminosity (e.g., Gilli et al., 2007; Brodwin et al., 2008). Since each of the techniques used to select the populations of galaxies that lie above the BLAST lines has an IR component, it is tempting to conclude that all of these populations contribute to the total submillimeter CIB. The relative contribution of each of these populations could be explored through stacking, as Marsden et al. (2009) have done for BzKs. They found that although the BzKs make up about a quarter of the sources which completely resolve the CIB, they contribute $\sim 32\%$, $\sim 34\%$, and $\sim 42\%$, at 250, 350, and 500 μm , to the total BLAST intensity. This indication that the resolved sources pick out parts of the background highlights the complementary nature of the clustering measurements of the CIB and resolved sources in forming a complete picture of the environments of star-forming galaxies.

Although the correlation length of the background galaxies appears to change very little with redshift, the bias is a strong function of redshift (see Figure 4.24). While both the bias and the correlation length are indicators of galaxy clustering, their behaviour is not in contradiction because the clustering strength of the host dark matter halos is rapidly increasing with decreasing redshift as well, thus in this sense, it is the bias that is a more telling description of how star formation relates to structure formation. This strong evolution of the bias is in agreement with Lagache et al. (2007), who found a redshift-independent linear bias parameter of $b \sim 3.5$ at $z \sim 1$, for the sources which make up the CIB at 160 μm ⁶, and our result of $b \simeq 4$ for galaxies which lie at higher redshifts (see Section 4.6.2). Thus, in the scenario of a strongly evolving bias parameter (e.g., Figure 4.24), from anti-biased in the local Universe, to highly biased at $z \sim 1$ and beyond (e.g., Sheth et al., 2006; Elbaz et al., 2007), our result is consistent.

5.3 Clustering Evolution

To roughly explore the clustering histories of BLAST-like host dark matter halos, we follow Farrah et al. (2006) and adopt a simple model which parameterizes the spatial correlation function, ξ , as a

⁵Note that Millennium Simulation cosmology is $\sigma_8 = 0.9$ and $\Omega_M = 0.25$, which has a minimal impact on the prediction. Catalogues can be found at <http://www.mpa-garching.mpg.de/Millennium>

⁶Note that the value $b = 1.7$ reported in Lagache et al. (2007) is for $\sigma_8 = 1.1$, and not $\sigma_8 = 0.8$, as quoted in the text. The correct value of the measured bias parameter is 2.4 ± 0.2 (Lagache, private communication). Furthermore, due to a $(1+z)^2$ difference in formalism, their bias in our notation is $b = 3.5$.

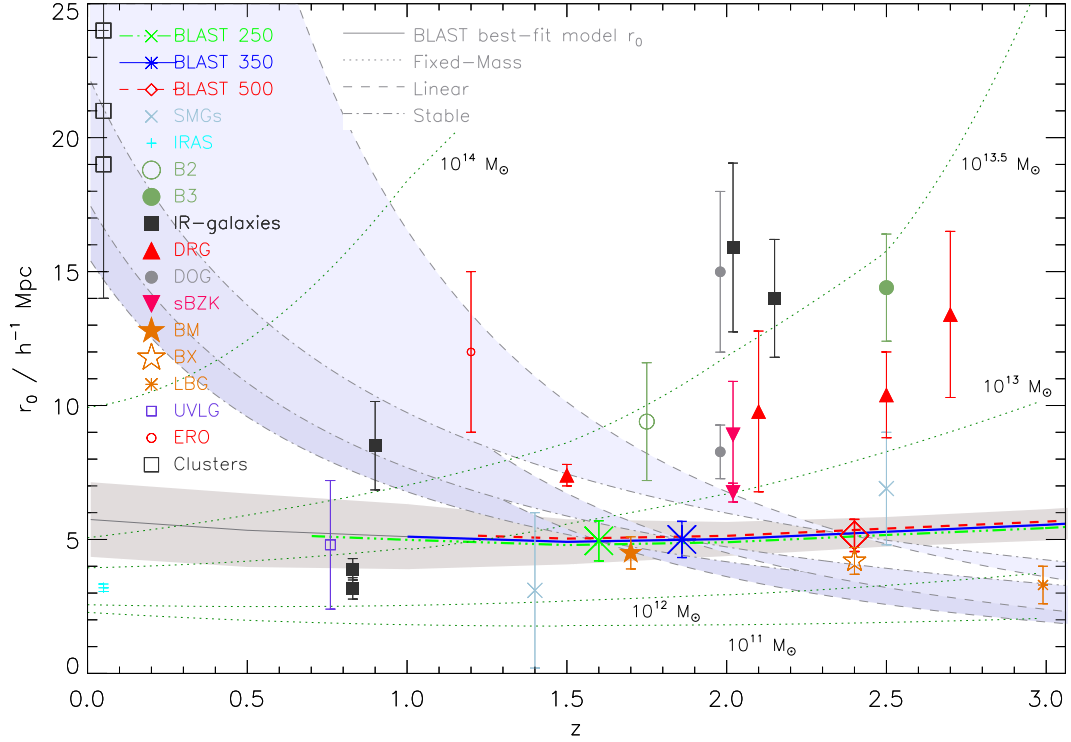


FIGURE 5.2: Comoving correlation length vs. redshift for star-forming galaxies selected with a variety of techniques. Other data taken from: IRAS – Saunders et al. (1992); SMG – Webb et al. (2003); Blain et al. (2004); B2 and B3 – Farrah et al. (2006); IR – Magliocchetti et al. (2007, 2008); Gilli et al. (2007); DRG – Grazian et al. (2006); Quadri et al. (2008); DOG – Brodwin et al. (2008); BzK – Blanc et al. (2008); Hartley et al. (2008); BM and BX – Adelberger et al. (2005); LBG – Giavalisco et al. (1998); Adelberger et al. (2005); UVLG – Basu-Zych et al. (2009); ERO – Daddi et al. (2001) and Clusters – Bahcall & Soneira (1983); Lahav et al. (1989); Dalton et al. (1994). The dotted fixed mass lines show the predicted clustering lengths of halos of a given mass at a given redshift, found with the *Millennium Simulation* (Springel et al., 2005). The model-dependent BLAST values for r_0 are shown as a solid line with a shaded area representing $3\text{-}\sigma$ uncertainties. The three BLAST points are plotted at the median redshifts of the distributions from which the signal originates (i.e., the distributions shown in Figure 4.21). The ranges from which 90% of the power originates are illustrated as corresponding colored lines. Simple models for the evolution of clustering strength are described in the text, and shown here as dashed lines for the “Linear” model, and dot-dashed lines for the “Stable” model. According to these simple models, the clustering properties of LBGs and BM/BX galaxies will evolve to have similar clustering properties as BLAST galaxies at later times. Although it is enticing to attempt to draw a connection, really this plot should be remade to incorporate number densities before any conclusions are drawn, as discussed in the text.

power law in comoving coordinates,

$$\xi(r, z) = \left(\frac{r}{r_0}\right)^{-\gamma} (1+z)^{\gamma-(3+\epsilon)}, \quad (5.1)$$

where ϵ determines the redshift evolution (Overzier et al., 2003). We explore the range bracketed by the ‘stable’ clustering model ($\epsilon = 0$; where clusters have fixed physical sizes, so that the expansion

of the background mass distribution increases the apparent clustering strength of the halos) and the ‘linear’ clustering model ($\epsilon = 1$; where clustering grows as expected under linear perturbation theory), and plot this as shaded regions in Figure 5.2.

It appears that halos similar in mass to those that host LBGs at $z \sim 3$, BXs at $z \sim 2.4$, and BMs at $z \sim 1.7$ evolve into halos with similar mass and clustering properties as those which host BLAST galaxies. While this is certainly intriguing, it is difficult to reconcile with number density arguments. From Adelberger et al. (2005), we see that LBGs have number densities of $n_{LBG} = (4 \pm 2) \times 10^{-3} h^3 \text{ Mpc}^{-3}$ over the redshift range $z \sim 2.6 - 3.3$; and from Tacconi et al. (2008) BM/BXs have number densities of $n_{BM/BX} = (1.1 \pm 0.3) \times 10^{-4} h^3 \text{ Mpc}^{-3}$ over the redshift range $z \sim 1.4 - 2.5$. If these galaxies are or eventually become BLAST galaxies, then in the rough redshift range of $z \sim 1.5 - 2.5$, $n_{BLAST} \approx (2.8 \pm 0.4) \times 10^{-4} h^3 \text{ Mpc}^{-3}$, which slightly overestimates the BM/BXs, and severely underestimates the LBGs, by about a factor of 4. The overestimation of the BM/BX may just be a product of the choice of flux cut. For example, the number density can be matched if only considering BLAST galaxies with flux greater than 1.5 mJy, i.e., $n_{BLAST}(S > 1.5\text{mJy}) \approx 1.1 \times 10^{-4} h^3 \text{ Mpc}^{-3}$. On the other hand, even after counting *all* of the BLAST galaxies, there is still a 4 fewer BLAST galaxies than there are LBGs. Further studies exploring this link could explore the possibility that i) they’ve merged together to trigger BLAST galaxies, or ii) have fallen into the center of the halos and ceased forming stars, or iii) not all of the BLAST galaxies are accounted for, i.e., the number counts are biased low by the beam blending together faint sources. It may well be some combination of these. We will explore the third scenario in § 5.6.1.

As for possible descendants of BLAST galaxies, we briefly compare to two known strongly clustered red-and-dead populations. First are the extremely red objects (EROs; Daddi et al., 2001), with which Blain et al. (2004) seem to find an evolutionary link with SMGs. Daddi et al. (2001) find a correlation length of $r_0 = 12 \pm 3$ at $z \sim 1$. These lie directly on the evolutionary path of the $500 \mu\text{m}$ population, and thus a possible link is not ruled out. Finally, the most clustered objects in the Universe are the aptly named clusters of galaxies, of which we cite a few examples. Bahcall & Soneira (1983) find $r_0 = 24 \pm 9$ for rich Abell clusters; Lahav et al. (1989) find $r_0 = 21 \pm 7$ for the brightest x-ray identified clusters; and Dalton et al. (1994) find $r_0 = 19 \pm 5$ for clusters selected from the APM Galaxy Survey. Again, these lie on the evolutionary path of the halos which host BLAST galaxies at higher redshift, and thus BLAST galaxies are not ruled out as progenitors to local cluster galaxies.

5.4 Implications

Le Floc’h et al. (2005) show that IR-luminous galaxies (LIRGs and ULIRGS) represent $\sim 70\%$ of the IR energy density, and by $z \sim 0.5-1.0$ are responsible for most of the star formation. Rodighiero et al. (2009) extend that analysis to show that by $z \sim 2$, it is as much as $\sim 98\%$. Furthermore, stacking work (e.g., Marsden et al., 2009) shows that most of the objects responsible for the CIB are fainter than the flux density limit of the BLAST catalogs (Devlin et al., 2009), and equals roughly 1 mJy. At redshifts beyond $z \sim 1$, this corresponds to LIRG-like luminosities for those sources.

Therefore, by identifying the locations of active star formation at $z \sim 1 - 3$, we are also identifying the locations of the formation of the majority of stars in the present day Universe!

With this in mind we ask: where are active star-forming galaxies preferentially found through cosmic time? From Figure 5.1, it appears that the most active star-forming galaxies are found occupying halos whose mass increases from roughly 10^{12} to $10^{13.5} M_{\odot}$ over the redshift range $z = 0$ to 2, after which it appears to remain roughly constant. This appears to be consistent with *downsizing* (Cowie et al., 1996), the scenario in which the sites of most active star formation shifts to ever larger galaxies at higher redshifts. However, according to the model, which is only constrained for redshifts greater than ~ 1.1 , the galaxies which make up the background do not exhibit the same trend. While the bias is still a strong increasing function of redshift, the clustering strength of the host halos remains roughly constant. This would mean that star formation is less dependent on halo mass than it is on local number density of halos. In other words, halos with the same clustering behavior at higher redshift are *less* massive. Since this is very much a model-dependent claim, it may be indicative of a flaw in the model (perhaps assuming $M_{\min}^{-\alpha}$ remain constant with z is incorrect); future studies should clarify this picture.

5.5 Understanding the Clustering Signal

In § 4.6.4 we attempted to fit the BLAST clustering results with a halo model. We found that on small scales the model did not adequately match the signal due to a dearth of signal. Curiously, the clustering signal seems to obey a power-law with slope of -2 , which was confirmed with further analysis to scales as small as $k_{\theta} \approx 0.6 \text{ arcmin}^{-1}$. We then argued that perhaps the halo model we used was too restrictive, and relaxed the model so that the profile of halos was allowed to extend to 2, 3 and 4 times the virial radius, thereby allowing satellite galaxies to lie further out from the halo center. While this improved the minimum χ^2 of the fit by $\sim 10\%$, the data still appeared to be better fit by the linear model.

Now we ask, how could we change the model to better fit the data? For clues, we explore observations at other wavelengths, as well as what is seen in simulations. We suggest modifications for future analyses with better data, where the small scale features will be unambiguously resolved.

5.5.1 Observations

Locally, observations of groups and clusters may provide some idea of the environments which star formation prefers (or avoids). For example, BLAST observations of Abell 3112 (Braglia et al., in prep. 2010) show that a significant amount of star-formation activity is taking place in the region surrounding R_{500} , which is the radius where the over-density of the cluster with respect to the background density exceeds 500. A typical virial radius would be R_{200} . Other studies at infrared wavelengths confirm this behaviour. For example, at $24 \mu\text{m}$ Bai et al. (2007), Saintonge et al. (2008), Haines et al. (2009), and Tran et al. (2009) all find dusty star-forming galaxies in the infall regions between R_{200} and R_{500} . Additionally, they universally find a global decrease of the fraction of IR

luminous galaxies towards the innermost regions of clusters, which is usually interpreted as quenching due to environmental effects.

Extending this to higher redshift, [Elbaz et al. \(2007\)](#) observe a group at $z = 1.0163$. They show LIRG-like galaxies occupying a volume spanning several Mpc, with most of the brightest galaxies concentrated within about two virial radii, as well as several scattered outside that volume as well. For much larger and more dynamically relaxed clusters and large groups, infrared observations almost universally show a lack of IR emission at their centers (e.g., [Coia et al., 2005](#); [Marcillac et al., 2007](#)), that star-forming satellites are found on the cluster outskirts (e.g., [Coia et al., 2005](#); [Marcillac et al., 2007](#)), and that they appear to be accreting onto the cluster ([Gallazzi et al., 2009](#)). The idea to take away is that star-formation seems to prefer *medium density* environments. This is seen as well by [Fadda et al. \(2008\)](#), who find star-forming galaxies in filamentary structures leading the infall of outskirts, or 5–10 Mpc from the cluster core.

5.5.2 Simulations

5.5.2.1 The tri-axial nature of dark matter halos

The halos in our halo model are spherically symmetric, with NFW density profiles, and are truncated at arbitrary radii of $1-4r_{vir}$. Each of these approximations is questionable. First of all, simulations unanimously show that halos are tri-axial ellipsoids, meaning that they are described with different profiles along each axis (e.g., [Barnes & Efstathiou, 1987](#); [Dubinski & Carlberg, 1991](#); [Katz, 1991](#); [Warren et al., 1992](#); [Dubinski, 1994](#); [Jing et al., 1995](#); [Tormen, 1997](#); [Jing & Suto, 2000](#)).

These ellipsoids can be characterized by three axes, a , b and c , with $a \geq b \geq c$, which can also be represented in terms of scale-independent ratios, $s \equiv c/a$, $q \equiv b/a$, and $p \equiv c/b$. There are three kinds of ellipsoids which are defined in the following way: prolate (sausage shaped) ellipsoids, with $a > b \approx c$ and $s \approx q < p$; oblate (pancake shaped) ellipsoids with $a \approx b > c$ and $s \approx p < q$; and triaxial ellipsoids, with $a > b > c$, whose shape is between prolate and oblate (see [Figure 5.3](#)). Purely oblate ellipsoids have $a = b$, in which case only q is used, since s and q are degenerate.

Often, ellipsoids are described in terms of their tri-axiality, expressed by the tri-axiality parameter of [Franx, Illingworth, & de Zeeuw \(1991\)](#)

$$T \equiv \frac{a^2 - b^2}{a^2 - c^2} = \frac{1 - q^2}{1 - s^2}, \quad (5.2)$$

thus an ellipsoid is oblate if $0 < T < 1/3$; triaxial if $1/3 < T < 2/3$; and prolate if $2/3 < T < 1$. The tri-axiality of simulated halos from [Allgood et al. \(2006\)](#) is shown in [Figure 5.4](#).

A general summary of the findings of models is provided in [Jing & Suto \(2002\)](#), as well as [Allgood et al. \(2006\)](#). They find that not only are halos typically triaxial, but that their shape depends on a number of other parameters as well, such as mass, redshift and radius. Particularly, they find that halos of larger mass tend to be more prolate (sausage shaped), as is shown in [Figure 5.4](#). In general,

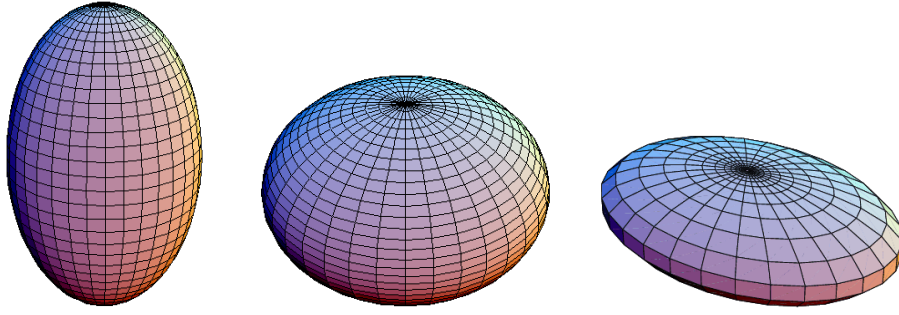


FIGURE 5.3: From left to right, Prolate, Oblate and Triaxial ellipsoids.

however, the smallest-to-largest axis ratio is well described by the simple power-law relation

$$\langle s \rangle = (0.54 \pm 0.03) \left(\frac{M_{vir}}{M_*(z)} \right)^{-0.050 \pm 0.003} \quad (5.3)$$

where s is measured at $0.3 R_{vir}$, and z and σ_8 are governed by the characteristic non-linear mass $M_* = M_*(z, \sigma_8)$.

Birnboim & Dekel (2003) and Kereš et al. (2005) find that in hydrodynamical simulations of halos $M \gtrsim 3 \times 10^{11} M_\odot$, a virial shock forms at about the virial radius, so that the gas falling within this radius is shock heated to the virial temperature, quenching star formation. They also find that this behaviour is typically limited to halos at redshifts $z \lesssim 2$. Other groups loosely base their models on this idea of a halo-mass dependent “shut-down” of star formation, and find that it quite successfully explains downsizing (e.g., Birnboim & Dekel, 2003; Dekel & Birnboim, 2006; Cattaneo et al., 2008).

However, as was pointed out by Brodwin et al. (2008), this appears to be at odds with several observations. As illustrated in Figure 5.1, a sharp cut-off can be seen for $M \geq 10^{13.5} M_\odot$ halos, which appears to hold out to $z \sim 2.5$. Dekel et al. (2009) attempt to resolve this dilemma with a model where cold streams penetrate the shock-heated media. On the other hand, if the shock radius does roughly follow the virial radius, then finding satellites actively forming stars outside of the shock-heated volume would satisfy both the model and the observations.

5.6 Applications for Future Models

Presently, we have been using spherically symmetric halos with NFW profiles. In our different models, we truncate our halos at 1 to 4 times the virial radius. We use a central-satellite configuration, and assign the number of galaxies to halos as a function of their mass; an assignment scheme otherwise known as a halo occupation number (HON). We have a minimum mass, M_{min} , below which no galaxies are found, and above which the first assigned galaxy is always a central galaxy, and further galaxies in the same halo are satellites. M_1 is the halo mass for which exactly one galaxy is assigned, and this value evolves with redshift in order to match both the abundance of sources and clustering

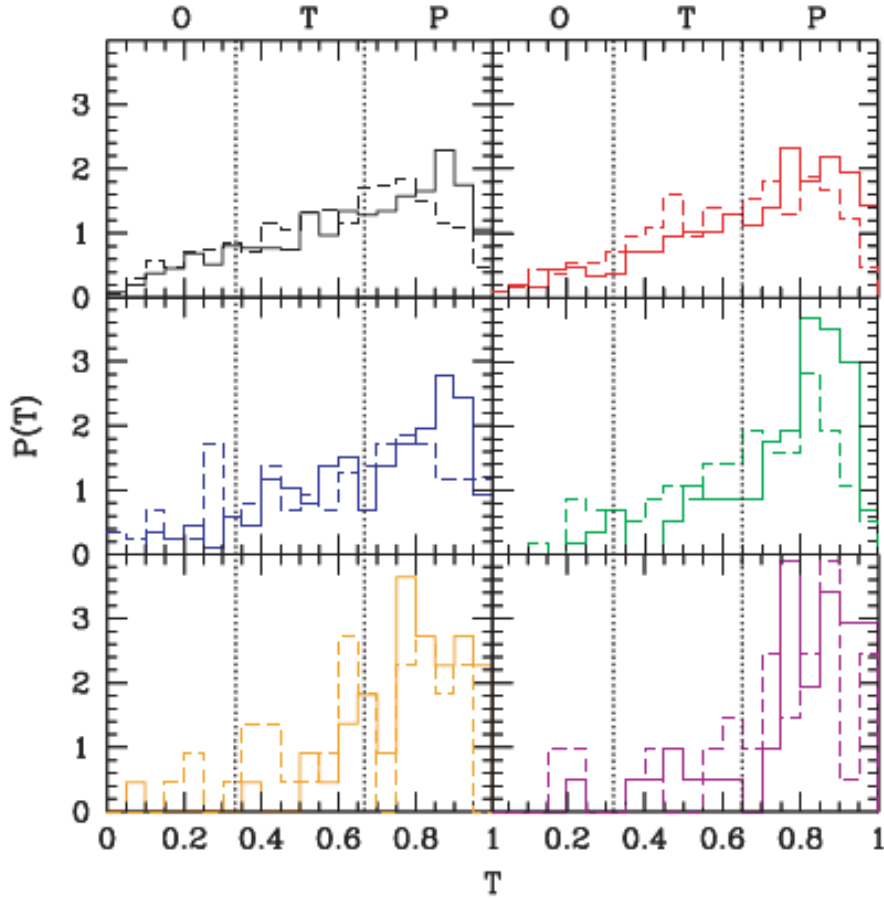


FIGURE 5.4: Tri-axiality of halos at $z = 0$ and $R = 0.3R_{vir}$ (solid) and $R = R_{vir}$ (dashed). The top left and moving right then down, the halos are divided into mass bins of: $1.6 < M_{vir} \leq 3.2$, $3.2 < M_{vir} \leq 6.4$, $6.4 < M_{vir} \leq 12.8$, $12.8 < M_{vir} \leq 25.6$, $25.6 < M_{vir} \leq 51.2$, and $51.2 < M_{vir}$. Image reproduced with permission from Allgood et al. (2006).

signal simultaneously. On the other hand, M_{min} and α remain constant with redshift, which as we've seen, may be the cause of contradictions at high redshift.

We now propose possible changes to the halo model to be explored in future studies with better data. These changes are motivated by the observations and simulations described above. Most of these suggestions are not trivial to implement, and may introduce degeneracies, which is why extremely high quality data revealing subtle features in the curve (i.e., deviations from a simple power-law) would be needed to justify the addition of parameters to the halo model.

1) No central galaxy in large halos. The central-satellite description is the logical approach for typical groups and clusters, usually local, which are observed in the optical. Typically, these systems are such that the largest and most luminous galaxy is the central one — typically elliptical and dust-free — surrounded by other also typically red and dead cluster members. Since the central ellipticals are not the kind of galaxy that BLAST is sensitive to, and because shocking is seen to quench star formation in the centers of large halos, it may be reasonable to omit the central galaxy from halos greater than $\sim 10^{12} M_{\odot}$, and instead have only satellites in these halos.

2) Modify how the galaxy distribution traces halos. This is in many ways an extension of the previous argument. The spatial distribution of satellite galaxies is assigned according to a probability distribution which follows the halo's NFW profile. Of course, since the NFW extends radially as $\rho(r) \propto r^{-3}$, this means that the assignment of satellites is heavily weighted towards the center of the halo. From observations, this is clearly not optimal. Star formation seems to prefer a medium density environment, between the radii $r_{SF} \sim R_{500} - R_{200}$. Thus, the probability distribution governing the spatial distribution of satellite galaxies could be one that peaks at r_{SF} , and that function could be, for example, the NFW profile multiplied by the appropriate function.

3) Make halo profiles more realistic. As we've seen, spherically symmetric halos are not physically realistic. In particular, the larger the halo, the more prolate the halo becomes. However, spherically symmetric halos are very easy to model, largely because their Fourier transform, $u_{DM}(\mathbf{k}|m)$ (Equation 3.53) is analytic. Tri-axial ellipsoids on the other hand have no analytic Fourier transform solution, and therefore they would have to be calculated numerically for each halo.

4) Dependence of virial radius with z . Although the exact definition of the virial radius depends on who you ask, in general the virial mass and radius correspond to regions within which the density contrast with respect to the mean matter density is a defined to be some amount. Quite often this will take the form $\Delta_{vir} = 200$ in the literature, which is based on observational limitations. An evolving virial radius can be problematic when considering a large range of redshifts, since the density of the background itself changes with redshift. Following Bryan & Norman (1998), if we define $\Delta_{vir} = 18\pi^2 + 82x - 39x^2$, where $x \equiv \Omega(z) = 1$, then at $z = 0$, $\Delta_{vir} = 337$ and asymptotes to 180 at high redshift. Thus, the virial radius will take the form

$$r_{vir}^3 = \frac{3M}{4\pi\rho_{crit}\Delta_c}, \quad (5.4)$$

and is shown for different masses in Figure 5.5. Note that the virial radius of a halo at $z = 1.4$ is twice the size of one at $z = 4$. This may explain why the one-halo bump that Ouchi et al. (2004) see (i.e., in excess from a power law) for LBGs at $z \sim 4$ is on such small scales (i.e., $\lesssim 10''$). At that redshift, the virial radius of halos of mass $\sim 2 \times 10^{12} M_\odot$ is ~ 0.08 Mpc, as opposed to at $z = 1.5$, were it's ~ 0.15 Mpc. Thus, considering that high-redshift halos are smaller and significantly more concentrated than low-redshift counterparts, there may be more subtle physics taking place on scales of the halo that must be included in the model.

5) Using the cross-band correlations. Currently, the halo model is fit to the three bands simultaneously, but has no cross-band component. While the BLAST cross-band signal is perhaps too noisy to add many constraints, future work with more data should include this extra component which contains valuable information about the redshift distribution of sources.

6) Redshift dependent α and M_{min} . As was already pointed out, α and M_{min} are held constant in our model. This could be modified by changing M_{min} to agree with simulations or observations, and adjusting M_1 and α in order to match abundances. Conversely, given a luminosity function for BLAST sources (eventually), M_{min} could be altered to match abundances of dark matter halos from simulations. In order to make meaningful changes more information would be required to do this correctly.

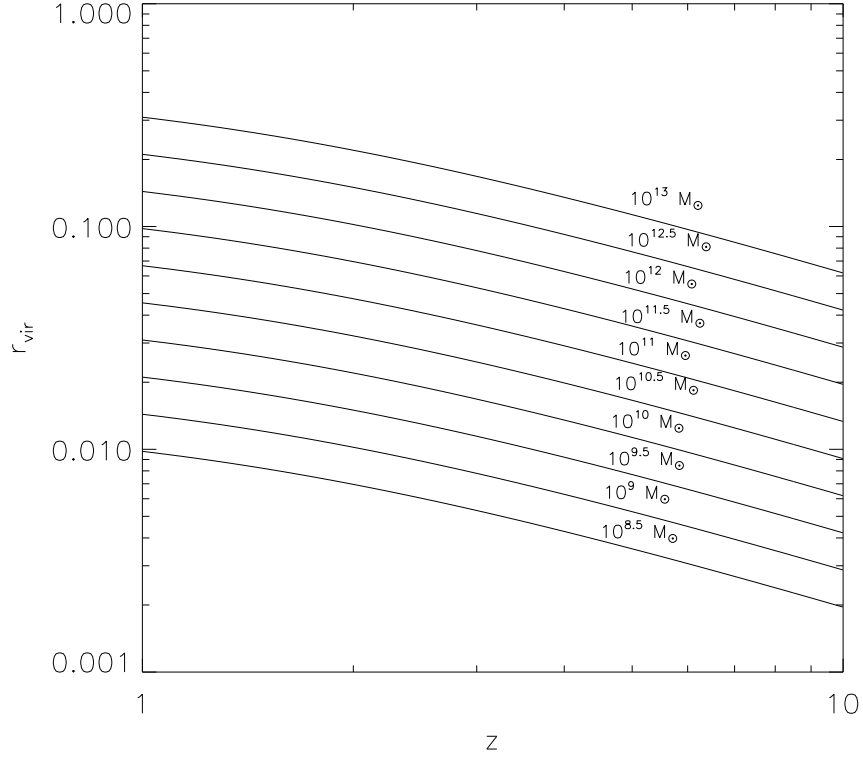


FIGURE 5.5: The virial radius as a function of redshift for different mass halos according to the parameterization of [Bryan & Norman \(1998\)](#).

5.6.1 Shot Noise Degeneracy

As described in § 3.2.3.1, the shot noise is the integral of $S^2 dN/dS$. For argument's sake, let's imagine that each of the BLAST galaxies is in fact two galaxies of equal flux, blended together by the beam. In this scenario, the number counts, dN/dS , would be doubled, and the fluxes, S , would be halved, and the shot noise estimate would be $(1/2)^2 \times 2 = 1/2$ of what is observed. Recall that the measured signal is the sum of contributions dominated by the shot and clustering signals. If the shot signal is less, then that would imply that the signal from clustered galaxies is in fact higher, as illustrated in Figure 5.6. Here, the measured data are green points; the shot noise is fit directly to the data (purple solid horizontal line); and another “imagined” shot noise is drawn with $\sim 30\%$ less power (yellow solid horizontal line). The clustering signal (i.e., signal minus shot_{fit}) is shown as purple circles, and the “imagined” clustering signal (i.e., signal minus shot_{im}) is shown as red stars. The power-law fit to the data is shown as a solid blue line, and finally the model 1-halo curve of Mattia Negrello is shown as a solid red curve. Notice that the imaginary signal follows the model 1-halo term quite nicely.

Clearly a degeneracy exists, but is it physically possible? We have seen already that confusing multiple sources for one source is quite easy to do with BLAST's beam (§ 3.2.2.2). This would imply multiple sources at distances $\theta \lesssim 1.5'$, or physical distances $\lesssim 1.5$ Mpc at $z \sim 1$, which is

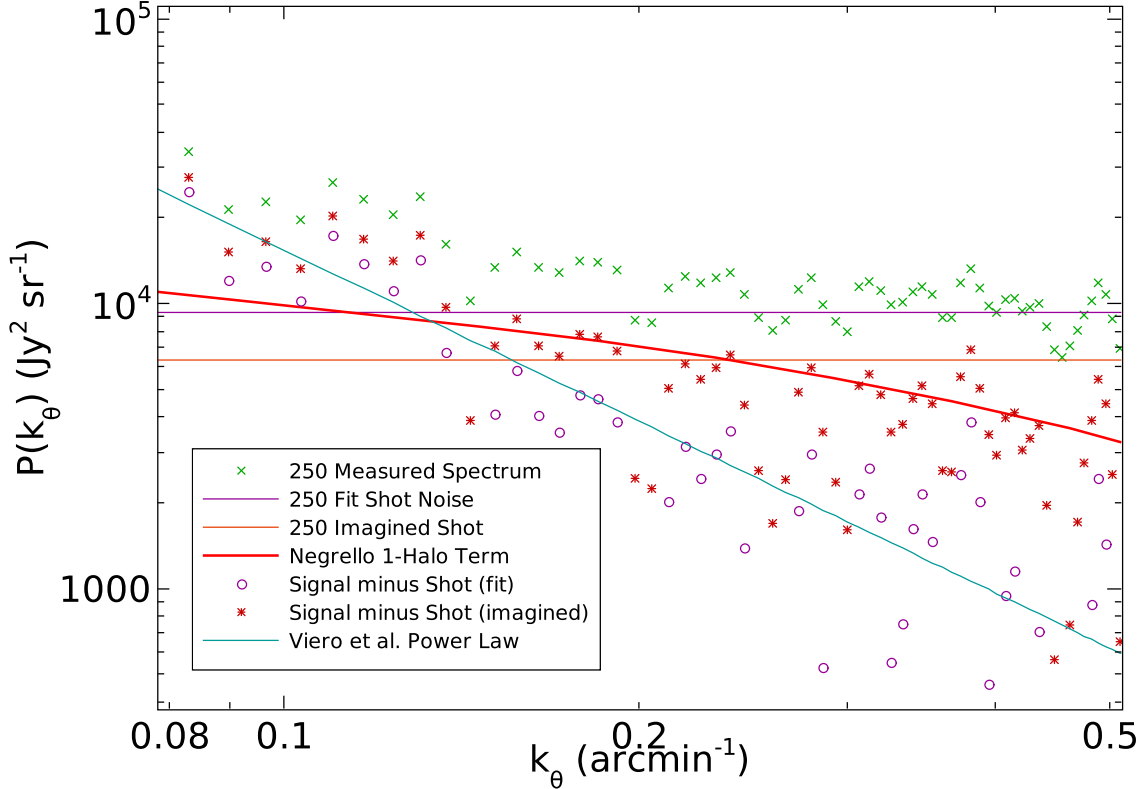


FIGURE 5.6: Demonstration of degeneracy in BLAST power spectrum. The measured data are green exes; the shot noise is fit directly to the data (purple solid horizontal line); and another “imagined” shot noise is drawn with $\sim 30\%$ less power (yellow solid horizontal line). The clustering signal (i.e., signal minus shot_{fit}) is shown as purple circles, and the “imagined” clustering signal (i.e., signal minus shot_{im}) is shown as red stars. The power-law fit to the data is shown as a solid blue line, and finally the model 1-halo curve of Mattia Negrello is shown as a solid red curve. Notice that the imaginary signal follows the model 1-halo term quite nicely. In other words, if the BLAST beam is blending multiple sources together, the shot noise would be overestimated resulting in an underestimation of clustering signal on small scales.

not unlikely. Therefore, we are faced with a fundamental limitation of observing with a large beam which can only be resolved with future experiments, such as *Herschel* or SCUBA2.

5.7 Summary

We detect the clustering of star-forming galaxies which make up the unresolved CIB at 250, 350 and $500\ \mu\text{m}$. This represents the first measurement of galaxy clustering at these wavelengths, and was made possible by the use of CMB techniques on submillimeter data. The measured correlations are well fit by a power law over scales of 5–25 arcminutes, with $\Delta I/I = 15.1 \pm 1.7\%$. We adopt a specific model for submillimeter sources in which the contribution to clustering comes from sources in the redshift ranges $1.3 \leq z \leq 2.2$, $1.5 \leq z \leq 2.7$, and $1.7 \leq z \leq 3.2$, at 250, 350 and $500\ \mu\text{m}$, respectively. With these distributions, our measurement of the power spectrum, $P(k_\theta)$, corresponds

to linear bias parameters, $b = 3.8 \pm 0.6, 3.9 \pm 0.6$ and 4.4 ± 0.7 , respectively. In other words, we learn that star-forming galaxies in the redshift range $\sim 1-3$ are biased tracers of the underlying dark matter.

We further interpret the results in terms of the halo model, and find that at the smaller scales, the simplest halo model fails to fit our results. We attempt to improve the fit by increasing the radius at which dark matter halos are artificially truncated in the model, which is equivalent to having some star-forming galaxies at $z \geq 1$ located in the outskirts of groups and clusters. We find that this improves the fit, and that it is consistent with what is seen in observations of star-forming galaxies in groups and clusters, as well as being consistent with models of dark matter halo assembly.

In the context of this model we find a minimum halo mass required to host a galaxy is $\log(M_{\min}/M_{\odot}) = 11.5^{+0.4}_{-0.1}$, and we derive effective biases $b_{\text{eff}} = 2.2 \pm 0.2, 2.4 \pm 0.2$, and 2.6 ± 0.2 , and effective masses $\log(M_{\text{eff}}/M_{\odot}) = 12.9 \pm 0.3, 12.8 \pm 0.2$, and 12.7 ± 0.2 , at 250, 350 and 500 μm , corresponding to spatial correlation lengths of $r_0 = 4.9, 5.0$, and $5.2 \pm 0.7 h^{-1}$ Mpc, respectively.

5.8 Future Work

The successful launch of *Planck* and *Herschel* will revolutionize the state of (sub)mm observations. Full sky maps made by *Planck* will allow determination of the galaxy bias to unprecedented levels. Furthermore, cross correlations of the galaxy bands will allow for separation of the fluctuation signal from low and high redshift galaxies, thus tracing the evolution of the bias. Cross-correlations will also allow for separation of fluctuations from dusty and radio galaxies, which have different spectral signals, which will have applications for measuring the high ℓ CMB and SZ signals.

The SPIRE instrument on *Herschel*, which has the same detector array as BLAST, will provide maps of unprecedented size, depth and angular resolution. In particular, the FWHM of the beams — which are at or below the average distance between galaxies — will finally make studying the properties of individual galaxies feasible. The two-point correlation function, which to-date has been elusive, will finally be measured with confidence. However, the CMB techniques discussed and applied in this thesis are still very relevant. As shown in Knox et al. (2001), tens of thousands of sources are required to achieve the same level of uncertainty as measuring brightness fluctuations. Furthermore, source blending will still be an issue that must be considered and compensated for. Just how significant an effect it will have remains to be seen.

Ground based instruments are also adding to this landscape of cutting-edge instrumentation. SCUBA 2 on the JCMT is currently being installed and commissioned, and should provide large maps with angular resolutions complementary to SPIRE. The AzTEC camera is working and collecting data, and will soon arrive at its ultimate site on the LMT in Mexico. The ALMA array and CCAT 25 m class telescope in Chile, which are still some years from arriving, ensure that the arrival of new and ground-breaking IR/(sub)mm data will be continuous for years to come.

The possibilities of combining CMB techniques with astronomical data are rich indeed. Overwhelming amounts of data will be available very soon, which due to the fact that it will be confusion limited,

will require a different approach from those conventionally adopted in astronomy. For example, in this thesis we showed how CMB techniques can uncover the clustering properties of galaxies, where more conventional techniques have failed. BLAST has set the stage for a very new type of astronomy, a fusion, if you will, of two previously independent fields of astrophysics. It is an exciting time to be a submillimeter astronomer.

Bibliography

- Abazajian, K., Zheng, Z., Zehavi, I., Weinberg, D. H., Frieman, J. A., Berlind, A. A., Blanton, M. R., Bahcall, N. A., Brinkmann, J., Schneider, D. P., & Tegmark, M. 2005, *ApJ*, 625, 613
- Adelberger, K. L., Steidel, C. C., Giavalisco, M., Dickinson, M., Pettini, M., & Kellogg, M. 1998, *ApJ*, 505, 18
- Adelberger, K. L., Steidel, C. C., Pettini, M., Shapley, A. E., Reddy, N. A., & Erb, D. K. 2005, *ApJ*, 619, 697
- Allgood, B., Flores, R. A., Primack, J. R., Kravtsov, A. V., Wechsler, R. H., Faltenbacher, A., & Bullock, J. S. 2006, *MNRAS*, 367, 1781
- Almaini, O., Dunlop, J. S., Willott, C. J., Alexander, D. M., Bauer, F. E., & Liu, C. T. 2005, *MNRAS*, 358, 875
- Almaini, O., Scott, S. E., Dunlop, J. S., Manners, J. C., Willott, C. J., Lawrence, A., Ivison, R. J., Johnson, O., Blain, A. W., Peacock, J. A., Oliver, S. J., Fox, M. J., Mann, R. G., Pérez-Fournon, I., González-Solares, E., Rowan-Robinson, M., Serjeant, S., Cabrera-Guerra, F., & Hughes, D. H. 2003, *MNRAS*, 338, 303
- Amblard, A. & Cooray, A. 2007, *ApJ*, 670, 903
- Arendt, R. G., Odegard, N., Weiland, J. L., Sodroski, T. J., Hauser, M. G., Dwek, E., Kelsall, T., Moseley, S. H., Silverberg, R. F., Leisawitz, D., Mitchell, K., Reach, W. T., & Wright, E. L. 1998, *ApJ*, 508, 74
- Bahcall, N. A. & Soneira, R. M. 1983, *ApJ*, 270, 20
- Bai, L., Marcillac, D., Rieke, G. H., Rieke, M. J., Tran, K., Hinz, J. L., Rudnick, G., Kelly, D. M., & Blaylock, M. 2007, *ApJ*, 664, 181
- Bardeen, J. M., Bond, J. R., Kaiser, N., & Szalay, A. S. 1986, *ApJ*, 304, 15
- Barger, A. J., Cowie, L. L., Smail, I., Ivison, R. J., Blain, A. W., & Kneib, J.-P. 1999, *AJ*, 117, 2656
- Barnes, J. & Efstathiou, G. 1987, *ApJ*, 319, 575
- Bartelmann, M. & Schneider, P. 2001, *Phys. Rep.*, 340, 291

- Basu-Zych, A. R., Schiminovich, D., Heinis, S., Overzier, R., Heckman, T., Zamojski, M., Ilbert, O., Koekemoer, A. M., Barlow, T. A., Bianchi, L., Conrow, T., Donas, J., Forster, K. G., Friedman, P. G., Lee, Y.-W., Madore, B. F., Martin, D. C., Milliard, B., Morrissey, P., Neff, S. G., Rich, R. M., Salim, S., Seibert, M., Small, T. A., Szalay, A. S., Wyder, T. K., & Yi, S. 2009, *ApJ*, 699, 1307
- Baugh, C. M., Benson, A. J., Cole, S., Frenk, C. S., & Lacey, C. G. 1999, *MNRAS*, 305, L21
- Berlind, A. A., Narayanan, V. K., & Weinberg, D. H. 2000, *ApJ*, 537, 537
- Berlind, A. A., Weinberg, D. H., Benson, A. J., Baugh, C. M., Cole, S., Davé, R., Frenk, C. S., Jenkins, A., Katz, N., & Lacey, C. G. 2003, *ApJ*, 593, 1
- Bertoldi, F., Carilli, C. L., Menten, K. M., Owen, F., Dey, A., Gueth, F., Graham, J. R., Kreysa, E., Ledlow, M., Liu, M. C., Motte, F., Reichertz, L., Schilke, P., & Zylka, R. 2000, *A&A*, 360, 92
- Birnboim, Y. & Dekel, A. 2003, *MNRAS*, 345, 349
- Blain, A. W. 1997, *MNRAS*, 290, 553
- Blain, A. W., Chapman, S. C., Smail, I., & Ivison, R. 2004, *ApJ*, 611, 725
- Blake, C., Pope, A., Scott, D., & Mobasher, B. 2006, *MNRAS*, 368, 732
- Blanc, G. A., Lira, P., Barrientos, L. F., Aguirre, P., Francke, H., Taylor, E. N., Quadri, R., Marchesini, D., Infante, L., Gawiser, E., Hall, P. B., Willis, J. P., Herrera, D., & Maza, J. 2008, *ApJ*, 681, 1099
- Blumenthal, G. R., Faber, S. M., Primack, J. R., & Rees, M. J. 1984, *Nature*, 311, 517
- Bond, J. R., Carr, B. J., & Hogan, C. J. 1986, *ApJ*, 306, 428
- Borys, C., Scott, D., Chapman, S., Halpern, M., Nandra, K., & Pope, A. 2004, *MNRAS*, 355, 485
- Boulanger, F., Abergel, A., Bernard, J.-P., Burton, W. B., Desert, F.-X., Hartmann, D., Lagache, G., & Puget, J.-L. 1996, *A&A*, 312, 256
- Brodwin, M., Dey, A., Brown, M. J. I., Pope, A., Armus, L., Bussmann, S., Desai, V., Jannuzi, B. T., & Le Floch, E. 2008, *ApJ*, 687, L65
- Bryan, G. L. & Norman, M. L. 1998, *ApJ*, 495, 80
- Bullock, J. S., Dekel, A., Kolatt, T. S., Kravtsov, A. V., Klypin, A. A., Porciani, C., & Primack, J. R. 2001, *ApJ*, 555, 240
- Burigana, C. & Popa, L. 1998, *A&A*, 334, 420
- Carroll, S. M., Press, W. H., & Turner, E. L. 1992, *ARA&A*, 30, 499
- Cattaneo, A., Dekel, A., Faber, S. M., & Guiderdoni, B. 2008, *MNRAS*, 389, 567
- Chapman, S. C., Blain, A. W., Smail, I., & Ivison, R. J. 2005, *ApJ*, 622, 772

- Coia, D., McBreen, B., Metcalfe, L., Biviano, A., Altieri, B., Ott, S., Fort, B., Kneib, J.-P., Mellier, Y., Miville-Deschênes, M.-A., O'Halloran, B., & Sanchez-Fernandez, C. 2005, *A&A*, 431, 433
- Cole, S. & Kaiser, N. 1989, *MNRAS*, 237, 1127
- Condon, J. J. 1974, *ApJ*, 188, 279
- Cooray, A. 2006, *MNRAS*, 365, 842
- Cooray, A. & Sheth, R. 2002, *Phys. Rep.*, 372, 1
- Coppin, K., Chapin, E. L., Mortier, A. M. J., Scott, S. E., Borys, C., Dunlop, J. S., Halpern, M., Hughes, D. H., Pope, A., Scott, D., Serjeant, S., Wagg, J., Alexander, D. M., Almaini, O., Aretxaga, I., Babbedge, T., Best, P. N., Blain, A., Chapman, S., Clements, D. L., Crawford, M., Dunne, L., Eales, S. A., Edge, A. C., Farrah, D., Gaztañaga, E., Gear, W. K., Granato, G. L., Greve, T. R., Fox, M., Ivison, R. J., Jarvis, M. J., Jenness, T., Lacey, C., Lepage, K., Mann, R. G., Marsden, G., Martinez-Sansigre, A., Oliver, S., Page, M. J., Peacock, J. A., Pearson, C. P., Percival, W. J., Priddey, R. S., Rawlings, S., Rowan-Robinson, M., Savage, R. S., Seigar, M., Sekiguchi, K., Silva, L., Simpson, C., Smail, I., Stevens, J. A., Takagi, T., Vaccari, M., van Kampen, E., & Willott, C. J. 2006, *MNRAS*, 372, 1621
- Cowie, L. L., Songaila, A., Hu, E. M., & Cohen, J. G. 1996, *AJ*, 112, 839
- Daddi, E., Broadhurst, T., Zamorani, G., Cimatti, A., Röttgering, H., & Renzini, A. 2001, *A&A*, 376, 825
- Daddi, E., Dickinson, M., Chary, R., Pope, A., Morrison, G., Alexander, D. M., Bauer, F. E., Brandt, W. N., Gialalisco, M., Ferguson, H., Lee, K.-S., Lehmer, B. D., Papovich, C., & Renzini, A. 2005, *ApJ*, 631, L13
- Dalton, G. B., Croft, R. A. C., Efstathiou, G., Sutherland, W. J., Maddox, S. J., & Davis, M. 1994, *MNRAS*, 271, L47+
- Davis, M., Efstathiou, G., Frenk, C. S., & White, S. D. M. 1985, *ApJ*, 292, 371
- Davis, M. & Peebles, P. J. E. 1983, *ApJ*, 267, 465
- Dekel, A. & Birnboim, Y. 2006, *MNRAS*, 368, 2
- Dekel, A., Birnboim, Y., Engel, G., Freundlich, J., Goerdt, T., Mumcuoglu, M., Neistein, E., Pichon, C., Teyssier, R., & Zinger, E. 2009, *Nature*, 457, 451
- Dekel, A. & Silk, J. 1986, *ApJ*, 303, 39
- Devlin, M. J., Ade, P. A. R., Aretxaga, I., Bock, J. J., Chapin, E. L., Griffin, M., Gundersen, J. O., Halpern, M., Hargrave, P. C., Hughes, D. H., Klein, J., Marsden, G., Martin, P. G., Maukopf, P., Moncelsi, L., Netterfield, C. B., Ngo, H., Olmi, L., Pascale, E., Patanchon, G., Rex, M., Scott, D., Semisch, C., Thomas, N., Truch, M. D. P., Tucker, C., Tucker, G. S., Viero, M. P., & Wiebe, D. V. 2009, *Nature*, 458, 737

- Diaferio, A., Kauffmann, G., Colberg, J. M., & White, S. D. M. 1999, *MNRAS*, 307, 537
- Dickinson, M., Papovich, C., Ferguson, H. C., & Budavári, T. 2003, *ApJ*, 587, 25
- Draine, B. T. & Lee, H. M. 1984, *ApJ*, 285, 89
- Dubinski, J. 1994, *ApJ*, 431, 617
- Dubinski, J. & Carlberg, R. G. 1991, *ApJ*, 378, 496
- Dunlop, J. S., Ade, P. A. R., Bock, J. J., Chapin, E. L., Cirasuolo, M., Coppin, K. E. K., Devlin, M. J., Griffin, M., Greve, T. R., Gundersen, J. O., Halpern, M., Hargrave, P. C., Hughes, D. H., Ivison, R. J., Klein, J., Kovacs, A., Marsden, G., Mauskopf, P., Netterfield, C. B., Olmi, L., Pascale, E., Patanchon, G., Rex, M., Scott, D., Semisch, C., Smail, I., Targett, T. A., Thomas, N., Truch, M. D. P., Tucker, C., Tucker, G. S., Viero, M. P., Walter, F., Wardlow, J. L., Weiss, A., & Wiebe, D. V. 2009, *ArXiv e-prints*
- Dye, S., Ade, P. A. R., Bock, J. J., Chapin, E. L., Devlin, M. J., Dunlop, J. S., Eales, S. A., Griffin, M., Gundersen, J. O., Halpern, M., Hargrave, P. C., Hughes, D. H., Klein, J., Magnelli, B., Marsden, G., Mauskopf, P., Moncelsi, L., Netterfield, C. B., Olmi, L., Pascale, E., Patanchon, G., Rex, M., Scott, D., Semisch, C., Targett, T., Thomas, N., Truch, M. D. P., Tucker, C., Tucker, G. S., Viero, M. P., & Wiebe, D. V. 2009, *ApJ*, 703, 285
- Eales, S., Lilly, S., Gear, W., Dunne, L., Bond, J. R., Hammer, F., Le Fèvre, O., & Crampton, D. 1999, *ApJ*, 515, 518
- Eisenstein, D. J. & Hu, W. 1998, *ApJ*, 496, 605
- Elbaz, D., Daddi, E., Le Borgne, D., Dickinson, M., Alexander, D. M., Chary, R.-R., Starck, J.-L., Brandt, W. N., Kitzbichler, M., MacDonald, E., Nonino, M., Popesso, P., Stern, D., & Vanzella, E. 2007, *A&A*, 468, 33
- Fadda, D., Biviano, A., Marleau, F. R., Storrie-Lombardi, L. J., & Durret, F. 2008, *ApJ*, 672, L9
- Farrah, D., Lonsdale, C. J., Borys, C., Fang, F., Waddington, I., Oliver, S., Rowan-Robinson, M., Babbedge, T., Shupe, D., Polletta, M., Smith, H. E., & Surace, J. 2006, *ApJ*, 641, L17
- Finkbeiner, D. P., Davis, M., & Schlegel, D. J. 2000, *ApJ*, 544, 81
- Fixsen, D. J. 2009, *ApJ*, 707, 916
- Fixsen, D. J., Dwek, E., Mather, J. C., Bennett, C. L., & Shafer, R. A. 1998, *ApJ*, 508, 123
- Fowler, J. W. 2004, in *Society of Photo-Optical Instrumentation Engineers (SPIE) Conference Series*, Vol. 5498, *Society of Photo-Optical Instrumentation Engineers (SPIE) Conference Series*, ed. C. M. Bradford, P. A. R. Ade, J. E. Aguirre, J. J. Bock, M. Dragovan, L. Duband, L. Earle, J. Glenn, H. Matsuhara, B. J. Naylor, H. T. Nguyen, M. Yun, & J. Zmuidzinas, 1–10
- Franx, M., Illingworth, G., & de Zeeuw, T. 1991, *ApJ*, 383, 112
- Fukugita, M. & Peebles, P. J. E. 2004, *ApJ*, 616, 643

- Gallazzi, A., Bell, E. F., Wolf, C., Gray, M. E., Papovich, C., Barden, M., Peng, C. Y., Meisenheimer, K., Heymans, C., van Kampen, E., Gilmour, R., Balogh, M., McIntosh, D. H., Bacon, D., Barazza, F. D., Böhm, A., Caldwell, J. A. R., Häußler, B., Jahnke, K., Jogee, S., Lane, K., Robaina, A. R., Sanchez, S. F., Taylor, A., Wisotzki, L., & Zheng, X. 2009, *ApJ*, 690, 1883
- Gautier, III, T. N., Boulanger, F., Perault, M., & Puget, J. L. 1992, *AJ*, 103, 1313
- Giavalisco, M. & Dickinson, M. 2001, *ApJ*, 550, 177
- Giavalisco, M., Ferguson, H. C., Koekemoer, A. M., Dickinson, M., Alexander, D. M., Bauer, F. E., Bergeron, J., Biagetti, C., Brandt, W. N., Casertano, S., Cesarsky, C., Chatzichristou, E., Con-
selice, C., Cristiani, S., Da Costa, L., Dahlen, T., de Mello, D., Eisenhardt, P., Erben, T., Fall,
S. M., Fasnacht, C., Fosbury, R., Fruchter, A., Gardner, J. P., Grogin, N., Hook, R. N., Horn-
schemeier, A. E., Idzi, R., Jogee, S., Kretchmer, C., Laidler, V., Lee, K. S., Livio, M., Lucas, R.,
Madau, P., Mobasher, B., Moustakas, L. A., Nonino, M., Padovani, P., Papovich, C., Park, Y.,
Ravindranath, S., Renzini, A., Richardson, M., Riess, A., Rosati, P., Schirmer, M., Schreier, E.,
Somerville, R. S., Spinrad, H., Stern, D., Stiavelli, M., Strolger, L., Urry, C. M., Vandame, B.,
Williams, R., & Wolf, C. 2004, *ApJ*, 600, L93
- Giavalisco, M., Steidel, C. C., Adelberger, K. L., Dickinson, M. E., Pettini, M., & Kellogg, M. 1998,
ApJ, 503, 543
- Gilli, R., Daddi, E., Chary, R., Dickinson, M., Elbaz, D., Giavalisco, M., Kitzbichler, M., Stern, D.,
& Vanzella, E. 2007, *A&A*, 475, 83
- Grazian, A., Fontana, A., Moscardini, L., Salimbeni, S., Menci, N., Giallongo, E., de Santis, C.,
Gallozzi, S., Nonino, M., Cristiani, S., & Vanzella, E. 2006, *A&A*, 453, 507
- Greve, T. R., Ivison, R. J., Bertoldi, F., Stevens, J. A., Dunlop, J. S., Lutz, D., & Carilli, C. L. 2004,
MNRAS, 354, 779
- Griffin, M. J., Swinyard, B. M., & Vigroux, L. G. 2003, in Presented at the Society of Photo-Optical
Instrumentation Engineers (SPIE) Conference, Vol. 4850, *IR Space Telescopes and Instruments*.
Edited by John C. Mather . Proceedings of the SPIE, Volume 4850, pp. 686-697 (2003)., ed. J. C.
Mather, 686–697
- Grossan, B. & Smoot, G. F. 2007, *A&A*, 474, 731
- Groth, E. J. & Peebles, P. J. E. 1977, *ApJ*, 217, 385
- Gunn, J. E. & Gott, J. R. I. 1972, *ApJ*, 176, 1
- Guzzo, L., Strauss, M. A., Fisher, K. B., Giovanelli, R., & Haynes, M. P. 1997, *ApJ*, 489, 37
- Haiman, Z. & Knox, L. 2000, *ApJ*, 530, 124
- Haines, C. P., Smith, G. P., Egami, E., Okabe, N., Takada, M., Ellis, R. S., Moran, S. M., & Umetsu,
K. 2009, *MNRAS*, 396, 1297
- Hamilton, A. J. S. 1993, *ApJ*, 417, 19

- Hartley, W. G., Lane, K. P., Almaini, O., Cirasuolo, M., Foucaud, S., Simpson, C., Maddox, S., Smail, I., Conselice, C. J., McLure, R. J., & Dunlop, J. S. 2008, *MNRAS*, 391, 1301
- Hauser, M. G., Arendt, R. G., Kelsall, T., Dwek, E., Odegard, N., Weiland, J. L., Freudenreich, H. T., Reach, W. T., Silverberg, R. F., Moseley, S. H., Pei, Y. C., Lubin, P., Mather, J. C., Shafer, R. A., Smoot, G. F., Weiss, R., Wilkinson, D. T., & Wright, E. L. 1998, *ApJ*, 508, 25
- Heim, G. B., Henderson, M. L., Macfeely, K. I., McMahon, T. J., Michika, D., Pearson, R. J., Rieke, G. H., Schwenker, J. P., Strecker, D. W., Thompson, C. L., Warden, R. M., Wilson, D. A., & Young, E. T. 1998, in *Society of Photo-Optical Instrumentation Engineers (SPIE) Conference Series*, Vol. 3356, Society of Photo-Optical Instrumentation Engineers (SPIE) Conference Series, ed. P. Y. Bely & J. B. Breckinridge, 985–1000
- Hinshaw, G., Weiland, J. L., Hill, R. S., Odegard, N., Larson, D., Bennett, C. L., Dunkley, J., Gold, B., Greason, M. R., Jarosik, N., Komatsu, E., Nolta, M. R., Page, L., Spergel, D. N., Wollack, E., Halpern, M., Kogut, A., Limon, M., Meyer, S. S., Tucker, G. S., & Wright, E. L. 2009, *ApJS*, 180, 225
- Hogg, D. W. 2001, *AJ*, 121, 1207
- Holland, W. S., Duncan, W., Kelly, B. D., Irwin, K. D., Walton, A. J., Ade, P. A. R., & Robson, E. I. 2003, in *Society of Photo-Optical Instrumentation Engineers (SPIE) Conference Series*, Vol. 4855, Society of Photo-Optical Instrumentation Engineers (SPIE) Conference Series, ed. T. G. Phillips & J. Zmuidzinas, 1–18
- Holland, W. S., Robson, E. I., Gear, W. K., Cunningham, C. R., Lightfoot, J. F., Jenness, T., Ivison, R. J., Stevens, J. A., Ade, P. A. R., Griffin, M. J., Duncan, W. D., Murphy, J. A., & Naylor, D. A. 1999, *MNRAS*, 303, 659
- Hopkins, A. M. 2004, *ApJ*, 615, 209
- Hughes, D. H., Serjeant, S., Dunlop, J., Rowan-Robinson, M., Blain, A., Mann, R. G., Ivison, R., Peacock, J., Efstathiou, A., Gear, W., Oliver, S., Lawrence, A., Longair, M., Goldschmidt, P., & Jenness, T. 1998, *Nature*, 394, 241
- Humason, M. L., Mayall, N. U., & Sandage, A. R. 1956, *AJ*, 61, 97
- Infante, L. 1994, *A&A*, 282, 353
- Ivison, R. J., Alexander, D. M., Biggs, A. D., Brandt, W. N., Chapin, E. L., Coppin, K. E. K., Devlin, M. J., Dickinson, M., Dunlop, J., Dye, S., Eales, S. A., Frayer, D. T., Halpern, M., Hughes, D. H., Ibar, E., Kovács, A., Marsden, G., Monceli, L., Netterfield, C. B., Pascale, E., Patanchon, G., Rafferty, D. A., Rex, M., Schinnerer, E., Scott, D., Semisch, C., Smail, I., Swinbank, A. M., Truch, M. D. P., Tucker, G. S., Viero, M. P., Walter, F., Weiß, A., Wiebe, D. V., & Xue, Y. Q. 2009, *MNRAS*, 1794
- Ivison, R. J., Smail, I., Barger, A. J., Kneib, J.-P., Blain, A. W., Owen, F. N., Kerr, T. H., & Cowie, L. L. 2000, *MNRAS*, 315, 209

- Jing, Y. P. 2000, *ApJ*, 535, 30
- Jing, Y. P., Mo, H. J., Borner, G., & Fang, L. Z. 1995, *MNRAS*, 276, 417
- Jing, Y. P. & Suto, Y. 1998, *ApJ*, 494, L5+
- . 2000, *ApJ*, 529, L69
- . 2002, *ApJ*, 574, 538
- Kaiser, N. 1984, *ApJ*, 284, L9
- Kamen, E. W. & Su, J. K. 1999, *Introduction to Optimal Estimation* (London, UK: Springer-Verlag, 1999.)
- Kashlinsky, A. & Odenwald, S. 2000, *ApJ*, 528, 74
- Katz, N. 1991, *ApJ*, 368, 325
- Kauffmann, G., Nusser, A., & Steinmetz, M. 1997, *MNRAS*, 286, 795
- Kelsall, T., Weiland, J. L., Franz, B. A., Reach, W. T., Arendt, R. G., Dwek, E., Freudenreich, H. T., Hauser, M. G., Moseley, S. H., Odegard, N. P., Silverberg, R. F., & Wright, E. L. 1998, *ApJ*, 508, 44
- Kereš, D., Katz, N., Weinberg, D. H., & Davé, R. 2005, *MNRAS*, 363, 2
- Kerscher, M., Szapudi, I., & Szalay, A. S. 2000, *ApJ*, 535, L13
- Knox, L., Cooray, A., Eisenstein, D., & Haiman, Z. 2001, *ApJ*, 550, 7
- Kolatt, T. S., Bullock, J. S., Somerville, R. S., Sigad, Y., Jonsson, P., Kravtsov, A. V., Klypin, A. A., Primack, J. R., Faber, S. M., & Dekel, A. 1999, *ApJ*, 523, L109
- Komatsu, E., Dunkley, J., Nolta, M. R., Bennett, C. L., Gold, B., Hinshaw, G., Jarosik, N., Larson, D., Limon, M., Page, L., Spergel, D. N., Halpern, M., Hill, R. S., Kogut, A., Meyer, S. S., Tucker, G. S., Weiland, J. L., Wollack, E., & Wright, E. L. 2009, *ApJS*, 180, 330
- Lagache, G., Bavouzet, N., Fernandez-Conde, N., Ponthieu, N., Rodet, T., Dole, H., Miville-Deschênes, M.-A., & Puget, J.-L. 2007, *ApJ*, 665, L89
- Lagache, G., Dole, H., Puget, J.-L., Pérez-González, P. G., Le Floc'h, E., Rieke, G. H., Papovich, C., Egami, E., Alonso-Herrero, A., Engelbracht, C. W., Gordon, K. D., Misselt, K. A., & Morrison, J. E. 2004, *ApJS*, 154, 112
- Lagache, G. & Puget, J. L. 2000, *A&A*, 355, 17
- Lagache, G., Puget, J.-L., Abergel, A., Desert, F.-X., Dole, H., Bouchet, F. R., Boulanger, F., Ciliegi, P., Clements, D. L., Cesarsky, C., Elbaz, D., Franceschini, A., Gispert, R., Guiderdoni, B., Haffner, L. M., Harwit, M., Laureijs, R., Lemke, D., Moorwood, A. F. M., Oliver, S., Reach, W. T., Reynolds, R. J., Rowan-Robinson, M., Stickel, M., & Tufte, S. L. 2000, in *Lecture Notes in Physics*, Berlin Springer Verlag, Vol. 548, *ISO Survey of a Dusty Universe*, ed. D. Lemke, M. Stickel, & K. Wilke, 81–+

- Lahav, O., Fabian, A. C., Edge, A. C., & Putney, A. 1989, *MNRAS*, 238, 881
- Landy, S. D. & Szalay, A. S. 1993, *ApJ*, 412, 64
- Law, D. R., Majewski, S. R., & Johnston, K. V. 2009, *ApJ*, 703, L67
- Le Floch, E., Papovich, C., Dole, H., Bell, E. F., Lagache, G., Rieke, G. H., Egami, E., Pérez-González, P. G., Alonso-Herrero, A., Rieke, M. J., Blaylock, M., Engelbracht, C. W., Gordon, K. D., Hines, D. C., Misselt, K. A., Morrison, J. E., & Mould, J. 2005, *ApJ*, 632, 169
- Li, A. & Draine, B. T. 2001, *ApJ*, 554, 778
- Limber, D. N. 1953, *ApJ*, 117, 134
- Low, F. J. & Tucker, W. H. 1968, *Physical Review Letters*, 21, 1538
- Magliocchetti, M., Cirasuolo, M., McLure, R. J., Dunlop, J. S., Almaini, O., Foucaud, S., de Zotti, G., Simpson, C., & Sekiguchi, K. 2008, *MNRAS*, 383, 1131
- Magliocchetti, M., Maddox, S. J., Hawkins, E., Peacock, J. A., Bland-Hawthorn, J., Bridges, T., Cannon, R., Cole, S., Colless, M., Collins, C., Couch, W., Dalton, G., de Propriis, R., Driver, S. P., Efstathiou, G., Ellis, R. S., Frenk, C. S., Glazebrook, K., Jackson, C. A., Jones, B., Lahav, O., Lewis, I., Lumsden, S., Norberg, P., Peterson, B. A., Sutherland, W., & Taylor, K. 2004, *MNRAS*, 350, 1485
- Magliocchetti, M., Moscardini, L., Panuzzo, P., Granato, G. L., De Zotti, G., & Danese, L. 2001, *MNRAS*, 325, 1553
- Magliocchetti, M. & Porciani, C. 2003, *MNRAS*, 346, 186
- Magliocchetti, M., Silva, L., Lapi, A., de Zotti, G., Granato, G. L., Fadda, D., & Danese, L. 2007, *MNRAS*, 375, 1121
- Magnelli, B., Elbaz, D., Chary, R. R., Dickinson, M., Le Borgne, D., Frayer, D. T., & Willmer, C. N. A. 2009, *A&A*, 496, 57
- Marcillac, D., Rigby, J. R., Rieke, G. H., & Kelly, D. M. 2007, *ApJ*, 654, 825
- Marsden, G., Ade, P. A. R., Bock, J. J., Chapin, E. L., Devlin, M. J., Dicker, S. R., Griffin, M., Gundersen, J. O., Halpern, M., Hargrave, P. C., Hughes, D. H., Klein, J., Mauskopf, P., Magnelli, B., Moncelsi, L., Netterfield, C. B., Ngo, H., Olmi, L., Pascale, E., Patanchon, G., Rex, M., Scott, D., Semisch, C., Thomas, N., Truch, M. D. P., Tucker, C., Tucker, G. S., Viero, M. P., & Wiebe, D. V. 2009, *ApJ*, 707, 1729
- Marsden, G. A. 2007, PhD thesis, University of British Columbia
- Matsuhara, H., Wada, T., Matsuura, S., Nakagawa, T., Kawada, M., Ohyama, Y., Pearson, C. P., Oyabu, S., Takagi, T., Serjeant, S., White, G. J., Hanami, H., Watarai, H., Takeuchi, T. T., Kodama, T., Arimoto, N., Okamura, S., Lee, H. M., Pak, S., Im, M. S., Lee, M. G., Kim, W., Jeong, W., Imai, K., Fujishiro, N., Shirahata, M., Suzuki, T., Ihara, C., & Sakon, I. 2006, *PASJ*, 58, 673

- Miller, N. A., Fomalont, E. B., Kellermann, K. I., Mainieri, V., Norman, C., Padovani, P., Rosati, P., & Tozzi, P. 2008, *ApJS*, 179, 114
- Miville-Deschênes, M.-A. & Lagache, G. 2005, *ApJS*, 157, 302
- Miville-Deschênes, M.-A., Lagache, G., Boulanger, F., & Puget, J.-L. 2007, *A&A*, 469, 595
- Mo, H. J. & White, S. D. M. 1996, *MNRAS*, 282, 347
- Moore, B., Governato, F., Quinn, T., Stadel, J., & Lake, G. 1998, *ApJ*, 499, L5+
- Moscardini, L., Coles, P., Lucchin, F., & Matarrese, S. 1998, *MNRAS*, 299, 95
- Munshi, D., Valageas, P., van Waerbeke, L., & Heavens, A. 2008, *Phys. Rep.*, 462, 67
- Navarro, J. F., Frenk, C. S., & White, S. D. M. 1997, *ApJ*, 490, 493
- Negrello, M., Perrotta, F., González, J. G.-N., Silva, L., de Zotti, G., Granato, G. L., Baccigalupi, C., & Danese, L. 2007, *MNRAS*, 377, 1557
- Netterfield, C. B., Ade, P. A. R., Bock, J. J., Bond, J. R., Borrill, J., Boscaleri, A., Coble, K., Contaldi, C. R., Crill, B. P., de Bernardis, P., Farese, P., Ganga, K., Giacometti, M., Hivon, E., Hristov, V. V., Iacoangeli, A., Jaffe, A. H., Jones, W. C., Lange, A. E., Martinis, L., Masi, S., Mason, P., Mauskopf, P. D., Melchiorri, A., Montroy, T., Pascale, E., Piacentini, F., Pogosyan, D., Pongetti, F., Prunet, S., Romeo, G., Ruhl, J. E., & Scaramuzzi, F. 2002, *ApJ*, 571, 604
- Neyman, J., Scott, E. L., & Shane, C. D. 1953, *ApJ*, 117, 92
- Oke, J. B. 1971, *ApJ*, 170, 193
- Ouchi, M., Shimasaku, K., Okamura, S., Furusawa, H., Kashikawa, N., Ota, K., Doi, M., Hamabe, M., Kimura, M., Komiyama, Y., Miyazaki, M., Miyazaki, S., Nakata, F., Sekiguchi, M., Yagi, M., & Yasuda, N. 2004, *ApJ*, 611, 685
- Overzier, R. A., Röttgering, H. J. A., Rengelink, R. B., & Wilman, R. J. 2003, *A&A*, 405, 53
- Pascale, E. 2007, PhD thesis, University of Toronto
- Pascale, E., Ade, P. A. R., Bock, J. J., Chapin, E. L., Chung, J., Devlin, M. J., Dicker, S., Griffin, M., Gundersen, J. O., Halpern, M., Hargrave, P. C., Hughes, D. H., Klein, J., MacTavish, C. J., Marsden, G., Martin, P. G., Martin, T. G., Mauskopf, P., Netterfield, C. B., Olmi, L., Patanchon, G., Rex, M., Scott, D., Semisch, C., Thomas, N., Truch, M. D. P., Tucker, C., Tucker, G. S., Viero, M. P., & Wiebe, D. V. 2008, *ApJ*, 681, 400
- Pascale, E., Ade, P. A. R., Bock, J. J., Chapin, E. L., Devlin, M. J., Dye, S., Eales, S. A., Griffin, M., Gundersen, J. O., Halpern, M., Hargrave, P. C., Hughes, D. H., Klein, J., Marsden, G., Mauskopf, P., Monceli, L., Ngo, H., Netterfield, C. B., Olmi, L., Patanchon, G., Rex, M., Scott, D., Semisch, C., Thomas, N., Truch, M. D. P., Tucker, C., Tucker, G. S., Viero, M. P., & Wiebe, D. V. 2009, *ApJ*, 707, 1740

- Patanchon, G., Ade, P. A. R., Bock, J. J., Chapin, E. L., Devlin, M. J., Dicker, S., Griffin, M., Gundersen, J. O., Halpern, M., Hargrave, P. C., Hughes, D. H., Klein, J., Marsden, G., Martin, P. G., Mauskopf, P., Netterfield, C. B., Olmi, L., Pascale, E., Rex, M., Scott, D., Semisch, C., Truch, M. D. P., Tucker, C., Tucker, G. S., Viero, M. P., & Wiebe, D. V. 2008, *ApJ*, 681, 708
- Patanchon, G., Ade, P. A. R., Bock, J. J., Chapin, E. L., Devlin, M. J., Dicker, S. R., Griffin, M., Gundersen, J. O., Halpern, M., Hargrave, P. C., Hughes, D. H., Klein, J., Marsden, G., Mauskopf, P., Moncelsi, L., Netterfield, C. B., Olmi, L., Pascale, E., Rex, M., Scott, D., Semisch, C., Thomas, N., Truch, M. D. P., Tucker, C., Tucker, G. S., Viero, M. P., & Wiebe, D. V. 2009, *ApJ*, 707, 1750
- Peacock, J. A. 1999, *Cosmological Physics* (*Cosmological Physics*, by John A. Peacock, pp. 704. ISBN 052141072X. Cambridge, UK: Cambridge University Press, January 1999.)
- Peacock, J. A., Cole, S., Norberg, P., Baugh, C. M., Bland-Hawthorn, J., Bridges, T., Cannon, R. D., Colless, M., Collins, C., Couch, W., Dalton, G., Deeley, K., De Propriis, R., Driver, S. P., Efstathiou, G., Ellis, R. S., Frenk, C. S., Glazebrook, K., Jackson, C., Lahav, O., Lewis, I., Lumsden, S., Maddox, S., Percival, W. J., Peterson, B. A., Price, I., Sutherland, W., & Taylor, K. 2001, *Nature*, 410, 169
- Peacock, J. A., Rowan-Robinson, M., Blain, A. W., Dunlop, J. S., Efstathiou, A., Hughes, D. H., Jenness, T., Ivison, R. J., Lawrence, A., Longair, M. S., Mann, R. G., Oliver, S. J., & Serjeant, S. 2000, *MNRAS*, 318, 535
- Peacock, J. A. & Smith, R. E. 2000, *MNRAS*, 318, 1144
- Peebles, P. J. E. 1980, *The large-scale structure of the universe* (Princeton University Press)
- . 1993, *Principles of physical cosmology* (Princeton University Press)
- Peebles, P. J. E. & Hauser, M. G. 1974, *ApJS*, 28, 19
- Penzias, A. A. & Wilson, R. W. 1965, *ApJ*, 142, 419
- Perrotta, F., Magliocchetti, M., Baccigalupi, C., Bartelmann, M., De Zotti, G., Granato, G. L., Silva, L., & Danese, L. 2003, *MNRAS*, 338, 623
- Porciani, C., Magliocchetti, M., & Norberg, P. 2004, *MNRAS*, 355, 1010
- Press, W. H. 2002, *Numerical recipes in C++ : the art of scientific computing* (*Numerical recipes in C++ : the art of scientific computing* by William H. Press. xxviii, 1,002 p. : ill. ; 26 cm. Includes bibliographical references and index. ISBN : 0521750334)
- Press, W. H. & Schechter, P. 1974, *ApJ*, 187, 425
- Puget, J.-L., Abergel, A., Bernard, J.-P., Boulanger, F., Burton, W. B., Desert, F.-X., & Hartmann, D. 1996, *A&A*, 308, L5+
- Quadri, R. F., Williams, R. J., Lee, K.-S., Franx, M., van Dokkum, P., & Brammer, G. B. 2008, *ApJ*, 685, L1

- Reddy, N. A., Erb, D. K., Steidel, C. C., Shapley, A. E., Adelberger, K. L., & Pettini, M. 2005, *ApJ*, 633, 748
- Refregier, A. 2003, *ARA&A*, 41, 645
- Roche, N. & Eales, S. A. 1999, *MNRAS*, 307, 703
- Rodighiero, G., Vaccari, M., Franceschini, A., Tresse, L., Le Fevre, O., Le Brun, V., Mancini, C., Matute, I., Cimatti, A., Marchetti, L., Ilbert, O., Arnouts, S., Bolzonella, M., Zucca, E., Bardelli, S., Lonsdale, C. J., Shupe, D., Surace, J., Rowan-Robinson, M., Garilli, B., Zamorani, G., Pozzetti, L., Bondi, M., de la Torre, S., Vergani, D., Santini, P., Grazian, A., & Fontana, A. 2009, *ArXiv e-prints*
- Ruhl, J., Ade, P. A. R., Carlstrom, J. E., Cho, H., Crawford, T., Dobbs, M., Greer, C. H., Halverson, N. W., Holzzapfel, W. L., Lanting, T. M., Lee, A. T., Leitch, E. M., Leong, J., Lu, W., Lueker, M., Mehl, J., Meyer, S. S., Mohr, J. J., Padin, S., Plagge, T., Pryke, C., Runyan, M. C., Schwan, D., Sharp, M. K., Spieler, H., Staniszewski, Z., & Stark, A. A. 2004, in *Society of Photo-Optical Instrumentation Engineers (SPIE) Conference Series*, Vol. 5498, *Society of Photo-Optical Instrumentation Engineers (SPIE) Conference Series*, ed. C. M. Bradford, P. A. R. Ade, J. E. Aguirre, J. J. Bock, M. Dragovan, L. Duband, L. Earle, J. Glenn, H. Matsuhara, B. J. Naylor, H. T. Nguyen, M. Yun, & J. Zmuidzinas, 11–29
- Saintonge, A., Tran, K., & Holden, B. P. 2008, *ApJ*, 685, L113
- Saunders, W., Rowan-Robinson, M., & Lawrence, A. 1992, *MNRAS*, 258, 134
- Scheuer, P. A. G. & Ryle, M. 1957, in *Proceedings of the Cambridge Philosophical Society*, Vol. 53, *Proceedings of the Cambridge Philosophical Society*, 764–+
- Schlegel, D. J., Finkbeiner, D. P., & Davis, M. 1998, *ApJ*, 500, 525
- Scott, D. & White, M. 1999, *A&A*, 346, 1
- Scott, S. E., Dunlop, J. S., & Serjeant, S. 2006, *MNRAS*, 370, 1057
- Semisch, C. 2009, PhD thesis, University of Pennsylvania
- Sheth, R. K., Jimenez, R., Panter, B., & Heavens, A. F. 2006, *ApJ*, 650, L25
- Sheth, R. K., Mo, H. J., & Tormen, G. 2001, *MNRAS*, 323, 1
- Sheth, R. K. & Tormen, G. 1999, *MNRAS*, 308, 119
- Siringo, G., Kreysa, E., Kovács, A., Schuller, F., Weiß, A., Esch, W., Gemünd, H., Jethava, N., Lundershausen, G., Colin, A., Güsten, R., Menten, K. M., Beelen, A., Bertoldi, F., Beeman, J. W., & Haller, E. E. 2009, *A&A*, 497, 945
- Smail, I., Ivison, R. J., & Blain, A. W. 1997, *ApJ*, 490, L5+
- Soifer, B. T., Sanders, D. B., Madore, B. F., Neugebauer, G., Danielson, G. E., Elias, J. H., Lonsdale, C. J., & Rice, W. L. 1987, *ApJ*, 320, 238

- Spergel, D. N., Verde, L., Peiris, H. V., Komatsu, E., Nolta, M. R., Bennett, C. L., Halpern, M., Hinshaw, G., Jarosik, N., Kogut, A., Limon, M., Meyer, S. S., Page, L., Tucker, G. S., Weiland, J. L., Wollack, E., & Wright, E. L. 2003, *ApJS*, 148, 175
- Springel, V., White, S. D. M., Jenkins, A., Frenk, C. S., Yoshida, N., Gao, L., Navarro, J., Thacker, R., Croton, D., Helly, J., Peacock, J. A., Cole, S., Thomas, P., Couchman, H., Evrard, A., Colberg, J., & Pearce, F. 2005, *Nature*, 435, 629
- Stanford, S. A., Eisenhardt, P. R., & Dickinson, M. 1998, *ApJ*, 492, 461
- Steidel, C. C., Giavalisco, M., Pettini, M., Dickinson, M., & Adelberger, K. L. 1996, *ApJ*, 462, L17+
- Steidel, C. C., Shapley, A. E., Pettini, M., Adelberger, K. L., Erb, D. K., Reddy, N. A., & Hunt, M. P. 2004, *ApJ*, 604, 534
- Sunyaev, R. A. & Zeldovich, Y. B. 1972, *Comments on Astrophysics and Space Physics*, 4, 173
- Tacconi, L. J., Genzel, R., Smail, I., Neri, R., Chapman, S. C., Ivison, R. J., Blain, A., Cox, P., Omont, A., Bertoldi, F., Greve, T., Förster Schreiber, N. M., Genel, S., Lutz, D., Swinbank, A. M., Shapley, A. E., Erb, D. K., Cimatti, A., Daddi, E., & Baker, A. J. 2008, *ApJ*, 680, 246
- Tinker, J. L., Wechsler, R. H., & Zheng, Z. 2009, *ArXiv e-prints*
- Tormen, G. 1997, *MNRAS*, 290, 411
- Totsuji, H. & Kihara, T. 1969, *PASJ*, 21, 221
- Tran, K., Saintonge, A., Moustakas, J., Bai, L., Gonzalez, A. H., Holden, B. P., Zaritsky, D., & Kautsch, S. J. 2009, *ApJ*, 705, 809
- Truch, M. D. P. 2007, PhD thesis, Brown University
- Truch, M. D. P., Ade, P. A. R., Bock, J. J., Chapin, E. L., Devlin, M. J., Dicker, S., Griffin, M., Gundersen, J. O., Halpern, M., Hargrave, P. C., Hughes, D. H., Klein, J., Marsden, G., Martin, P. G., Maukopf, P., Netterfield, C. B., Olmi, L., Pascale, E., Patanchon, G., Rex, M., Scott, D., Semisch, C., Tucker, C., Tucker, G. S., Viero, M. P., & Wiebe, D. V. 2008, *ApJ*, 681, 415
- Truch, M. D. P., Ade, P. A. R., Bock, J. J., Chapin, E. L., Devlin, M. J., Dicker, S. R., Griffin, M., Gundersen, J. O., Halpern, M., Hargrave, P. C., Hughes, D. H., Klein, J., Marsden, G., Martin, P. G., Maukopf, P., Moncelsi, L., Barth Netterfield, C., Olmi, L., Pascale, E., Patanchon, G., Rex, M., Scott, D., Semisch, C., Thomas, N. E., Tucker, C., Tucker, G. S., Viero, M. P., & Wiebe, D. V. 2009, *ApJ*, 707, 1723
- Viero, M. P., Ade, P. A. R., Bock, J. J., Chapin, E. L., Devlin, M. J., Griffin, M., Gundersen, J. O., Halpern, M., Hargrave, P. C., Hughes, D. H., Klein, J., MacTavish, C. J., Marsden, G., Martin, P. G., Maukopf, P., Moncelsi, L., Negrello, M., Netterfield, C. B., Olmi, L., Pascale, E., Patanchon, G., Rex, M., Scott, D., Semisch, C., Thomas, N., Truch, M. D. P., Tucker, C., Tucker, G. S., & Wiebe, D. V. 2009, *ApJ*, 707, 1766

- Waddington, I., Oliver, S. J., Babbedge, T. S. R., Fang, F., Farrah, D., Franceschini, A., Gonzalez-Solares, E. A., Lonsdale, C. J., Rodighiero, G., Rowan-Robinson, M., Shupe, D. L., Surace, J. A., Vaccari, M., & Xu, C. K. 2007, *MNRAS*, 381, 1437
- Warren, M. S., Quinn, P. J., Salmon, J. K., & Zurek, W. H. 1992, *ApJ*, 399, 405
- Watson, D. F., Berlind, A. A., McBride, C. K., & Masjedi, M. 2009, *ArXiv e-prints*
- Webb, T. M., Eales, S. A., Lilly, S. J., Clements, D. L., Dunne, L., Gear, W. K., Ivison, R. J., Flores, H., & Yun, M. 2003, *ApJ*, 587, 41
- White, S. D. M. & Rees, M. J. 1978, *MNRAS*, 183, 341
- Wiebe, D. V. 2008, PhD thesis, University of Toronto
- Wilson, G. W., Austermann, J. E., Perera, T. A., Scott, K. S., Ade, P. A. R., Bock, J. J., Glenn, J., Golwala, S. R., Kim, S., Kang, Y., Lydon, D., Mauskopf, P. D., Predmore, C. R., Roberts, C. M., Souccar, K., & Yun, M. S. 2008, *MNRAS*, 386, 807
- Zehavi, I., Blanton, M. R., Frieman, J. A., Weinberg, D. H., Mo, H. J., Strauss, M. A., Anderson, S. F., Annis, J., Bahcall, N. A., Bernardi, M., Briggs, J. W., Brinkmann, J., Burles, S., Carey, L., Castander, F. J., Connolly, A. J., Csabai, I., Dalcanton, J. J., Dodelson, S., Doi, M., Eisenstein, D., Evans, M. L., Finkbeiner, D. P., Friedman, S., Fukugita, M., Gunn, J. E., Hennessy, G. S., Hindsley, R. B., Ivezić, Ž., Kent, S., Knapp, G. R., Kron, R., Kunszt, P., Lamb, D. Q., Leger, R. F., Long, D. C., Loveday, J., Lupton, R. H., McKay, T., Meiksin, A., Merrelli, A., Munn, J. A., Narayanan, V., Newcomb, M., Nichol, R. C., Owen, R., Peoples, J., Pope, A., Rockosi, C. M., Schlegel, D., Schneider, D. P., Scoccimarro, R., Sheth, R. K., Siegmund, W., Smee, S., Snir, Y., Stebbins, A., Stoughton, C., SubbaRao, M., Szalay, A. S., Szapudi, I., Tegmark, M., Tucker, D. L., Uomoto, A., Vanden Berk, D., Vogeley, M. S., Waddell, P., Yanny, B., & York, D. G. 2002, *ApJ*, 571, 172
- Zehavi, I., Zheng, Z., Weinberg, D. H., Frieman, J. A., Berlind, A. A., Blanton, M. R., Scoccimarro, R., Sheth, R. K., Strauss, M. A., Kayo, I., Suto, Y., Fukugita, M., Nakamura, O., Bahcall, N. A., Brinkmann, J., Gunn, J. E., Hennessy, G. S., Ivezić, Ž., Knapp, G. R., Loveday, J., Meiksin, A., Schlegel, D. J., Schneider, D. P., Szapudi, I., Tegmark, M., Vogeley, M. S., & York, D. G. 2005, *ApJ*, 630, 1
- Zheng, Z., Berlind, A. A., Weinberg, D. H., Benson, A. J., Baugh, C. M., Cole, S., Davé, R., Frenk, C. S., Katz, N., & Lacey, C. G. 2005, *ApJ*, 633, 791